# An investigation on the mechanics of nanometric cutting for hard-brittle materials at elevated temperatures

Saeed Zare Chavoshi

A dissertation submitted for the degree of Doctor of Philosophy in Manufacturing Engineering

University of Strathclyde

Department of Design, Manufacture and Engineering Management

September 2016

This copy of the thesis has been supplied on condition that anyone who consults it is understood to recognise that the copyright rests with its author and that no quotation from the thesis and no information derived from it may be published without the prior written consent of the author or of the University (as deemed to be appropriate).

# Abstract

Due to their exceptional physical and chemical properties such as high strength, high thermal conductivity, high stability at high temperature, high resistance to shocks, low thermal expansion and low density, silicon and silicon carbide (SiC) have become consummate candidates for optoelectronics, semiconductor and tribological applications. In particular, 3C-SiC, as a zinc blende structured SiC, possesses the highest fracture toughness, hardness, electron mobility and electron saturation velocity amongst the SiC polytypes. Thus, it has drawn substantial attention as a candidate substrate material for nano-devices which require high performance in extreme environments.

Nanometric cutting is a promising ultra precision manufacturing process for manufacturing of 3D silicon and SiC based components which require submicron form accuracy and nanometric smooth finish. However, silicon and 3C-SiC have poor machinability at room temperature due to their relatively low fracture toughness and high hardness. A common understanding is that the yield strength and hardness of silicon and 3C-SiC will reduce under high temperature. As such, their fracture toughness increase which will ease plastic deformation and improve their machinabilities primarily as a result of thermally-generated intrinsic defects and thermal softening processes. However, the extent has never been reported although this knowhow could be vital in implementing the hot machining of silicon and SiC with the assistance of laser processing.

This dissertation aims to gain an in-depth understanding of nanoscale mechanisms involved in nanometric cutting of hard-brittle materials such as silicon and 3C-SiC at elevated temperatures through molecular dynamics (MD) simulation and experimental trials. To this end, three-dimensional MD models of nanometric cutting were developed and different types of interatomic potential functions i.e. Tersoff, modified Tersoff, ABOP and SW were adopted to describe the interactions between atoms. In order to obtain reliable results, the equilibrium lattice constants were calculated at different temperatures for the employed potential functions. To perform the MD simulations, LAMMPS software was employed on a HPC service which was coupled with OVITO to visualise and post-process the atomistic data. Material flow behaviour, cutting chip characteristics, cutting forces and specific cutting energy, yielding stresses, stress and temperature on the cutting edge of the diamond tool, tool wear, defect-mediated plasticity and amorphization processes were calculated and analysed to quantify the differences in the cutting behaviour at different temperatures. Furthermore, In-

situ high temperature nanoscratching (~500°C) of silicon wafer under reduced oxygen condition through an overpressure of pure Argon was carried out using a Berkovich tip with a ramp load at low and high scratching speeds. Ex-situ Raman spectroscopy and AFM analysis were performed to characterize high pressure phase transformation, nanoscratch topography, nanoscratch hardness and condition of the nanoindenter tip in nanoscratching at room and elevated temperatures.

MD simulation results showed that the workpiece atoms underneath the cutting tool experienced a rotational flow akin to fluids. Moreover, the degree of flow in terms of vorticity was found higher on the (111) crystal plane, signifying better machinability on this orientation. Furthermore, it was observed that the degree of turbulence in the machining zone increases linearly with machining operation temperature. The cutting temperature showed significant dependence on the location and position of the stagnation region in the cutting zone of the substrate. In general, when cutting was performed on the (111) plane, the stagnation region (irrespective of the cutting temperature) was observed to locate at an upper position than that for the (010) and (110) planes. Also, at high temperatures, the stagnation region was observed to shift downwards than what was observed at room temperature. Another point of interest was the increase of subsurface deformation depth of the workpiece while cutting the (111) crystal plane at elevated temperatures.

Dislocation nucleation and formation of stacking faults were identified in conjunction with amorphization of silicon as the meditators of crystal plasticity in single crystal silicon during nanometric cutting process on different crystallographic planes at various temperatures. MD simulations revealed strong anisotropic dependence behaviour of dislocation activation and stacking fault formation. Likewise, while cutting 3C-SiC on the (110)<00$\bar{1}$>, formation and subsequent annihilation of stacking fault-couple at high temperatures, i.e. 2000 K and 3000 K, and generation of the cross-junctions between pairs of counter stacking faults meditated by the gliding of Shockley partials at 3000 K were observed. An observation of particular interest, while cutting 3C-SiC, was the shift to the (110) cleavage at cutting temperatures higher than 2000 K. The initial response of both the silicon and 3C-SiC substrates was found to be solid-state amorphization for all the studied cases. Further analysis through virtual X-ray diffraction (XRD) and radial distribution function (RDF) showed the crystal quality and structural changes of the substrate during nanometric cutting.

No symptom of any atom-by-atom attrition wear and plastic deformation of the diamond cutting tool was observed during nanometric cutting of silicon irrespective of the cutting

plane or the cutting temperature under vacuum condition. However, while cutting 3C-SiC, cutting tool showed severe wear and plastic deformation. It was found that the atom-by-atom attrition wear and plastic deformation of the diamond cutting tool could be alleviated while cutting 3C-SiC at high temperatures. Nevertheless, chemical wear i.e. dissolution-diffusion and adhesion wear is plausible to be accelerated at high temperatures.

Raman spectroscopy was successfully used to identify the formation of metastable silicon phases during nanoscratching experiments at room and high temperatures. The probability of forming high pressure phases of Si-III and Si-XII was found to increase above the threshold load of 5 mN during room temperature nanoscratching experiment at low scratching speed. At high scratching speed, small remnants of Si-XII and Si-III phases were detected when the scratching load was greater than a threshold value i.e. ~9.5 mN. When high temperature nanoscratching was carried out at low and high speeds, no remnants of polymorph phases were observed along the nanoscratch residual track, suggesting the transition of metastable silicon phases (Si-III and Si-XII) into thermodynamic stable Si-I. Further analysis using AFM showed that the residual scratch morphologies and nanoscratch hardness were profoundly influenced by the temperature and scratching speed.

# Acknowledgements

This thesis was completed with the support and encouragement of many colleagues. First and foremost, I would like to thank my supervisor, Prof. Xichun Luo, for his continued support and patience. I would also like to acknowledge the help of Dr. Saurav Goel from Cranfield University, UK, and Dr. Shuozhi Xu from Georgia Institute of Technology, USA, for their valuable advice.

Special thanks go to Prof. Hanshan Dong and Dr. Santiago Corujeira Gallo from the University of Birmingham, Dr. Shigeng Song and Hin On Martin Chu from the University of West of Scotland, and Dr. Richard Black from the University of Strathclyde, who provided me equipment, support and assistance for the experimental trials.

Financial support from the University of Strathclyde and EPSRC (EP/K018345/1) grant is thankfully acknowledged. I also acknowledge the use of the EPSRC (EP/K000586/1) funded ARCHIE-WeSt High Performance Computer at the University of Strathclyde.

## Declaration

This thesis is the result of the author's original research. It has been composed by the author and has not been previously submitted for examination which has led to the award of a degree.

The copyright of this thesis belongs to the author under the terms of the United Kingdom Copyright Acts as qualified by University of Strathclyde Regulation 3.50. Due acknowledgement must always be made of the use of any material contained in, or derived from, this thesis.

# Table of Content

Abstract ..... I
Acknowledgements ..... IV
Declaration ..... V
Table of Content ..... VI
List of Figures ..... IX
List of Tables ..... XIV
Abbreviations ..... XV
Nomenclature ..... XVII
List of Publications by the Candidate ..... XIX
Chapter 1: Introduction ..... 1
1.1. Research background ..... 1
1.2. Aim and objectives of the research ..... 6
1.3. Structure of the thesis ..... 6
Chapter 2: Literature review ..... 8
2.1. Hybrid MNM processes ..... 8
2.2. MD simulation approach ..... 11
2.2.1. Potential energy function ..... 14
2.2.2. Ensembles ..... 21
2.2.3. Boundary conditions ..... 22
2.3. Previous studies on nanometric cutting and nanoindentation at elevated temperatures ..... 22
2.4. Summary ..... 26
Chapter 3: Modelling and simulation of nanometric cutting process at elevated temperatures ..... 28
3.1. Generic scheme of performing an MD simulation of nanometric cutting ..... 28
3.2. Description of the nanometric cutting model ..... 28
3.3. Potential energy functions employed in MD simulations ..... 33
3.4. Geometry creation and simulation procedure ..... 35
3.5. Visualization of atomic trajectories ..... 38
3.6. Summary ..... 39
Chapter 4: MD simulation results for nanometric cutting of silicon at elevated temperatures ..... 40
4.1. Introduction ..... 40
4.2. Plastic flow behaviour ..... 40
4.2.1. Atomic flow field ..... 41
4.2.2. Stagnation region and friction angle ..... 49

4.3. Chip related phenomena ... 53
4.3.1. Chip formation and mechanisms ... 55
4.3.2. Geometry and characteristics of the chip ... 59
4.3.3. Forces and associates parameters exerted by the tool rake face on the chip ... 66
4.3.4. Extent of temperature increase during chip formation process ... 72
4.4. Cutting forces and specific cutting energies ... 73
4.5. Machining temperature ... 79
4.6. von Mises equivalent strain ... 81
4.7. Yielding stresses ... 83
4.8. Machining stress and temperature on the cutting edge of the tool ... 87
4.9. Deformation mechanisms ... 89
4.9.1. Structural changes ... 91
4.9.2. Defect-mediated plasticity ... 94
4.10. Summary ... 120
Chapter 5: MD simulation results for nanometric cutting of 3C-SiC at elevated temperatures ... 123
5.1. Introduction ... 123
5.2. Plastic flow behaviour ... 123
5.3. Stagnation region and friction angle ... 128
5.4. Occurrence of cleavage ... 130
5.5. Chip related phenomena ... 134
5.6. Cutting forces and specific cutting energies ... 139
5.7. Yielding stresses ... 142
5.8. Stress, temperature and wear of the cutting edge of the tool ... 144
5.9. Deformation mechanisms ... 149
5.9.1. Analysis of crystal defects ... 149
5.9.2. Structural changes ... 173
5.10. Summary ... 178
Chapter 6: Experimental studies on nanometric cutting of silicon at elevated temperatures ... 180
6.1. Introduction ... 180
6.2. Experimental setup and test procedure ... 181
6.2.1. Equipment ... 181
6.2.2. Workpiece and cutting tool ... 183
6.2.3. Experimental procedure ... 185
6.3. Experimental observations and discussion ... 188
6.3.1. Scratch topography ... 188

6.3.2. Nanoscratching-induced phase transformation ........ 191
6.3.3. Condition of the nanoindenter tip after nanoscratching ........ 197
6.4. Summary ........ 200
Chapter 7: Conclusions and recommendations ........ 202
7.1. Assessment of the research ........ 202
7.2. Conclusions ........ 203
7.3. Recommendations for future work ........ 208
7.3.1. Study on mechanisms involved in tool wear ........ 209
7.3.2. Research on polycrystalline silicon and silicon carbide ........ 209
7.3.3. Investigation on influence of coolant ........ 210
7.3.4. Development of interatomic potential functions ........ 210
7.3.5. In situ observation of the scratching-induced phase transformation ........ 211
7.3.6. Study on multi-pass nanometric cutting ........ 211
7.3.7. Investigation on effect of cutting speed ........ 211
Appendices ........ 213
A. Phase instability and melting temperature of silicon predicted by the ABOP and modified Tersoff ........ 213
B. Forces and associated parameters related to the chip while cutting silicon ........ 215
C. Accuracy of the modified Tersoff and ABOP potentials in reproducing the mechanical properties of silicon ........ 218
D. Cutting forces and associated parameters while cutting silicon ........ 222
E. Yielding stresses while cutting silicon ........ 224
F. Equations used for calculating yielding measures ........ 226
G. Stresses and temperatures on the cutting edge of the diamond tool while cutting silicon ........ 228
H. Testing of the SW potential energy function ........ 230
I. Testing of the ABOP and Tersoff potential energy functions for 3C-SiC ........ 234
J. Forces and specific cutting energy while cutting 3C-SiC ........ 239
K. Yielding stresses while cutting 3C-SiC ........ 241
L. Stresses and temperature on the cutting edge of the diamond tool while cutting 3C-SiC ........ 243
References ........ 245

# List of Figures


Figure 2.1: Classification of hybrid MNM processes ........................................................................ 11
Figure 2.2: Mechanical strength as a function of temperature [21] .................................................... 11
Figure 2.3: (a) Scheme for performing MD simulation of nanometric cutting (b) an atom '*i*' having mass '*m*' at a distance of '*r*' from the other atom exerts force '*F*' on other atom, when given a velocity '*v*' ................................................................................................................................................ 13
Figure 3.1: Generic scheme of performing an MD simulation of nanometric cutting .......................... 28
Figure 3.2: Schematic of MD simulation model .................................................................................. 29
Figure 3.3: 2D schematic of the MD simulation model illustrating the uncut chip thickness, tool tip radius, rake and clearance angles of the cutting tool ........................................................................... 31
Figure 4.1: Five regions in the substrate: I- Cut region, II- Underneath the flank face, III- Between the flank face and tool tip IV- Ahead and beneath the tool tip, V- Uncut region. Red arrows are flow vectors around the stagnation region. In the detailed snapshot, θs1,2 and h1,2 represent the limiting bounds of the stagnation angles respectively in the stagnation region. .............................................. 43
Figure 4.2: Snapshots of atomic flow field in the XY plane while cutting silicon on the different crystal planes at 300 K. The red arrows indicate displacement vectors of atoms and their lengths demonstrate the magnitude of displacement. The atoms of the cutting tool are deliberately kept hidden so the position of the cutting tool with regard to the five regions in the substrate can be traced from Figure 4.1. ........................................................................................................................................ 44
Figure 4.3: Snapshots of atomic flow field while cutting silicon on the different crystal planes at 1173 K. At high temperatures, the upward movement of atoms is eliminated, leading to decrease of the spring back on the flank face. More distorted atoms are highlighted by grey circles. ......................... 46
Figure 4.4: Snapshot of atomic flow field while cutting silicon on the (110) crystal plane at 1500 K. Substrate atoms move along the cutting and slip system directions owing to the very weak interaction between atoms and viscous flow of the material. Chaotic behaviour of the atoms can be observed as well.................................................................................................................................................. 48
Figure 4.5: Displacement of different layers in y direction ............................................................... 50
Figure 4.6: A snapshot of MD simulation demonstrating nominal rake angle, effective rake angle αef, shear plane angle, stagnation region, cutting and friction forces. The elemental volume represents the volume of material (1×1.5×3 $nm^3$) considered for monitoring the variations of temperature during chip formation (only 2D representation is shown here). ..................................................................... 52
Figure 4.7: Priamary and secondary shear zones ................................................................................ 54
Figure 4.8: Displacement vectors of chip atoms and their corresponding angles in the *XY* plane. The chip velocity angle was calculated for the atoms located on the right side of the chip. ....................... 56
Figure 4.9: Chip velocity angle as a function of temperature and crystal plane obtained by the modified Tersoff and ABOP potential functions .................................................................................. 58
Figure 4.10: Cross-sectional morphology of the cutting chip and subsurface crystal deformation of single crystal silicon while cutting the (010) crystal plane. Atoms in white colour are amorphous atoms. ................................................................................................................................................ 60
Figure 4.11: Variations of the chip thickness while cutting silicon on different crystallographic planes at various temperatures obtained by modified Tersoff and ABOP potential functions ........................ 61
Figure 4.12: Variations of the chip ratio while cutting silicon on different crystallographic planes at various temperatures ........................................................................................................................... 63
Figure 4.13: Number of atoms in the cutting chip as a function of temperature and crystal plane ...... 63

Figure 4.14: Increase of the subsurface deformation layer depth with temperature on different crystal planes ........ 64
Figure 4.15: Diamond cubic lattice structure of silicon ........ 68
Figure 4.16: Variations of the resultant force exerted by the tool rake face on the chip, and friction coefficient at the tool rake face/chip interface while cutting silicon on different crystallographic planes at various temperatures ........ 70
Figure 4.17: Chip temperature as a function of substrate temperature and crystal surface ........ 70
Figure 4.18: Variations of the shear plane angle while cutting silicon on different crystallographic planes at various temperatures obtained by modified Tersoff and ABOP potential functions ........ 72
Figure 4.19: Extent of temperature increase in the deformation zone during chip formation while cutting silicon on various crystal planes and at different temperatures ........ 73
Figure 4.20: An MD output of the force plot showing the region where the average cutting forces and specific cutting energy were measured ........ 75
Figure 4.21: Specific cutting energy as a function of temperature and crystal plane ........ 77
Figure 4.22: Variation in the average force ratio while cutting silicon on different crystallographic planes at various temperatures ........ 79
Figure 4.23: Evolution of the average temperature of Newtonian atoms of workpiece while cutting on the (110) crystal plane ........ 80
Figure 4.24: Anisotropy in the cutting temperature in the Newtonian atoms of the workpiece obtained from the two potentials ........ 80
Figure 4.25: The local von Mises strain distribution and cut chip thickness after 20 nm cutting distance. A wider primary shear zone can be seen on the (110) plane. ........ 83
Figure 4.26: Maximum von Mises stress in the cutting zone while machining silicon on different crystallographic planes at various temperatures ........ 85
Figure 4.27: Evolution of the temperature and von Mises stress in the cutting zone recorded on the same plot while cutting on the (010) plane ........ 87
Figure 4.28: Average von Mises stress measured on the cutting edge of the diamond tool while machining different orientations of silicon at different cutting temperatures ........ 89
Figure 4.29: Radial distribution function, *g(r)*, showing interatomic bond lengths at different temperatures before and during nanometric cutting of silicon on the (010) crystal plane. The pattern for the other crystal planes remained unchanged and hence not presented here. ........ 92
Figure 4.30: Virtual XRD patterns computed for silicon before nanometric cutting at a) 300 K b) 1173 k and c) after nanometric cutting d) Standard XRD pattern of silicon powders [115] ........ 94
Figure 4.31: MD simulation output illustrating amorphous atoms (white atoms) and dislocation nucleation while cutting the (010) plane at 300 K at a cutting distance of a) 10 nm b) 20 nm. Blue, green and red rods, respectively, stand for the perfect, Shockley partial and other partial dislocations. ........ 97
Figure 4.32: Dislocation nucleation while cutting the (010) plane at 750 K at a cutting distance of a) 10 nm b) 20 nm. ........ 98
Figure 4.33: Dislocation nucleation while cutting the (010) plane at 850 K at a cutting distance of a) 10 nm b) 20 nm. ........ 99
Figure 4.34: Dislocation nucleation while cutting the (010) plane at 1173 K at a cutting distance of a) 10 nm b) 20 nm. ........ 100
Figure 4.35: Dislocation nucleation while cutting the (010) plane at 1273 K at a cutting distance of a) 10 nm b) 20 nm. ........ 101
Figure 4.36: Dislocation nucleation while cutting the (010) plane at 1500 K at a cutting distance of a) 10 nm b) 20 nm. ........ 102

Figure 4.37: Dislocation nucleation while cutting the (110) plane at 300 K at a cutting distance of a) 10 nm b) 20 nm. 106
Figure 4.38: Formation of crystal defects while cutting the (110) plane at 750 K at a cutting distance of a) 10 nm b) 20 nm. Pink rod represents the stair-rod partial dislocation. 107
Figure 4.39: Formation of crystal defects while cutting the (110) plane at 850 K at a cutting distance of a) 10 nm b) 20 nm 108
Figure 4.40: Formation of crystal defects while cutting the (110) plane at 1173 K at a cutting distance of a) 10 nm b) 20 nm 109
Figure 4.41: Formation of crystal defects while cutting the (110) plane at 1273 K at a cutting distance of a) 10 nm b) 20 nm 110
Figure 4.42: Formation of crystal defects while cutting the (110) plane at 1500 K at a cutting distance of a) 10 nm b) 20 nm 111
Figure 4.43: Dislocation nucleation while cutting the (111) plane at 300 K at a cutting distance of a) 10 nm b) 20 nm. 114
Figure 4.44: Dislocation nucleation while cutting the (111) plane at 750 K at a cutting distance of a) 10 nm b) 20 nm. 115
Figure 4.45: Dislocation nucleation while cutting the (111) plane at 850 K at a cutting distance of a) 10 nm b) 20 nm. 116
Figure 4.46: Dislocation nucleation while cutting the (111) plane at 1173 K at a cutting distance of a) 10 nm b) 20 nm. 117
Figure 4.47: Dislocation nucleation while cutting the (111) plane at 1273 K at a cutting distance of a) 10 nm b) 20 nm. 118
Figure 4.48: Dislocation nucleation while cutting the (111) plane at 1500 K at a cutting distance of a) 10 nm b) 20 nm. 119
Figure 5.1: Atomic flow field in the *XY* plane during nanometric cutting of 3C-SiC on the various crystal planes at 300 K. The location of the cutting tool in connection with the different regions can be traced from Figure 4.1 125
Figure 5.2: Atomic flow field during nanometric cutting of 3C-SiC on the various crystallographic surfaces at 3000 K 127
Figure 5.3: Displacement of various layers in *y* direction while cutting 3C-SiC on the (110) crystal plane at 1400 K 128
Figure 5.4: a) Snapshots from the MD simulation while cutting the (111) crystal plane at 1400 K demonstrating the occurrence of cleavage at three stages and b) the corresponding drops of cutting forces 132
Figure 5.5: Snapshot from the MD simulation showing the event of cleavage while cutting the (110) crystal plane at 2000 K 133
Figure 5.6: Number of atoms in the cutting chip as a function of cutting temperature and crystal plane during nanometric cutting of 3C-SiC 135
Figure 5.7: Subsurface deformation layer depth as a function of cutting temperature and crystal plane during nanometric cutting of 3C-SiC 135
Figure 5.8: Variations of the resultant force exerted by the tool rake face on the chip, and friction coefficient at the tool rake face/chip interface while cutting 3C-SiC on different crystallographic planes at various temperatures 136
Figure 5.9: Extent of temperature increase in the primary deformation zone during chip formation. 138
Figure 5.10: Chip temperature as a function of cutting temperature and crystal plane 138
Figure 5.11: Specific cutting energy as a function of temperature and crystal plane 140
Figure 5.12: Variation of anisotropy in specific cutting energy as a function of temperature 141

Figure 5.13: Variation of peak von Mises stress in the cutting region while cutting 3C-SiC on different crystal planes and at different temperatures obtained by ABOP potential function .......................... 143
Figure 5.14: Evolution of the temperature and von Mises stress in the cutting region recorded on the same plot while cutting 3C-SiC on the (111) crystal plane at 1200 K.............................................. 144
Figure 5.15: Variation of the von Mises stress measured on the cutting edge of the diamond tool while machining different orientations of 3C-SiC at different cutting temperatures.................................. 145
Figure 5.16: Variation of temperature measured on the cutting edge of the diamond tool while machining different orientations of 3C-SiC at different cutting temperatures.................................. 145
Figure 5.17: Temperature distribution on atoms while cutting the (110) crystal plane at 3000 K ..... 147
Figure 5.18: The hardness of diamond as a function of temperature [127] ...................................... 147
Figure 5.19: Atom-by-atom attrition wear and slight distortion of diamond cutting tool while nanometric cutting of 3C-SiC at a) 1400 K b) 2000K ....................................................................... 149
Figure 5.20: MD simulation output illustrating amorphous atoms (white atoms), dislocation nucleation and formation of stacking faults while cutting the (110) plane at 300 K at a cutting distance of a, b) 10 nm c) 20 nm. Blue, green and red rods, respectively, stand for the perfect, Shockley partial and other partial dislocations. ............................................................................................................................ 153
Figure 5.21: Formation of crystal defects while cutting the (110) plane at 900 K at a cutting distance of a) 10 nm b) 20 nm. Pink and aqua rods represent the stair-rod and Frank partial dislocations..... 155
Figure 5.22: Formation of crystal defects while cutting the (110) plane at 1200 K at a cutting distance of a) 10 nm b) 20 nm. Pink and aqua rods represent the stair-rod and Frank partial dislocations..... 157
Figure 5.23: Formation of crystal defects while cutting the (110) plane at 1400 K at a cutting distance of a) 10 nm b) 20 nm. Stacking fault-couple and V-shape lock are formed. Pink and aqua rods represent the stair-rod and Frank partial dislocations. ...................................................................... 158
Figure 5.24: Formation of crystal defects while cutting the (110) plane at 1700 K at a cutting distance of a) 10 nm b) 20 nm.................................................................................................................... 159
Figure 5.25: Formation of crystal defects while cutting the (110) plane at 2000 K at a cutting distance of a) 10 nm b) 20 nm. Large stacking fault-couple is visible in the figure. ..................................... 162
Figure 5.26: Evolution of the cutting forces illustrating the locking/unlocking while cutting the (110) plane at 2000 K .................................................................................................................................. 163
Figure 5.27: Formation of crystal defects while cutting the (110) plane at 3000 K at a cutting distance of a) 10 nm b) 20 nm.................................................................................................................... 165
Figure 5.28: Formation of crystal defects while cutting the (010) plane at 300 K and at a cutting distance of a) 10 nm b) 20 nm, and at 3000 K at a cutting distance of c) 10 nm d) 20 nm ............... 168
Figure 5.29: Formation of crystal defects while cutting the (111) plane at 300 K and at a cutting distance of a) 10 nm b) 20 nm, and at 3000 K at a cutting distance of c) 10 nm d) 20 nm ............... 171
Figure 5.30: Radial distribution function showing interatomic bond lengths at different temperatures before and after nanometric cutting on the (010) crystal surface...................................................... 174
Figure 5.31: XRD spectrum of 3C-SiC in the cutting region a) before b) during and c) after nanometric cutting on the (010) crystal surface. d) Standard XRD pattern of 3C-SiC powders [144] ................................................................................................................................................... 176
Figure 6.1: Schematics of the heating arrangement of NanoTest Vantage [52] ................................ 182
Figure 6.2: NanoTest Vantage equipment used to perform nanoscratching trials ............................. 182
Figure 6.3: Surface roughness and PV of the etched wafer measured by white light interferometer. 184
Figure 6.4: SEM image of Berkovich nanoindenter used in the trials .............................................. 185
Figure 6.5: Glued silicon wafer on the hot stage .............................................................................. 186
Figure 6.6: A close snapshot of experimental system during high temperature nanoscratching ........ 187

Figure 6.7: Typical AFM image of the nanoscratch and cross section profiles measured in four different positions. Scratch depth (vertical height from a to c), scratch width (horizontal width b to d) and pile-ups (vertical height a to b and a to d) are shown on the top profile. .................................... 189
Figure 6.8: Variation of scratch depth, scratch width and total pile-up heights along the scratch length with the temperature and scratching speed ........................................................................................ 190
Figure 6.9: Raman spectra collected from five different locations of the nanoscratch shown in Figure 6.7, and machined under room temperature condition at constant scratching speed of a) 0.1 µm/s (low speed) and b) 10 µm/s (high speed) ........................................................................................ 194
Figure 6.10: Raman spectra collected from five different locations of the nanoscratch shown in Figure 6.7, and machined under high temperature condition (500°C) at constant scratching speed of a) 0.1 µm/s (low speed) and b) 10 µm/s (high speed) ................................................................................. 197
Figure 6.11: SEM image of Berkovich nanoindenter tip used for nanoscratching at a) room temperature and b) high temperature (500°C). The nanoindenter tips are not blunted under the present scratching conditions. ......................................................................................................................... 198
Figure 6.12: Raman spectra collected from four different locations of the nanoindenter shown in Figure 6.11a, used for nanoscratching at a) room temperature and b) high temperature (500°C). ..... 199

# List of Tables

Table 2.1: SW potential parameters for silicon ........ 16
Table 2.2: Tersoff potential parameters for silicon and carbon ........ 17
Table 2.3: Modified Tersoff potential parameters for silicon and carbon [43] ........ 18
Table 2.4: ABOP function parameters for silicon and carbon [44] ........ 20
Table 3.1: Details of the MD simulation model and the cutting parameters used in the study ........ 32
Table 3.2: Variation in the lattice constant of silicon and carbon in diamond cubic structure obtained from the modified Tersoff [43] and ABOP [44] potential functions at various temperatures ........ 37
Table 3.3: Calculated equilibrium lattice constant and cohesive energy of single crystal silicon at different temperatures using SW potential energy function [36] ........ 38
Table 3.4: Calculated equilibrium lattice constants and cohesive energy of single crystal 3C-SiC at different temperatures using ABOP [44] and Tersoff [42] potential energy functions ........ 38
Table 4.1: Stagnation region, stagnation angle and friction angle in nanometric cutting of single crystal silicon at various temperatures ........ 51
Table 4.2: Percentage reduction in tangential, thrust, resultant forces and specific cutting energy of silicon at high temperatures relative to room temperature ........ 78
Table 5.1: Stagnation region, stagnation angle and friction angle while cutting 3C-SiC ........ 129
Table 5.2: Percentage reduction in specific cutting energy of 3C-SiC at high temperatures relative to room temperature ........ 141
Table 6.1: Nanoscratching conditions ........ 186
Table 6.2: Scratch hardness at different conditions ........ 191

# Abbreviations

| | |
|---|---|
| *ABOP* | Analytical bond order potential |
| *BC* | Boundary condition |
| *BDT* | Brittle-ductile transition |
| *BOP* | Bond order potential |
| *CIRP* | College International Pour la Recherche en Productique |
| *DFT* | Density functional theory |
| *DXA* | Dislocation extraction algorithm |
| *EAM* | Embedded-Atom-Method |
| *EDIP* | Environment-Dependent Interatomic Potential |
| *FCC* | Face centred cubic |
| *FEA* | Finite element analysis |
| *FIB* | Focused ion beam |
| *GB* | Grain boundary |
| *GC* | Grain cell |
| *GSFE* | Generalized Stacking Faults Energy |
| *HF* | Hydrofluoric |
| *HPC* | High performance computer |
| *HPPT* | High pressure phase transformation |
| *JCPDS* | Joint Committee on Powder Diffraction Standards |
| *LAMMPS* | Large-scale Atomic/Molecular Massively Parallel Simulator |
| *LIGA* | Lithographie Galvanoformung Abformung |
| *LLNL* | Lawrence Livermore National Laboratory |
| *MC* | Monte Carlo |
| *MD* | Molecular dynamics |
| *MML* | Micro Materials Ltd. |
| *MNM* | Micro-/nano-machining |

| | |
|---|---|
| *NPH* | Isoenthalpic-isobaric ensemble |
| *NPT* | Isothermal-isobaric ensemble |
| *NVE* | Microcanonical ensemble |
| *NVT* | Canonical ensemble |
| *NW* | Nanowire |
| *OMS* | Odourless mineral spirits |
| *OVITO* | Open Visualization Tool |
| *PBC* | Periodic boundary conditions |
| *P-N* | Peierls-Nabarro |
| *RDF/g(r)* | Radial distribution function |
| *ReaxFF* | Reactive Force Field |
| *SEM* | Scanning electron microscope |
| *SERS* | Surface-enhanced Raman scattering |
| *Si* | Silicon |
| *SiC* | Silicon carbide |
| *SW* | Stillinger-Weber |
| *TB* | Tight binding |
| *TERS* | Tip-enhanced Raman scattering |
| *TJ* | Triple junction |
| *VP* | Vertex point |
| *XRD* | X-Ray Diffraction |

# Nomenclature

| | |
|---|---|
| $A$ | Anisotropy ratio |
| $a_0$ | Lattice constant |
| $B$ | Bulk modulus |
| $b$ | Width of cut |
| $d$ or $t$ | Uncut chip thickness |
| $E$ | Young's modulus |
| $F_c$ | Tangential cutting force |
| $F_t$ | Thrust/Normal force |
| $F_z$ | Axial force |
| $F_{cc}$ | Tangential force exerted by the rake face on the chip |
| $F_{tc}$ | Normal force exerted by the rake face on the chip |
| $G$ | Shear modulus |
| $H$ | Anisotropy factor, Scratch hardness |
| $h$ | bound of stagnation region |
| $R$ | Resultant force |
| $r$ | Tool tip radius |
| $T_m$ | Melting temperature |
| $T_{em}$ | Entirely molten temperature |
| $T_{inst}$ | Phase instability temperature |
| $u$ | specific cutting energy |
| $V_c$ | Cutting speed |
| $V_{chip}$ | Chip velocity |
| $\eta_i^{Mises}$ | von Mises shear strain |
| $\nu$ | Voigt Poisson's ratio |
| $\mu_c$ | Tool rake face/chip friction coefficient |

| | |
|---|---|
| $\mu$ | Voigt shear modulus |
| $\gamma_{us}$ | unstable stacking fault energy |
| $\gamma_{isf}$ | intrinsic stacking fault energy |
| $\gamma_{ut}$ | unstable twinning fault energy |
| $\theta_s$ | Stagnation angle |
| $\beta$ | Friction angle |
| $\alpha$ | Rake angle |
| $\alpha_{ef}$ | Effective rake angle |
| $\varphi$ | Shear plane angle |

# List of Publications by the Candidate

## Book Chapter

1. S. Goel, **S. Zare Chavoshi**, A. Murphy, (2016) "Molecular dynamics simulation (MDS) to study nanoscale machining processes", "Nanofinishing Science and Technology", Editor: V. K. Jain, Taylor and Francis, USA, ISBN (Electronic) 9781498745949, In press

## ISI Papers

1. **S. Zare Chavoshi**, X. Luo, (2015) "Hybrid Micro-machining Processes: A Review", Precision Engineering, 41, 1-23
2. **S. Zare Chavoshi**, S. Goel, X. Luo, (2016) "Molecular dynamics simulation investigation on plastic flow behaviour of silicon during nanometric cutting", Modelling and Simulation in Materials Science and Engineering, 24, 015002
3. **S. Zare Chavoshi**, X. Luo, (2016) "An atomistic simulation investigation on chip related phenomena in nanometric cutting of single crystal silicon at elevated temperatures", Computational Materials Science, 113, 1-10
4. **S. Zare Chavoshi**, X. Luo, (2016) "Molecular dynamics simulation study of deformation mechanisms in 3C-SiC during nanometric cutting at elevated temperatures", Materials Science and Engineering: A, 654, 400-417
5. **S. Zare Chavoshi**, S. Xu, X. Luo, (2016) "Dislocation-mediated plasticity in silicon during nanometric cutting: A molecular dynamics simulation study", Materials Science in Semiconductor Processing, 51, 60-70
6. **S. Zare Chavoshi**, S. Goel, X. Luo, (2016) "Influence of temperature on the anisotropic cutting behaviour of single crystal silicon: A molecular dynamics simulation investigation", Journal of Manufacturing Processes, 23, 201-210
7. **S. Zare Chavoshi**, X. Luo, (2016) "Atomic-scale characterization of occurring phenomena during hot nanometric cutting of single crystal 3C-SiC", RSC Advances, 6, 71409-71424

8. **S. Zare Chavoshi**, S. Corujeira Gallo, H. Dong, X. Luo (2016) "High temperature nanoscratching of single crystal silicon under reduced oxygen condition", Materials Science and Engineering: A, Accepted

**Conference Papers**

1. **S. Zare Chavoshi**, X. Luo, "Nanoscale elastic recovery of silicon while cutting at different temperatures: An MD simulation-based study", Advances in Manufacturing Technology: Proceedings of the 14$^{th}$ International Conference on Manufacturing Research, Incorporating the 31$^{st}$ National Conference on Manufacturing Research, 2016, Loughborough University, United Kingdom.
2. **S. Zare Chavoshi**, X. Luo, "Molecular dynamics simulation investigation of hot nanometric cutting of single crystal silicon", Proceedings of the 16$^{th}$ International Conference of the European Society for Precision Engineering and Nanotechnology, EUSPEN, 2016, Nottingham University, United Kingdom.
3. L. Rubio, W. Chang, W. Zhong, **S. Zare Chavoshi**, X. Luo, "Novel control architecture for 6-axis hybrid micro machine tool", 3rd EPSRC Manufacturing the Future Conference, 2014, Glasgow, United Kingdom.

# Chapter 1: Introduction

## 1.1. Research background

Ultra-precision manufacturing technology has appeared as a powerful tool for manipulating optical, electrical and mechanical properties of components by changing their surface and sub-surface structure at the nanometre length scale [1]. A rapid emergence of various micro-/nano-machining (MNM) processes has been observed in the past decades which can be applied to a variety of engineering materials, comprising metals, ceramics, plastics and composites. Miniaturization has pushed manufacturing improvements related to attainable accuracies and tolerances to the sub-micron range, especially in the fields of optics, electronics, medicine, biotechnology, communications, and avionics. Further improvements are necessary for applications relating to fuel cells, microscale pumps, valves and mixing devices, fluidic microchemical reactors, microfluidic systems, micronozzles for high-temperature jets, microholes for fibre optics, micromoulds and deep X-ray lithography masks etc. Additional examples include Fresnel lenses, pyramids array, polygon mirrors, aspheric lenses, multi- focal lenses, corner-cubes, two-dimensional planar encoders, and antireflective gratings or channels [2, 3].

MNM processes can be divided into three major categories based on whether they involve the addition of material, removal of material or no nominal change in the amount of material during the process, the last with or without a melt stage [2]. The first category involves deposition of material, and includes processes such as ultrasonic laser deposition, chemical vapour deposition, rapid prototyping, LIGA (from the German: Lithographie Galvanoformung Abformung) and electric discharge

deposition. The second category of micro-machining involves the removal of material. This might be accomplished by mechanical, chemical or physical means. The third category involving no gain or loss of material (i.e. micro-thermo forming and micro-injection moulding) is very suitable to form materials exhibiting low melting points, such as polymers. As mentioned above, the second category i.e. the material removal processes can be classified into mechanical, physical, or chemical processes depending on how machining is performed. While physical and chemical machining processes are restricted to specific materials and applications, machining by mechanical means is considered to be almost universal in its applicability to most materials. Meanwhile, machining can offer the least influence on the metallurgical properties of the finished component and is able to create desirable surface contour and surface textures within an acceptable tolerance.

Silicon (Si) is an archetypal semiconductor with physical and chemical properties that continue to draw massive research interest. It is abundant, non-toxic, and has an appropriate bandgap of 1.1 eV, dominating the solar cell and microelectronics industries. Photovoltaic solar cells based on the silicon account for more than 85% of the market share today. On the other hand, exceptional mechanical properties such as low density, high specific stiffness ($E/\rho$) and high temperature hardness, as well as outstanding thermal properties like high melting point, high thermal conductivity, high thermal shock resistance and low thermal expansion coefficient make silicon carbide (SiC) a consummate candidate for several high temperature and durability applications. In the 1950s, Shockley predicted that because of its superior materials properties, silicon carbide would quickly replace silicon. Indeed, it has now become one of the most promising materials for power electronics, heterogeneous catalyst

supports, hard- and biomaterials. On account of $sp^3$ orbital hybridization, both the silicon and carbon atoms in silicon carbide are tetravalent, resulting in formation of tetrahedral covalent bonds, which is common among semiconductor materials. However, silicon carbide exhibits one-dimensional polymorphism characterized by different stacking sequences and is indeed the most prominent polytypic material having more than 250 polytypes [4-6]. 3C-SiC, which is a zinc blende structured SiC, possesses the highest fracture toughness, hardness, electron mobility and electron saturation velocity amongst the silicon carbide polytypes. Thus, it has been in the centre of focus as a compound semiconductor to be utilized in the fabrication of nano-devices operating under harsh conditions.

Nanometric cutting can be employed for scale-up manufacturing of 3D silicon and silicon carbide based components requiring submicron form accuracy and nanometric smooth finish. However, these hard-brittle materials have poor machinability at room temperature due to their relatively low fracture toughness and high hardness. For instance, silicon has a fracture toughness of 0.9 MPa $m^{1/2}$ and hardness of 9.8 GPa [7] on the (100) family of planes whereas 3C-SiC possesses a fracture toughness of 2.02 MPa $m^{1/2}$ and hardness of 26.4 GPa [5]. A common understanding is that the yield strength and hardness reduce under high temperature. As such, the fracture toughness increases which in turn eases plastic deformation. In other words, at high temperatures, plasticity plays a greater role in the fracture and deformation processes of silicon and silicon carbide primarily as a result of thermally-generated intrinsic defects and thermal softening processes. However, its extent has never been reported although this knowhow could be vital in implementing the hot machining of silicon and silicon carbide with the assistance of

laser processing. In such thermally-enhanced processing, the workpiece can be heated by a continuous wave fibre laser and therefore is thermally softened. Laser provides intense localized heating to the workpiece ahead of the cutting region. In this way, the strength of the workpiece is reduced and therefore its machinability is improved.

Experimental studies of nanoscale manufacturing processes aside from being expensive are constrained by the fact that they do not permit direct observation of events occurring at the atomic level, especially at short timescales of a few femtoseconds. For this reason, molecular/atomic-level simulations have to be used in such processes. There are two main computational techniques for molecular/atomic-level simulations, which are Monte Carlo (MC) and molecular dynamics (MD) methods. MC method rests on probability distributions in statistical physics whereas MD is a deterministic approach to obtain trajectories of atoms through solving classical equations of motion at each time step. However, calculation of the heat capacity, compressibility, interfacial properties and dynamic quantities can be done more efficiently and accurately using MD simulation. Accordingly, MD simulation has evolved as an appropriate bottom-up simulation approach to investigate atomic scale events in nanoscale manufacturing processes. The beauty of MD simulation is that it is informed by Newton's equation thereby revealing discrete atomistic mechanics that is otherwise impossible to be investigated using the conventional engineering tool, e.g. finite element analysis (FEA). One of the principal differences between FEA and MD simulation is that the nodes and the distances between the nodes in MD simulation are not selected on an arbitrary basis but on the basis of more fundamental units of the material, namely, position of atom as the nodes and

inter-atomic distances as the distance between the nodes. Also, the shape and size of the crystal in MD simulation is dictated by the crystallographic structure of the material and is not used arbitrarily, such as triangular or rectangular shapes used in FEM [3]. The implementation of MD simulation was first developed through the pioneering work of Alder and Wainwright in the late 1950s [8] in their study of the interactions of hard spheres. Since then, MD simulation has transcended the field of ultra-precision manufacturing, materials science, physics, chemistry, and tribology and has contributed significantly towards improved understanding of our knowledge in the inaccessible atomic scale regime.

As the nanometric cutting process involves removal of few atomic layers from the workpiece surface, it is extremely difficult to observe the machining process and to measure the process parameters directly from the experiments. Thus, investigation of atomistic processes occurring at such small length scales is more amenable to MD simulation.

While there has been a modicum of success achieved on the understanding of high temperature nanoindentation behaviour, the area of high temperature nanometric cutting is relatively unexplored. It may be argued that high temperature nanoindentation study is helpful in understanding and characterizing the material behaviours. However, nanometric cutting unlike nanoindentation is a deviatoric stress-dominative process carrying pronounced component of shear [9]. It requests understanding of broader picture of the material deformation behaviour, especially at elevated temperatures during nanoscale deformation. A clear and unequivocal understanding of the macroscopic and microscopic aspects of the thermally-enhanced nanometric cutting of hard-brittle materials will enable us to improve this novel

nanoscale manufacturing process.

## 1.2. Aim and objectives of the research

This research work aims to gain an in-depth understanding of nanometric cutting mechanics for hard-brittle materials at elevated temperatures through MD simulation studies accompanied by experimental trials. The following key research objectives are targeted as they have been identified as the missing gaps in the literature:

- To explore the material removal phenomenon and anisotropic behaviour of silicon and 3C-SiC during contact mode machining at elevated temperatures
- To study the variation of cutting indicators like specific cutting energy, friction coefficient and cutting temperature as well as the yield stresses e.g. von Mises stress, octahedral stress, Tresca stress and Principal stresses during hot machining of silicon and 3C-SiC
- To investigate the cutting chip characteristics and chip formation mechanisms at high temperatures
- To explain the contribution of thermally-driven phenomena to the crystal plasticity and the role of amorphization in driving the plasticity of silicon and 3C-SiC during nanometric cutting at elevated temperatures
- To understand the phase transformation mechanisms through experimental trials of nanoscratching at elevated temperatures

## 1.3. Structure of the thesis

This dissertation is organized into seven chapters. After the introduction in Chapter 1, a review on the hybrid MNM i.e. assisted and combined MNM techniques, is

presented in the subsequent chapter. Chapter 2 also introduces the basic concept and framework of the MD simulation approach, followed by a detailed review of the previous work performed on the high temperature nanoindentation and nanometric cutting. Chapter 3 provides a thorough explanation of the MD simulation techniques employed in this study to explore nanometric cutting, including a detailed description of MD simulation procedure, boundary conditions, potential energy functions, ensembles, the equilibrium lattice constants, workpiece temperatures etc. In Chapter 4, the simulation results obtained from the MD simulations of nanometric cutting of silicon at elevated temperatures are presented. Aside from the variations of cutting forces, machining stresses and chip formation mechanisms, detailed aspects of nanoscale plasticity mechanisms, structural changes and atomic flow behaviour of the diamond cubic structure of silicon at different temperatures are discussed. Similarly, Chapter 5 describes MD simulation results and corresponding discussions for the nanometric cutting of 3C-SiC at elevated temperatures. Chapter 6 focuses on the experimental results of nanoscratching of silicon at room and elevated temperatures. The chapter explains how the phase transformation of silicon, obtained by Raman spectroscopy, changes during nanoscratching of silicon at room and high temperatures. Also, nanoscratch topography, nanoscratch hardness and condition of the tool tip in nanoscratching at elevated temperatures are described. Finally, Chapter 7 summarizes the conclusions of the present dissertation. According to the insights achieved and the problems confronted, possible future directions and recommendations are also provided in this chapter.

# Chapter 2: Literature review

## 2.1. Hybrid MNM processes

In recent years, the demand for micro-/nano components has increased at a rapid pace in various areas such as electronics, bio-medical, energy and optical industries [10]. The characteristics of these micro-/nano components are: (1) size of functional features in micro-/nano metre level; (2) high precision tolerances, typically better than 1 μm; (3) good surface finish, in general surface roughness Ra smaller than half micrometre; (4) 3D or complicated structures; (5) use of a variety of materials such as ceramics, hard steels, titanium alloys, etc. [11]. Many surface or bulk MNM processes based on mechanical removal, lithography, chemical or plasma etching, printing, moulding, transfer and assembly techniques have been proposed for micro/nano-device batch fabrication [12, 13]. They can provide components with small feature sizes in inorganic and organic materials and even 3D shapes. However, MNM by mechanical means can be applied for a large range of materials with a high relative accuracy and can offer the least influence on the metallurgical properties of the finished component.

Although traditional stand-alone (single function) machine tools have been used as a major means to fabricate micro-/nano components/products, it still remains a big issue of the predictability, producibility and productivity in fabrication of micro-/nano components/products, especially for those with complex surface forms/shapes made of hard-brittle materials [14]. In recent years some multifunctional machine tools have been developed to implement several mechanical machining operations on one machine in order to rapidly and economically fabricate those

components/products while research has also been drawn on the development of hybrid machines which will integrate conventional and non-conventional machining processes in them [15]. Some hybrid machining processes have been proved to be able to improve machinability of hard-to-machine materials, tool life, geometrical accuracy, surface integrity and machining efficiency.

There is no exact description of hybrid machining processes [16]. From time to time a number of definitions for hybrid machining processes have been proposed by researchers. Aspinwall *et al.* [17] explained that the combination of machining operations can be considered either in terms of a hybrid machining method, by which two or more machining processes are applied independently on a single machine, or in terms of an assisted machining approach, by which two or more processes are utilized simultaneously. She and Hung [18] stated that hybrid machines can perform different operations such as mechanical milling and turning at one place. Curtis et al. [19] provided a narrow definition, stating that only a method, where two or more material removal processes work simultaneously can be termed as “hybrid”. In 2014, the College International Pour la Recherche en Productique (CIRP) collaborative working group on hybrid processes put forward the following definition: hybrid machining processes are based on the simultaneous and controlled interaction of machining mechanisms and/or energy sources/tools having a significant effect on the process performance. The wording “simultaneous and controlled interaction” means that the processes/energy sources should interact more or less in the same processing zone and at the same time [20, 21]. Accordingly, in this dissertation, hybrid micro-/nano machining processes are classified as assisted and combined micro-/nano machining processes (as shown in Figure 2.1). For assisted MNM, the major

machining process is superimposed with input from one or several types of energy such as heat, fluid, ultrasonic vibration magnetic field etc. so as to improve the constituent MNM process [22]. For the purpose of brevity, this chapter provides the most relevant information regarding thermally-enhanced MNM process which is considered as an assisted hybrid MNM. Hard-brittle and heat resistant materials are often difficult to machine due to their physical and mechanical properties such as high strength and low thermal conductivity, which make the cutting forces and cutting temperature very high. Because the flow stress and strain hardening rate of materials normally decrease with the increase of temperature due to thermal softening, thermal-assisted machining becomes a possibility when machining the hard-to-machine materials (see Figure 2.2) [23]. In such process, an external heat source i.e. laser can be utilized to heat and soften the workpiece locally in front of the cutting tool. The temperature rise at the shear zone reduces the yield strength and work hardening of the workpiece, which make the plastic deformation of hard-to-machine materials easier during machining. Hence, thermal-assisted machining can be regarded as an excellent choice to machine hard-brittle materials such as silicon and silicon carbide.

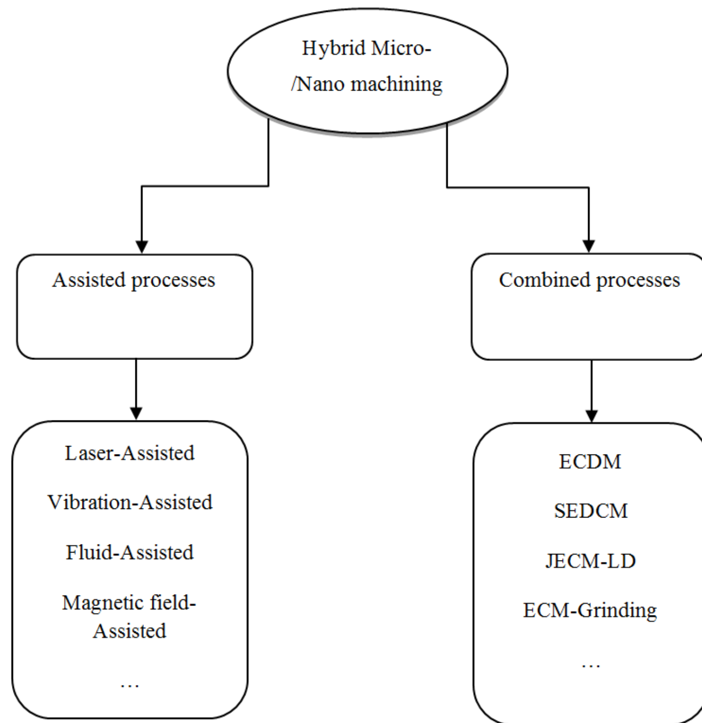


Figure 2.1: Classification of hybrid MNM processes

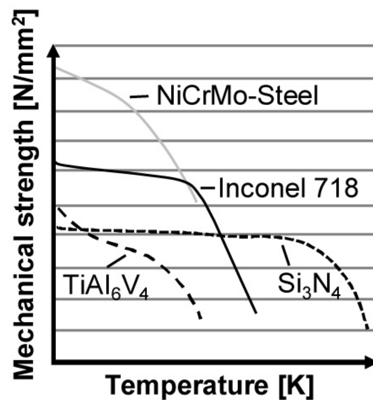


Figure 2.2: Mechanical strength as a function of temperature [21]

## 2.2. MD simulation approach

MD simulation was introduced for the first time by the pioneering work of Alder and Wainwright in the late 1950s [8] with their model of interaction between hard spheres; however its adoption to the domain of ultra-precision machining took place

at Lawrence Livermore National Laboratory (LLNL), USA, during the late 1980s [24]. Landman *et al.* [25], Belak [26] and Ikawa *et al.* [27] pioneered the concept of MD in the framework of contact loading studies followed by Voter *et al.* [28]. Since then, Inamura *et al.* [29], Rentsch *et al.* [30] and Komanduri *et al.* [31] have contributed significantly to this arena and set a sound foundation for the study of nanometric cutting processes using MD simulation.

The essence of the classical MD simulation method is the numerical solution of Newton's second equation of motion for an ensemble of atoms where the atoms are assumed to follow Newton's second law as follows:

$$a_{ix} = \frac{F_{ix}}{m_i} = \frac{d^2 x_i}{dt^2} \quad , \quad F_{ix} = -\frac{dV}{dx_i} \tag{2.1}$$

where $a_{ix}$ represents the $i^{th}$ atom's acceleration in the $x$ direction and $m_i$ is the mass of the $i^{th}$ atom. $F_{ix}$ is the interaction force acting on the $i^{th}$ atom by another atom in the $x$ direction, $x_i$ is $i^{th}$ atom's $x$-coordinate and $V$ is the potential energy function. In MD simulation, these equations are integrated using different algorithms such as Verlet [32], which is the most commonly used time integration algorithm to calculate trajectories of particles in MD simulation, for extremely short time intervals (1-100 pico-seconds (ps)); and equilibrium statistical averages are computed as temporal averages over the observation time. To render atomistic simulation studies practical, an interatomic potential function is necessary. During MD simulation, the interatomic bonding forces (both attractive and repulsive) are defined by an appropriate empirical potential energy function. The MD simulations can be likened to the dynamic response of numerous nonlinear spring-mass objects (atoms or positive ions) in a system under an applied load, velocity, or displacement conditions. From this point of view, MD simulation is similar to other analyses that engineers

routinely undertake, such as the investigation of vibrations of a mechanical system wherein a series of springless-masses and massless-springs are connected and the response of the system is investigated under given external loading conditions.

Figure 2.3 shows schematically a computer simulation of the deformation of a workpiece being machined with a diamond cutting edge. Every atom shown in Figure 2.3 is in motion and interacts with neighbouring atoms in a manner that can be determined from the interatomic potential energy function.

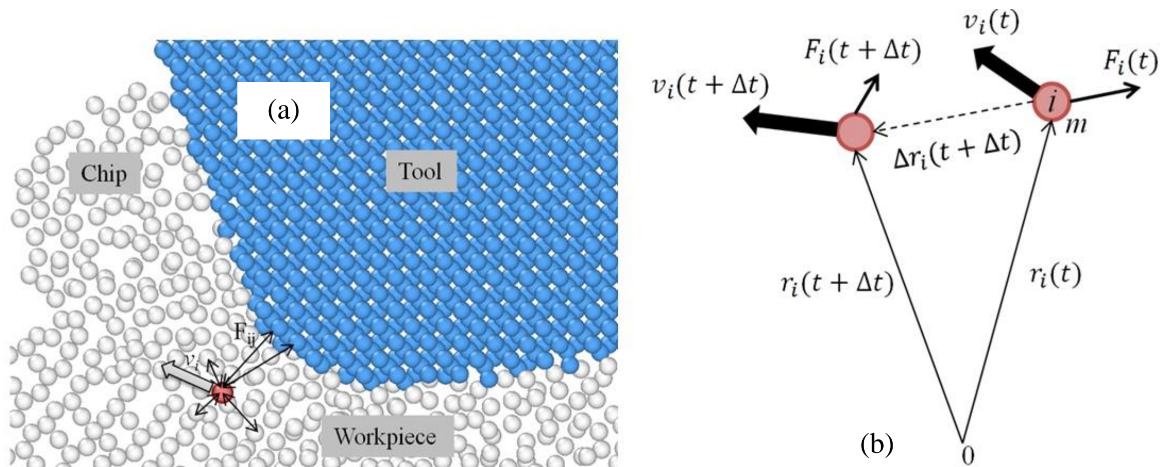


Figure 2.3: (a) Scheme for performing MD simulation of nanometric cutting (b) an atom '$i$' having mass '$m$' at a distance of '$r$' from the other atom exerts force '$F$' on other atom, when given a velocity '$v$'

In the simulation, the tool is fed in a stepwise procedure into the workpiece at time intervals of $\Delta t$, which are shorter than the period of lattice vibration [2, 3] As indicated in Figure 2.3, the position $r_i(t + \Delta t)$ and velocity $v_i(t + \Delta t)$ of the atom $i$ after the tool has been fed in the period of $\Delta t$ are calculated by employing finite difference method and using Equations (2.2) and (2.3). This calculation is then repeated in order to describe the motion of individual atoms. The behaviour of the

collection of atoms that comprise the tool/workpiece model can be then analysed through synthesis of the movement of the individual atoms [3].

$$r_i(t+\Delta t)=r_i(t)+\Delta t v_i(t)+\frac{(\Delta t)^2}{2m}F_i(t) \tag{2.2}$$

$$v_i(t+\Delta t)=v_i(t)+\frac{\Delta t}{2m}\left[F_i(t+\Delta t)+F_i(t)\right] \tag{2.3}$$

### 2.2.1. Potential energy function

Whenever an atomic scale problem is treated, we require a constitutive description of the atoms. Their interaction is governed by a potential energy function that roughly makes up quantum interactions between electron shells and denotes the physical properties of the atoms i.e. the elastic constants and other relevant mechanical properties. In general, there are two ways to construct an interatomic potential. The first way is the artistic route of empirical design using chemical and physical insights together with convenient functional forms. The second alternative is the rigorous approach of a bottom-up derivation of the functional forms from a higher level theory, in some cases, tight binding approaches (TB) [33]. Both of these procedures have been applied in the construction of bond order expressions, and both approaches turned out to be largely successful [34].

One of the most successful families of interatomic potentials that have been able to stand the demanding requirement of simultaneous efficiency and reliability is the family of models based on the quantum-mechanical concept of bond order. Empirical potential energy functions are classified into two-body potentials, three-body potentials and multi-body potentials, depending on the unit of atoms on which those potentials are based. The potentials which fall into two-body potentials category are

Morse, Born-Mayer, Lennard-Jones potentials, etc. It may however be noted that a common limitation of all the pair-potentials is their inability to reproduce the Cauchy pressure, which is a quantity that reflects the nature of the bonding at the atomic level of a material. This was one of the motivations for introducing multiple-body potentials such as Embedded-Atom-Method (EAM) [35], Stillinger-Weber (SW) [36] and Tersoff potential [37-40] in the 1980's. The EAM potentials are devised to describe the metallic bonding more accurately than the two-body potentials. SW potential function incorporates a linear combination of two- and three-body terms to describe interactions in solid and liquid forms of silicon. The mathematical formulation of the SW potential for a system of N atoms at position $r_i$, for $i = 1, 2, \dots, N$, is:

$$U(\{r_i\}) = \sum_{i<j} \varepsilon\phi_2(r_{ij}) + \sum_{i \neq j < k} \varepsilon\phi_3(r_{ij}, r_{ik}, r_{jk}) \tag{2.4}$$

The two- and three-body $\emptyset$ functions are:

$$\phi_2(r_{ij}) = A\left[B\left(\frac{\sigma}{r_{ij}}\right)^p - \left(\frac{\sigma}{r_{ij}}\right)^q\right]\exp\left(\frac{1}{r_{ij}/\sigma - a}\right) \tag{2.5}$$

$$\phi_3(r_{ij}, r_{ik}, \theta_{ijk}) = \lambda\left(\cos\theta_{ijk} + \frac{1}{3}\right)^2 \exp\left(\frac{\gamma}{r_{ij}/\sigma - a}\right)\exp\left(\frac{\gamma}{r_{ik}/\sigma - a}\right) \tag{2.6}$$

Table 2.1 summarizes the parameters of SW potential for silicon.

The three-body potentials such as Tersoff and analytical bond order potential (ABOP) are devised to represent covalent bonding which has a directional grip and can be used conveniently for material systems involving silicon, germanium, diamond, etc. Tersoff potential is based on an idea presented by Abell [41] few years

earlier on bond order potential (BOP), which has environmental dependence and no absolute minimum at the tetrahedral angle.

Table 2.1: SW potential parameters for silicon

| | |
|---|---|
| $\varepsilon(eV)$ | 2.1683 |
| $\sigma(\AA)$ | 2.0951 |
| $a$ | 1.80 |
| $\lambda$ | 21.0 |
| $\gamma$ | 1.20 |
| $A$ | 7.049556277 |
| $B$ | 0.6022245584 |
| $p$ | 4.0 |
| $q$ | 0.0 |

Indeed, the most popular BOP function for predicting material behaviour of silicon is the Tersoff potential function [39, 40]. The Tersoff potential function to describe interactions between the Si-Si, C-C and Si-C atoms is expressed as:

$$E = \sum_i Ei = \frac{1}{2}\sum_{i \neq j} V_{ij},\ V_{ij} = fc(r_{ij})[f_R(r_{ij}) + b_{ij} f_A(r_{ij})] \tag{2.7}$$

$$f_R(r_{ij}) = A_{ij}\exp(-\lambda_{ij} r_{ij}),\ f_A(r_{ij}) = -B_{ij}\exp(-\mu_{ij} r_{ij}) \tag{2.8}$$

$$fc(r_{ij}) = \begin{cases} 1 & r_{ij} < R_{ij} \\ \frac{1}{2} + \frac{1}{2}\cos[\pi \frac{r_{ij} - R_{ij}}{S_{ij} - R_{ij}}] & S_{ij} > r_{ij} > R_{ij} \\ 0 & r_{ij} > S_{ij} \end{cases} \tag{2.9}$$

$$b_{ij} = \chi_{ij}(1 + \beta_i^{ni} \zeta_{ij}^{\ ni})^{-1/2n_i},\ \zeta_{ij} = \sum_{k \neq i,j} fc(r_{ik})\omega_{ik} g(\theta_{ijk}) \tag{2.10}$$

$$g(\theta_{ijk}) = 1 + \frac{c_i^{\ 2}}{d_i^{\ 2}} - \frac{c_i^{\ 2}}{[d_i^{\ 2} + h_i - \cos\theta_{ijk}]} \tag{2.11}$$

where $E$ is the total energy of the system, which is decomposed for convenience into a site energy $E_i$, and a bond energy $V_{ij}$ (the energy between two atoms ($i$ and $j$)), ($i$, $j$, and $k$) are the atoms of the system, $f_R$ is a repulsive pair potential, $f_A$ is an attractive

pair potential, $f_C$ is a smooth cut-off function in order to restrict the range of the potential, $r_{ij}$ represents the length of the *i-j* bond, $b_{ij}$ determines the bond order term, $\zeta_{ij}$ counts the number of other bonds to atom *i* besides the *i-j* bond and $\theta_{ijk}$ is the bond angle between the bonds *i-j* and *i-k*. Parameter $\chi_{ij}$ determines the attractive interactions between two atoms. Table 2.2 shows the parameters of Tersoff 1990 and Tersoff 1994 for silicon and carbon.

Table 2.2: Tersoff potential parameters for silicon and carbon

| | Tersoff 1990 [39, 40] | | Tersoff 1994 [42] | |
|---|---|---|---|---|
| | Si-Si | C-C | Si-Si | C-C |
| $A(eV)$ | 1830.8 | 1544.8 | 1830.8 | 1544.8 |
| $B(eV)$ | 471.18 | 389.63 | 471.18 | 389.63 |
| $\lambda(Å^{-1})$ | 2.4799 | 3.4653 | 2.4799 | 3.4653 |
| $\mu(Å^{-1})$ | 1.7322 | 2.3064 | 1.7322 | 2.3064 |
| $\beta$ | $1.1\times10^{-6}$ | $41.612\times10^{-7}$ | $1.1\times10^{-6}$ | $41.612\times10^{-7}$ |
| $n$ | 0.78734 | 0.99054 | 0.78734 | 0.99054 |
| $c$ | 100390 | 19981 | 100390 | 19981 |
| $d$ | 16.217 | 7.034 | 16.217 | 7.034 |
| $h$ | -0.59825 | -0.33953 | -0.59825 | -0.33953 |
| $R(Å)$ | 2.5 | 2.5 | 2.7 | 1.8 |
| $S(Å)$ | 2.5 | 2.5 | 3 | 2.1 |
| $\chi_{Si\text{-}C}$ | 0.9972 | | 1.0086 | |

However, Tersoff potential function fails to correctly predict the melting point and the dimer properties of silicon such as binding energy, $D_0$, the equilibrium bonding

distance, *r*, and the wave number, *k*, of the ground-state oscillation. The drawback of incorrect prediction of melting point was addressed by Agrawal *et al.* [43] through a modified parameterisation of Tersoff potential function. However, while the modified version of the Tersoff variant was proposed, it was not made clear by Agrawal *et al.* [43] whether it is robust in predicting mechanical properties of silicon. Table 2.3 summarizes the parameters of the modified Tersoff potential. The modified parameters have been highlighted in the table.

Table 2.3: Modified Tersoff potential parameters for silicon and carbon [43]

| | Si-Si | C-C |
|---|---|---|
| $A$ (eV) | 1,830.8 | 1,544.8 |
| $B$ (eV) | 471.18 | 389.63 |
| $\lambda$ (Å$^{-1}$) | 2.4799 | 3.4653 |
| $\mu$ (Å$^{-1}$) | 1.7322 | 2.3064 |
| $\beta$ | **$1.15 \times 10^{-6}$** | $4.1612 \times 10^{-6}$ |
| $n$ | **0.988** | 0.99054 |
| $c$ | $1.0039 \times 10^{5}$ | 19981 |
| $d$ | 16.217 | 7.034 |
| $h$ | **−0.74525** | −0.33953 |
| $R$ (Å) | 2.7 | 1.8 |
| $S$ (Å) | 3.0 | 2.1 |
| $\chi_{\text{Si-C}}$ | 1.0 | 1.0086 |

The other shortcoming of Tersoff potential function i.e. description of correct dimer properties was overcome by the ABOP function proposed by Erhart and Albe [44]. ABOP is of the following form:

$$\text{Total energy } E = \sum_{i>j} f_c(r_{ij})[V_R(r_{ij}) - \underbrace{\frac{b_{ij} + b_{ji}}{2}}_{\bar{b}_{ij}} V_A(r_{ij})] \tag{2.12}$$

where $E$ is the cohesive energy which is the sum of individual bond energies with following repulsive and attractive contributions:

$$V_R(r) = \frac{D_0}{S-1}\exp\left[-\beta\sqrt{2S}(r-r_0)\right] \tag{2.13}$$

$$V_A(r) = \frac{SD_0}{S-1}\exp\left[-\beta\sqrt{2/S}(r-r_0)\right] \tag{2.14}$$

where $D_0$ and $r_0$ are the dimer energy and bond length. The cutoff function is given by:

$$f_c(r) = \begin{cases} 1 & r < R-D \\ 0 & r > R+D \\ \frac{1}{2} - \frac{1}{2}\sin\left(\frac{\pi}{2}\frac{r-R}{D}\right) & |R-r| \le D \end{cases} \tag{2.15}$$

where parameters $R$ and $D$ specify the position and the width of the cutoff region. The bond order is given by:

$$b_{ij} = \left(1+\chi_{ij}\right)^{-1/2} \tag{2.16}$$

$$\chi_{ij} = \sum_{k(\neq i,j)} f_c\left(r_{ik}\right)\exp[2\mu(r_{ij}-r_{ik})g\left(\theta_{ijk}\right) \tag{2.17}$$

and angular function is given by:

$$g(\theta) = \lambda\left(1+\frac{c^2}{d_2}-\frac{c^2}{d^2+(h+\cos\theta)^2}\right) \tag{2.18}$$

Table 2.4 depicts the parameters of ABOP function.

Table 2.4: ABOP function parameters for silicon and carbon [44]

| | Si-Si | C-C | Si-C |
|---|---|---|---|
| $D_0\,(eV)$ | 3.24 | 6 | 4.36 |
| $r_0\,(Å)$ | 2.232 | 1.4276 | 1.79 |
| $S$ | 1.842 | 2.167 | 1.847 |
| $\beta\,(Å^{-1})$ | 1.4761 | 2.0099 | 1.6991 |
| $\gamma$ | 0.114354 | 0.11233 | 0.011877 |
| $c$ | 2.00494 | 181.910 | 273987 |
| $d$ | 0.81472 | 6.28433 | 180.314 |
| $h$ | 0.259 | 0.5556 | 0.68 |
| $2\mu\,(Å^{-1})$ | 0 | 0 | 0 |
| $R\,(Å)$ | 2.82 | 2 | 2.4 |
| $D\,(Å)$ | 0.14 | 0.15 | 0.2 |

It is of note that most empirical potential energy functions developed for silicon possess only restricted transferability, which is regarded as the nature of empirical potentials. Thus, each potential function works well for a specific condition. While newly developed formalisms provide greater accuracy, they are sometimes computationally very expensive i.e. reactive force field (ReaxFF) [45], which is capable of bond breaking and bond-formation during the simulation, and screened potential functions [46, 47], which are long-range ABOP and provide a more accurate picture of the atomic-scale mechanisms of brittle fracture, ductile plasticity, and structural changes.

The key message of this section is that a potential energy function is a momentous consideration for an accurate MD simulation. There are some shortcomings of the currently used potential functions. While potential energy functions are extremely efficient computationally, they cannot fully capture the many-bodied nature of electronic bonding, particularly its complex and consistent variation as a function of

local structure and chemistry in the vicinity of defects. Similarly, the ductile-brittle transition during nanometric cutting of silicon and silicon carbide cannot be described well by the Tersoff potential energy function (that has been a heavily used potential function). Finally, MD considers the environment as a vacuum, however the real experimental environment is known to play a key role in influencing the machining outcome and hence a more robust potential function would involve representation of the influence of coolants etc.

### 2.2.2. Ensembles

A key concept in statistical mechanics is the ensemble. An ensemble is a collection of microstates of system of molecules, all having in common one or more extensive properties. MD simulation is performed under certain equilibrium ensembles. The frequently used ensembles are: NVE, NVT, NPT and NPH, where N is the number of atoms, V is the volume of the system, E is the energy, T is the temperature, P is the pressure and H is the enthalpy of the system. The constant-volume, constant-energy ensemble (NVE), also known as the microcanonical ensemble, is achieved by solving the standard Newton equation without any temperature and pressure control. Most of simulations could use this ensemble, while the NVE models are isolated systems which have constant energy. The energy of the system is conserved, so that transfer of the energy inside the system can be more clearly distinguished. The constant-volume, constant-temperature ensemble (NVT), also known as the canonical ensemble, is obtained by controlling the thermodynamic temperature. Generally, the NVT system could be thought like a system transport heat with an infinite heat source. The constant-pressure, constant-temperature ensemble (NPT), also known as

the isothermal-isobaric ensemble, allows control over both the temperature and pressure whereas the constant-pressure, constant-enthalpy ensemble (NPH), also known as the isoenthalpic-isobaric ensemble, permits control over both the pressure and enthalpy of the system.

#### 2.2.3. Boundary conditions

The choice of the boundary condition (BC) in MD simulation is also important. The most commonly used boundary condition is the periodic boundary condition (PBC) since it can represent an infinite number of atoms by performing the simulation in only a single unit cell. Non-PBCs such as fixed or free boundary conditions are among the other possibilities. Each type of BC has its own advantages and drawbacks. For instance, PBC means infinite size which will block the free boundary effect. Non-PBC can be utilized to study the non-equilibrium systems, but always induce a free boundary effect.

### 2.3. Previous studies on nanometric cutting and nanoindentation at elevated temperatures

The previous work on nanoscale cutting by MD simulation has primarily focused on demystifying the material removal mechanisms at “room temperature”. Recently, Goel *et al.* [2, 5] have reviewed relevant MD simulation studies on nanometric cutting of silicon and silicon carbide at room temperature. What is known from these studies is that the current pool of knowledge on the nanometric cutting of silicon and silicon carbide at elevated temperatures is still sparse. Only rudimentary work has been done so far on studying hot machining. In a preliminary investigation

performed in our research group, hot machining of single crystal 3C-SiC at 1200 K was compared with the cutting at 300 K. It was found that hot machining results in lowering tangential cutting forces and thrust forces, yet shear plane angle remained unchanged [48]. Fang *et al*. [49] and Liu *et al*. [50] performed MD simulations to examine the variation in Young's modulus, hardness and elastic recovery of copper, diamond and gold during nanoindentation at high temperatures (up to 600 K). They concluded that Young's modulus, hardness and the extent of elastic recovery decrease with the increase of temperature. Hsieh *et al*. [51] used MD simulation to investigate the effect of temperature on maximal normal forces and elastic recovery during nanoindentation of copper. They reported a reduction in the aforementioned parameters with an increase in the substrate temperature.

On the experimental side, there is no study on high temperature nanometric cutting. However, there is a history of using 'hot hardness' microindentation tests, beginning with Atkins and Tabor [34]. Nevertheless, instrumented hardness tests at high temperatures have a shorter history. Wheeler and co-workers [52-54] have described the general nano-mechanical test platform capable of performing variable temperature and variable strain rate testing. The thermal management and measurement techniques and vacuum nanoindentation have been discussed in their review papers. Similarly, Schuh and his colleagues [55, 56] produced an elegant discussion of the technical issues surrounding high temperature nanoindentation in ambient and inert environments.

In 1996, Suzuki and Ohmura [57] performed ultra-microindentations on {110} surfaces of single crystal silicon in the temperature range of 20-600°C and concluded that below 500°C, the temperature-insensitive hardness is determined by the

transformation to the metallic β-tin phase, which amorphizes or nanocrystallizes during unloading, while above 500°C, plastic deformation due to dislocation activity causes temperature-dependent hardness. Smith and Zheng [58] modified a depth sensing indentation instrument to measure small scale hardness and elastic modulus of glass, gold, and single crystal silicon at 200°C. The hardness and elastic modulus of soda lime glass and gold were found to be lower than that at room temperature. In contrast, indentation testing of Si(100) at 200°C produced a similar hardness value to that obtained at room temperature, although the modulus was reduced, from 140.3 to 66 GPa. In addition, the well-known 'pop out' event, which is observed during unloading of a silicon indentation at room temperature, disappeared at 200°C. Beake and Smith [59] demonstrated that mechanical properties of fused silica exhibit a completely different temperature dependence from those of soda-lime glass during high temperature nanoindenation at 400°C, since fused silica is an anomalous glass. Xia *et al.* [60] observed that the surface hardness of Fe-40Al, an iron aluminide, is higher and the elastic modulus is lower at elevated temperatures (400°C) than the corresponding values at room temperature. Lund *et al.* [61] investigated the effect of temperature during nanoindentation of pure platinum. They reported that the transition from elastic to plastic deformation takes place at progressively lower stress levels as temperature is increased. By adapting a commercial nanoindenter to allow testing at up to 200°C, Schuh *et al.* [62] explored the deformation map of two type of metallic glasses, and found that increasing the temperature at a constant indentation rate sees the gradual emergence of homogeneous flow, as thermal relaxations allow dissipation of strain localization into general viscous flow. Nanoindentation studies of single crystal Ni-base superalloy CMSX-4 oriented in the ⟨001⟩ and ⟨110⟩

directions were conducted by Sawant and Tin [63] over a range of temperatures from 30°C to 400°C. Trelewicz and Schuh [64] carried out high-temperature nanoindentation experiments to assess the activation enthalpy for deformation of nanocrystalline Ni-W alloys, for grain sizes between 3 and 80 nm. They reported that thermal softening becomes less pronounced at finer grain sizes, and the activation enthalpy has an apparent inflection at a grain size near ~10-20 nm, in the vicinity of the Hall-Petch breakdown. It should be noted here that studies have been performed on the high temperature nanoindentation of various materials [65-74]. However, for the sake of brevity, only studies on Si are discussed in the following paragraphs. Bradby and his co-workers [75, 76] reported that in hot nanoindentation of silicon, increasing temperature enhances the nucleation of Si-III and Si-XII during unloading but the final composition of the phase transformed zone is also dependent on the thermal stability of the phases in their respective matrices. Besides, they found that the region under the indenter undergoes rapid volume expansion at temperatures above 125°C during unloading. Moreover, polycrystalline Si-I was the predominant end phase for indentation in crystalline silicon whereas high-pressure Si-III/Si-XII phases were the result of indentation in amorphous silicon. They also concluded that the Si-II phase is unstable in a c-Si matrix at elevated temperatures. In a similar work, Domnich *et al.* [77] carried out high-temperature nanoindentation using Berkovich probe and observed that until a certain critical temperature (350°C), the nanoindentation hardness of silicon is dictated by the pressure required to transform the semiconducting Si-I phase into the metallic Si-II phase of silicon. However, no phase transformation was observed above 350°C and it was suggested that the nanoindentation hardness in silicon above 350°C is dictated by dislocation glide.

From what was discussed above, it can be inferred that although some studies have been performed so as to improve our understanding of high temperature nanoindentation behaviour, no methodical work is available to date on the area of high temperature nanometric cutting. Accordingly, it is suggested that there is a strong need to understand the high temperature nanometric cutting mechanisms for hard-brittle materials.

## 2.4. Summary

This chapter began with an overview of the hybrid MNM processes and their application in micro-/nano manufacturing. Over the period of time, researchers have been able to integrate some of the MNM processes to harness combined advantages of the independent MNM processes. Such processes are known as hybrid MNM processes and can be classified as assisted and combined MNM processes. Thermally-enhanced MNM process, which is considered as an assisted hybrid MNM, is an efficient hybrid process to fabricate micro-/nano components made of hard-brittle materials since in a such process, the workpiece is soften locally in front of the cutting tool by heat. The temperature rise at the shear zone reduces the yield strength and work hardening of the workpiece, which make the plastic deformation of hard-to-machine material easier during machining.

The concept and the background of MD simulation methodology, potential energy functions, ensembles and boundary conditions used in MD simulation were also described in details. The key message was that a potential energy function is an important consideration for an accurate MD simulation. It was argued that most empirical potential energy functions possess only restricted transferability, which is

regarded as the nature of empirical potentials; thus, each potential function works well for a specific condition.

In continuation, an overall review on MD simulation and experimental trials of nanometric cutting and nanoindentation at elevated temperatures were presented. An important information that came to the light from this section was that the available literature regarding MD simulation of nanoscale cutting has mainly concentrated on elucidating material removal at "room temperature". Moreover, although there have been some attempts to understand the high temperature nanoindentation behaviour, the current pool of knowledge on the nanometric cutting at elevated temperatures is still sparse. Indeed, there is no experimental data available on high temperature nanometric cutting.

# Chapter 3: Modelling and simulation of nanometric cutting process at elevated temperatures

## 3.1. Generic scheme of performing an MD simulation of nanometric cutting

Steps involved in an MD simulation of nanometric cutting at elevated temperatures are described briefly in the following sections. Figure 3.1 provides a general scheme of how an MD simulation of nanometric cutting is performed. This scheme is generic and can well be extended to study other contact loading processes such as nanoindentation, impact loading etc. Also, the description is generalized and may be adapted to any software platform. In brief, as shown in Figure 3.1, performing an MD study requires a set of steps which could be organized into definition of boundary conditions, geometry models, interatomic potential functions, ensambles and equilibration, process parameters and post processing. All of these steps are normally repeated for different models or different simulations.

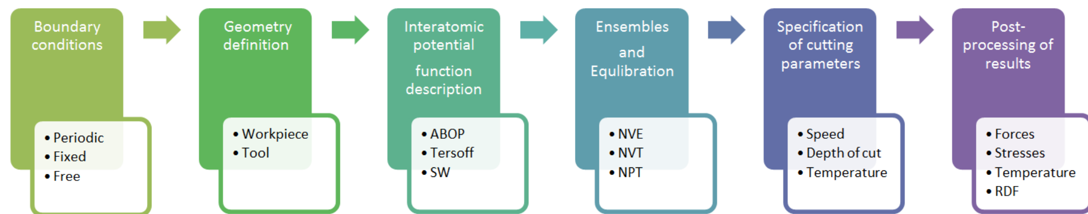


Figure 3.1: Generic scheme of performing an MD simulation of nanometric cutting

## 3.2. Description of the nanometric cutting model

The three-dimensional MD model used in this study (which is basically a plane-stress representation of actual machining operation) is illustrated in Figure 3.2. In this model, the workpiece and the cutting tool were modelled as deformable bodies in order to permit tribological interactions between them. However, if the workpiece

is very soft (such as copper and brass), the diamond tool can be modelled as a rigid body since the cutting tool will not wear even after a cutting length of the order of 30 km [78]. The model shown in Figure 3.2 can be seen to have a negative rake angle tool, as this is generally the recommendation for machining of hard and brittle materials such as silicon and silicon carbide. It should be noted that the force components along the *x, y* and *z* directions referred to as tangential cutting ($F_c$), thrust or normal force ($F_t$) and axial force ($F_z$), respectively. It may be noted that $F_z$ is being introduced here only for awareness; however since the simulation model is assumed to be a plane-stress condition, the average magnitude of $F_z$ during cutting is expected to be zero.

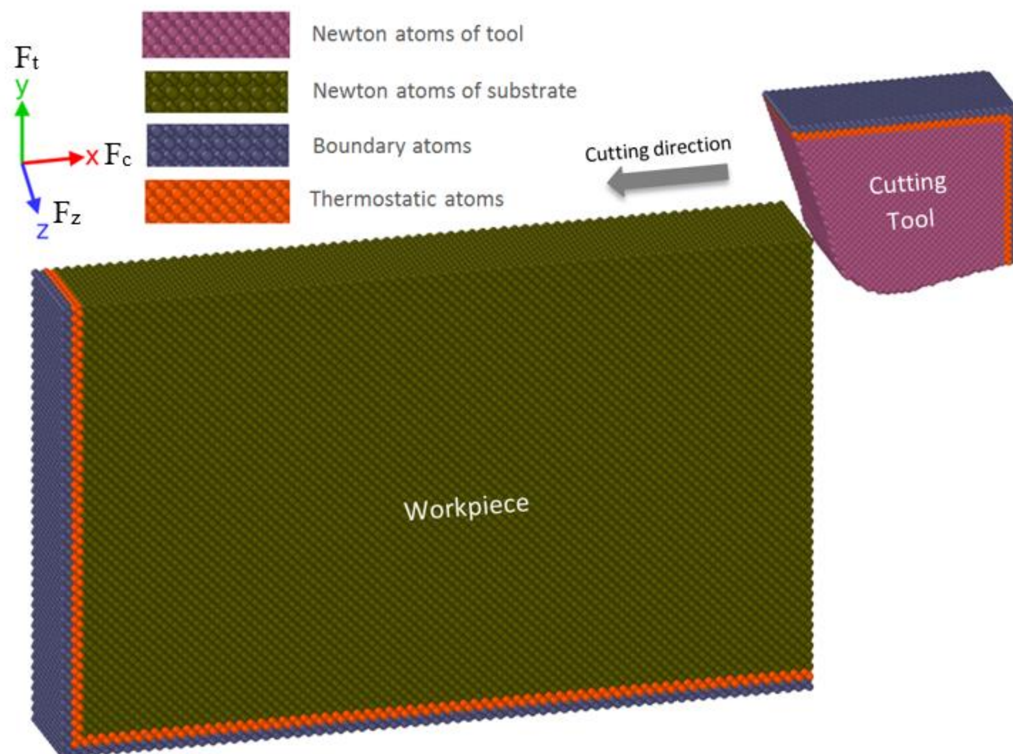


Figure 3.2: Schematic of MD simulation model

In Figure 3.2, the region of atoms in the workpiece and tool were divided into three zones namely, boundary atom zone, thermostatic atom zone and Newtonian atom zone. The boundary atoms are held rigid to reduce the boundary effects and to ensure structure stability and to maintain the symmetry of the lattice. In conventional machining operations, the energy from plastic deformation in the primary shear zone and friction at the tool-chip interface generates heat, which is carried away by chips, lubricant and by conduction into the tool and workpiece. The nanometric cutting model is, however, extremely small and is not capable of dissipating the heat itself. The velocity of the thermostatic atoms is therefore re-scaled to a desired temperature at each step of the computation to dissipate the artificial heat. Accordingly, the thermostat zone was allowed to follow Berendsen thermostatic dynamics (LAMMPS NVT dynamics). In order to minimize the boundary effects and to avoid significant heat transfer between the thermostat layer and the cutting region, the length and height of the substrate were chosen to be sufficiently large. The third category of atoms is called Newtonian atoms, which were allowed to follow the microcanonical (LAMMPS NVE dynamics) dynamics in accord with the routine MD principles. The velocity Verlet algorithm [32] with the single time step of 1 fs was employed for the time-marching method in the simulations. The model developed here is based on the boundary condition of fixing the bottom and outer sides of the workpiece since it is recommended to be a suitable configuration to simulate a nanometric cutting process [79]. The PBC was imposed along the $z$ direction of the simulation domain for the sake of reducing the effects of simulation scale and to mimic the plane-stress condition. To keep the simulation model simple, a major assumption was to use the vacuum environment. This consideration although discards the role of oxidation of

silicon and 3C-SiC which is a practical reality but at the same time, it provides a healthy data to compare, contrast and highlight purely the role of temperature in influencing the deformation behaviour of silicon and 3C-SiC. Yet, such study should be seen as a test bed with the follow-on work aiming to address these points as well.

Table 3.1 shows the details of MD model and the cutting parameters employed in the simulations. High temperature nanometric cuttings of single crystal silicon and 3C-SiC were performed at different temperatures using various potential functions. In Figure 3.3, which is a 2D schematic diagram of the nanometric cutting simulation model, uncut chip thickness, tool tip radius, rake and clearance angles of the cutting tool are illustrated for the sake of clarification.

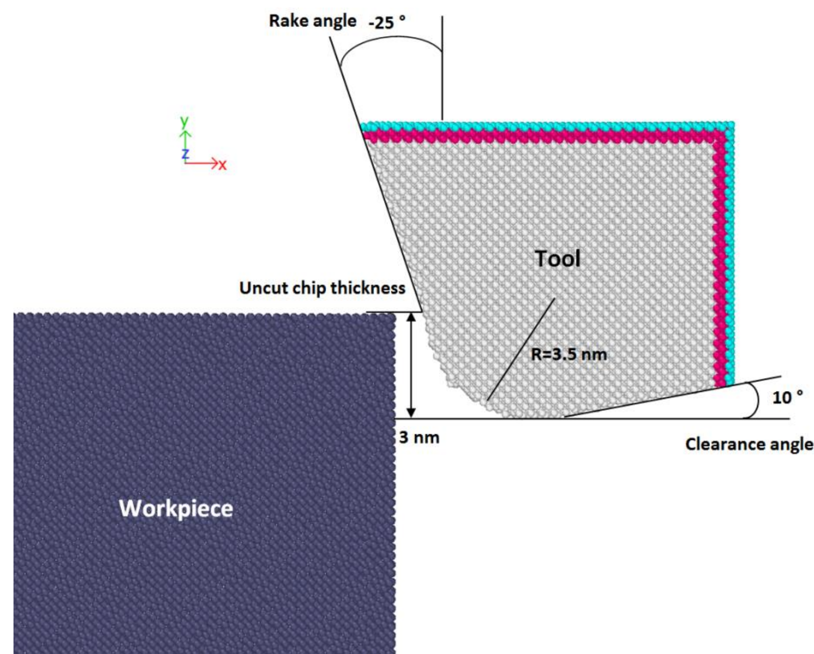


Figure 3.3: 2D schematic of the MD simulation model illustrating the uncut chip thickness, tool tip radius, rake and clearance angles of the cutting tool

Table 3.1: Details of the MD simulation model and the cutting parameters used in the study

| Parameter | Value |
|---|---|
| Workpiece material | Single crystal silicon (Si) |
| | Single crystal cubic silicon carbide (3C-SiC) |
| Workpiece dimensions | Si: $38\times19\times5.4$ $nm^3$ |
| | 3C-SiC: $34.8\times19.6\times4.4$ $nm^3$ |
| Tool material | Single crystal diamond |
| Cutting edge radius (tip radius) | 3.5 nm |
| Uncut chip thickness (cutting depth in 2D) | 3 nm |
| Cutting orientation and cutting direction | Case 1: (010)<100><br>Case 2: (110)<00$\bar{1}$><br>Case 3: (111)<$\bar{1}$10> |
| Rake and clearance angle of the cutting tool | -25° and 10° |
| Workpiece temperature | Si: 300 K, 500 K, 750 K, 850 K, 1173 K, 1273 K and 1500 K |
| | 3C-SiC: 300 K, 900 K, 1200 K, 1400 K, 1700 K, 2000 K and 3000 K |
| Cutting speed | 50 m/s |
| Time step | 1 fs |
| Potential energy functions used for nanometric cutting | Si: Modified Tersoff [43], ABOP [44], SW [36] |
| | 3C-SiC: ABOP [44], Tersoff [42] |

### 3.3. Potential energy functions employed in MD simulations

Development of potential energy function is a fertile area in the MD simulation arena. For this reason, various potential functions have been developed to describe the interaction between constituent atoms. Since the accuracy and reliability of classical MD simulations is governed by the potential function, precautions are needed while selecting interatomic potential for a specific system and process. Pair potentials such as Lennard-Jones or Morse have long been used in the past but they fail to predict the Cauchy pressure. Also, study of wear, fracture and plasticity involves bond reconfiguration and complex interactions and unlike in simple metals, this becomes even more complex situation in a diamond cubic material like silicon and in a zinc blende material such as 3C-SiC. Therefore, a three-body potential is a minimal choice for the purpose of studying nanometric cutting. Pastewka *et al.* [46] recently highlighted some key considerations required to employ a potential energy function to model the phenomena of fracture, wear or plasticity in materials such as silicon, carbon and silicon carbide. The most popular bond order potential function for simulating silicon has been the Tersoff potential function [39, 40]. However, Yoo *et al.* [80] and Cook and Clancy [81] revealed that the Tersoff potential is not suitable for temperature sensitive phenomena as it overestimates the melting temperature of silicon by approximately 50% higher and underestimates the density of the liquid by nearly 14% lower than the experimental values. This motivated Agrawal *et al.* [43] to develop a modified version of the Tersoff potential to overcome the aforementioned shortcomings. Nevertheless, its robustness to predict the mechanical properties are yet to be explored which will be done in this desertion through a simple test of elastic constants. Furthermore, Tersoff potential fails to correctly predict the dimer

properties of silicon such as binding energy, $D_0$, the equilibrium bonding distance, *r*, and the wave number, *k*, of the ground-state oscillation. One such shortcoming i.e. description of correct dimer properties was overcome by the ABOP proposed by Erhart and Albe [44]. An advantage of Tersoff and ABOP potential functions is that they offer interaction between carbon atoms (diamond tool) and silicon atoms (workpiece) and therefore become a choice for this study. SW potential function [36] was another choice which was also employed in this study to describe the atomic interactions between silicon atoms (Si-Si) in the substrate. Nonetheless, this potential function does not offer the interaction between silicon atoms and carbon atoms. To overcome this problem, a combination of SW and ABOP was utilized through defining a hybrid pair style which enabled us to dictate the interactions between diamond atoms (C-C) in the cutting tool, and the interaction between substrate and tool atoms (Si-C).

Regarding the SiC material, the most broadly adopted formalism for simulating Si-C system is another version of Tersoff potential function [42], which was developed in 1994 to appropriately estimate the ground-state structure, energies, and elastic properties of both 3C-SiC and amorphous SiC. One decade later, ABOP [44] was proposed which could describe both bulk as well as the dimer properties of SiC more properly than Tersoff potential. Therefore, in this dissertation, both the ABOP and Tersoff potentials were utilized to define the interactions between the atoms of silicon and carbon and to make a comparison between the results.

### 3.4. Geometry creation and simulation procedure

Using improper equilibrium lattice constant will force the simulation system to be far away from equilibrium and consequently the MD simulation results would be inaccurate. Hence, the simulation model has to be fed with the appropriate lattice constants at various temperatures from the potentials employed in this study.

The total energy content of the system is affected by the lattice constant; hence, it can influence the accuracy of the simulation results. The equilibrium lattice constant, which is defined as the length of unit cell at the equilibrium volume, ought to be calculated at different temperatures for the employed potential functions in order to utilize it in the simulations and attain reliable results. The lattice constant can be determined from the cohesive energy ($E_{coh}$ or $\Phi_{minimum}(\rho)$) which is described as the minimum energy needed for breaking the atoms of the solid into isolated atomic species.

$$\Phi = \frac{E_{pot}}{N} \tag{3.1}$$

$$\rho = \frac{N}{V} \tag{3.2}$$

where $\Phi$ is the lattice energy, $E_{pot}$ is the potential energy of the lattice, $\rho$ is density and $N$ is total number of atoms in the simulation cell with volume $V$ [82]. Accordingly, the cohesive energy is calculated for the diamond cubic structure of silicon and carbon, and zinc blende structure of 3C-SiC. The calculated minimum cohesive energies and their corresponding lattice constants for single crystal silicon and carbon at different temperatures for the modified Tersoff and ABOP functions are shown in Table 3.2, which are compared with the experimental values. It may be noted that the values for lattice constant of diamond are shown here only for the sake

of information and were not used during the simulation, mainly because the temperature of the tool was kept at 300 K in all the simulation and therefore lattice constants of 3.563 Å and 3.568 Å, respectively, were used as the equilibrium lattice constants of carbon for the modified Tersoff and ABOP potential functions. The cohesive energy corresponding to the equilibrium lattice constant of silicon obtained from the simulation at different temperatures for SW potential energy function has been shown in Table 3.3. The equilibrium lattice constant of diamond (cutting tool) at 300 K using ABOP function (3.568 Å) was used to build the tool in this case.

Similarly, equilibrium lattice constants and cohesive energies of single crystal 3C-SiC at different temperatures using ABOP and Tersoff potential energy functions were calculated and summarized in Table 3.4. The equilibrium lattice constant of diamond (cutting tool) at 300 K was computed as 3.568 Å and 3.558 Å for the ABOP and Tersoff potentials, respectively.

MD simulations were implemented by using a public-domain computer code, known as "large-scale atomic/molecular massively parallel simulator" (LAMMPS) [83]. At the start of the simulation, the diamond tool was set at a distance of 10 Å (1 nm) from the workpiece (free travel before cutting), in order to ensure that the tool atoms are far from the equilibrium cut-off range of the Si-C interaction potential. The simulation model was equilibrated for a total time of 30 ps before the commencement of cutting to achieve the desired temperature. In this work, although High Performance Computer (HPC) was employed, yet, the realistic cutting speeds (about 1 to 2 m/s) would have needed long computation times and therefore, 50 m/s was chosen as an optimal cutting speed to run a large set of simulations presented in this work.

Table 3.2: Variation in the lattice constant of silicon and carbon in diamond cubic structure obtained from the modified Tersoff [43] and ABOP [44] potential functions at various temperatures

| Temperature (K) | | Single crystal silicon | | | Carbon | | |
|---|---|---|---|---|---|---|---|
| | | Calculated lattice constant (Å) | Cohesive energy (eV) | Experimental lattice constant (Å) [84] | Calculated lattice constant (Å) | Cohesive energy (eV) | Experimental lattice constant (Å) [82] |
| 300 | Modified Tersoff | 5.436 | -4.628 | 5.431 | 3.563 | -7.423 | 3.566 |
| | ABOP | 5.433 | -4.627 | | 3.568 | -7.372 | |
| 500 | Modified Tersoff | 5.439 | -4.627 | 5.434 | 3.564 | -7.422 | - |
| | ABOP | 5.436 | -4.626 | | 3.569 | -7.371 | |
| 750 | Modified Tersoff | 5.443 | -4.626 | 5.439 | 3.566 | -7.421 | - |
| | ABOP | 5.439 | -4.625 | | 3.571 | -7.37 | |
| 850 | Modified Tersoff | 5.444 | -4.625 | - | 3.567 | -7.420 | - |
| | ABOP | 5.441 | -4.624 | | 3.572 | -7.369 | |
| 1173 | Modified Tersoff | 5.449 | -4.623 | 5.449 | 3.569 | -7.419 | - |
| | ABOP | 5.446 | -4.623 | | 3.574 | -7.367 | |
| 1500 | Modified Tersoff | 5.454 | -4.622 | 5.457 | 3.572 | -7.416 | - |

Table 3.3: Calculated equilibrium lattice constant and cohesive energy of single crystal silicon at different temperatures using SW potential energy function [36]

| Temperature (K) | lattice constant (Å) | cohesive energy (eV) | Experimental lattice constant (Å) [84] |
|---|---|---|---|
| 300 | 5.4348 | -4.3355 | 5.431 |
| 750 | 5.4405 | -4.3338 | 5.439 |
| 850 | 5.4423 | -4.3326 | - |
| 1173 | 5.4458 | -4.332 | ~ 5.449 |
| 1273 | 5.4473 | -4.3312 | ~ 5.452 |
| 1500 | 5.4502 | -4.3308 | ~ 5.457 |

Table 3.4: Calculated equilibrium lattice constants and cohesive energy of single crystal 3C-SiC at different temperatures using ABOP [44] and Tersoff [42] potential energy functions

| Temperature (K) | ABOP lattice constant (Å) | ABOP cohesive energy (eV) | Tersoff lattice constant (Å) | Tersoff cohesive energy (eV) | Experimental lattice constant (Å) [85] |
|---|---|---|---|---|---|
| 300 | 4.3623 | -6.3376 | 4.3113 | -6.4005 | 4.3581 |
| 900 | 4.3681 | -6.3342 | 4.3534 | -6.3269 | 4.3689 |
| 1200 | 4.3712 | -6.3325 | 4.3703 | -6.2878 | 4.3754 |
| 1400 | 4.3738 | -6.3297 | 4.3806 | -6.26088 | 4.3798 |
| 1700 | 4.4291 | -6.1401 | 4.3963 | -6.21971 | - |
| 2000 | 4.4409 | -6.1033 | 4.4109 | -6.17797 | - |
| 3000 | 4.4838 | -5.9718 | 4.452 | -6.04078 | - |

### 3.5. Visualization of atomic trajectories

LAMMPS generates three-dimensional atomic configurations or trajectories, which typically require to be further analysed so as to generate new scientific insights. To this end, raw atomic coordinates have to be translated into a meaningful graphical representation. In this dissertation, the visualization of atomic trajectories was carried out using “Open Visualization Tool” (OVITO) [86]. Its primary application area is large simulations based on classical potentials ($10^3$ - $10^8$ particles). OVITO is able to calculate coordination number and radial distribution function, displacement vector,

atomic strain tensor and identifying diamond structure. Moreover, it has incorporated the "Dislocation Extraction Algorithm" (DXA) [87] which can be used to analyse dislocation and defects.

### 3.6. Summary

In this chapter, the MD simulation methodology used for the nanometric cutting of silicon and 3C-SiC at elevated temperatures was described in detail. In brief, the atoms in the workpiece and cutting tool were divided into Newtonian atoms, thermostat atoms and boundary atoms. The Newtonian region was allowed to follow the Newtonian dynamics (LAMMPS NVE dynamics) while the thermostat zone was allowed to follow Berendsen thermostatic dynamics (LAMMPS NVT dynamics). Tersoff, modified Tersoff, ABOP and SW interatomic potential functions were adopted to describe the interactions between atoms. In order to obtain reliable results, the equilibrium lattice constants were calculated at different temperatures for the employed potential functions. In order to ensure the atoms of the tool are far from the equilibrium cut-off range of the Si-C interaction, at the beginning of simulation, the diamond tool was set at a distance of 10 Å (1 nm) from the substrate. Then, the model was relaxed for 30 ps to the specified temperature. To perform the simulations, LAMMPS software was employed on a HPC service which was coupled with OVITO to visualise and post-process the atomistic data.

# Chapter 4: MD simulation results for nanometric cutting of silicon at elevated temperatures

## 4.1. Introduction

During nanometric cutting of silicon at elevated temperatures, various concurrently occurring processes such as material flow behaviour, cutting chip characteristics, specific cutting energy, nanoscale friction, defect formation, etc. change with the temperature and crystal plane. However, such alterations associated with the high temperature nano-mechanical machining of silicon have not been documented up to now. A good understanding of the aforementioned phenomena would aid to acquire a broad picture of nanometric cutting of silicon at high temperatures which can lead us to enhance the cutting performance of silicon in this process. This chapter provides the MD simulation results regarding the plastic flow behaviour, stagnation region, chip related phenomena, cutting forces, specific cutting energies, yielding stresses, defect-mediated plasticity of silicon and the state of the diamond cutting tool post-machining in nanometric cutting on the (010), (110) and (111) crystal planes at a wide range of cutting temperatures i.e. 300 K-1500 K.

## 4.2. Plastic flow behaviour

An in-depth understanding of the plastic deformation mediated flow behaviour of single crystal silicon during its nanometric cutting at different temperatures is of significant relevance to adjudge surface quality of the machined substrate. Despite a substantial interest in studying nanometric cutting of silicon, there has been no theory till date suggesting material flow in different regions of the silicon substrate during

its ductile-regime machining [2]. In this section, an attempt is made to study the plastic deformation mediated flow behaviour of single crystal silicon during nanometric cutting process at different machining temperatures. The research of this sort will help address an important research question which is at the pinnacle of nanotechnology i.e. what is the fate of silicon when it is acted upon by high deviatoric stresses and to what an extent is it sensitive to the temperature of the substrate? The methodology adopted to perform the simulation has been described in Chapter 3. Since the point of interest was to study the flow behaviour of silicon at varying (high) cutting temperatures, a potential robust in predicting the melting point and thermal softening behaviour of silicon was required. Accordingly, the modified variant of the Tersoff interatomic potential function refined by Agrawal *et al.* [43], which is robust in predicting the melting point and thermal softening behaviour of silicon at elevated temperatures, was adopted here.

### 4.2.1. Atomic flow field

In order to explore the atomic flow field within the substrate, the substrate was divided into five distinct regions, as shown in Figure 4.1, and these were cut region, region underneath the tool flank face, region between the flank face and the tool tip, region ahead and beneath the tool tip and uncut region. This division was adopted for the ease of illustration. The stagnation region is the region where the shearing action (leading to chip formation) separates from the compressive action underneath the cutting edge of the tool (eventually leading to spring-back effect) resulting in the appearance of two stagnation angles ($\theta_s$) shown in Figure 4.1, and this can be calculated from:

$$\theta_{s1,2} = cos^{-1}(1 - \frac{h_{1,2}}{r}) \quad (4.1)$$

where $h_{1,2}$ stands respectively for the upper and lower bounds of stagnation region, and $r$ for the tool tip radius.

A snapshot from the MD simulation after 20 nm of cutting is presented in Figure 4.2 depicting the displacement vector of silicon atoms in the *XY* plane while machining at 300 K on the (010), (110) and the (111) crystal planes. Following conventional crystallographic convention, this dissertation uses ( ) and [ ] notations to represent crystallographic plane orientations (direction of plane normal) and crystallographic directions, such as cutting and slip, respectively. From Figure 4.2, one can observe a rotational flow of atoms underneath the cutting tool akin to fluid flow and a distinct distribution of atomic flow field in different regions of the substrate. It should be noted here that in order to determine the atomic flow field in different regions of the substrate, the atomic displacement of each atom from its initial configuration was calculated and accordingly the displacement vectors were plotted.

In a nanometric cutting process, there exists a so called stagnation/neutral region around the tool tip (as shown in Figure 4.1) whereby the atomic flow separates into two opposite directions. The atoms above the stagnation region are separated from the substrate and flow upward on the rake face of the cutting tool forming the cutting chips whereas atoms below the stagnation region are compressed downward by the tool tip, eventually resulting in the observed spring back effect.

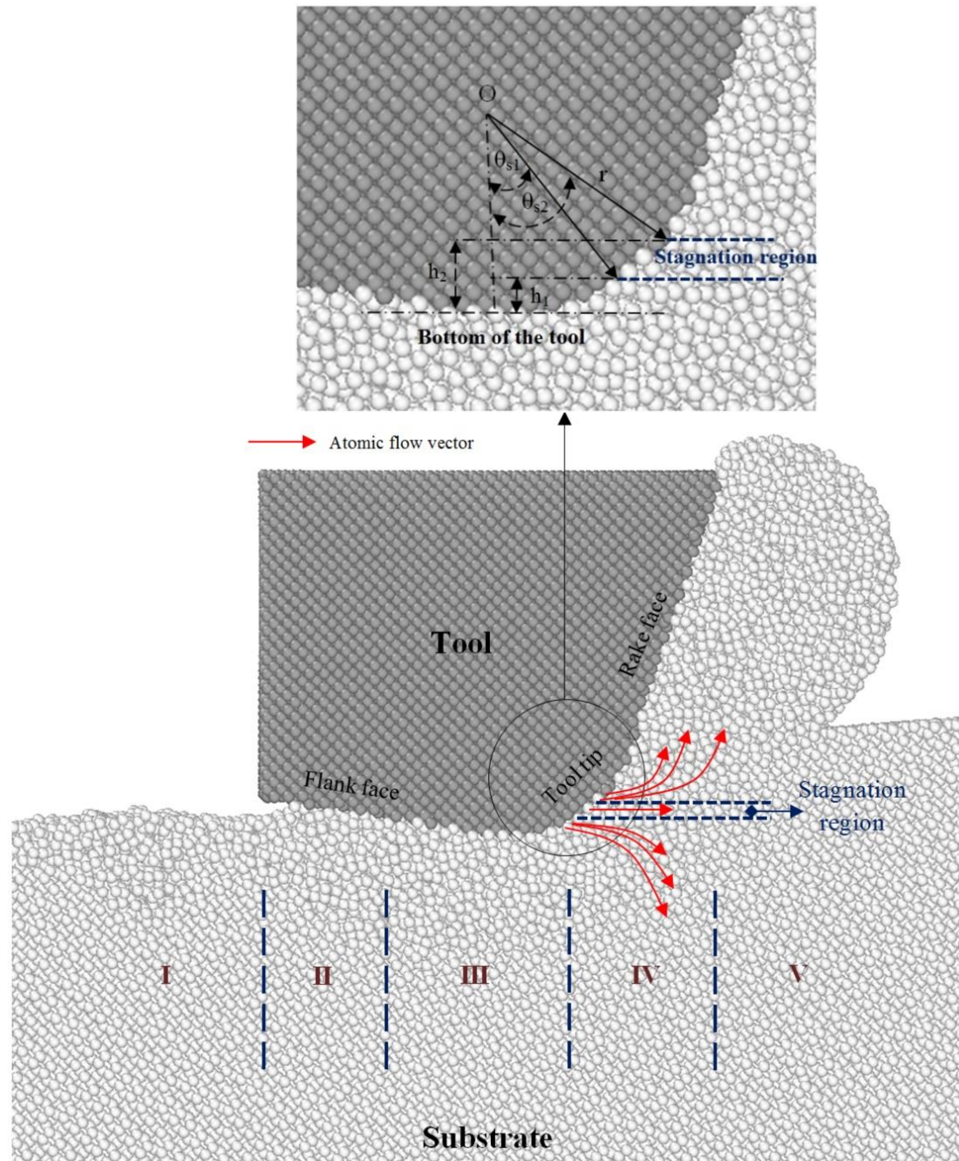


Figure 4.1: Five regions in the substrate: I- Cut region, II- Underneath the flank face, III- Between the flank face and tool tip IV- Ahead and beneath the tool tip, V- Uncut region. Red arrows are flow vectors around the stagnation region. In the detailed snapshot, $\theta_{s1,2}$ and $h_{1,2}$ represent the limiting bounds of the stagnation angles respectively in the stagnation region.

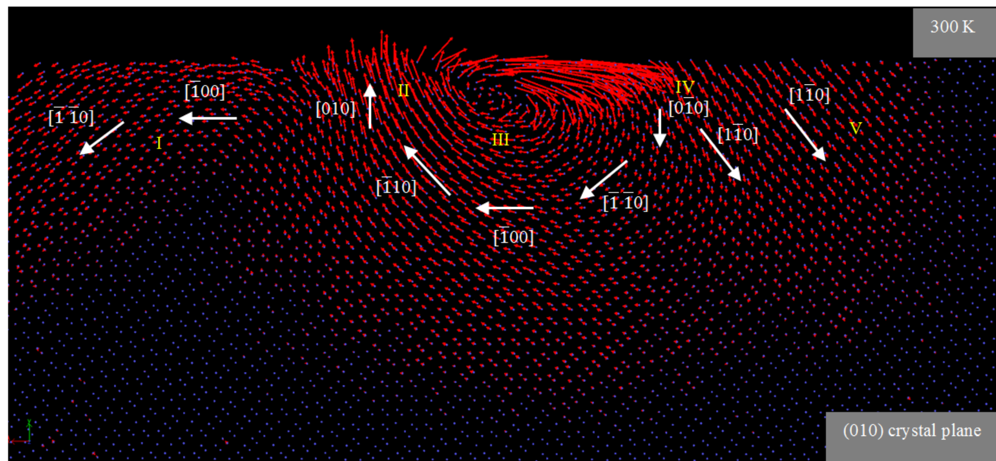


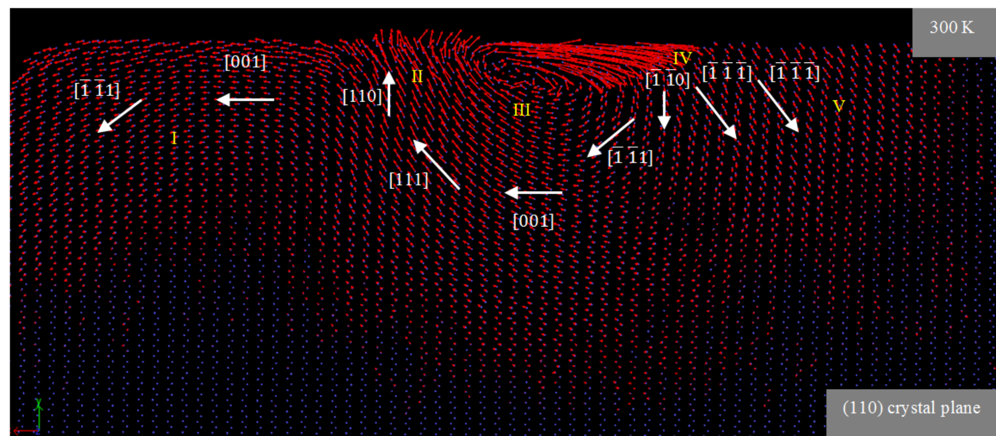


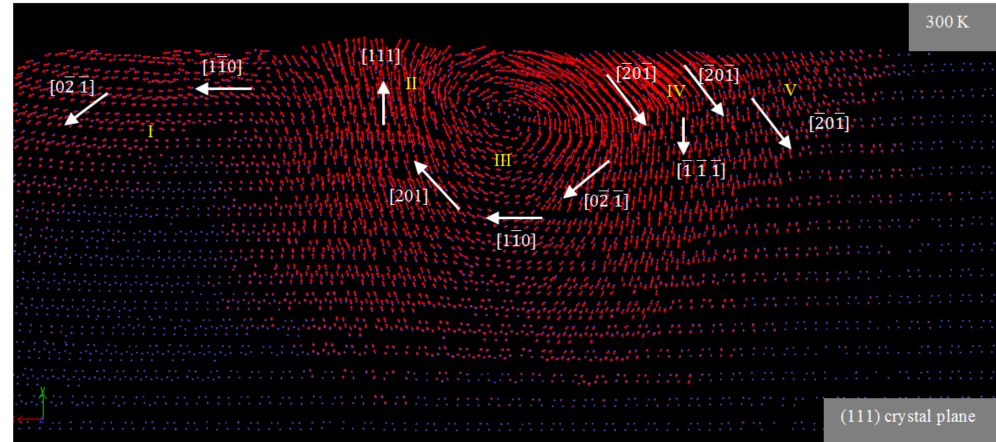


Figure 4.2: Snapshots of atomic flow field in the XY plane while cutting silicon on the different crystal planes at 300 K. The red arrows indicate displacement vectors of atoms and their lengths demonstrate the magnitude of displacement. The atoms of the cutting tool are deliberately kept hidden so the position of the cutting tool with regard to the five regions in the substrate can be traced from Figure 4.1.

Although shown explicitly in Figure 4.2, by and large, the five manifold distribution of the atomic flow field for the three crystal planes was found identical and hence only the (110) plane has been used here for illustration purposes. The chip formation process during nanometric cutting of single crystal silicon involves extrusion of the material [88] and in this study it was observed that on the (110) surface it proceeds in the $[00\bar{1}]$ and $[11\bar{1}]$ directions. As the cutting tool goes past region *I*, the highly compressed atoms in this region tend to restore their equilibrium positions in order to relieve the residual stresses. At macroscopic scale, this is recognized as material recovery or spring back effect. Consequently, few distinct backward and transverse movements along the [001] and $[\bar{1}\bar{1}1]$ directions were observed in the region *I*. As the substrate temperature increases, the magnitude of atomic displacement decreases in both the aforementioned directions, as shown in Figure 4.3. In region *II* (underneath the flank face), the upward motion of the atoms along the [110] direction results in elastic recovery on the flank face. As the substrate temperature increases, the movement of the atoms in this region was observed to change from the [110] to $[11\bar{1}]$ and $[00\bar{1}]$ directions, indicating reduced spring back underneath the flank face. One plausible reason for this phenomenon could be the fact that an increase of the substrate temperature results in an increase in the amplitude of atomic vibration signifying increased number of phonons which in turn contributes to additional atomic displacements. The atomic displacements within the substrate result in an increase in the interatomic distances and a decrease in the restoring forces due to thermal expansion, leading to the lowering of the energy required to change the atomic bonds. Consequently, thermal softening enhances the plasticity of the silicon substrate.

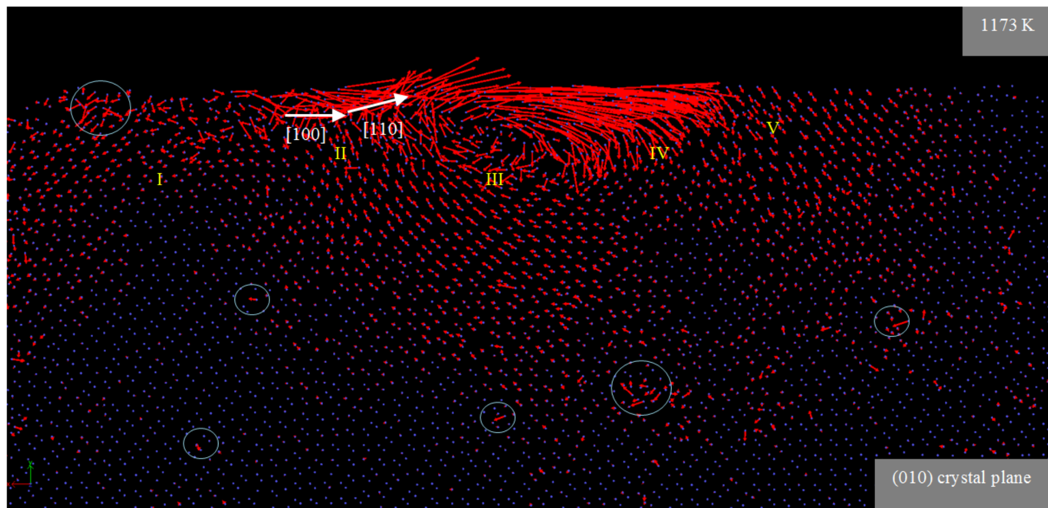


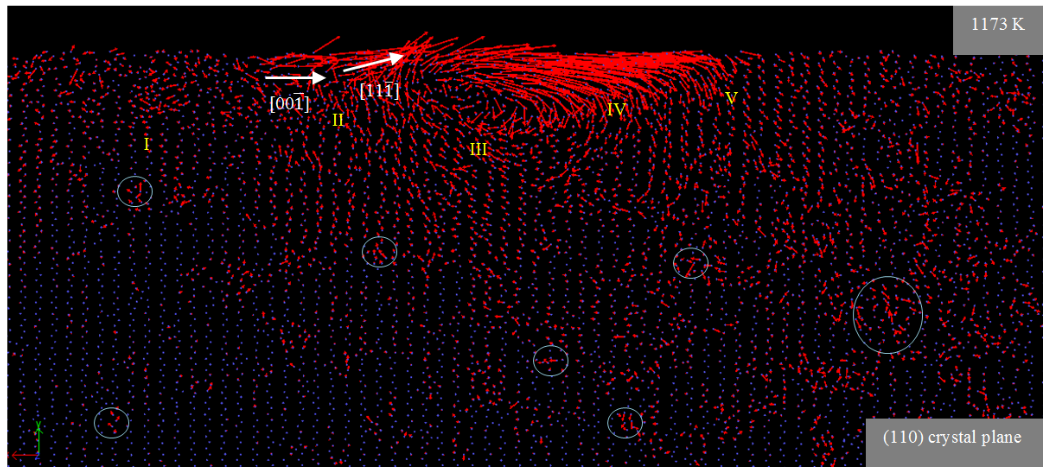


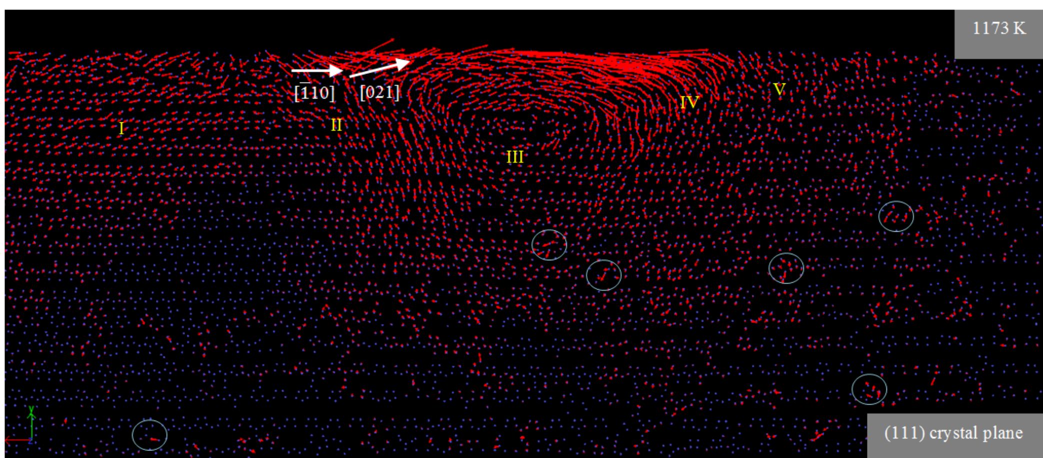


Figure 4.3: Snapshots of atomic flow field while cutting silicon on the different crystal planes at 1173 K. At high temperatures, the upward movement of atoms is eliminated, leading to decrease of the spring back on the flank face. More distorted atoms are highlighted by grey circles.

The highly strained atoms in region *III* (between the tool flank face and tool tip) under the wake of the cutting tool experience flow (site of vorticity), which comprises movement of the atoms in the $[\bar{1}\bar{1}1]$, $[001]$, $[111]$ and [110] directions. The initiation of the material flow, $[\bar{1}\bar{1}0]$, occurs underneath the lowest part of the tool tip. The centre of the flow region can be perceived as a stagnant point of the atomic flow where the theoretical displacement of the material approaches zero. Interestingly, except for 1500 K, the vortex flow of the atoms in region *III* was a consistent observation at all the simulated temperatures. From a visual perspective, the flow was seemingly a laminar flow whereas at higher temperatures, such as at 1173 K and 1500 K, the flow of the material was seemingly turbulent. The flow characterisation of plastically deformed material is a newly identified area of research from this dissertation, which can be expanded later.

In region *IV*, the tool tip pushes the atoms downward and along the $[\bar{1}\bar{1}\bar{1}]$ direction. It is well acknowledged that slip in a diamond cubic lattice structure occurs preferentially in the <110> family of directions on the {111} family of planes. Atoms in region *V* move downward along the $[\bar{1}\bar{1}\bar{1}]$ direction, which is consistent with the slip system of silicon on the (111) plane. Slip in single crystal silicon is normally expected to take place on broadly spaced shuffle planes, yet micro-compression experiments at high temperatures showed that slip in silicon occurs by the movement of dislocations on more closely spaced glide planes [89]. Figure 4.4 demonstrates that when the nanometric cutting was performed at 1500 K, the substrate atoms move along the $[00\bar{1}]$ and $[\bar{1}\bar{1}\bar{1}]$ directions plausibly due to weaker van der Waals interactions between atoms. Additionally it can also be seen that the turbulence in the substrate atoms increases with the increase in the machining temperature.

Another key finding from Figure 4.2 is that when the nanometric cutting was performed on the (111) plane, the position of the centre of rotational flow in region *III* was observed to be located lower than those on the other crystal planes, and thereby contributing to a more influential flow of the atoms in the substrate which facilitates the material removal process during nanometric cutting. The observed phenomenon can be considered as a confirmation for the fact that the $[\bar{1}10]$ is the easy cutting direction on the (111) plane of silicon [90]. In addition, by comparing the distorted atoms highlighted by grey circles in Figure 4.3, one can deduce that when hot nanometric cutting is performed on the (110) crystal plane, the number of displaced atoms will be higher than those on other crystal planes.

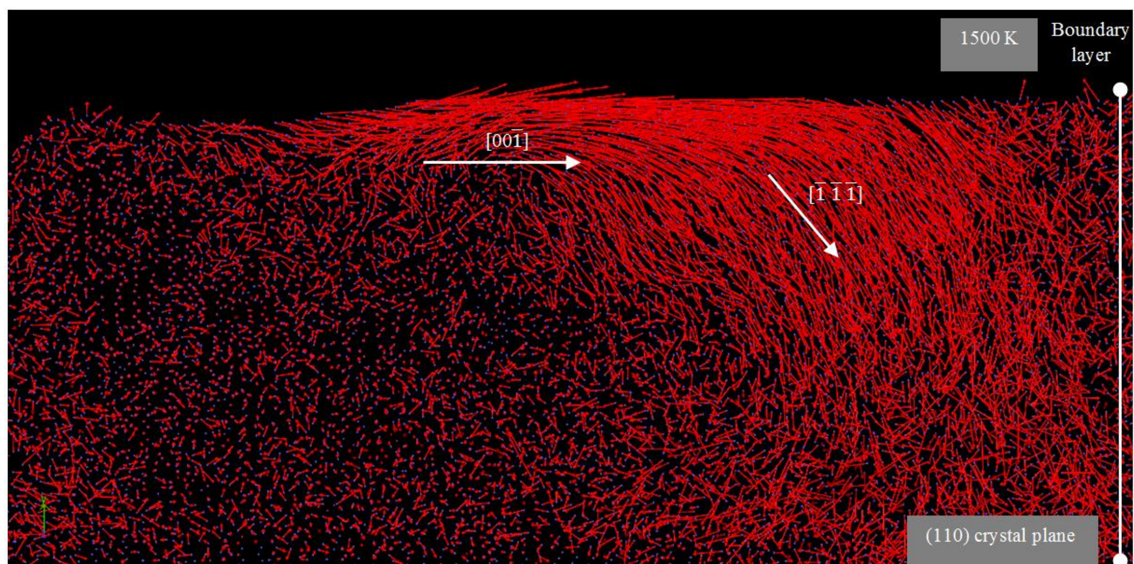


Figure 4.4: Snapshot of atomic flow field while cutting silicon on the (110) crystal plane at 1500 K. Substrate atoms move along the cutting and slip system directions owing to the very weak interaction between atoms and viscous flow of the material. Chaotic behaviour of the atoms can be observed as well.

### 4.2.2. Stagnation region and friction angle

A stagnant region is assumed on the tool, below which the material flows downward without any chip formation. This phenomenon is called ploughing, which is elastic-plastic deformation without material removal. Above this stagnation region, the material flows up and forms as chips. At the stagnation region, there is no chip formation, and shear strain approaches to infinite, since the material is stagnant. The stagnant region represents the minimum power needed for the material removal. In order to locate the stagnation region during the nanometric cutting process, the average displacement of substrate atoms in the $y$ direction in different layers were plotted. Figure 4.5 shows the quantified displacements of various layers within the substrate while cutting silicon on the (110) crystal plane at 300 K. In Figure 4.5, the slope alteration from positive (+) to negative (-) indicates the stagnation region. Thus, the region in the space of 0.2 nm to 0.4 nm (from the bottom of the tool) was identified as the stagnation region for the simulated cutting configuration for the cutting at 300 K on the (110) plane. Table 4.1 summarizes the position of stagnation region and corresponding angles while cutting silicon on the different crystal planes and at various temperatures. This table highlights strong influence of the orientation and temperature on the stagnation region.

In general, when cutting was performed on the (111) plane, the stagnation region (irrespective of the cutting temperature) was observed to locate at an upper position than for the (010) and (110) planes. This signifies that ploughing due to compression is relatively higher on the (111) plane and thus the extent of deformed surface and sub-surface leading to higher spring-back is more pronounced on this orientation. Also, at high temperatures, the stagnation region was observed to shift downwards

compared to what was observed at room temperature.

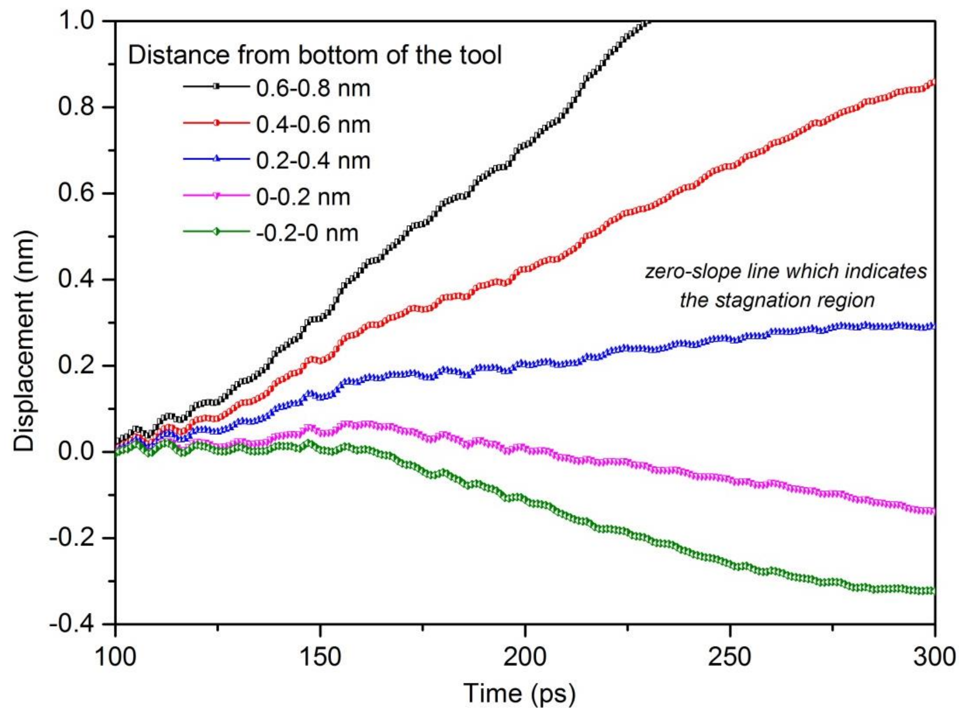


Figure 4.5: Displacement of different layers in y direction

Analytical and experimental approaches have shown a clear correlation between stagnation angle and friction angle between the workpiece and the rake face during shearing especially during cutting of soft materials [91]. Therefore, it is instructive at this point to examine the relation between stagnation angle and friction angle in single crystal silicon in order to find out whether there is any correlation between stagnation angle and friction angle for hard-brittle material. Friction angle, whose tangent is equal to friction coefficient, controls the heat generation at the tool-chip interface.

Table 4.1: Stagnation region, stagnation angle and friction angle in nanometric cutting of single crystal silicon at various temperatures

| Substrate Temperature (K) | Crystal plane | Position of Stagnation region from bottom of the tool ($h_{1,2}$) (nm) | Stagnation angles ($\theta_{s1,2}$) (degree) | Friction angle (β) (degree) |
|---|---|---|---|---|
| 300 | (010) | 0.5-0.7 | 31-36.9 | 39.3 |
| | (110) | 0.2-0.4 | 19.5-27.7 | 38.6 |
| | (111) | 0.7-0.9 | 36.9-42 | 38.3 |
| 500 | (010) | 0.5-0.7 | 31-36.9 | 38.7 |
| | (110) | 0.2-0.4 | 19.5-27.7 | 38.9 |
| | (111) | 0.8-1 | 39.9-44.4 | 40.6 |
| 750 | (010) | 0.3-0.5 | 23.9-31 | 38.2 |
| | (110) | 0.2-0.4 | 19.5-27.7 | 36.3 |
| | (111) | 0.5-0.7 | 31-36.9 | 37.1 |
| 850 | (010) | 0.4-0.6 | 27.7-34 | 36.7 |
| | (110) | 0.1-0.3 | 13.7-23.9 | 38.2 |
| | (111) | 0.8-1 | 39.9-44.4 | 42.8 |
| 1173 | (010) | 0.2-0.4 | 19.5-27.7 | 35.9 |
| | (110) | 0.1-0.3 | 13.7-23.9 | 37.7 |
| | (111) | 0.4-0.6 | 27.7-34 | 43.2 |
| 1500 | (010) | 0.2-0.4 | 19.5-27.7 | 50.6 |
| | (110) | 0.2-0.4 | 19.5-27.7 | 45.7 |
| | (111) | 0.3-0.5 | 23.9-31 | 53.1 |

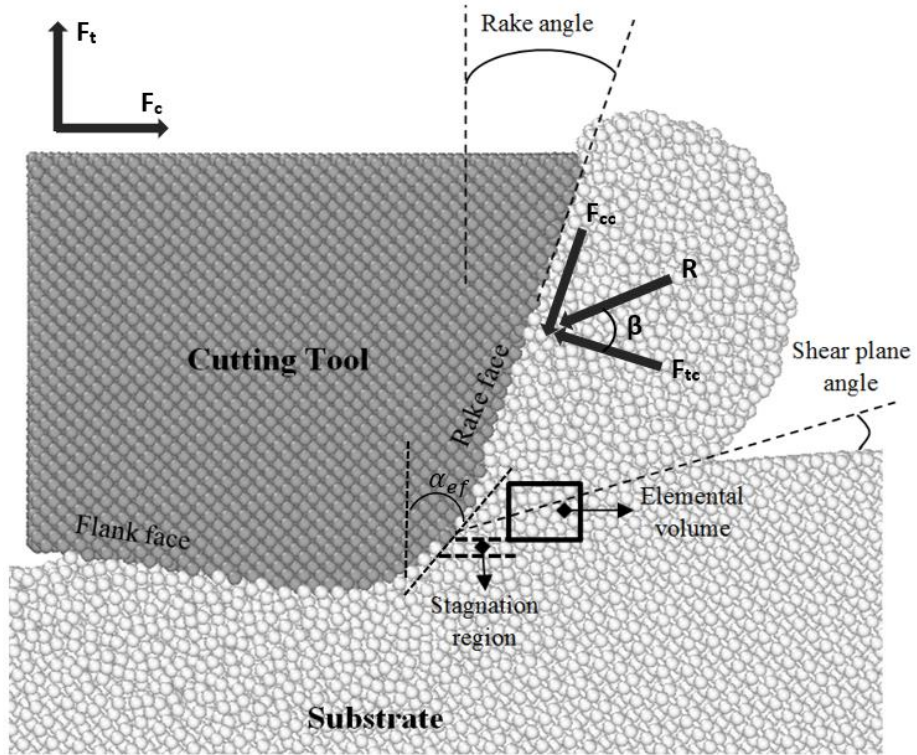


Figure 4.6: A snapshot of MD simulation demonstrating nominal rake angle, effective rake angle $\alpha_{ef}$, shear plane angle, stagnation region, cutting and friction forces. The elemental volume represents the volume of material (1×1.5×3 $nm^3$) considered for monitoring the variations of temperature during chip formation (only 2D representation is shown here).

The friction angle (*β*) for a rounded edge tool was estimated through equations (4.2) and (4.3), which uses the effective rake angle in place of nominal rake angle, as shown in Figure 4.6.

$$\beta = \alpha_{ef} + tan^{-1}(\frac{F_c}{F_t}) \quad (4.2)$$

$$\alpha_{ef} = sin^{-1}(1 - \frac{d}{r}) \quad (4.3)$$

where $\alpha_{ef}$ is the effective rake angle, $F_c$ is the tangential cutting force, $F_t$ is the thrust

force and $d$ is the uncut chip thickness. The values of friction angle have been listed in Table 4.1.

While cutting silicon on the (111) and (010) at lower machining temperatures *viz.* 300 K to 850 K, the magnitude of stagnation and friction angle were observed to be closely related. However, an inconsistency was observed as soon as the machining conditions were changed i.e. on the (110) crystal plane, an average difference of 15° to 25° was observed between the two angles. A noteworthy finding is that the discrepancy between stagnation and friction angle increases with the increase of the substrate temperature for the different crystallographic planes.

### 4.3. Chip related phenomena

In nanometric cutting of single crystal silicon, the cutting edge of the tool penetrates into the substrate surfaces, which are therefore plastically deformed and slide off along the rake face of the cutting tool at a constant velocity in a stationary flow, resulting in chip formation. Hence, the relative movement of the cutting tool and substrate leads to removing a layer of atoms (chip) from the substrate. The processes of chip formation can be examined within the orthogonal plane, since essential parts of the material flow take place within this plane. The major portion of the plastic deformation during chip formation occurs in the primary shear zone (area between the cut and chip shown in Figure 4.7). The substrate material is deformed under the action of high friction forces in the secondary shear zones (area along the cutting tool face) in front of the rake face and the flank face [92].

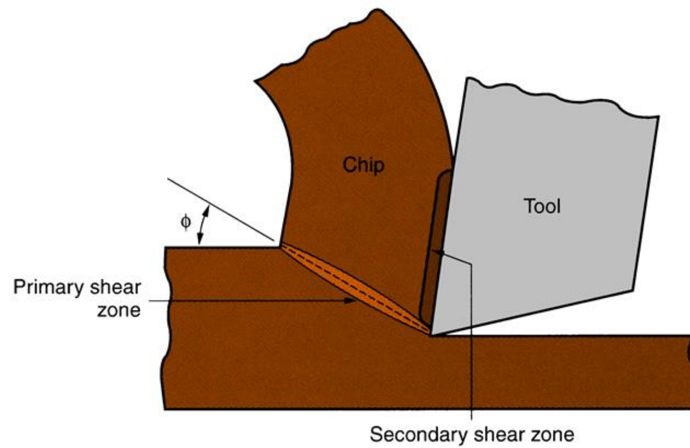


Figure 4.7: Priamary and secondary shear zones

Chip related phenomena refer to the complex phenomena encountered in nanometric cutting such as behaviour of the work material, required specific energy and degree of interaction at the tool/chip interfaces. Appreciation of chip related phenomena is thus indispensable to acquire a wide picture of nanometirc cutting of silicon at different temperatures and to clarify what occurs around the cutting edge when the chip is generated at high temperatures. This section therefore aims at applying MD simulation by using two types of interatomic potential functions, the modified version of the Tersoff [43] and ABOP [44] in order to compare the results obtained by both potential functions, to explore chip related phenomena on the tool/chip interface during nanometric cutting of single crystal silicon on three crystal planes i.e. the (010), (110) and the (111) at a range of machining temperatures from 300 K to 1500 K. The unique application of the two potential functions was based on the fact that the modified Tersoff was developed to overcome the shortcomings of the original Tersoff function [39, 40] which overestimates the melting point of silicon while the ABOP is more robust in accurately describing the bulk and dimer properties of silicon with a poor prediction of melting point. Indeed, the poor

estimation of melting point is a common problem intrinsic to bond order potentials for semiconductors.

### 4.3.1. Chip formation and mechanisms

In nanometric cutting, substrate atoms adjacent to the tool tip are subjected to the high compressive energy, resulting in forming highly displaced and disordered atoms. As the cutting tool advances, the atoms near the tool tip pile up in front of the tool tip leading to the formation of cutting chips. It is believed that the chips are formed based upon an extrusion-like process triggered by the effective rake angle of the cutting tool [88]. The extrusion-like mechanism might be a consequence of pressure drop (owing to a rise in the contact area) from the tool tip towards the region of the cutting edge [93]. Figure 4.8 demonstrates the displacement vectors of chip atoms in the *XY* plane on the different crystal planes. The chip formation mechanism in nanometric cutting of single crystal silicon on the (010) crystal plane comprises the extrusion of the workpiece atoms in the cutting direction, [100], and the transverse direction along the [110] direction. Other miller indices of direction during chip extrusion while cutting silicon on the (110) and (111) planes can be traced from the Figure 4.8.

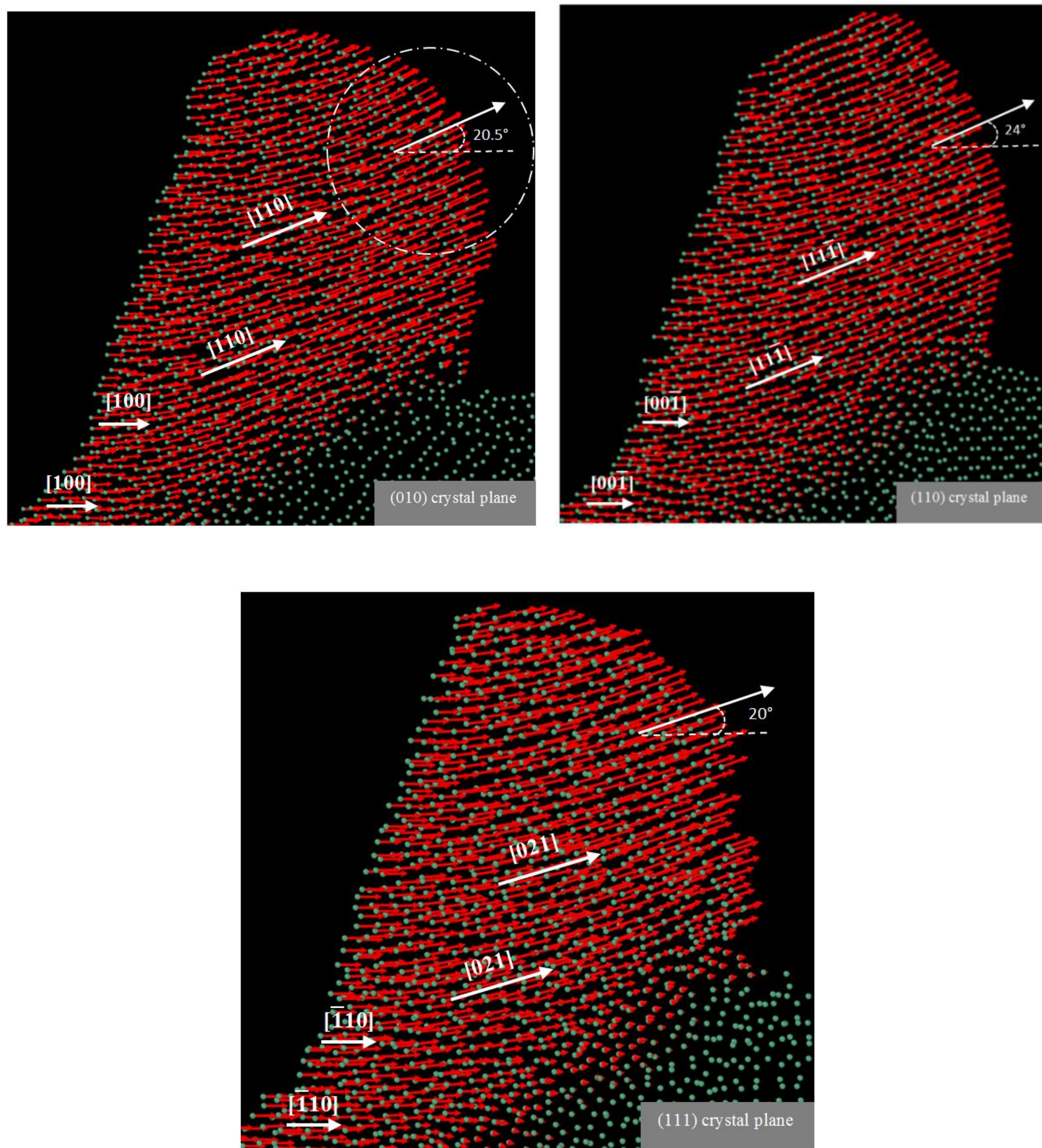


Figure 4.8: Displacement vectors of chip atoms and their corresponding angles in the *XY* plane. The chip velocity angle was calculated for the atoms located on the right side of the chip.

Figure 4.8 also demonstrates the angle of displacement vectors of the chip atoms (chip velocity angle) relative to the horizontal direction while cutting silicon on the different crystal planes. Note that the chip velocity angle was calculated on the right side of the cutting chip (shown in Figure 4.8) for all the cases since the atoms on the

left side of the cutting chip are profoundly affected by the rake face of the tool. In cutting operations, controlling chip formation and chip flow is essential to improve chip evacuation and to avoid interaction during cutting between chips and the machined part. In such a situation chips may alter the surface finish and part quality if it is not properly directed away from the cutting zone. Therefore estimating the chip flow direction allows improving the cutting operation by choosing adequate cutting conditions as well as geometric characteristics of cutting tools [94]. Figure 4.9 demonstrates the variations of the chip velocity angle with the temperature of the substrate while cutting silicon on the different crystal planes. It can be seen from Figure 4.9 that regardless of temperature of the substrate the minimum chip velocity angle appears while cutting the (111) crystal plane whereas it reaches the maximum while cutting the (110) surface. Comparing the chip velocity angle at different temperatures of the substrate, it can be found that, using the modified Tersoff potential function, the chip velocity angle slightly increases (by ~3°) with the rise of the temperature of the substrate up to ~1200 K. However, a remarkable decrease in the angle can be seen at higher temperature, i.e. 1500 K (0.88 $T_m$), attributable to the very weak van der Waals interactions between the substrate atoms leading to the movement of chip atoms along the cutting direction rather than along the transvers direction. Nevertheless, such behaviour did not realize when the ABOP potential was employed; hence the chip velocity angle rose constantly with the increase of temperature of the substrate up to 1500 K. The reason for such observation could be traced at the melting point of silicon predicted by the ABOP potential. Since the ABOP potential energy function has not been parameterized to precisely reproduce the melting point of silicon, it is likely that it overestimates the melting temperature

of silicon. As a consequence, satisfactory thermal softening which ought to be occurred at high temperature of 1500 K cannot be achieved. An attempt was made so as to calculate the phase instability and entirely molten temperatures of silicon using the one-phase method with reflective boundaries so as to diminish the hysteresis phenomenon. The phase instability and entirely molten temperatures of silicon given by ABOP were calculated at 2481 K and 2549 K, respectively, which are far above the experimental value (1687 K). Hence at 1500 K, very weak interatomic interactions cannot be precisely described by ABOP. In the same way, the phase instability and entirely molten temperatures of silicon predicted by the modified Tersoff were calculated to be 1397 K and 1616 K, which are more close to the experimental values. Further details on the calculations of the melting temperatures can be found in Appendix A.

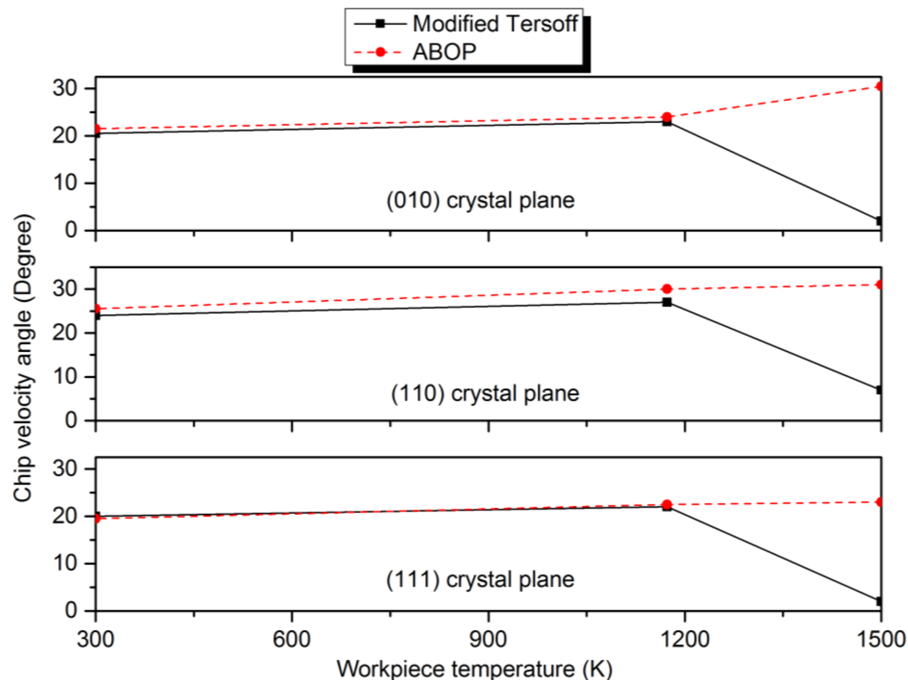


Figure 4.9: Chip velocity angle as a function of temperature and crystal plane obtained by the modified Tersoff and ABOP potential functions

### 4.3.2. Geometry and characteristics of the chip

The chip form is a key index of the cutting as it would determine the behaviour of material under the cutting action. Figure 4.10 demonstrates a representative cross-sectional morphology of the cutting chip and subsurface crystal deformation of single crystal silicon while cutting the (010) crystal surface at 300 K and 1173 K obtained by the modified Tersoff potential function. White atoms in the figure signify atoms which have transformed from their pristine diamond cubic structure to the amorphous state, obtained via monitoring the local environment of atoms up to the second neighbor shell using the diamond structure identification tool in OVITO [95]. The subsurface deformation depth shown in Figure 4.10 was calculated through measuring the height of the lowest layer of the generated amorphous atoms (white atoms) underneath the tool. In addition, the distance between atoms on the upper and bottom surface of the chip, where the chip possesses the maximum radius of curvature, was considered as the chip thickness.

It can be clearly observed that thinner and taller chip is formed when nanometric cutting is implemented at 1173 K. In addition, when nanometric cutting is performed at room temperature, the depth of subsurface deformation layer is smaller than that of 1173 K. Thus, the deformation depth becomes deeper when the temperature of the substrate rises. As mentioned earlier, when the temperature of the substrate increases, the amplitude of atomic vibration of the substrate atoms increases, which is considered as an increase in the number of phonons. Consequently, atomic displacements are generated which lead to the increase of interatomic distances between atoms and thus weaker interatomic bonding. The weaker bonding between atoms at higher temperature causes more crystal deformation within subsurface

atoms. Thus, the layer depth of deformation becomes greater.

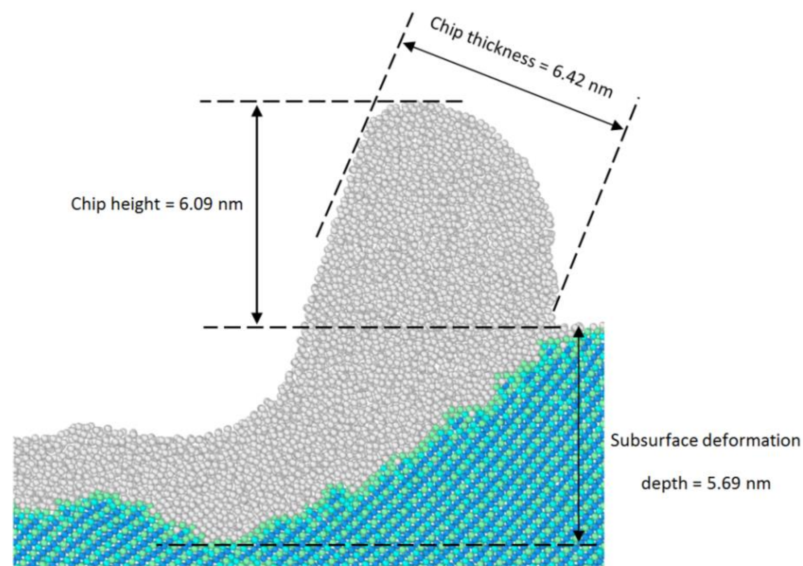


(a) 300 K

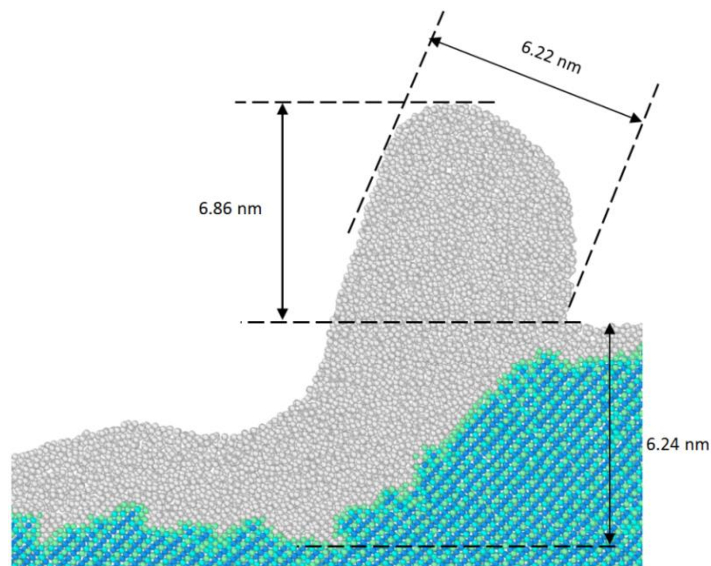


(b) 1173 K

Figure 4.10: Cross-sectional morphology of the cutting chip and subsurface crystal deformation of single crystal silicon while cutting the (010) crystal plane. Atoms in white colour are amorphous atoms.

It can be observed from Figure 4.11 that as the temperature of the substrate increases up to ~1200 K, thinner chips are produced, which indicates that lower cutting forces are needed to form the chip. Nevertheless, at temperatures higher than ~1200 K, the chip starts thickening owing to the more pile-up of atoms ahead of the cutting tool due to relatively easier flow of the substrate atoms at high temperatures. However, as will be shown in sections 4.3.3 and 4.4, the cutting forces, specific cutting energies and forces exerted by the tool rake face on the chip keep decreasing as long as the temperature of the substrate is raised. Similar trend was witnessed for the chip height, which has not been shown here. It is interesting to see that while cutting the (010) plane modelled by the modified Tersoff potential function, the chip thickness decreases constantly even at high temperature of 1500 K.

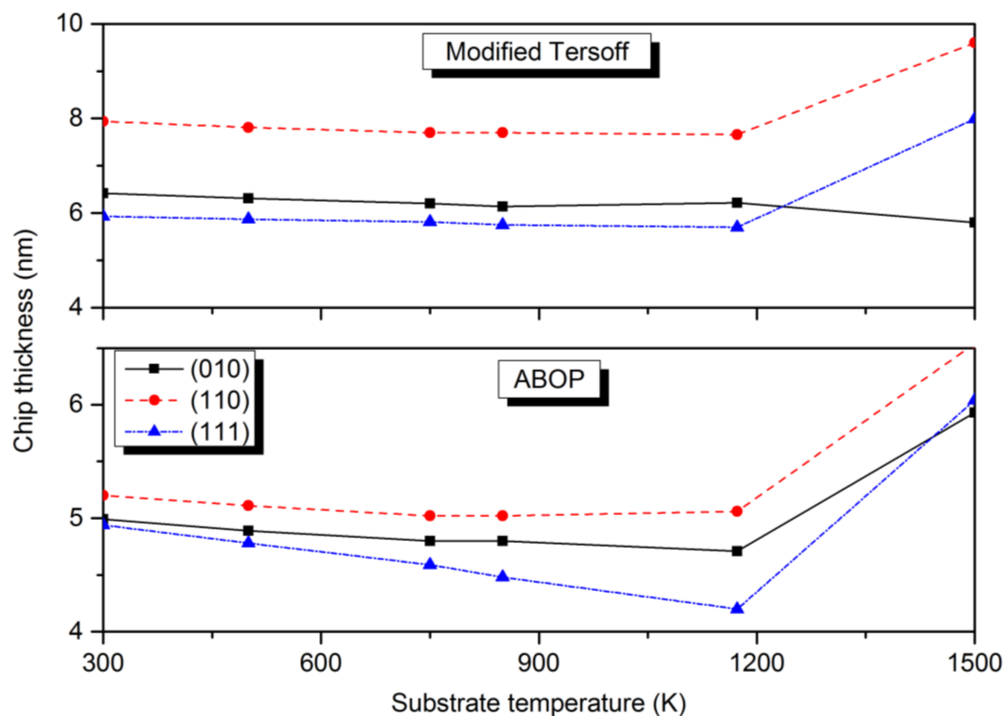


Figure 4.11: Variations of the chip thickness while cutting silicon on different crystallographic planes at various temperatures obtained by modified Tersoff and ABOP potential functions

The chip ratio (ratio of the uncut chip thickness to the cut chip thickness) is regarded as a measure of plastic deformation and indeed it is a beneficial gauge to indicate machinability characteristics of the substrate, which signifies energy consumed on plastic deformation in nanometric cutting. A large magnitude of chip ratio implies less thickening of the cutting chip thus smaller degree of deformation occurs during chip formation. This suggests that less force or energy is required to cut the substrate. It is observed from Figure 4.12 that, in general, the chip ratio increases with the increase of temperature of the substrate, suggesting that the machinability of the substrate improves at higher temperatures. More apparent rise of the chip ratio is observed in Figure 4.12 when the ABOP potential function is used. As mentioned before, due to more pile-up of atoms at higher temperatures, viz. 1500 K, the chip ratio decreases at these temperatures. The same scenario observed in the above is seen for the chip ratio modelled by the modified Tersoff potential function.

The variation of number of the atoms in the chip with the temperature is demonstrated in Figure 4.13, where the number of atoms in the chip increases up to ~1200 K while cutting silicon on the (010) and (110) planes. However, when nanometric cutting is performed on the (111) plane, the number of atoms in the chip increases constantly up to 1500 K. Such trend is observed for both the employed potential functions. More importantly, using both the potential functions, increase of the subsurface deformation layer depth is observed during cutting at higher temperatures, as demonstrated in Figure 4.14. The key information from this analysis is that hot machining comes at an expense of relative increase in the subsurface deformation.

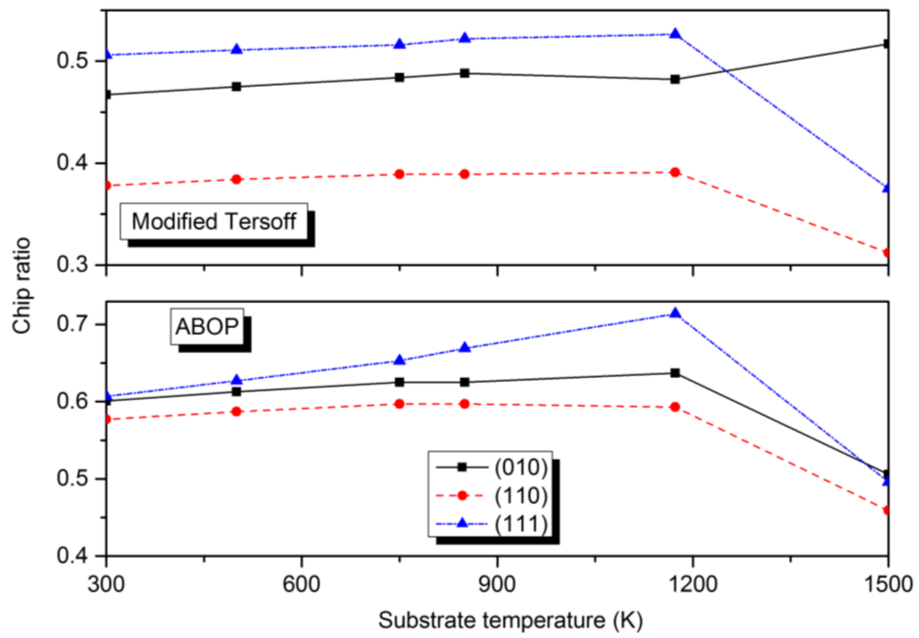


Figure 4.12: Variations of the chip ratio while cutting silicon on different crystallographic planes at various temperatures

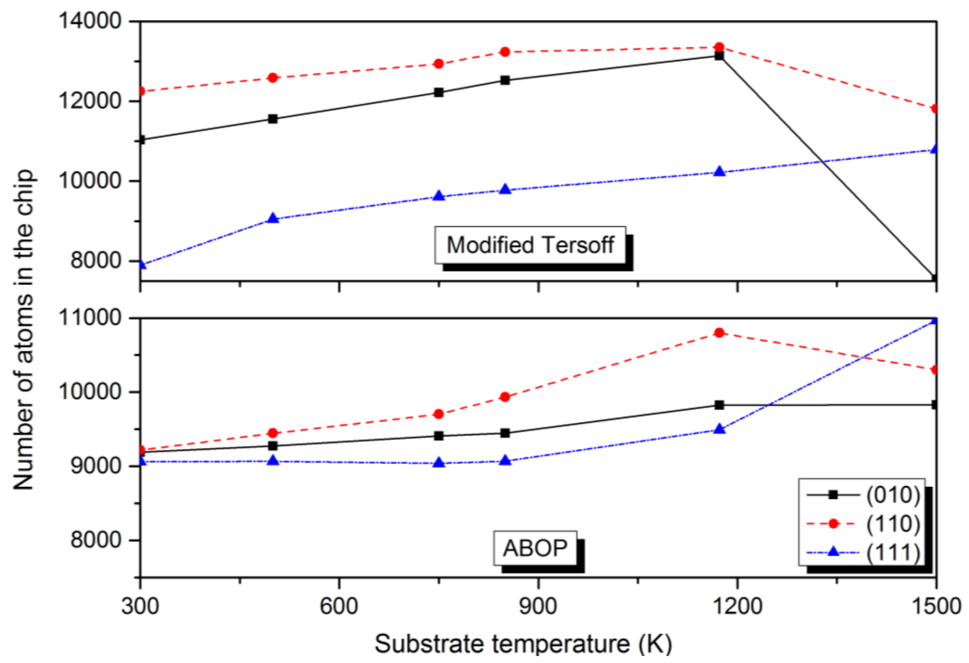


Figure 4.13: Number of atoms in the cutting chip as a function of temperature and crystal plane

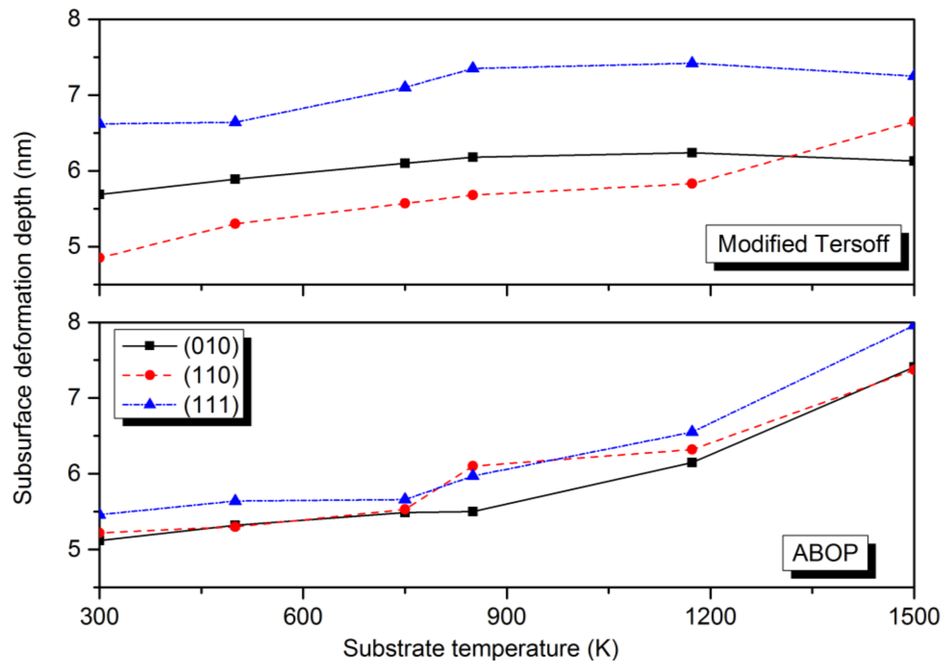


Figure 4.14: Increase of the subsurface deformation layer depth with temperature on different crystal planes

Another light that can be brought by the Figure 4.12, Figure 4.13 and Figure 4.14 is the variation of the aforementioned parameters on the different crystal planes. Experiments [96] and simulations [97] have shown that silicon is an intrinsically-anisotropic material even during cutting at room temperature. Hence, the aforementioned parameters are influenced by the crystallographic microstructure of the substrate. Irrespective to the machining temperature, the largest chip ratio is found on the (111) plane while the smallest value appears on the (110) surface. It indicates that machinability is higher when nanometric cutting of silicon is performed on the (111) crystal plane. Thus, the (111) crystal plane can be considered as the easy cutting plane whereas the (110) surface is the difficult to cut crystalline plane. However, Figure 4.12 shows some inconsistencies at temperatures higher than ~1200 K when the modified Tersoff potential function is used.

Regardless of the temperature of substrate, the maximum number of atoms in the chip was found while cutting silicon on the (110) surface, whereas the minimum number was observed on the (111) crystal plane. This observation may be closely related to the position of the stagnation region during cutting on different crystal planes. It was revealed in section 4.2.2 that when cutting of silicon is carried out on the (111) crystal plane, the stagnation region (shown in Figure 4.1) is located higher (from the bottom of the tool) than those on the other crystal planes. For instance, when cutting was performed on the (111) crystal plane at 750 K, the stagnation region was positioned at 0.5-0.7 nm from the bottom of the tool as opposed to 0.2-0.4 nm for the (110) plane. This fact suggests that more atoms are compressed to the machined surface and less atoms flow upward on the rake face of the cutting tool to form the chips. This implies that ploughing due to compression is more pronounced on the (111) plane and thus a thicker subsurface deformation layer is generated, as demonstrated in Figure 4.14. The converse scenario occurs when cutting is implemented on the (110) crystal plane of the substrate, where the stagnation region is placed at lower position leading to less ploughing action of the cutting tool and, therefore, higher number of atoms in the cutting chip and reduced subsurface deformation layer depth. However, there may be some other unidentified phenomena involved in the chip extrusion during nanometric cutting of silicon at room and at high temperatures since this process encompasses complex interplay among a multitude of various variables such as adhesive forces, interfacial energies, anisotropy, contact areas, number of dangling bonds dictating the nanoscale friction, etc.

#### 4.3.3. Forces and associates parameters exerted by the tool rake face on the chip

A quantitative analysis of the forces acting on the chip, rake face/chip friction, shear plane angle, chip velocity and temperature will help obtain better appreciation of the mechanism of chip formation and chip morphology in hot nanometric cutting of silicon. The tangential force ($F_{cc}$), normal force ($F_{tc}$) and resultant force ($R$) exerted by the rake face on the chip can be calculated by:

$$F_{cc} = F_c \times \tan(\alpha) + F_t \quad (4.4)$$

$$F_{tc} = F_c - F_t \times \tan(\alpha) \quad (4.5)$$

$$R = \sqrt{{F_{cc}}^2 + {F_{tc}}^2} \quad (4.6)$$

where $F_c$ is the tangential cutting force, $F_t$ is the thrust force and $\alpha$ is the tool rake angle (shown in Figure 4.6). Accordingly, the tool rake face/chip friction coefficient can be obtained by:

$$\mu_c = \frac{F_{cc}}{F_{tc}} \quad (4.7)$$

In ductile mode cutting, the value of the shear plane angle characterizes the machinability of the substrate material. The shear plane angle describes the position of the primary shear zone with respect to the horizontal line, as demonstrated in Figure 4.6. Thus, it is beneficial to assess this parameter during nanometric cutting. Shear plane angle (φ) can be calculated using the following equation:

$$\varphi = tan^{-1}(\frac{r \times \cos(\alpha)}{1 - r \times \sin(\alpha)}) \quad (4.8)$$

where $r$ is the chip ratio [98]. Table B1 in Appendix B lists the magnitude of the above-mentioned parameters obtained from the simulation data in all the test cases at varying temperatures and crystallographic planes.

As mentioned in section 3.3, ABOP function is known to be robust in accurately describing the bulk and dimer properties of silicon with a poor prediction of melting point while the modified Tersoff was developed to overcome the shortcomings of the original Tersoff potential function to correctly describe the melting point and thermal softening behaviour of silicon at elevated temperatures. However, while the modified version of the Tersoff variant was proposed, it was not made clear whether it is robust and transferable to predict forces and fracture stress of silicon. To make clear this issue, mechanical properties of silicon such as elastic constants, bulk modulus, shear modulus, Young's modulus etc. predicted by modified Tersoff and ABOP potentials were calculated in this dissertation and nanoscale tensile and shear tests on silicon nanowire were carried to cross-examine the robustness of these potential functions in predicting forces and fracture stresses. Details can be found in Appendix C. It was found that the modified variant of Tersoff potential is not robust in describing the mechanical properties of silicon. Therefore, the following analysis concerning forces and associates parameters exerted by the tool rake face on the chip is carried out based on the results obtained by the ABOP potential. As a result of thermal softening, the magnitudes of the forces exerted by the tool rake face on the chip were observed to decrease with the increase of temperature of the substrate for all the crystallographic planes. Particularly, the resultant force was found to decrease by 24% when cutting the (111) surface at 1173 K compared to that at room temperature.

Silicon has diamond cubic lattice as shown in Figure 4.15. It is documented that the slip in diamond cubic lattice is analogous to face-centered cubic (FCC) crystals and occurs preferentially on the (111) slip planes, meaning thereby that the (111) plane

should lead to low resultant force. As evidenced in Figure 4.16, the magnitudes of resultant force and friction coefficient at the rake face/chip interface are found to be smallest while cutting silicon on its (111) crystal plane, whereas they were largest on the (110) plane.

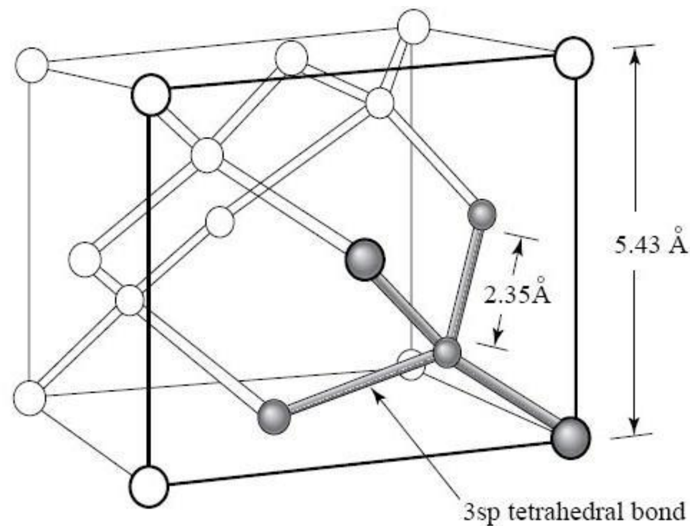


Figure 4.15: Diamond cubic lattice structure of silicon

The importance of temperature prediction for the machining processes has been well recognized in the machining research community primarily due to its effects on tool wear and its constraints on the productivity. It is well observed that particularly the rate of wear is greatly dependent on the chip temperature [99]. A more detailed analysis, shown in Figure 4.17, revealed that the minimum chip temperature is found on the (111) crystal plane while the maximum chip temperature appears on the (110) surface, which is in agreement with the above-mentioned results. It can be also inferred that lower values of friction could lead to the lower chip temperature while cutting the (111) crystal plane. In addition, more friction at the tool rake face/chip interface may play a role in forming thicker chips on the (110) planes, where the chip

atoms cannot simply slide over the atoms of tool rake face, resulting in more piling up of the cutting chip atoms. Accordingly, thicker cutting chips are observed while cutting silicon on the (110) plane, and contrarily, thinner ones on the (111) surface.

The calculation of chip velocity can provide the fundamental information for the determination of other cutting variables according to Merchant model. Strain rate in machining is a very important parameter evaluating chip formation, while the variation of material velocity can appropriately express the strain rate of deformed material. Hence the determination of chip velocity is significant in metal cutting [100]. The chip velocity in nanometric cutting is defined as the velocity of the chip relative to the tool and directed along the tool rake face. As the chip velocity is a function of the chip ratio, $r$, ($V_{chip} = r \times V_c$), $V_c$ is the cutting speed, thus it increases with the increase of the temperature of the substrate, and follows the same trend observed in Figure 4.12. In addition, the highest chip velocity is observed on the (111) crystal plane while the lowest chip velocity appears on the (110) surface. It is worth pointing out that less friction on the (111) surface could facilitate the sliding up motion of the atoms on the tool rake face, leading to higher chip velocity on this crystallographic plane.

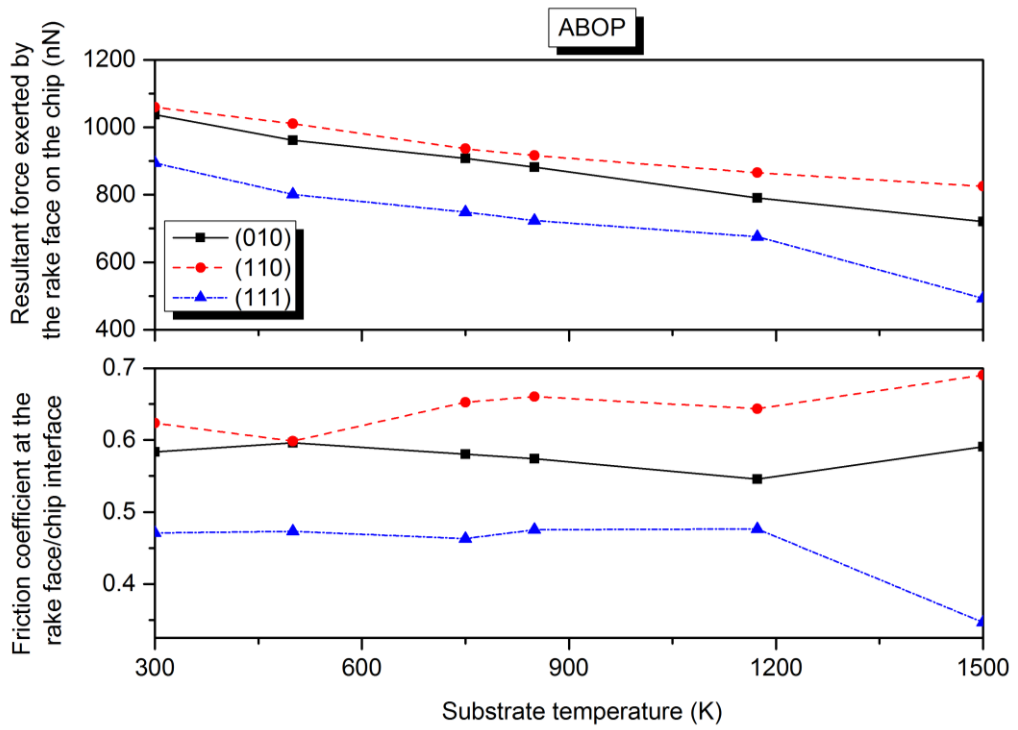


Figure 4.16: Variations of the resultant force exerted by the tool rake face on the chip, and friction coefficient at the tool rake face/chip interface while cutting silicon on different crystallographic planes at various temperatures

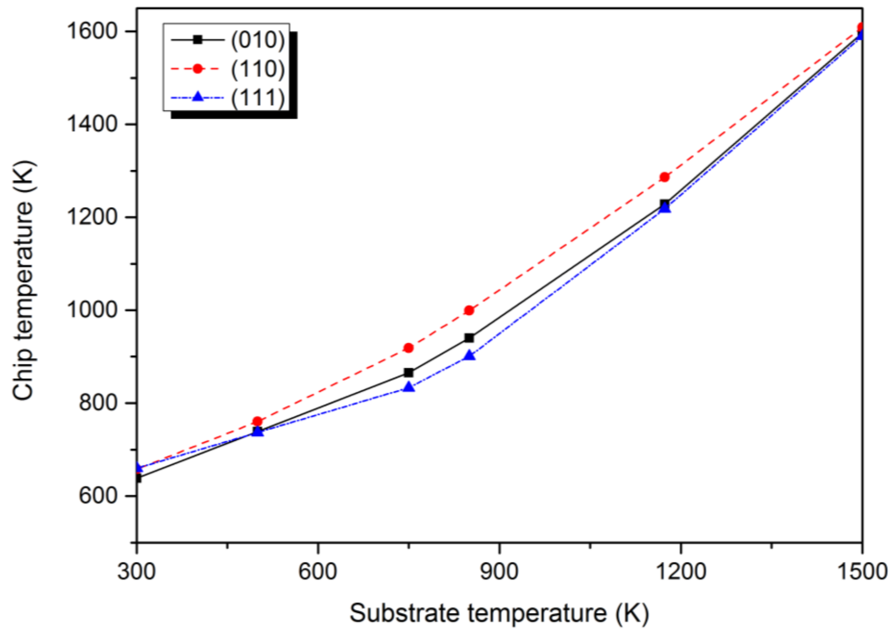


Figure 4.17: Chip temperature as a function of substrate temperature and crystal surface

As noted earlier, the shear plane angle is known as one of the important parameters to determine the machinability of materials. This angle can vary over a fairly wide range, depending on the conditions existing during cutting. Increase of the shear plane angle with the temperature of the substrate can be seen up to ~1200 K in Figure 4.18. As observed before, the modified Tersoff shows almost the same trend like ABOP, yet the shear plane angle demonstrates slightly different pattern on the (010) plane. Higher magnitudes of shear plane angle correspond to the smaller shear plane area, implying that shear takes place in a more confined area culminating in lowering shear forces, and in turn, lowering the cutting forces. However, once again, some inconsistency can be seen at high temperature of 1500 K. Smaller shear plane angle is observed when hot nanometric cutting is carried out on the (110) crystal plane, signifying that higher shear forces are required to form the chip on this crystal surface. Hence, the (110) plane once again can be regarded as the difficult to cut plane. On the contrary, larger shear plane angle is witnessed while cutting silicon on the (111) crystal plane, manifesting higher machinability which confirms that (111)<$\bar{1}$10> crystal setup is the easy cutting direction, in agreement with the experimental results [90, 96].

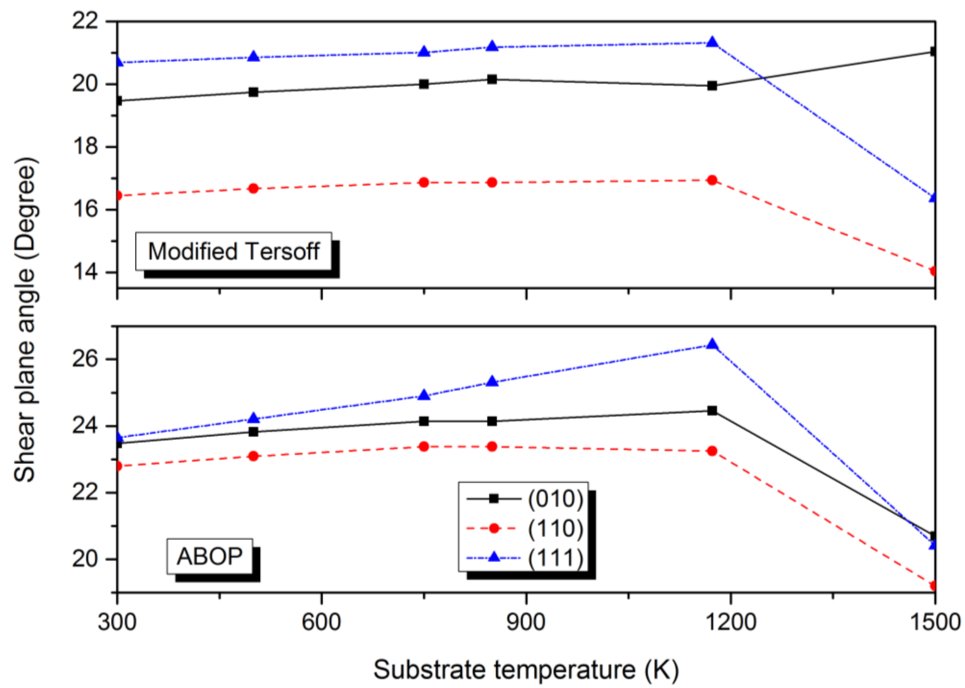


Figure 4.18: Variations of the shear plane angle while cutting silicon on different crystallographic planes at various temperatures obtained by modified Tersoff and ABOP potential functions

### 4.3.4. Extent of temperature increase during chip formation process

Chip formation process in nanometric cutting is driven by the plastic deformation mainly occurring in the primary deformation zone. Successive bond breaking and bond reforming will take place in the primary deformation zone leading to generation of thermal energy (heat). The bulk of the generated heat is dissipated into the chip thus the chip carries a great amount of heat during its separation from the substrate. In order to study the heat generated during the chip formation process and the extent of temperature increase (due to the generated heat) from the initial substrate temperature, a volume of material (1×1.5×3 $nm^3$ ~ 210 atoms), shown in Figure 4.6, was considered in the deformation zone and the variations of the temperature were monitored on this volume. As seen in Figure 4.19, the amount of temperature

increase from the initial substrate temperature decreases with the increase of the temperature of substrate, signifying less release of thermal energy during the deformation phase at higher temperatures due to weaker bonding between atoms. Also, the maximum and minimum thermal energies are found on the (110) and (111) crystal planes, respectively. The generated heat in the deformation zone during the chip formation process is transferred to the chip, leading to the higher and lower local temperatures on the (110) and (111) planes, respectively, which is analogous to the already observed behaviour in the chip temperature shown in Figure 4.17.

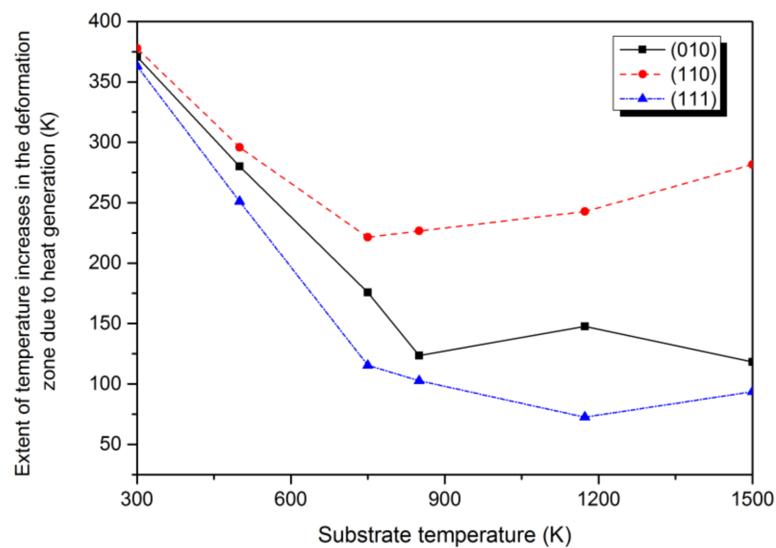


Figure 4.19: Extent of temperature increase in the deformation zone during chip formation while cutting silicon on various crystal planes and at different temperatures

## 4.4. Cutting forces and specific cutting energies

From the MD simulation standpoint, the cutting forces can be calculated by summing up the total forces exerted by the carbon atoms of the cutting tool to the silicon workpiece. The force components along the $x$, $y$ and $z$ directions describe tangential, thrust and axial forces, respectively. Surface form error is chiefly affected by thrust

force since this component of force has tendency to separate the tool away from the workpiece. The tangential force brings about displacements in the direction of cut chip thickness and its variation therefore associates to chatter. The cutting behaviour changes dynamically i.e. wear, fracture, elastic-plastic transition, displacement of the material, heat generation, wear of the tool, dislocation slip etc. leading to change of the force as per the length of cut. Hence, calculation of machining force was necessary and to do this, the total force exerted by the carbon atoms of the cutting tool on the silicon workpiece was calculated. The average values of the forces were calculated only after the tool penetrated in the workpiece by 15 to 25 nm, as shown in Figure 4.20. At the beginning stage of cutting, both the tangential and thrust forces are zero. As the diamond cutting tool starts moving towards the single crystal silicon workpiece, the negative forces are observed, as illustrated in Figure 4.20, signifying the effects of long-range attraction forces. Atoms attract each other when the instantaneous distance between two atoms is longer than the equilibrium distance between them. As the cutting tool advances more, cutting forces on the tool atoms alter to repulsive and climb proportionally, in a sense of average, with the cutting length.

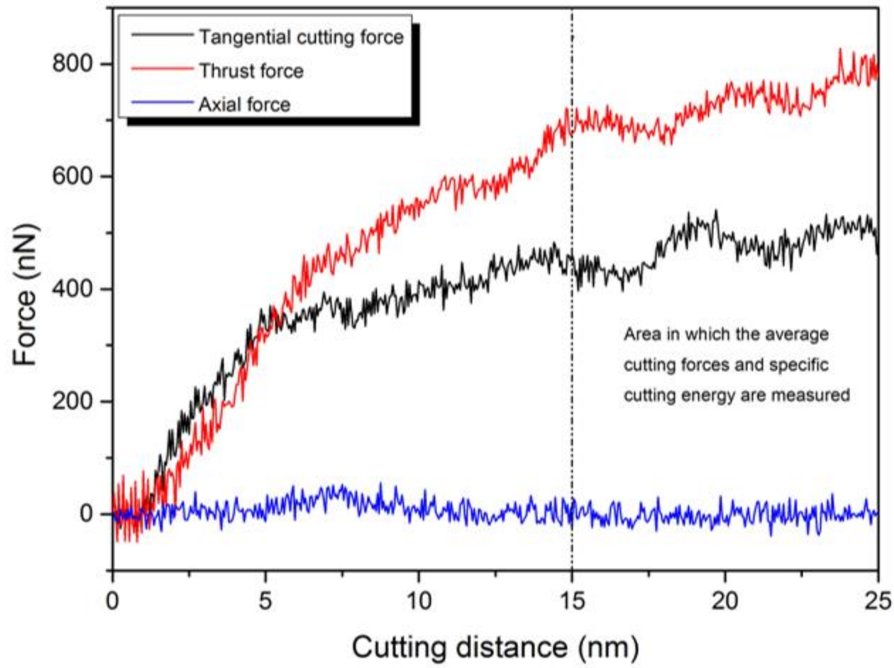


Figure 4.20: An MD output of the force plot showing the region where the average cutting forces and specific cutting energy were measured

The magnitude of the average tangential cutting forces ($F_c$ in nN), thrust forces ($F_t$ in nN), resultant forces ($R$=($sqrt(Fc^2 + Ft^2)$) in nN), force ratio ($F_c$/$F_t$) and specific cutting energy ($u$ in GPa) for all the simulated temperatures and crystal planes were calculated and are provided as appendix (see Table D1 in Appendix D). It is evident from the force data that the magnitude of tangential, thrust and resultant forces decreases with an increase in the workpiece temperature on different crystallographic planes. As mentioned before, when the workpiece temperature increases, the amplitude of atomic vibration of the workpiece atoms increases, which is regarded as an increase in the number of phonons. This phenomenon results in generating atomic displacements. The atomic displacements within the workpiece cause an increase in the interatomic distances and a decrease in the restoring forces due to thermal expansion, leading to lowering of the energy required to break the atomic bonds. As

a consequence, thermal softening occurs which reduces the cutting force required to deform the silicon substrate at high temperatures.

Figure 4.21 presents the variation of specific cutting energy at different cutting temperatures and crystal planes. The cutting resistance in general is indicated by the term called as “specific cutting energy”. The specific cutting energy "$u$" expressed in N/m$^2$ or J/m$^3$, is defined as the work done by the cutting tool in removing the unit volume of material and is expressed as:

$$u = \frac{R \times v_c}{b \times t \times v_c} \tag{4.9}$$

where $R$ is the resultant force in nN equal to $sqrt(Fc^2 + Ft^2)$ in plane-stress condition, $v_c$ is the cutting velocity (m/s), $b$ is the width of cut (nm) and $t$ is the uncut chip thickness (nm) or cutting depth (in plane-stress condition). In general, lower specific cutting energy indicates better machinability. Figure 4.21 shows that low temperature machining leads to large specific cutting energy which is in accord with the data of cutting forces. A common observation evident from Figure 4.21 is that anisotropy persists even at high temperatures. It may be seen that the (111) plane requires least specific cutting energy whereas the highest values appears on the (110) plane. As stated before, the slip in diamond cubic lattice is analogous to FCC crystals and occurs preferentially on the (111) slip planes, meaning thereby that the (111) plane should result in low specific cutting energy. Moreover, it has been experimentally demonstrated that the (111) silicon surface provides a finer quality of machined surface roughness [2] and requires low specific cutting energy. Overall, it can be inferred that the $(111)\langle\bar{1}10\rangle$ and $(010)\langle 100\rangle$ crystal setups are the easy cutting combinations of plane and directions for cutting silicon which is in accord with the published experimental results [96].

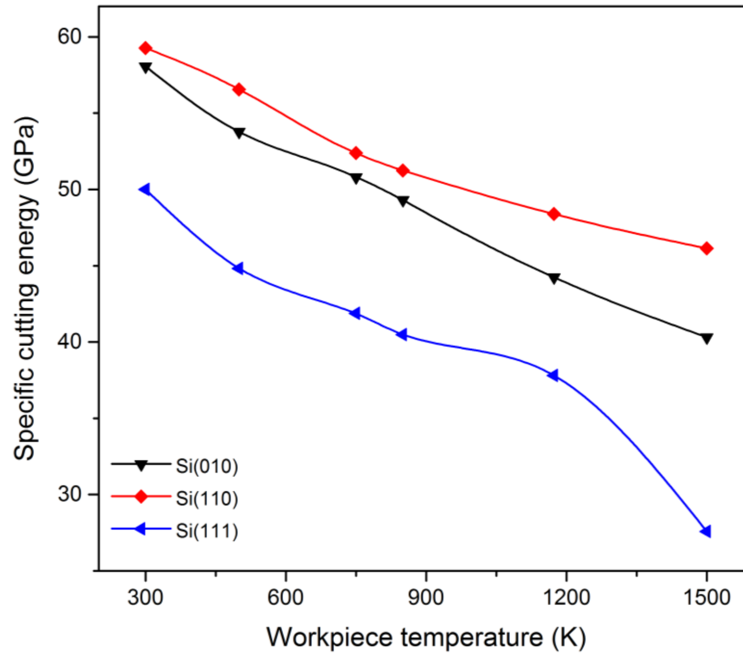


Figure 4.21: Specific cutting energy as a function of temperature and crystal plane

The percentage reduction in the tangential force, thrust force, resultant force and specific cutting energy during elevated temperature cutting with respect to cutting at 300 K on different crystal planes obtained by ABOP is highlighted in Table 4.2. It was observed that the maximum reduction occurs on the (111) and (010) crystal planes, which is up to 25%. Furthermore, the anisotropy (cutting forces and specific cutting energy) was found to increase with the rise of temperature i.e. it increases from ~16% at 300 K to ~20% at 1173 K and to ~40% at 1500 K, respectively.

Table 4.2: Percentage reduction in tangential, thrust, resultant forces and specific cutting energy of silicon at high temperatures relative to room temperature

| Crystal plane | % reduction in machining energy at 850 K compared to 300 K | % reduction in machining energy at 1173 K compared to 300 K |
|---|---|---|
| (010) | Up to 15% | Up to 24% |
| (110) | Up to 14% | Up to 19% |
| (111) | Up to 19% | Up to 25% |

The ratio of the tangential cutting force to the thrust force provides the force ratio, which is also called as coefficient of kinetic friction. Figure 4.22 presents variation in the average force ratio during nanometric cutting of silicon obtained from ABOP in the range of 300 K-1500 K for each crystal plane. The error bars in Figure 4.22 signify the magnitude of standard deviation and fluctuations in the average force ratio. The force ratio varies from 0.58 to 1.03 on different crystal planes and temperatures. It may be noted that the force ratio is maximum on the (111) plane while it is minimum on the (110) plane. A notable observation is that the force ratio remains unchanged up to 1173 K on all the three crystallographic planes and a sudden and abrupt change occurs beyond 1173 K.

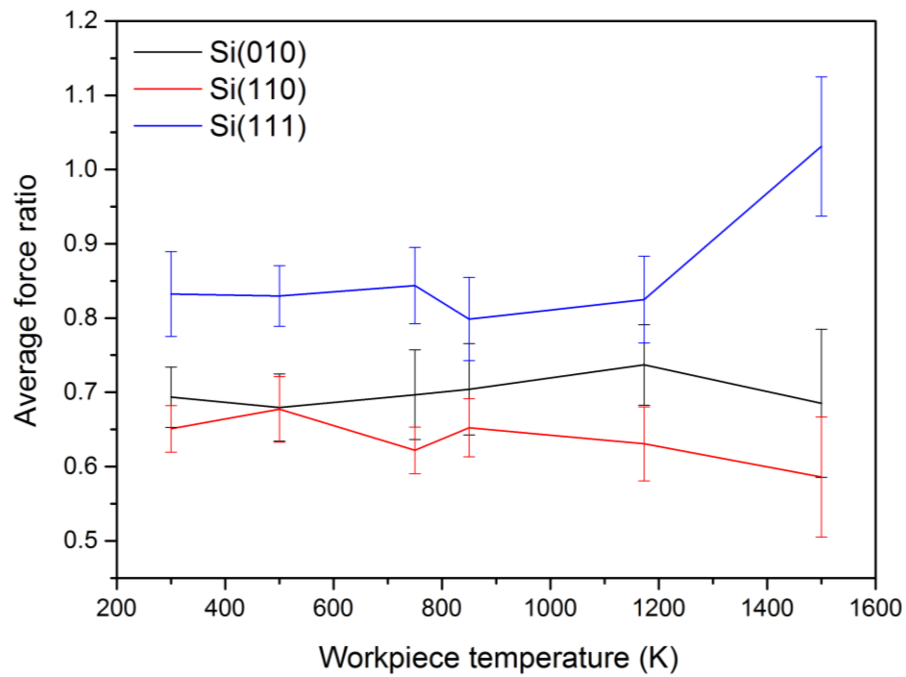


Figure 4.22: Variation in the average force ratio while cutting silicon on different crystallographic planes at various temperatures

**4.5. Machining temperature**

During nanometric cutting, heat is generated due to the reconfiguration of the bonding arrangements in the cutting zone and due to the friction between the cutting tool and the workpiece. Figure 4.23 illustrates the temperature evolution in the Newtonian atoms of the workpiece while cutting single crystal silicon on the (110) crystal surface at different temperatures. It should be noted here that the same trend was observed for the other two crystal planes and hence are not repeated for brevity.

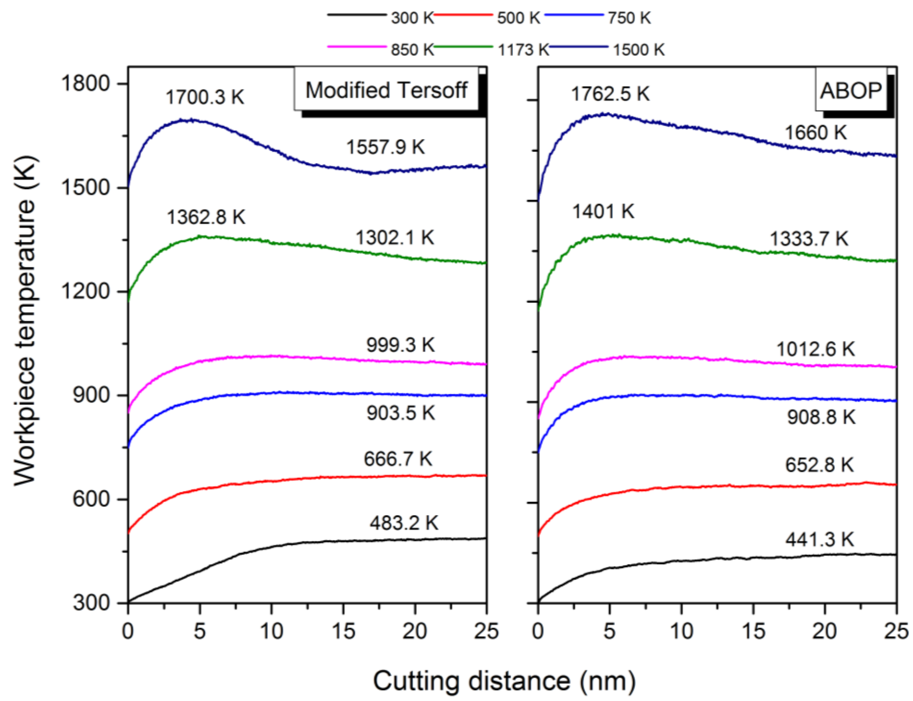


Figure 4.23: Evolution of the average temperature of Newtonian atoms of workpiece while cutting on the (110) crystal plane

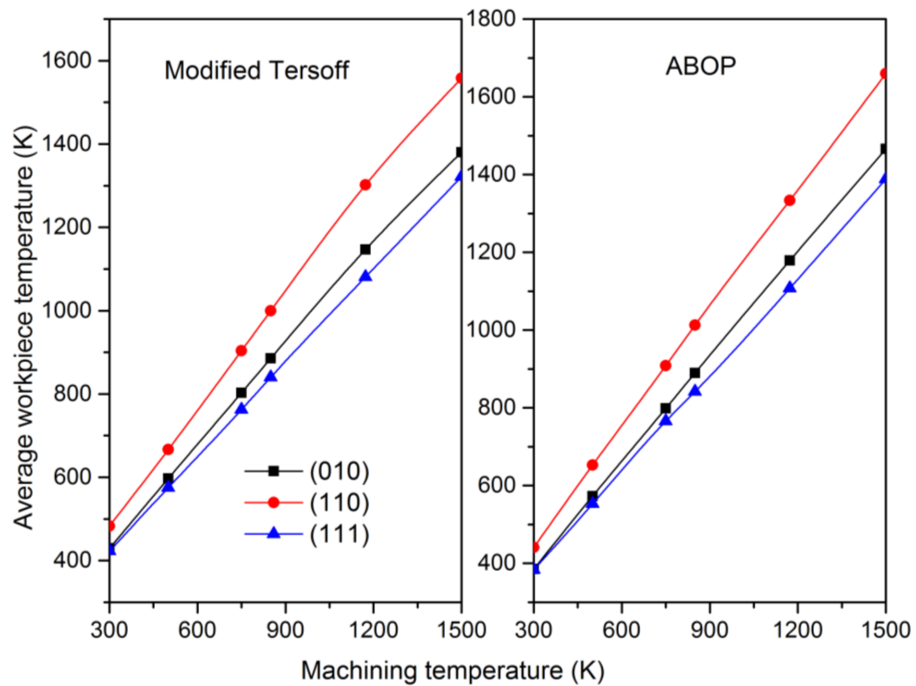


Figure 4.24: Anisotropy in the cutting temperature in the Newtonian atoms of the workpiece obtained from the two potentials

The average (stable) cutting temperature in the silicon workpiece on the three principal planes for both the potential functions is shown in Figure 4.24. It may be seen from Figure 4.24, that hot machining on the (111) crystal plane showed least temperature in comparison to the other two planes, which is in agreement with the results obtained for cutting forces and specific cutting energy in different scenarios. It may also be seen that at high temperatures, ABOP predicts higher average temperatures of the workpiece than the modified Tersoff, coming from the overestimated melting temperature of silicon by the ABOP.

The anisotropy in the cutting temperature was observed to increase with the rise of machining temperature i.e. it increases from ~12% at 300 K to ~17% at 1173 K and 1500 K, respectively. The trend is similar to what was seen in the anisotropy of cutting force and specific cutting energy required to cut silicon in three planes.

## 4.6. von Mises equivalent strain

In order to quantitatively and qualitatively assert the degree of deformation in the shear zone, an algorithm proposed by Shimizu *et al.* [101] was used in this study. Two atomic configurations (during cutting and before cutting) were compared and then the atomic local equivalent strain (von Mises strain) was calculated for the configuration of atoms. The local Lagrangian strain matrix was computed by using a local deformation matrix $J_i$ and Equation (4.10), so as to calculate the von Mises shear strain for each atom $i$. The von Mises equivalent strain $\eta_i^{Mises}$, which has been documented as an excellent measure of the local inelastic deformation, was calculated through Equation (4.11) where $\eta_{ij}$ are six strain tensor componnents.

$$\eta_i = \frac{1}{2}(J_i J_i^T - I) \tag{4.10}$$

$$\eta_i^{Mises} = \sqrt{\eta_{yz}^2 + \eta_{xz}^2 + \eta_{xy}^2 + \frac{\left(\eta_{yy}^2 - \eta_{zz}^2\right) + \left(\eta_{xx}^2 - \eta_{zz}^2\right) + \left(\eta_{xx}^2 - \eta_{yy}^2\right)}{6}} \quad (4.11)$$

Figure 4.25 illustrates the atomic equivalent strain distribution in the workpiece for the representative temperatures of 300 K and 850 K and crystal planes of (010), (110) and (111). In the simulation snapshots shown in Figure 4.25, lighter regions (white and yellowish regions) can be seen to exhibit higher strain. It is evident that equivalent strain localizes in the primary shear zone and underneath the flank face of cutting tool where the material undergoes intense deformation. Machining experiments and simulations have helped in identifying that chip formation is driven by the shearing process primarily in the primary shear zone leading to release of heat. Due to the ease of deformation of the workpiece at high temperatures, a narrower primary shear zone can be observed during hot machining. Smaller primary shear zone implies that shear occurs in a more confined area leading to lowering of the cutting forces. As demonstrated in Figure 4.25b and Figure 4.25d, a wider primary shear zone is observed whilst hot nanometric cutting was performed on the (110) crystal surface, indicating that higher shear forces are associated with the chip formation on this plane. Thus, the (110) plane can be considered as the difficult to cut orientation while the (111) plane offers easy machinability once again confirming the same findings as observed in the experiments [90].

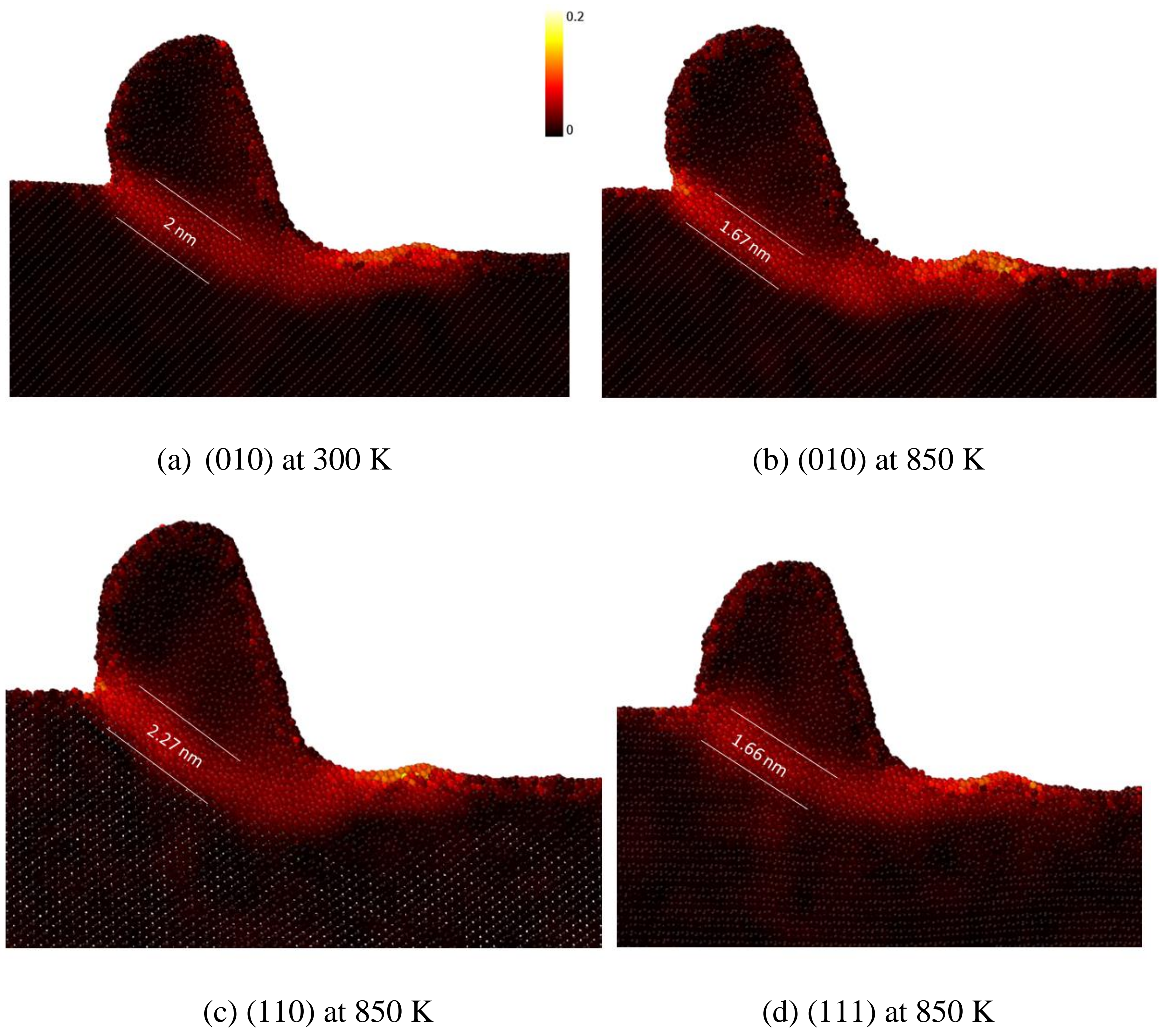


(a) (010) at 300 K

(b) (010) at 850 K

(c) (110) at 850 K

(d) (111) at 850 K

Figure 4.25: The local von Mises strain distribution and cut chip thickness after 20 nm cutting distance. A wider primary shear zone can be seen on the (110) plane.

### 4.7. Yielding stresses

The von Mises stress is a very commonly used yield criterion to predict yielding of a material and is based on the assumption that it is the maximum deviatoric strain energy that brings yielding in the material. In addition to von Mises stress measure, there are other material dependent stress measures that are proposed to predict yielding such as Principal stress measure, Tresca stress measure and these were also evaluated and are shown in Table E1 in Appendix E. Equations shown in Appendix F

were adopted to calculate the aforementioned yielding measures. Table E1 summarizes the magnitude of all the stress measures and temperatures in the cutting zone for all the simulated cases. An elemental atomic volume (1×1.5×3 $nm^3$ ~ 210 atoms) was considered in the cutting region for the sake of calculating the atomic stress tensor based on the procedure defined in LAMMPS[1]. Figure 4.26 compares von Mises stress obtained from the ABOP potential function at different machining temperatures and crystal planes while cutting silicon. It has been experimentally reported that at room temperature, the onset of plastic yielding in single crystal silicon occurs in the stress range of 9 to 16 GPa [102]. It may be seen that the ABOP potential predicts the critical von Mises stress of silicon during cutting at 300 K in the range of ~12.9 GPa to 14.6 GPa which is consistent with the formerly reported magnitude of ~14 GPa [103]. The dummy trials performed using the modified Tersoff potential function predicted the von Mises stress in the range of ~7.1 GPa to 8.7 GPa, signifying that this potential underestimates the yielding in single crystal silicon.

A noteworthy finding is that the maximum reduction in the von Mises stress at 1500 K with respect to the room temperature machining takes place on the (111) plane, which is up to 37%, followed by the (010) crystal plane, consistent with the already witnessed behaviour in specific cutting energy. It may also be seen that the von Mises stress in the temperature range of 300 K to 1173 K varies only slightly while cutting silicon on the (110) crystal plane. Such behaviour was observed for the (010) surface in the range of 750 K to 1173 K. It is also interesting to note that the largest value of the required von Mises stress to cause yielding on the (111) crystal plane

---

[1] http://lammps.sandia.gov/doc/compute_stress_atom.html

appears at low temperatures, i.e. 300 K and 500 K. Another key finding is that the anisotropy in von Mises stress was found to increase from ~12% at 300 K to up to ~20% at high temperatures of 1173 K and 1500 K obtained from the ABOP function. In general, the maximum and minimum heat in the cutting zone is generated on the (010) and (111) crystal planes, respectively, which is analogous to the already observed behaviour in workpiece temperature. Moreover, the anisotropy in the temperature at the onset of plastic yielding is found to increase from ~7% at 300 K to 20% at 1500 K. Similar to the observed trend in the anisotropy of cutting forces, specific cutting energies, workpiece and tool temperature, the anisotropy in the peak temperature in the cutting zone and temperature at the maximum equivalent stress is witnessed to increase with the increase of machining temperature.

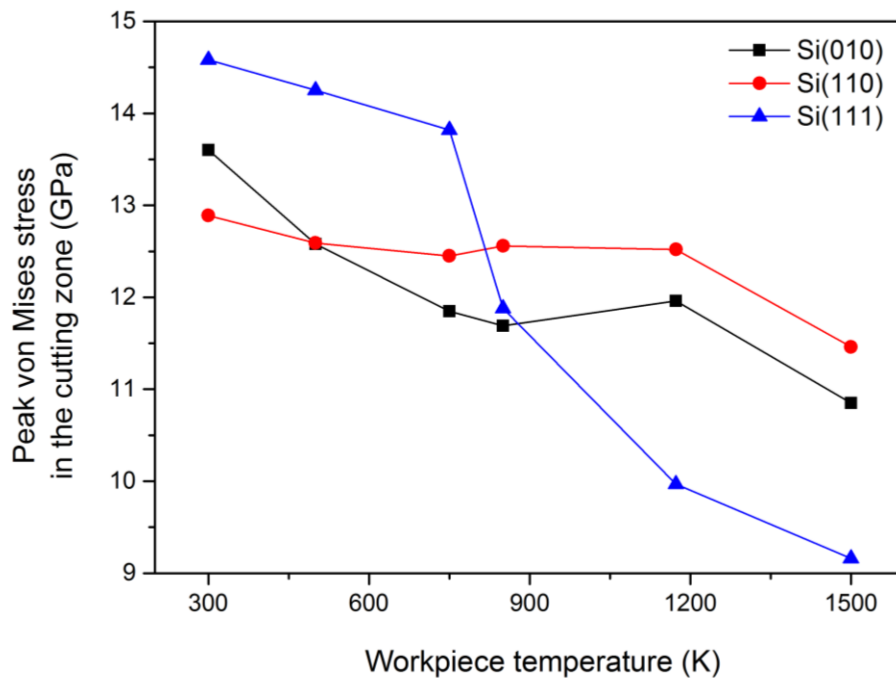


Figure 4.26: Maximum von Mises stress in the cutting zone while machining silicon on different crystallographic planes at various temperatures

In order to gain further insights on the behaviour of the substrate, evolution of average local temperature and von Mises stress in the cutting zone while cutting silicon on the (010) is shown in Figure 4.27. The trend was observed to be the same for the other crystal planes and hence not repeated. It was observed that the peak temperature in the cutting zone follows peak stress at low temperatures, i.e. 300 K, whereas at high temperatures, viz. 1173 K, the peak temperature lags the peak stress. It can be inferred from Figure 4.27 that the peak temperature and peak stress required to cause yielding in the cutting zone do not occur concurrently. This difference exists because the energy required to cause the breaking of bonds is directly dependent on the cutting temperature which means, higher the temperature, lower is the stress required to yield the material. This is why yielding at 595 K takes place at 13.6 GPa during cutting at 300 K whereas yielding at 1152 K takes place at 11.96 GPa at elevated temperature cutting. This confirms the initial hypothesis quantitatively that hot machining reduces the cutting resistance of silicon. It can be also seen in Figure 4.27 that while cutting at 1173 K, temperature of atoms in the elemental volume reaches to maximum, followed by a slight drop. It might be postulated that the atoms gradually scatter on the machined surface during and after cutting, leading to heat transfer to ambient, and consequently, a reduction in their temperature.

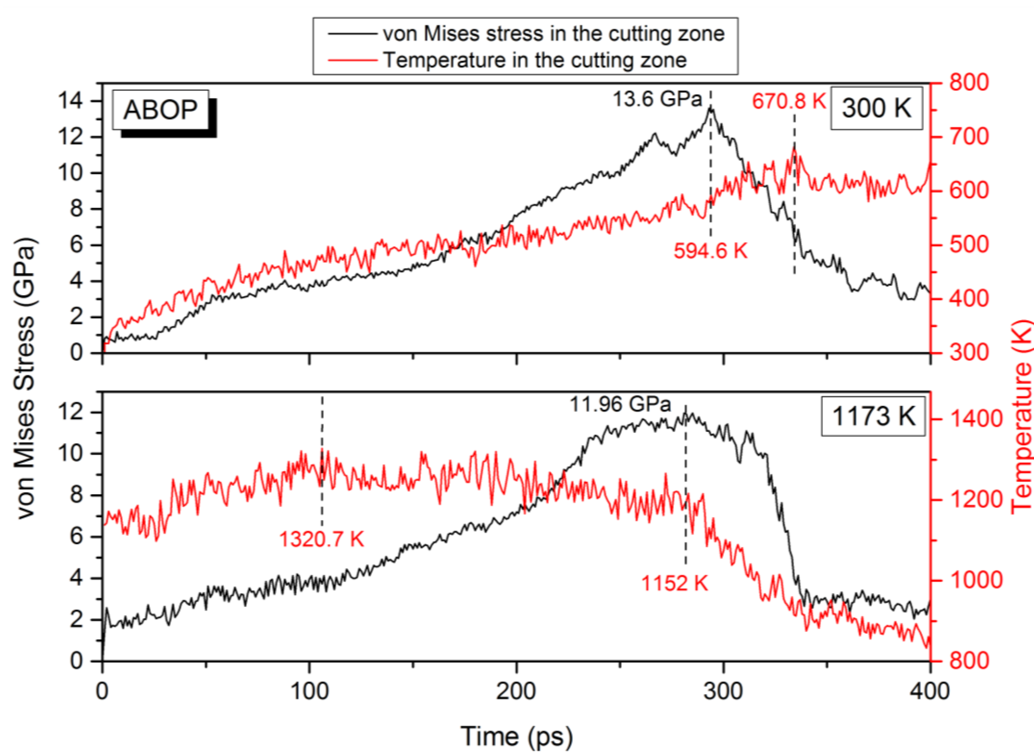


Figure 4.27: Evolution of the temperature and von Mises stress in the cutting zone recorded on the same plot while cutting on the (010) plane

**4.8. Machining stress and temperature on the cutting edge of the tool**

Following discussions on machining of silicon, an attempt was made to examine the state of the diamond tool post-machining. It has been reported that under confined pressure (3.5 GPa to 5 GPa) and at high temperatures (>1200 K-1300 K) diamond may exhibit ductile flow, which is meditated by dislocation glide and twinning [104, 105]. During nanometric cutting, cutting edge of the diamond tool experiences high stress and consistent exposure to high temperature conditions that could promote its ductile deformation. The observations witnessed in the above description prove that high machining temperature enhances ductile response of silicon which leads us to anticipate lower tool wear during the high temperature cutting process. It must however be recalled that high heat content is closely associated with the wear of

diamond i.e. hot environment can bring about accelerated wear of carbon atoms via diffusion, attrition, adhesion and so on. It was therefore felt necessary to examine this hypothesis during the current investigation. Figure 4.28 shows the anisotropy in the average von Mises stress observed on the cutting edge of the diamond tool during nanometric cutting of single crystal silicon at different temperatures. Table G1 in Appendix G summarizes the average magnitude of von Mises stress measure, Tresca stress measure and temperature on the cutting edge in all the simulated test cases. Figure 4.28 suggests that the cutting tool experiences least stress and temperature on the (111) plane compared to others, which makes it an easy cutting plane as has been verified from the experiments [90]. The general pattern is that the magnitude of average von Mises stress and Tresca stress on the cutting edge of the tool decreases with an increase in the machining temperature for the different crystallographic planes. It was seen that the average von Mises stress and Tresca stress acting on the cutting edge of the tool at low and high temperatures were in the range of 18 to 26 GPa and 10 to 15 GPa, respectively. First-principle calculation suggests that the minimum stress needed to cause structural instability in the diamond structure is around 95 GPa that brings a direct diamond to graphite transformation [106]. Apparently, the assessment of the state of the stress on the cutting edge of the tool is not supportive of a direct diamond-graphite transformation under vacuum condition.

A notable observation was that even when the nanometric cutting was simulated at 1500 K, the peak average temperature on the cutting edge remains as low as ~413 K, suggesting that plastic deformation of diamond cutting tool is also unlikely. The question then arises as to what happens to diamond during nanometric cutting of silicon. Some investigations in our research group in this regard were made [103]

yet, the post-machining phase of diamond was not found owing primarily to the unavailability of a robust potential function to predict all the phases of carbon. This is another interesting area of further research which can be pursued further in the follow on work.

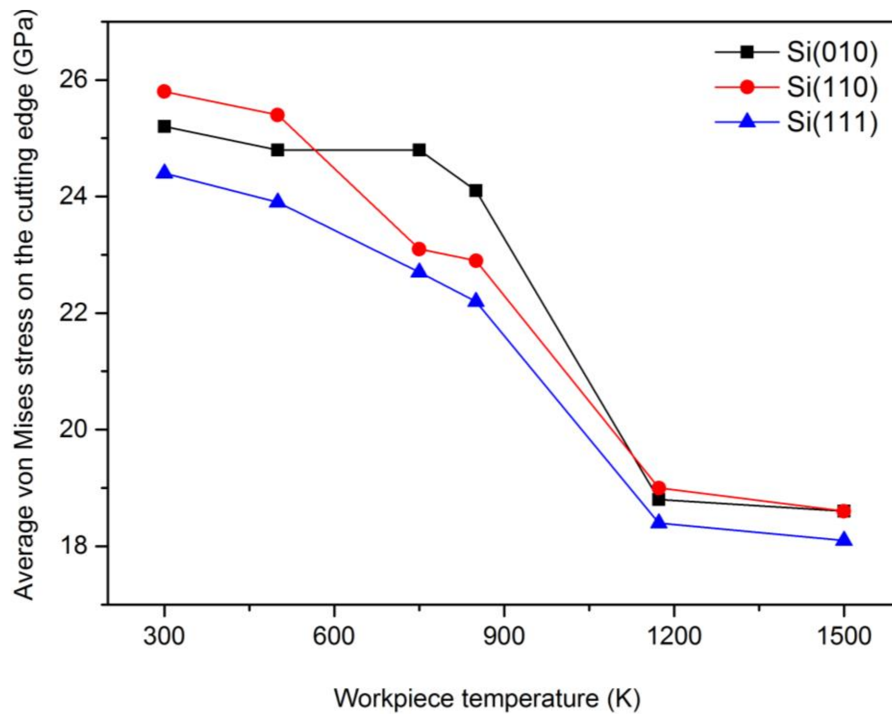


Figure 4.28: Average von Mises stress measured on the cutting edge of the diamond tool while machining different orientations of silicon at different cutting temperatures

### 4.9. Deformation mechanisms

MD simulation studies of high-power, pulsed, laser-driven shock compression of silicon have recently revealed that partial dislocations and stacking faults can be emitted from the surface under slightly higher pressures than 10 GPa [107, 108]. Likewise, in MD simulations of strained silicon nanowires (NWs) of different lengths, dislocation nucleation was witnessed when both ductile and brittle

behaviours were initiated. Additionally, the yield process in silicon NWs was observed to be first mediated by dislocation nucleation [109, 110]. Nevertheless, the current pool of knowledge concerning nucleation and propagation of dislocations and its consequence on the defect structure in silicon during nanometric cutting is not very well acknowledged. On the other hand, amorphization and high pressure phase transformation studies on silicon have remained at the epicentre of research across various disparate disciplines for over a decade now [2].

A key question thus is whether dislocation nucleation and other crystal defects assist crystal plasticity of silicon during nanometric cutting at room and high temperatures. Previous MD studies failed to answer this question primarily due to the application of an improper interatomic potential function, i.e. Tersoff [39, 40], to describe the dislocation cores [111]. Accordingly, this section aims to gain an in-depth understanding of the mechanisms involved in the plasticity of silicon during nanometric cutting at different temperatures. In order to assert the observations the crystal plasticity behaviour was examined using SW potential function [36], and DXA [87] was utilized in order to elucidate whether the plasticity of silicon during nanometric cutting at room and high temperatures can be governed by the defect formation strictly at the length scale of few nanometres. The DXA has a proven ability to identify dislocations in diamond structure such as Si [112] and Ge [95]; its algorithm is based on a discrete Burgers circuit integral over the elastic displacement field and is not limited to specific lattices or dislocation types [87]. Additionally, virtual X-ray diffraction (XRD) and radial distribution function (RDF) analysis is carried out to qualify the structural changes of silicon during nanometric cutting. Prior to use of SW potential, its robustness in reproducing the generalized stacking

faults energy (GSFE) surfaces, melting temperature, the elastic constants and other relevant mechanical properties of silicon were assessed so as to ensure that the appropriate potential function has been selected for this specific study, which deals with the defect-mediated plasticity at a wide range of temperatures. Details can be found in Appendix H. It should be noted here that a silicon workpiece with the dimensions of $38\times19\times10.8$ nm$^3$ was adopted here.

#### 4.9.1. Structural changes

The RDF, *g(r)*, or pair distribution function is regarded as the major connection between macroscopic thermodynamic characteristics and interatomic distances. In order to shed light on the structural changes in the diamond lattice of silicon, the RDF was plotted (Figure 4.29) for different cutting temperatures and the (010) crystal plane. In Figure 4.29, the atoms with the peak showing at an interatomic distance of 2.35 Å before the cutting are representative of the diamond cubic lattice structure. The second peak at an interatomic distance of 3.85 Å represents the inter-planar spacing in an ideal tetrahedral geometry of silicon. It can be seen that the peaks visible in the RDF vary with the cutting temperature. This is in accord with the crystal rule, which signifies that less damaged lattice leads to reduced number of crystal defects [113]. It is apparent from Figure 4.29 that the peaks in the RDF related to the diamond cubic structure become weaker as the temperature of substrate increases, which indicates increased amplitude of atomic vibrations and corresponding atomic displacements from their original equilibrium positions. Apart from the peaks, the bond length increases with the increase of temperature, representing the enhanced structural changes and consequently superior plasticity of

silicon before and during the cutting. A qualitative analogous behaviour in decrease and increase of the bond lengths is observed at different temperatures signifying rudimentary differences in the plastic deformation behaviour of silicon at elevated temperatures. Similar qualitative trend was observed in MD simulations for the three crystal planes. It should be asserted here that the available empirical potentials are not robust in describing and capturing all the structural phases. Moreover, the analysis techniques i.e. coordination number adopted to explore phase transformation in MD simulations are inadequate. A recent MD study [112] has revealed that silicon does not undergo Si-I to Si-II (beta tin) transformation during cutting, which is in direct contrast to many previously published MD studies on this topic.

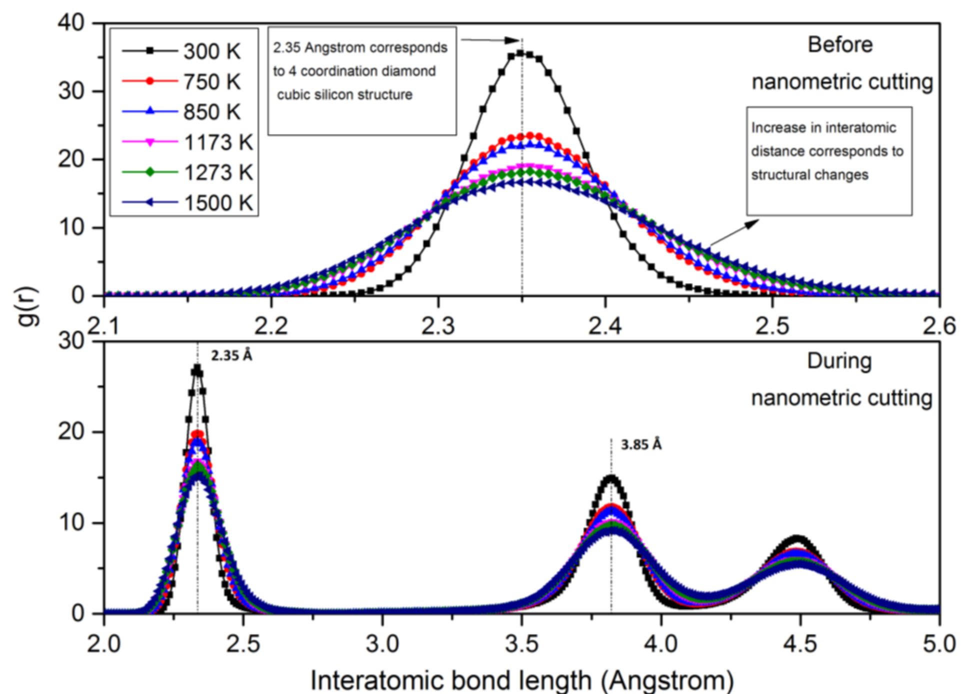


Figure 4.29: Radial distribution function, *g(r)*, showing interatomic bond lengths at different temperatures before and during nanometric cutting of silicon on the (010) crystal plane. The pattern for the other crystal planes remained unchanged and hence not presented here.

To provide further description of the crystal qualities of silicon substrate during nanometric cutting, virtual XRD line profiles were created in this work using the algorithm developed by Coleman *et al.* [114]. XRD spectrums were constructed from the 3-D intensity data using Cu Kα x-rays (λ=1.5418 Å) and the benchmarked reciprocal mesh spacing parameter of 0.092 between diffraction angles (2θ) ranging 10-100° on an elemental atomic volume ($2\times1\times2$ $nm^3$) in the cutting deformation zone. Virtual $2\theta$ x-ray diffraction patterns are demonstrated in Figure 4.30. Peaks at 2θ value of 28.41°, 47.3°, 56.12°, 69.17°, 76.37°, 87.16° and 94.91° shown in Figure 4.30a and Figure 4.30b correspond to the crystalline silicon, which is well-matched with the XRD pattern of standard silicon powder in Figure 4.30d [115]. The strongest reflection, Si (111), at 2θ=28.41° corresponds to an interplanar spacing of 3.14 Å. As evident from Figure 4.30b, no shift of the intensity peaks is observed after increasing the temperature of substrate before nanometric cutting, signifying no alteration in interplanar spacings. Figure 4.30c reveals that after cutting the main peaks are diminished remarkably and several new diffractions appear, suggesting that a transformation towards an amorphous configuration has happened for the atoms in the cutting region.

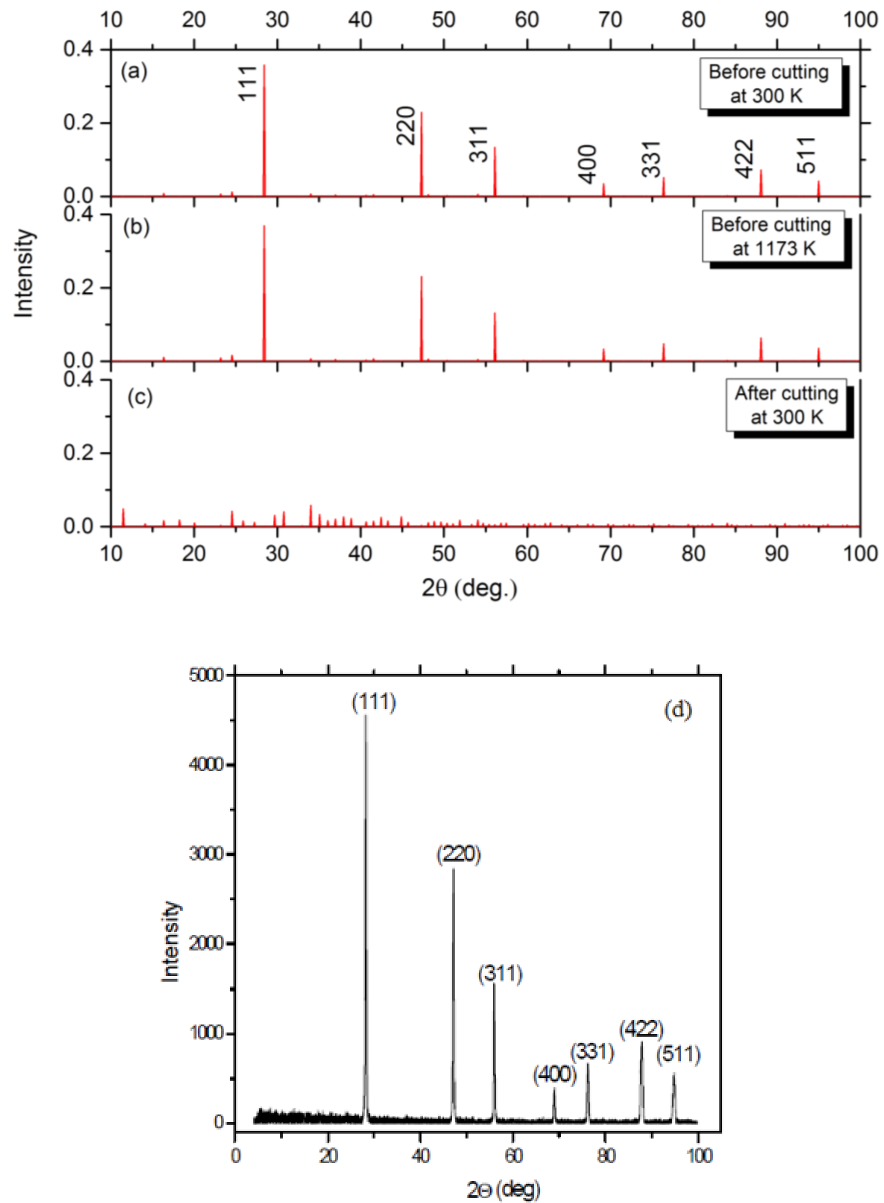


Figure 4.30: Virtual XRD patterns computed for silicon before nanometric cutting at a) 300 K b) 1173 k and c) after nanometric cutting d) Standard XRD pattern of silicon powders [115]

### 4.9.2. Defect-mediated plasticity

Nanometric cutting involves plastic deformation of the material at high strain rates resulting in considerable storage of the elastic energy during plastic deformation. The abrupt release of stored energy at the elastic relaxation stage (spring-back) could

trigger activation of the slip system with the largest resolved shear stress along the Burgers vector and leading to nucleation of dislocations. Dislocation glide in the silicon crystal occurs in two widely and narrowly spaced {111} dense planes, shuffle and glide sets. However, at high temperatures slip could also take place in the {110} and {100} planes [116]. Figure 4.31, Figure 4.32, Figure 4.33, Figure 4.34, Figure 4.35 and Figure 4.36 show the formation of defects during nanometric cutting of silicon on the (010) crystal plane at two cutting distances, 10 nm and 20 nm, for different temperatures. The white atoms demonstrated in these figures signify the highly-disordered (amorphous) atoms, obtained via monitoring the local environment of atoms up to the second neighbor shell using the diamond structure identification tool in OVITO [95]. As shown in the figures, the cutting chip and subsurface obtain amorphous state, indicating amorphization of silicon atoms. Indeed, the initial response of silicon substrate was witnessed to be amorphization followed by defect formation. Perfect dislocation segments with $1/2 < 110 >$ Burgers vectors are observed to glide ahead and underneath of the tool tip at different temperatures, which facilitate the crystal plasticity of silicon during nanometric cutting. It can be seen from Figure 4.31b that with the progress of cutting, dislocations are further nucleated within the substrate which improves the plasticity of silicon. Moreover, Shockley partial with $1/6 < 112 >$ Burgers vectors and another partial segment are nucleated in this case. It can be supposed that the perfect dislocation dissociates into partials. Dissociated partial dislocations building loops can be also observed while cutting silicon at high temperatures, as shown in Figure 4.32b, Figure 4.34b, Figure 4.35b and Figure 4.36b. It is well known that the dislocation loop in silicon exhibits a hexagonal shape whose edges are parallel to the <110> Peierls valley on the {111}

slip plane [117]. Also, the DXA analysis reveals some partial dislocations, which cannot be regarded as physical dislocations and they are merely an artefact since no continuous chain of core atoms along the dislocation line was observed in Figure 4.32b.

It is noteworthy that when nanometric cutting is performed at 1500 K, at the short cutting distance i.e. 10 nm, a perfect dislocation segment is nucleated underneath the cutting tool. However, this dislocation is somehow immobile, suggesting that it hardly improves the plasticity of silicon during nanometric cutting at the short cutting distances. Note that, generally, mobile dislocations ahead of the tool tip in the substrate are of importance in the case of one-pass nanometric cutting. Hence, it can be postulated that in some cases dislocation nucleation is less effective in driving the plasticity of silicon since the dislocations are mostly located beneath and behind the cutting tool rather than ahead of the tool. In such cases, the plasticity is primarily driven by amorphization and weaker bonding between atoms at high temperatures. Note that amorphization is considered as a nanoplasticity mechanism for semiconductor materials like silicon [2]. It has been ascribed to either chemical disordering or volumetric expansion of the crystal. In silicon, amorphization occurs when the free energy of the damaged crystalline phase is higher than that of the amorphous phase [118, 119].

Furthermore, the total length of dislocations was found to vary haphazardly from 11.4 nm to 14.4 nm and from 40.1 nm to 60 nm at the short and long cutting distances, respectively, over the studied temperatures. Accordingly, defect formation can be considered somewhat stochastic; thus there may be some differences in the pattern of defect formation at different cutting distances and temperatures.

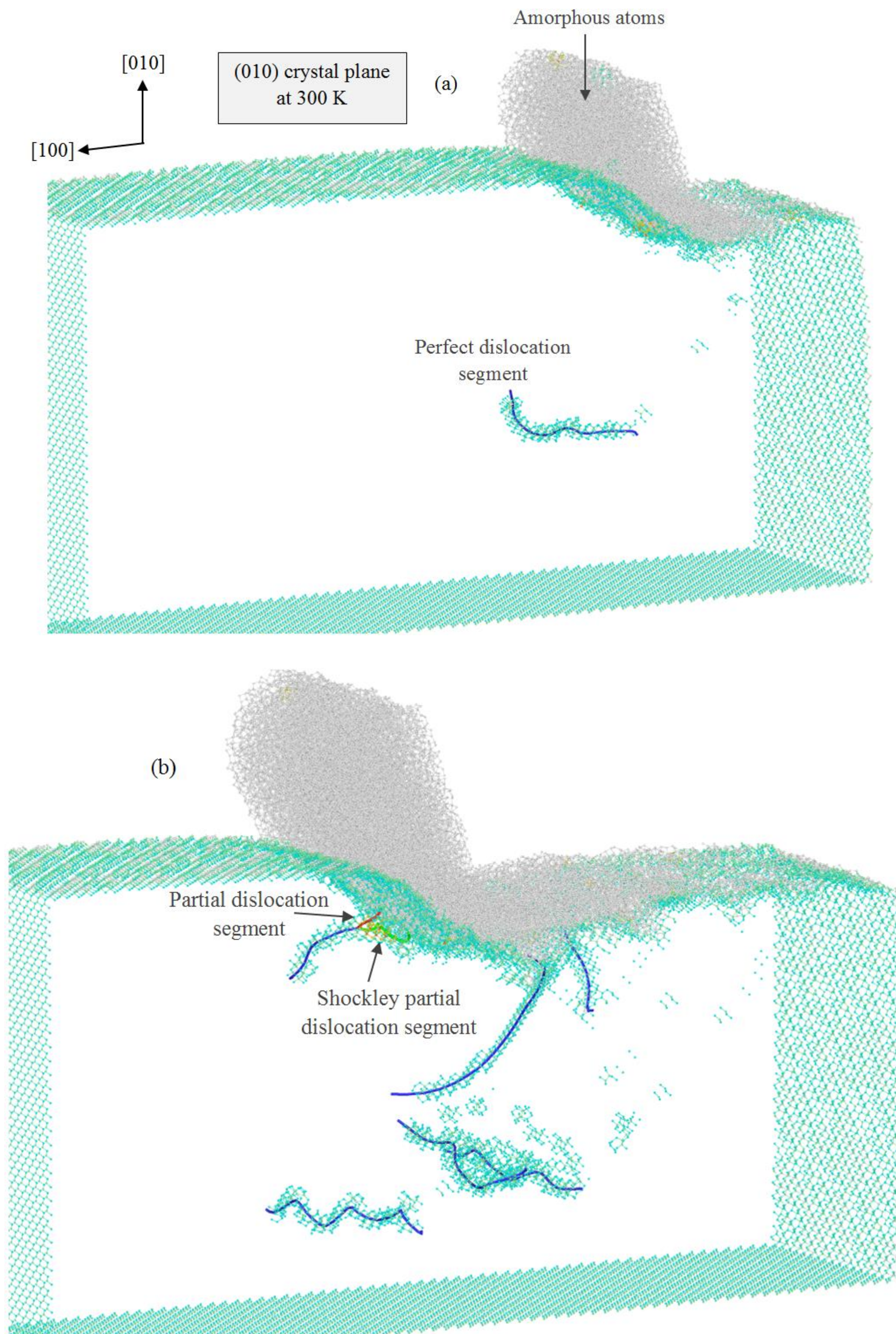


Figure 4.31: MD simulation output illustrating amorphous atoms (white atoms) and dislocation nucleation while cutting the (010) plane at 300 K at a cutting distance of a) 10 nm b) 20 nm. Blue, green and red rods, respectively, stand for the perfect, Shockley partial and other partial dislocations.

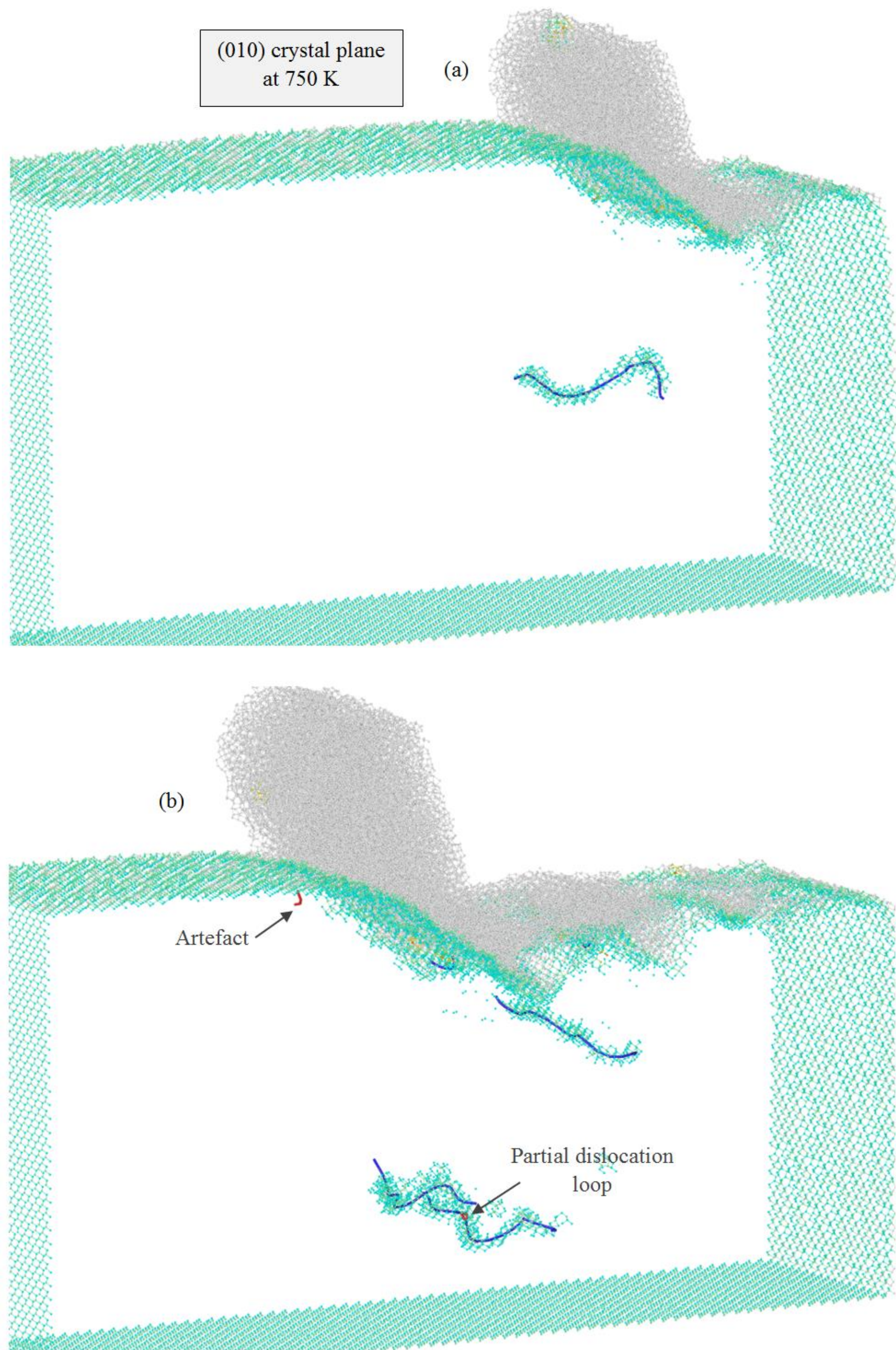


Figure 4.32: Dislocation nucleation while cutting the (010) plane at 750 K at a cutting distance of a) 10 nm b) 20 nm.

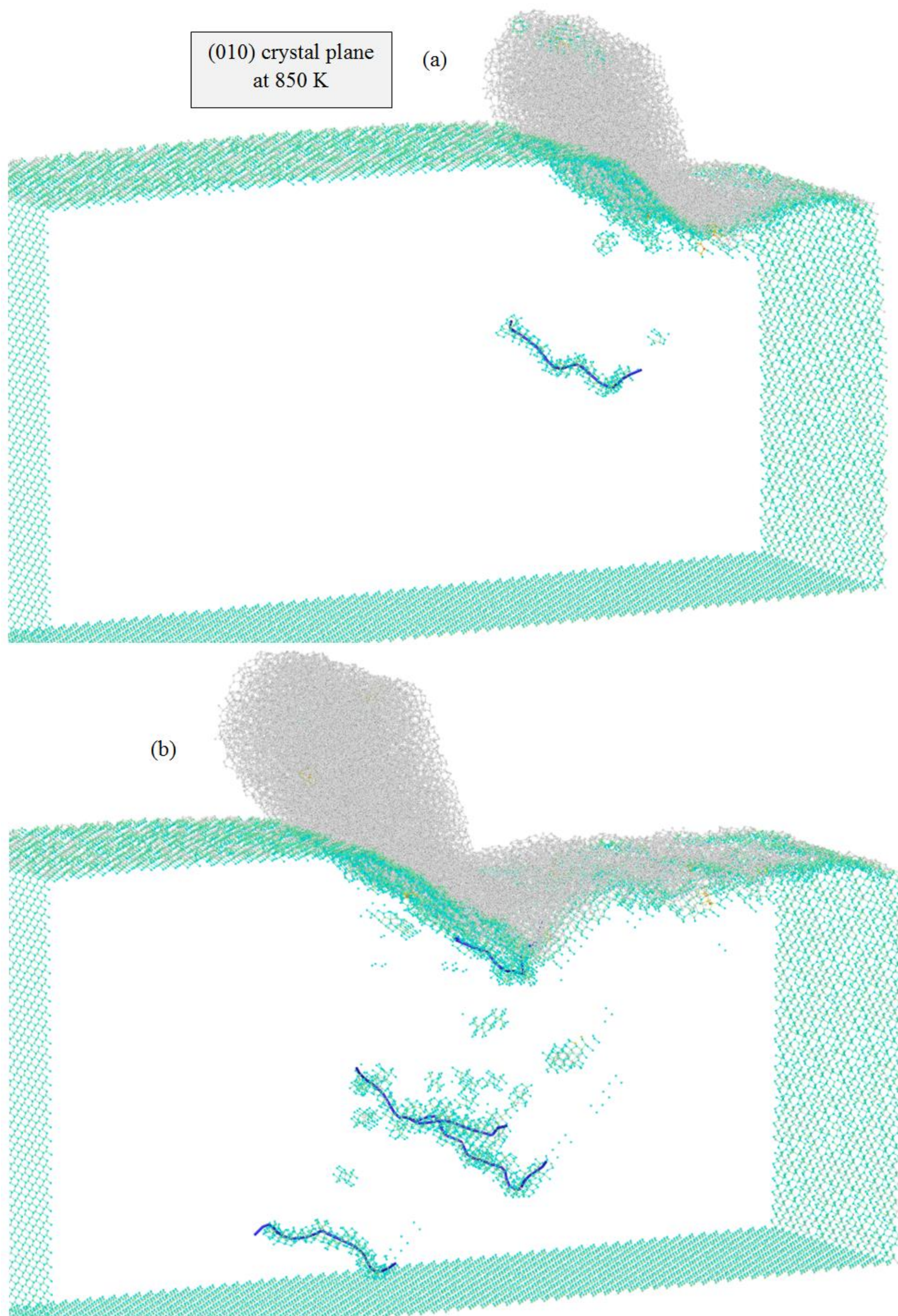


Figure 4.33: Dislocation nucleation while cutting the (010) plane at 850 K at a cutting distance of a) 10 nm b) 20 nm.

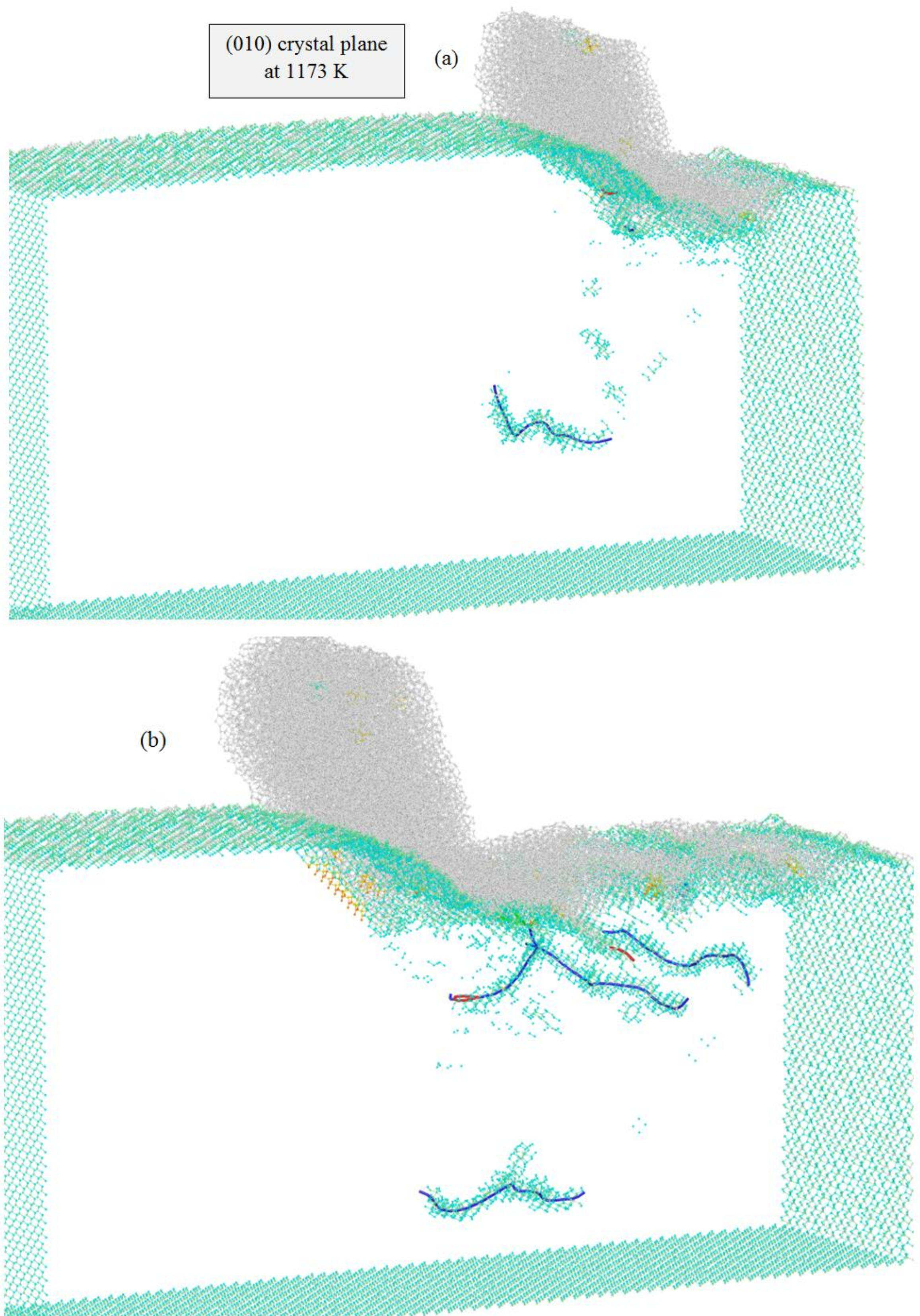


Figure 4.34: Dislocation nucleation while cutting the (010) plane at 1173 K at a cutting distance of a) 10 nm b) 20 nm.

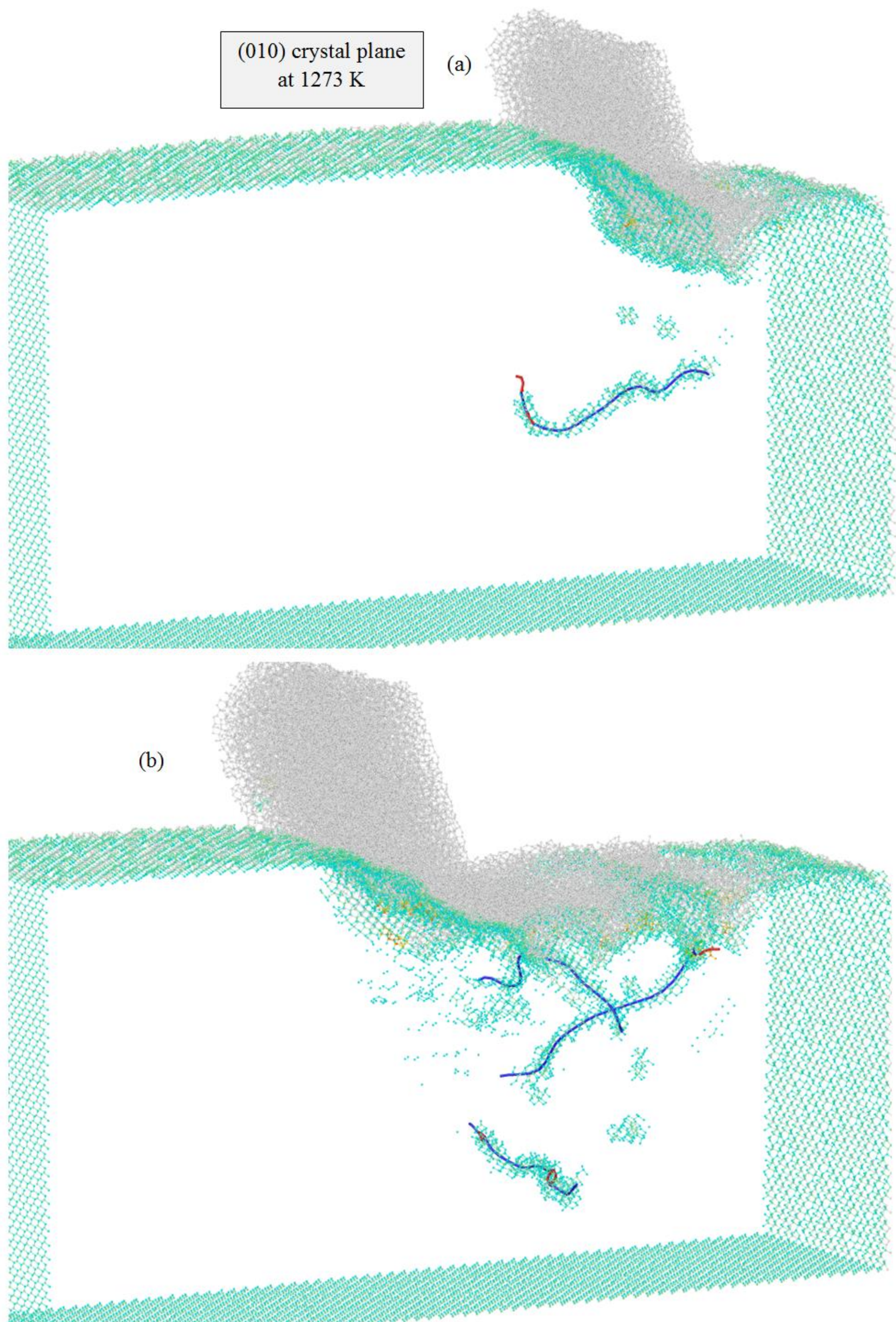


Figure 4.35: Dislocation nucleation while cutting the (010) plane at 1273 K at a cutting distance of a) 10 nm b) 20 nm.

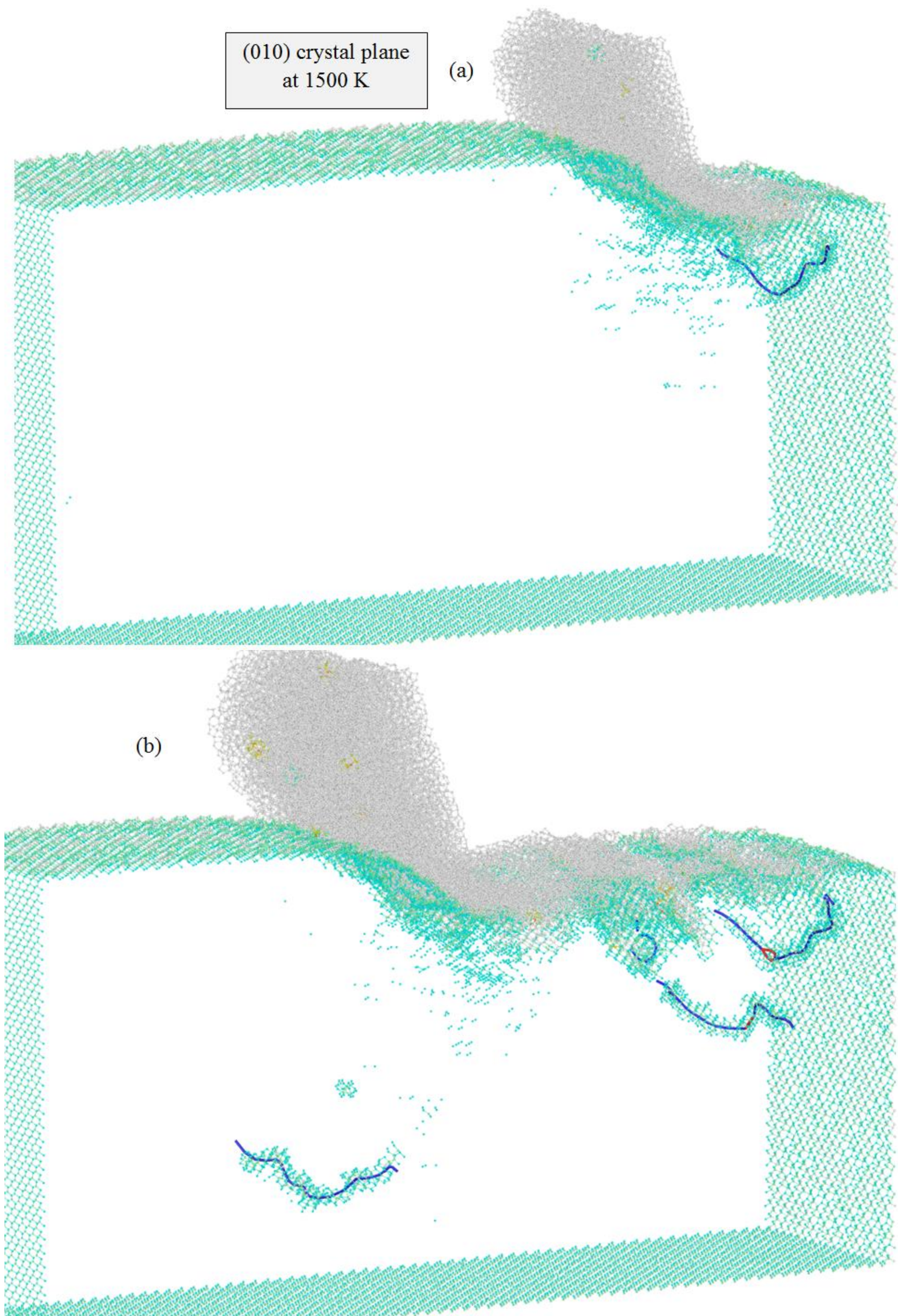


Figure 4.36: Dislocation nucleation while cutting the (010) plane at 1500 K at a cutting distance of a) 10 nm b) 20 nm.

As seen in Figure 4.37, while cutting the (110) surface at 300 K, perfect dislocation segments and small partial loops are nucleated ahead of the cutting tool. While the cutting process advances, dislocations are multiplied continuously, as shown in Figure 4.37b, which is in accord with the already observed behaviour for the (010) plane. In Figure 4.37, some partial dislocations are visible, which have been attached to the surface. Nonetheless, they are mere artefacts owing to the restrictions of the DXA. From Figure 4.38a, it may be seen that when the nanometric cutting is performed on the (110) crystal surface at 750 K, stair-rod partials with $1/6 < 110 >$ Burgers vectors become apparent. In addition, a quadric-shape stacking fault created by the partial dislocation interactions and bounded between them is formed, in accordance with the experimental observation [116]. It appears that the partial dislocations (and hence the stacking faults) do not arise from dissociation of perfect dislocations, but rather that they nucleate independently. The dislocation-originated stacking fault consists of three atomic layers. As the Burgers vector of partial dislocations does not connect the two points of the crystal lattice, the nucleation of partial dislocations may be accompanied by a stacking fault. This observation demonstrates that higher-order defects, such as the defect of stacking fault, can be formed within the restricted volume of silicon substrate during nanometric cutting, which could be regarded as a crucial plasticity mechanism strictly at the nanometre length scale. However, in some special cases, it is likely that the mobility of dislocations and other defects is limited by the creation of the stacking faults. It is observed from Figure 4.38b that numerous dislocations and a large stacking fault are formed at the cutting distance of 20 nm. Phonon and thermal vibration of the atoms within the substrate increase due to the thermal excitation, leading to an increase in

the probability of having atoms with higher energy state in the system. When the thermal energy is adequately high, there exists the possibility of having an atom jump out of the lattice, creating a point defect in the material, which can give rise to the formation of dislocations and staking faults. Moreover, thermal fluctuations facilitate overcoming the energy barrier for dislocation nucleation. Some partial loops, V-shaped perfect and Shockley dislocations, interactions and junctions are also observed in Figure 4.38b. It should be noted here that at low temperatures, dislocation activation and nucleation events can be a result of the mechanical stress activation rather than thermal one. It has been reported that, at the nanoscale level and under high temperature and low stress conditions, dislocations are nucleated in the glide set whereas shuffle-set dislocations are identified to be nucleated at low temperatures and high stresses [117, 120]. Li and Picu [111] reported that pressure increase leads to a reduction in the activation energy for nucleation in the shuffle-set, confirming that dislocations have tendency to be nucleated in the shuffle-set at high stress levels.

At 850 K, perfect dislocation segments, U-shaped perfect dislocation and partial segment are nucleated at the short cutting distance i.e. 10 nm, as shown in Figure 4.39a. It can be seen from Figure 4.39b that with the progress of cutting, a stacking fault, long perfect dislocation segments and partial loops are formed. It is worth mentioning that while cutting the (110) at 850 K, at short cutting distances, no stacking fault formation was observed as opposed to the corresponding case at 750 K. This observation lends credit to the previously perceived behaviour i.e. the defect formation is rather stochastic while nanometric cutting of silicon. As shown in Figure 4.40a, when the temperature of substrate is raised to 1173 K, a quadric-shape

stacking fault including three atomic layers sandwiched between two partial dislocations is formed underneath the cutting tool at the short cutting distance of 10 nm. Also, perfect dislocation segments and a partial loop are observed to nucleate within the substrate. As evident from Figure 4.40b, the size of stacking fault scales up with the progress of cutting. Figure 4.41a illustrates that the defect formation mode at 1273 K includes nucleation of perfect dislocations ahead of the tool and three atomic layers-stacking faults bounded between Shockley partials and other partial segments underneath the cutting tool. It is found that the shape of stacking fault is not well-ordered in this case.

Quadric-shape stacking fault, perfect and partial dislocations are observed to form at 1500 K, while the nanometric cutting is carried out on the (110) crystal plane at the short cutting distances, as demonstrated in Figure 4.42a. Interestingly, the stacking fault does not grow with the progress of cutting in this case. At long cutting distances, perfect dislocations and partial loops are nucleated ahead of the cutting tool. It is of note that the likelihood of formation of partial dislocations is more at high temperatures than at low temperature. It has been experimentally proved that under high temperature conditions, partial dislocations are generated which nucleate on the glide set planes [121]. However, there is no sharp transition between two regimes of dissociated and non-dissociated dislocations at high temperatures; hence both can be perceived during nanometric cutting of silicon at high temperatures. The total length of dislocations was found to vary randomly from 27.8 nm to 89.6 nm and from 105.6 nm to 258.7 nm at the short and long cutting distances, respectively, over the studied temperatures while cutting the (110) crystal plane.

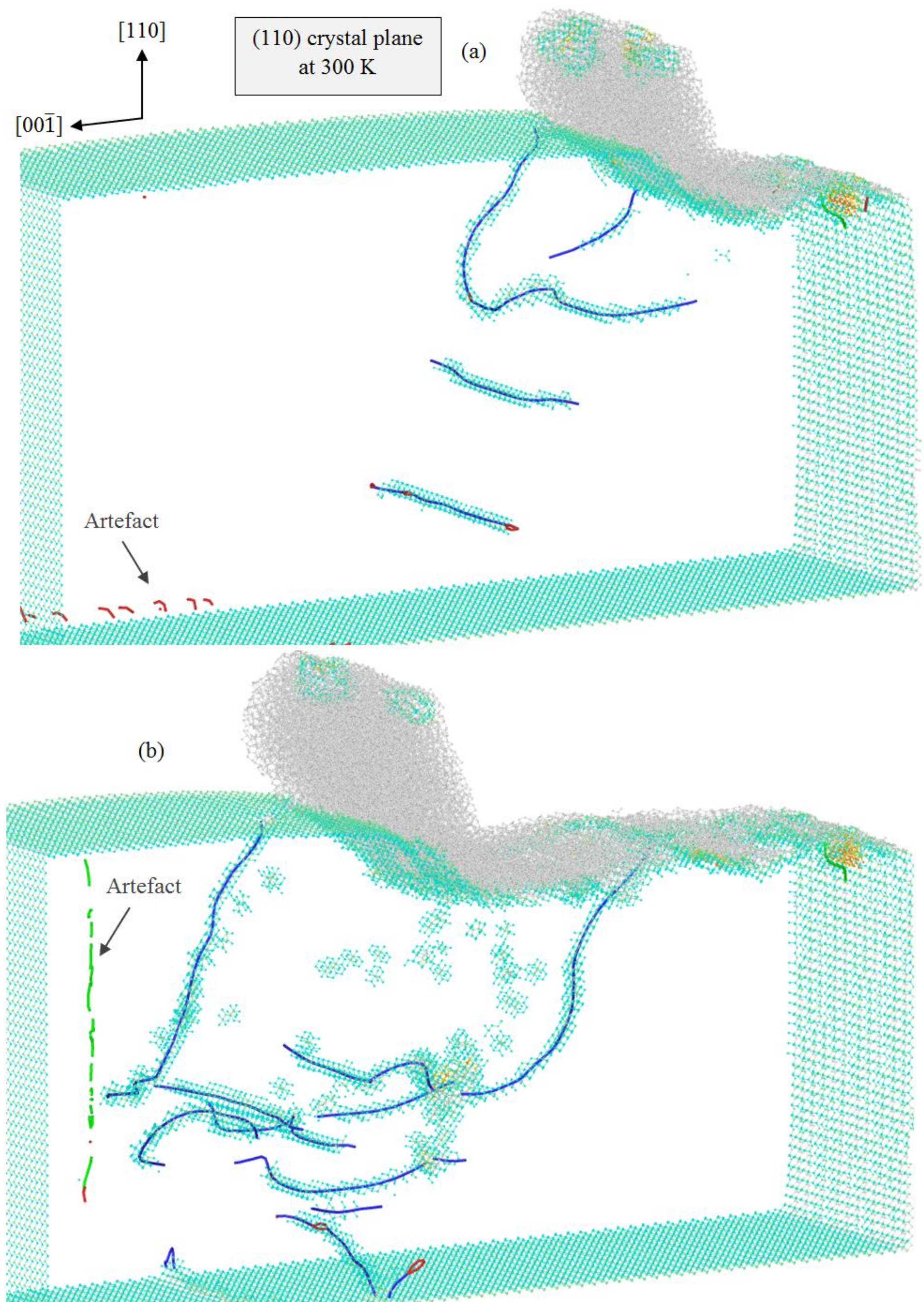


Figure 4.37: Dislocation nucleation while cutting the (110) plane at 300 K at a cutting distance of a) 10 nm b) 20 nm.

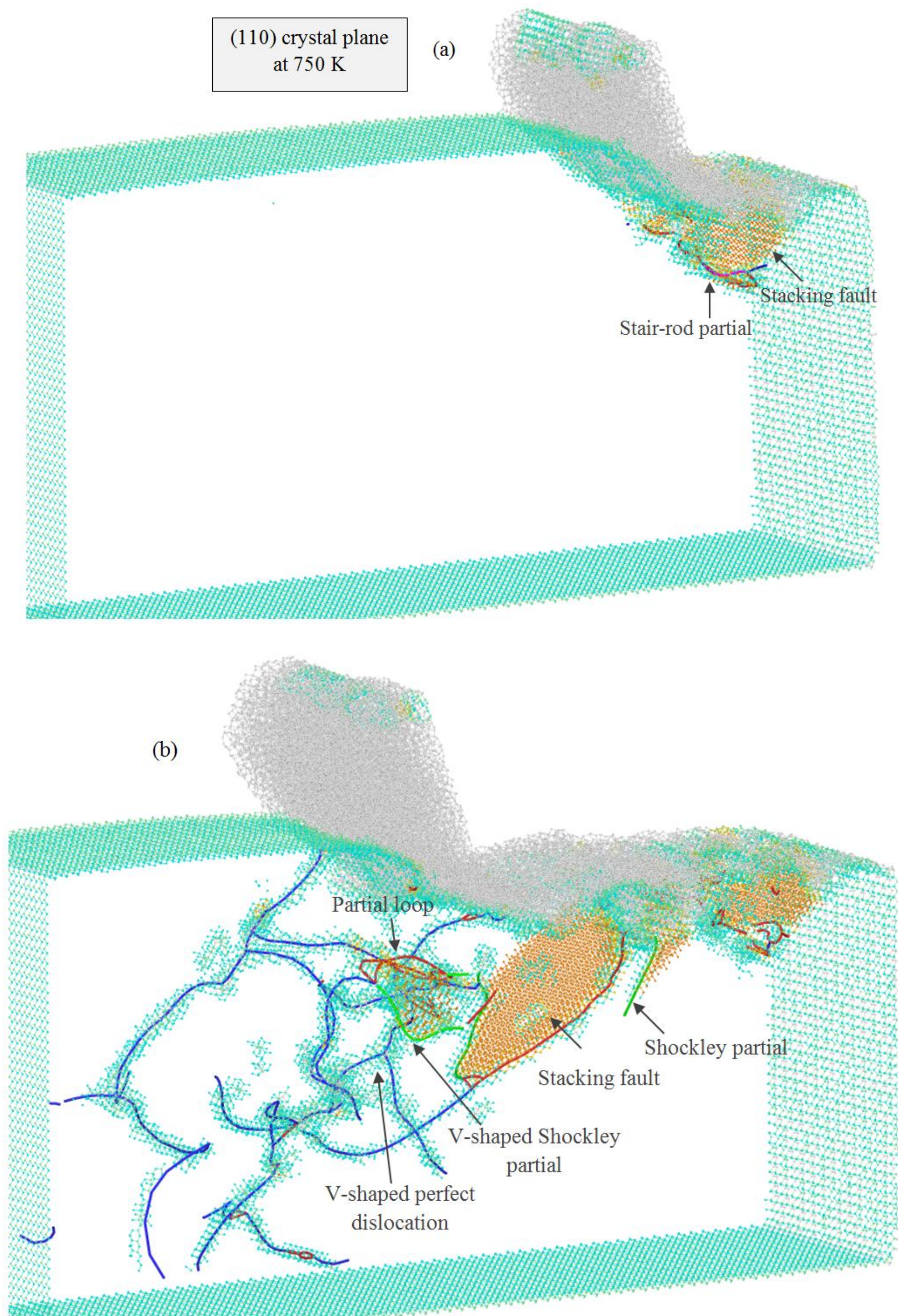


Figure 4.38: Formation of crystal defects while cutting the (110) plane at 750 K at a cutting distance of a) 10 nm b) 20 nm. Pink rod represents the stair-rod partial dislocation.

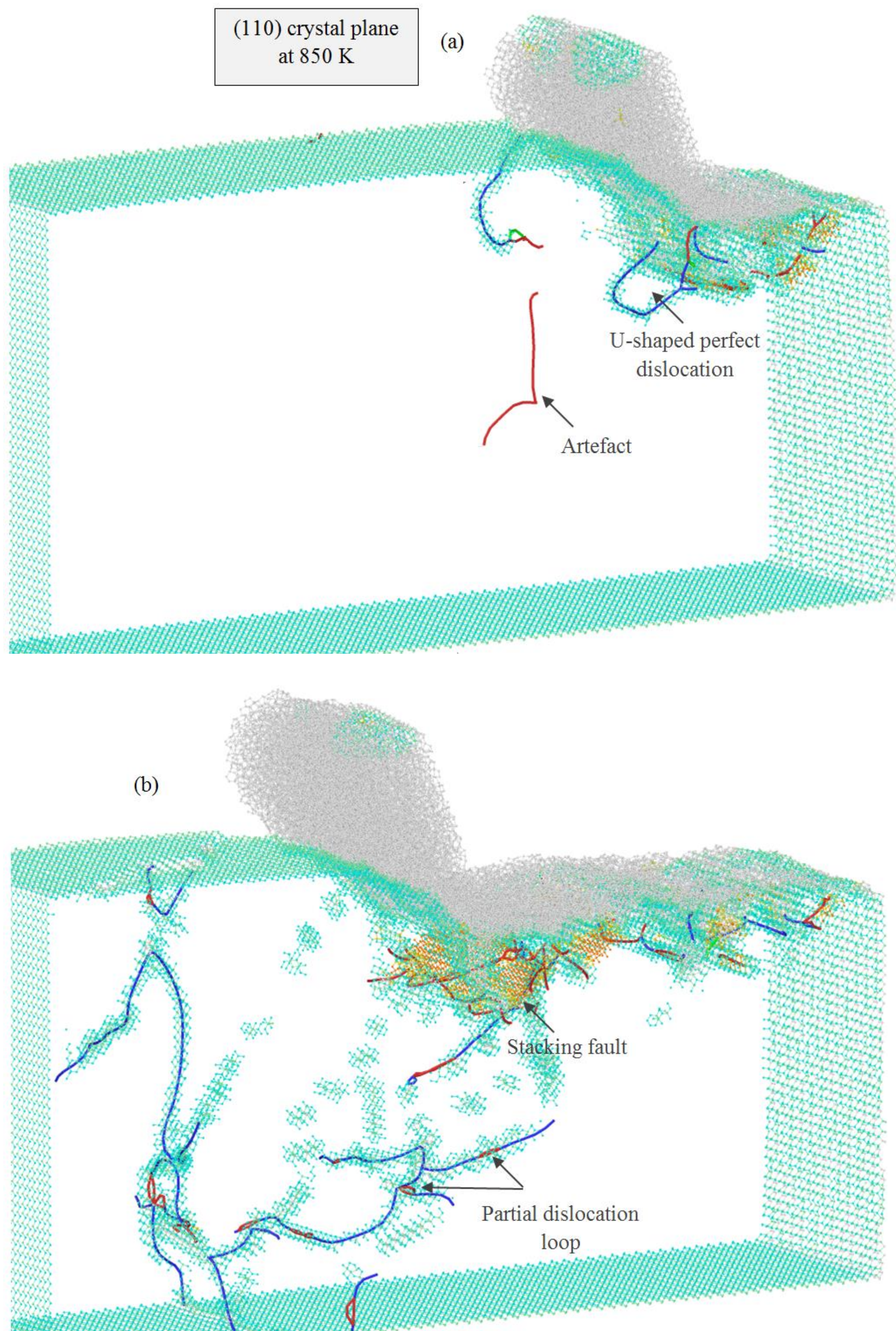


Figure 4.39: Formation of crystal defects while cutting the (110) plane at 850 K at a cutting distance of a) 10 nm b) 20 nm

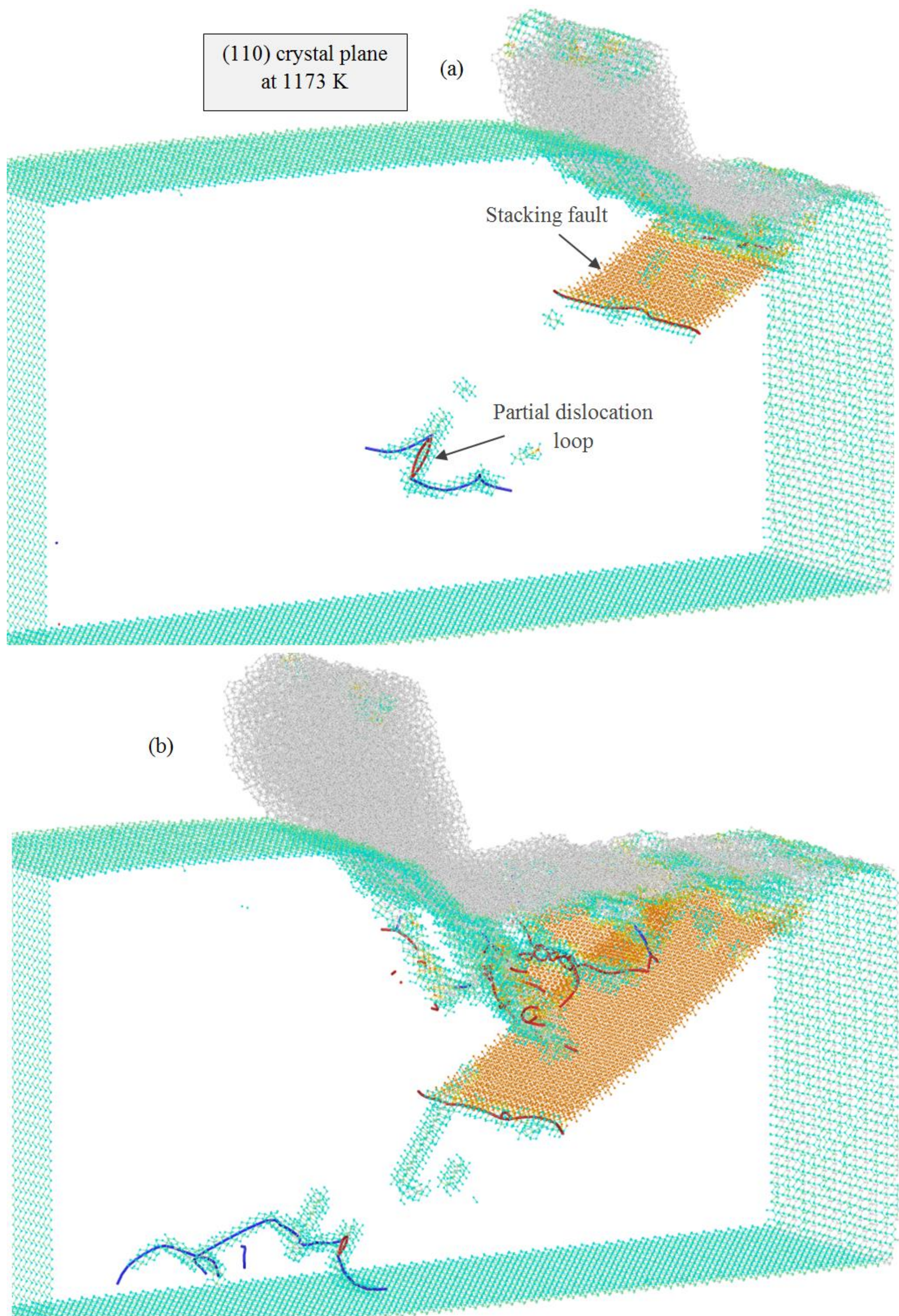


Figure 4.40: Formation of crystal defects while cutting the (110) plane at 1173 K at a cutting distance of a) 10 nm b) 20 nm

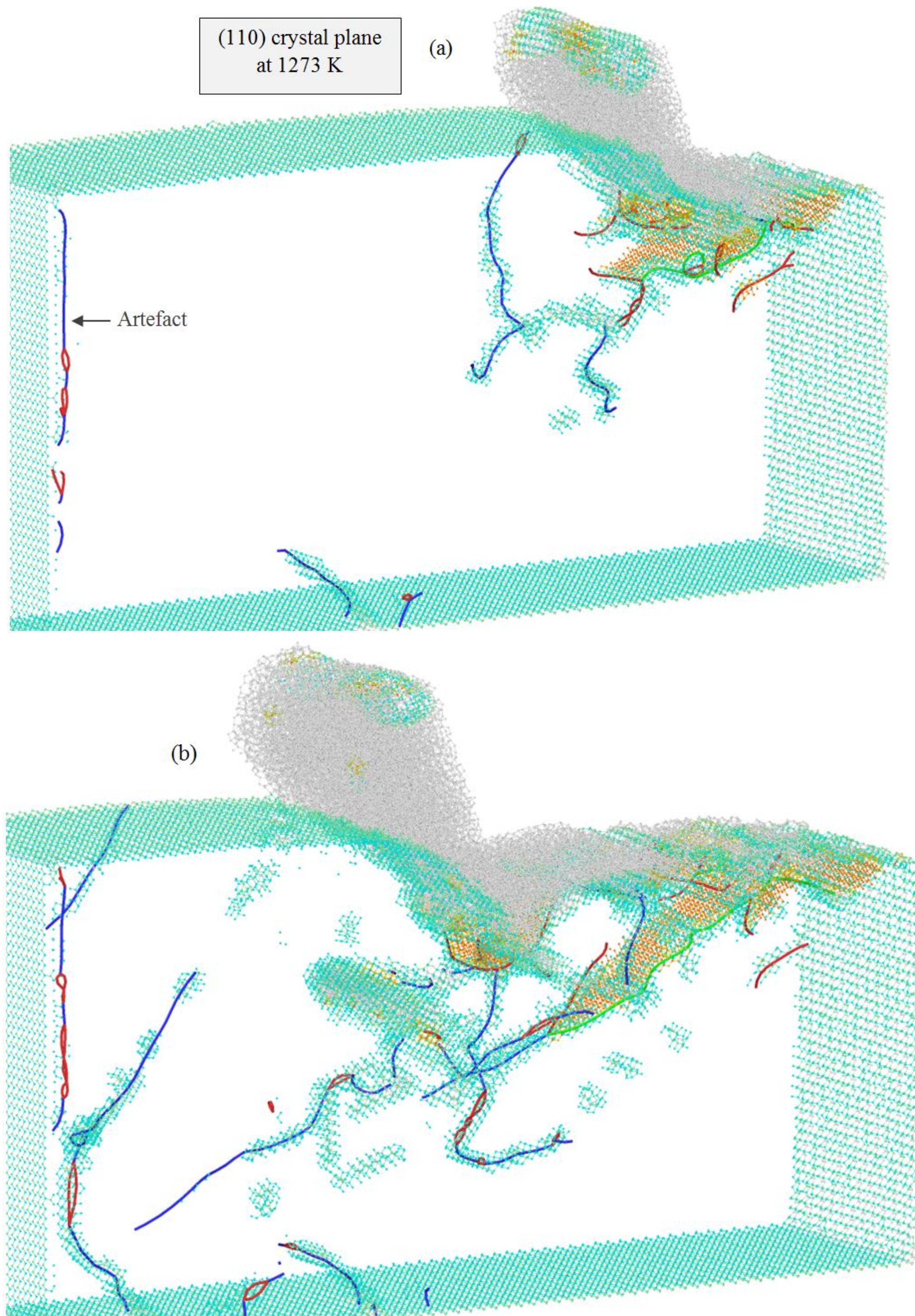


Figure 4.41: Formation of crystal defects while cutting the (110) plane at 1273 K at a cutting distance of a) 10 nm b) 20 nm

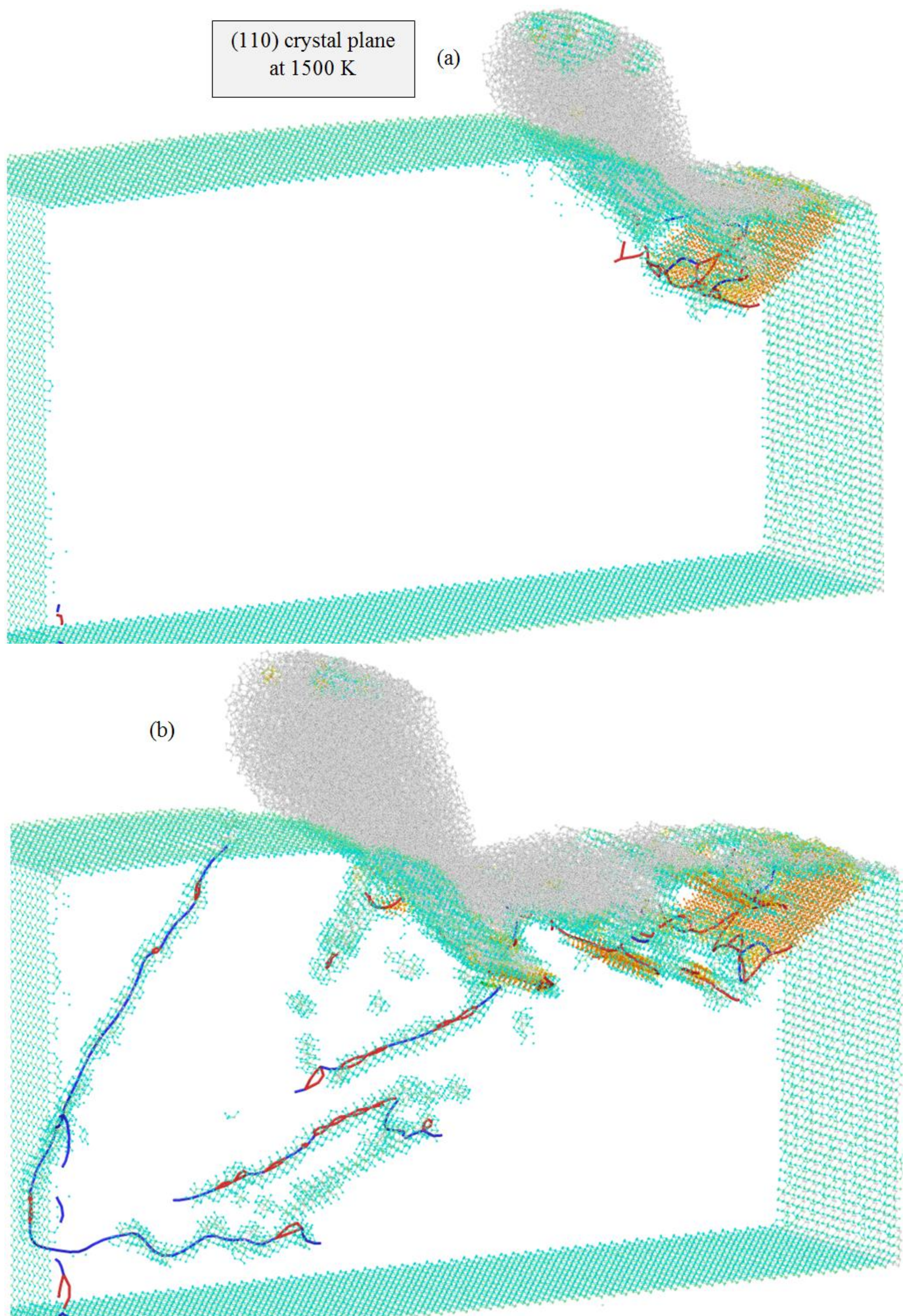


Figure 4.42: Formation of crystal defects while cutting the (110) plane at 1500 K at a cutting distance of a) 10 nm b) 20 nm

During nanometric cutting of silicon on the (111) crystal plane at different temperatures, aside from formation of perfect dislocation segments, partial segments and partial loops are nucleated ahead of the cutting tool, as illustrated in Figure 4.43, Figure 4.44, Figure 4.45, Figure 4.46, Figure 4.47 and Figure 4.48. The total length of dislocations was found to vary stochastically from 22.1 nm to 48.4 nm and from 24.4 nm to 59.6 nm at the short and long cutting distances, respectively, over the studied temperatures. It can be seen from the figures that the pattern of dislocation emission is almost alike for the studied cases i.e. nucleation of dislocations ahead of the cutting tool and near the free surface. Besides, more partial dislocations are seen to nucleate ahead of the cutting tool at higher temperatures, which can be regarded as a dissociation of perfect dislocations to partial ones at high temperatures. Some artefacts are also noticeable in the figures. No stacking fault formation was observed for this case. In general, lower degree of defect formation than that of the $(110)<00\bar{1}>$ crystal setup is observed for the $(111)<\bar{1}10>$ and (010)<100> crystal setups, attributable to the difficulty of activating slip systems in single crystal silicon. However, a Schmid factor analysis is not suitable due to the complicated stress state adjacent to the cutting tool. Note that some crystallites of silicon in the cutting chip can be seen while cutiing the (111) plane, suggesting the occurance of cleavage.

Taking everything into account, it can be inferred that while cutting the (010)<100> and $(111)<\bar{1}10>$, dislocation nucleation marginally assists the crystal plasticity of silicon at low and high temperatures and the plasticity is primarily meditated by the amorphization and weak bonding between atoms at high temperatures. Interestingly, irrespective of the cutting temperature, no stacking fault was observed to form while cutting silicon on the aforementioned planes. In contrast, a large number of defects is

formed while cutting silicon on the $(110)\langle 00\bar{1}\rangle$ at different temperatures; hence dislocation nucleation and stacking fault formation have an inevitable influence on the deformation response of silicon for this crystal setup. However, at room and high temperatures, amorphization also aids the crystal plasticity of silicon. Furthermore, amorphization of silicon atoms was observed to be more likely and dominative over defect formation at the initial stage of cutting, implying that the incipient plasticity of silicon in nanometric cutting takes place by amorphization. Additionally, it was found that the possibility of formation of perfect dislocations at both low and high temperatures is higher than partial ones during nanometric cutting of silicon on the different crystallographic planes.

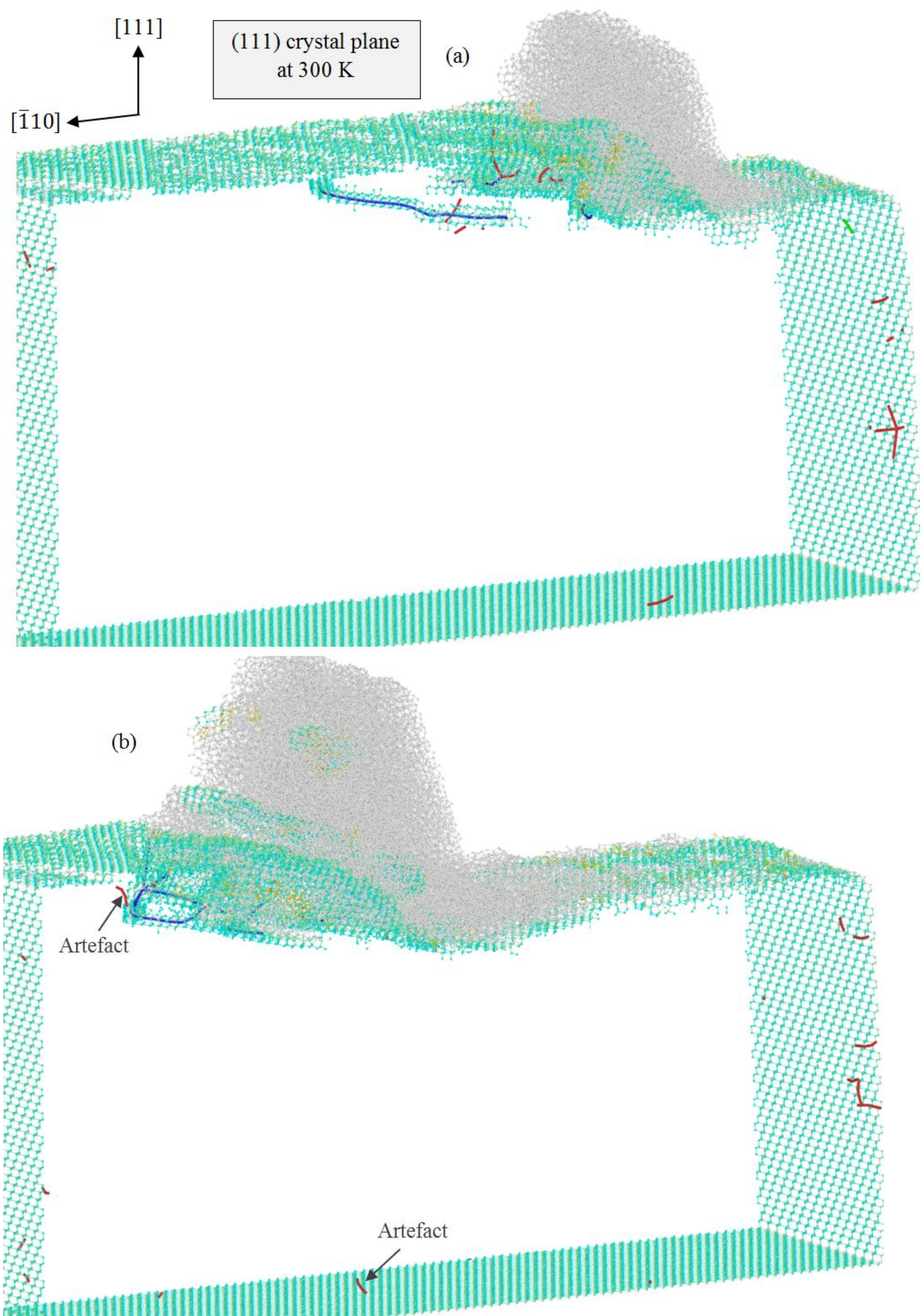


Figure 4.43: Dislocation nucleation while cutting the (111) plane at 300 K at a cutting distance of a) 10 nm b) 20 nm.

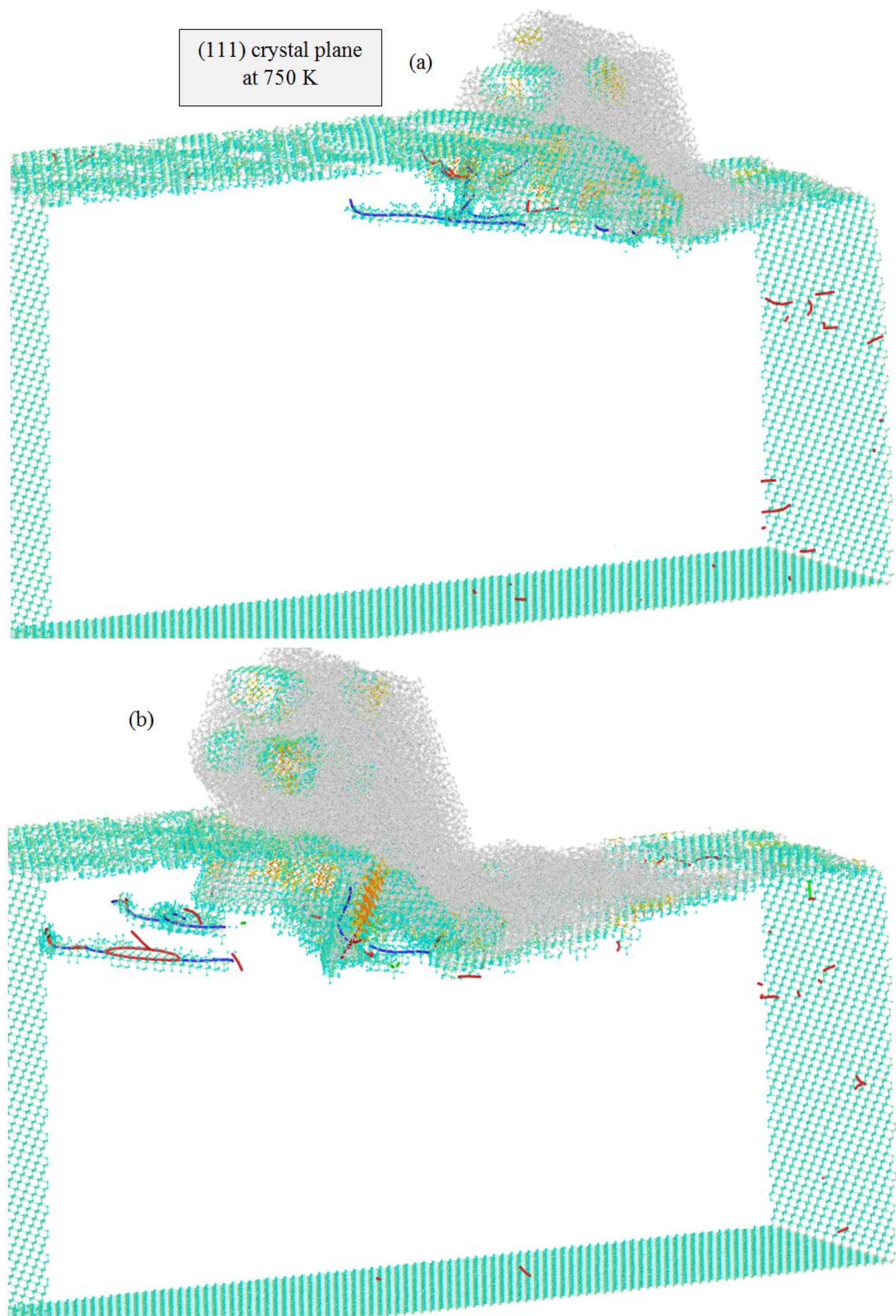


Figure 4.44: Dislocation nucleation while cutting the (111) plane at 750 K at a cutting distance of a) 10 nm b) 20 nm.

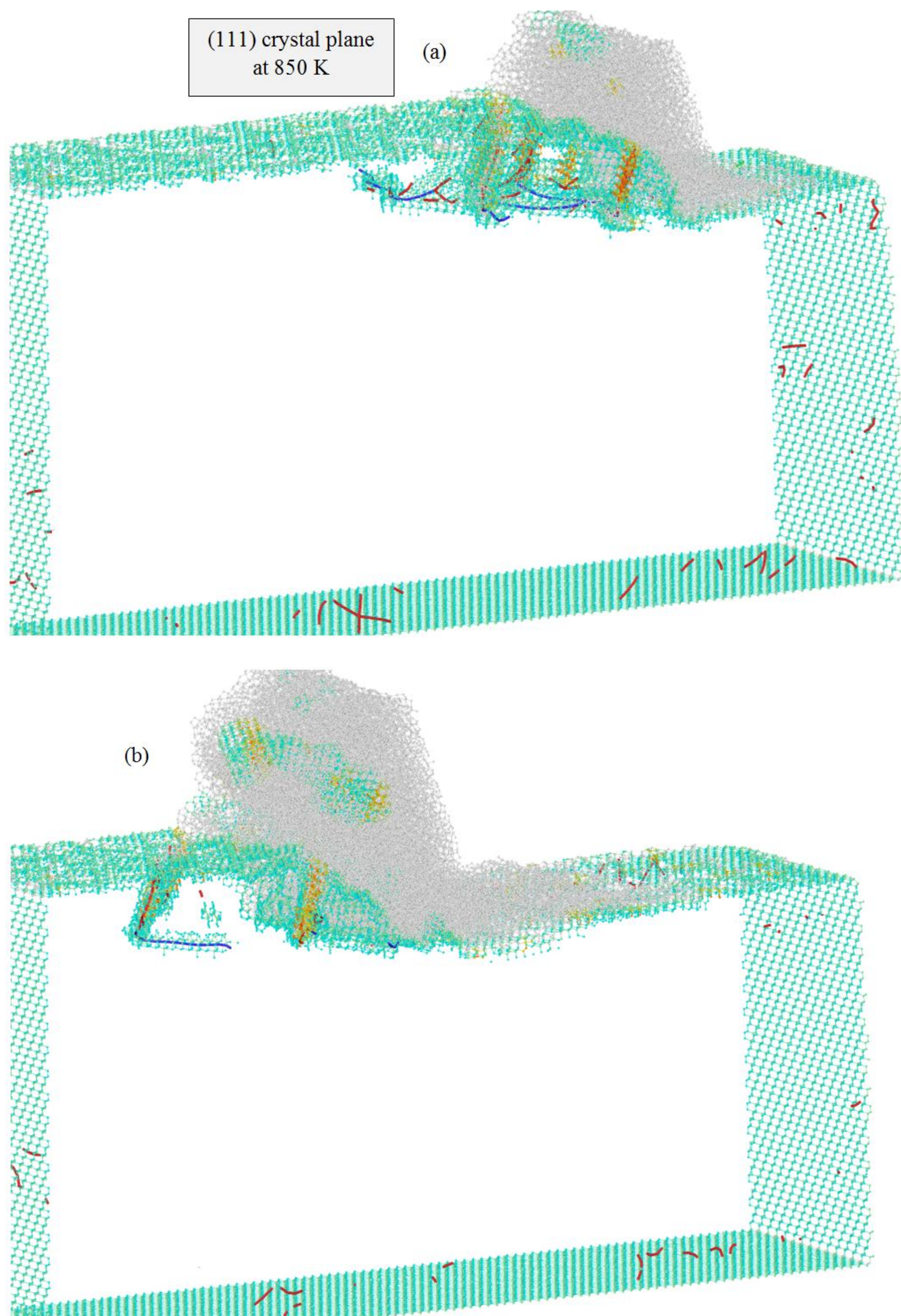


Figure 4.45: Dislocation nucleation while cutting the (111) plane at 850 K at a cutting distance of a) 10 nm b) 20 nm.

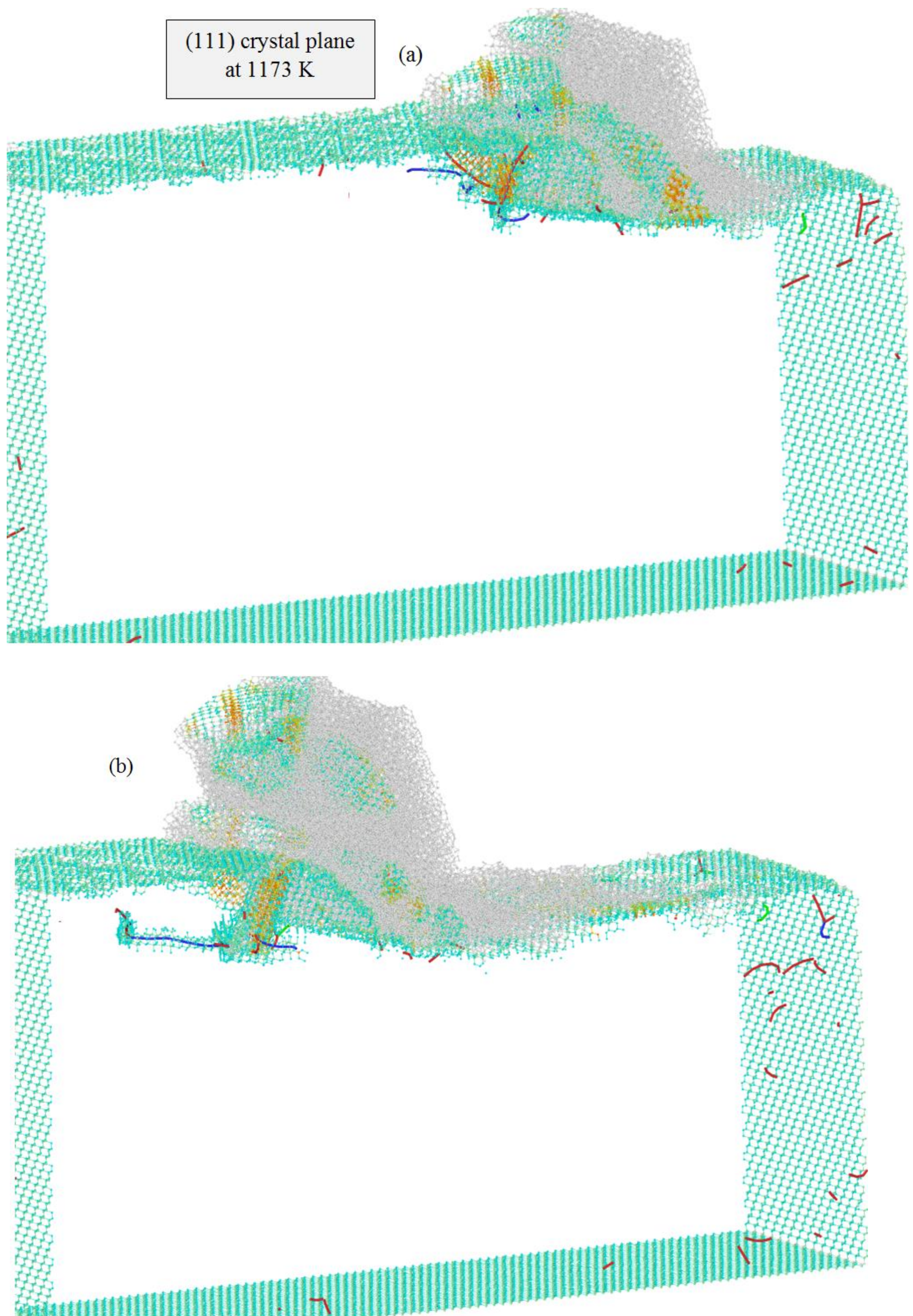


Figure 4.46: Dislocation nucleation while cutting the (111) plane at 1173 K at a cutting distance of a) 10 nm b) 20 nm.

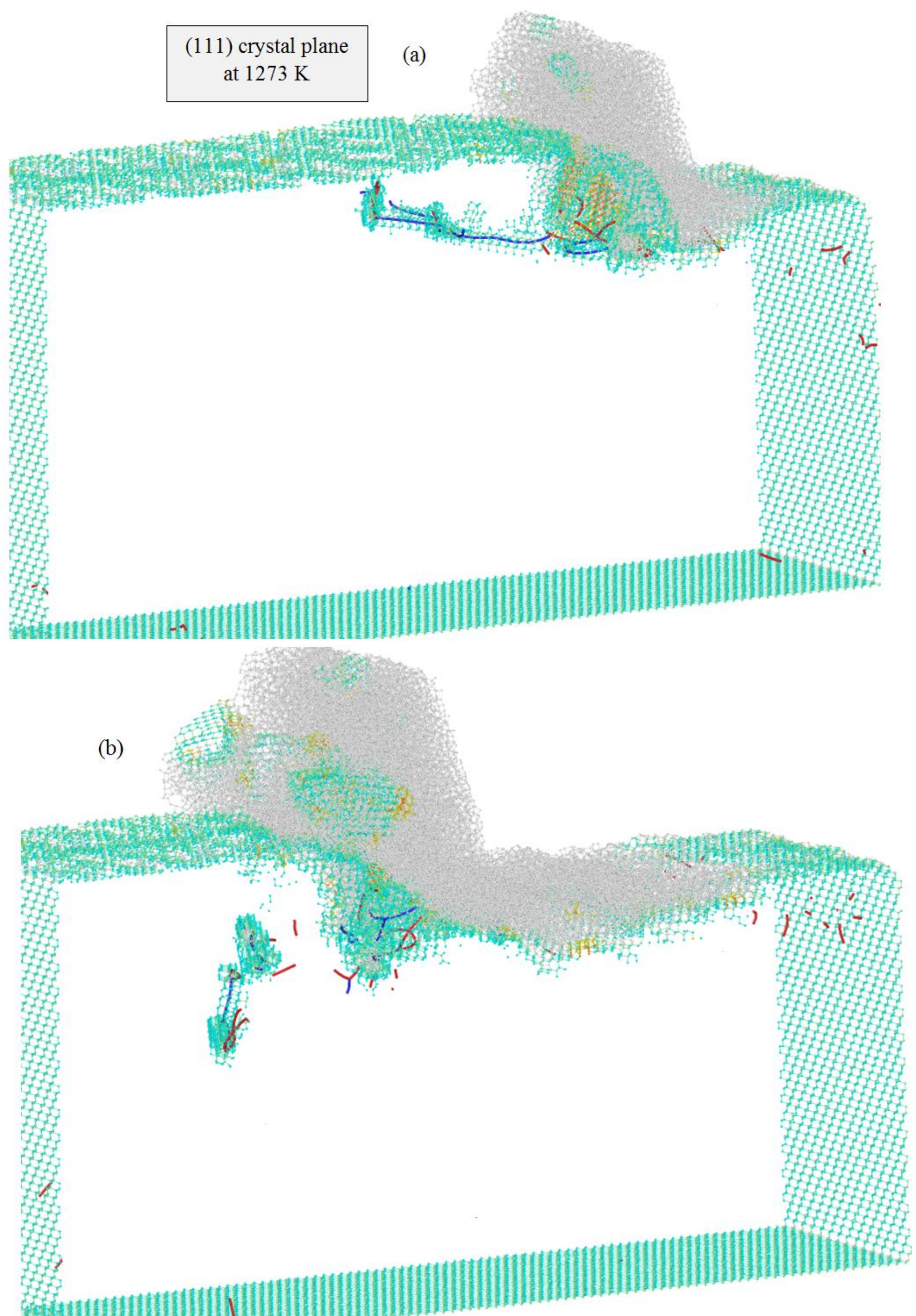


Figure 4.47: Dislocation nucleation while cutting the (111) plane at 1273 K at a cutting distance of a) 10 nm b) 20 nm.

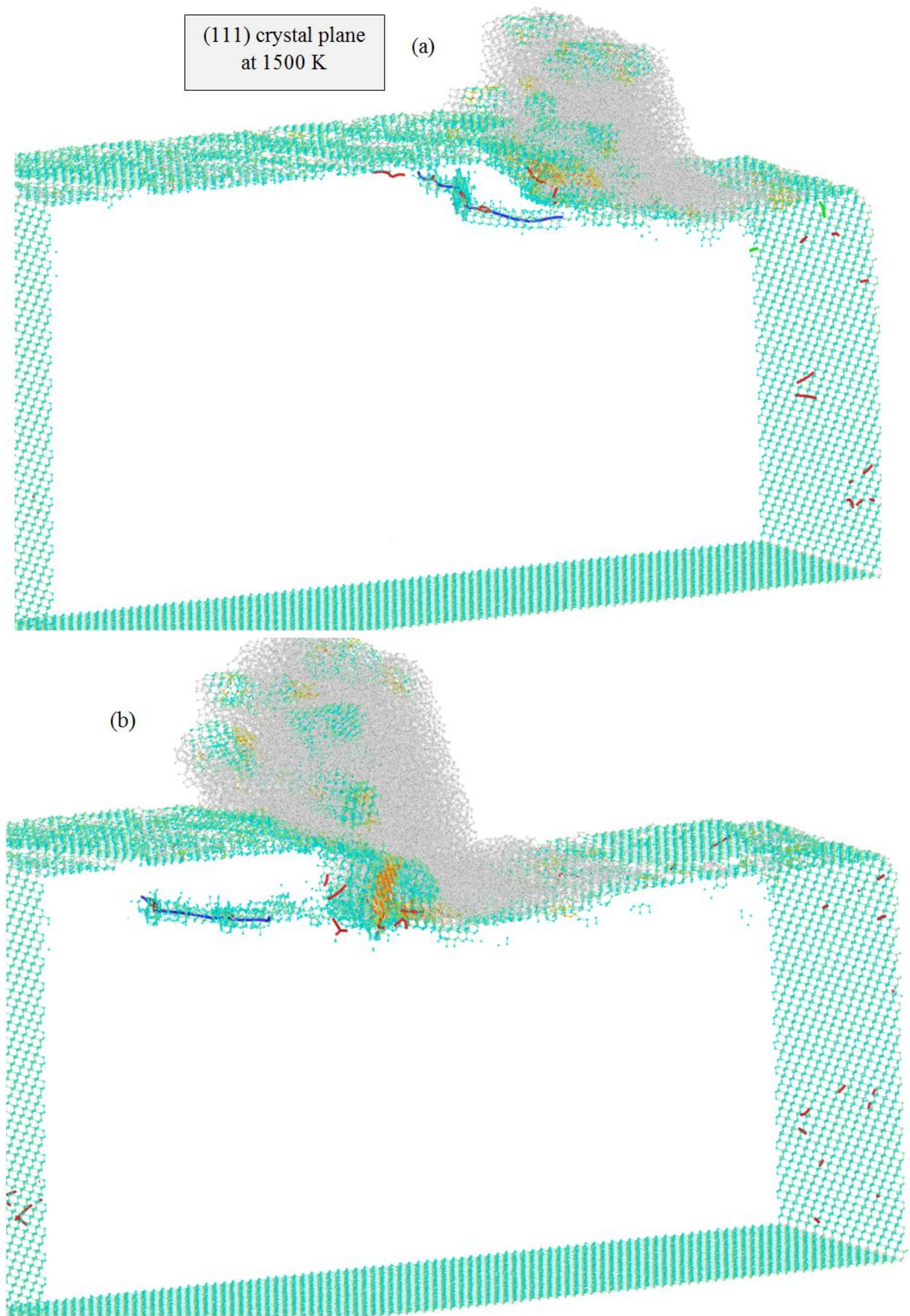


Figure 4.48: Dislocation nucleation while cutting the (111) plane at 1500 K at a cutting distance of a) 10 nm b) 20 nm.

### 4.10. Summary

This chapter provided the MD simulation results obtained during the nanometric cutting of silicon on the (010), (110) and (111) crystal planes at various temperatures (300 K-1500 K). The substrate material underneath the cutting tool was observed to experience a rotational flow akin to fluids at all the tested temperatures up to 1200 K. Additionally, the degree of flow in terms of vorticity was found higher on the (111) crystal plane signifying better machinability on this plane in accord with the current pool of knowledge. An increase in the machining temperature reduced the spring-back effect and thereby the elastic recovery and the cutting plane and the cutting temperature showed significant influence on the location and position of the stagnation region in the cutting zone of the substrate.

Smaller released thermal energy and larger values of chip ratio as well as shear plane angle were obtained when cutting was performed at higher temperatures or on the (111) crystal plane, implying an enhancement in machinability of silicon. Nonetheless, the subsurface deformation depth was observed to become deeper under the aforementioned conditions. Further analysis revealed a higher number of atoms in the chip when cutting was implemented on the (110) crystal plane, attributable to the lower position of the stagnation region which triggered less ploughing action of the tool on the silicon substrate. Regardless of temperature of the substrate the minimum chip velocity angle was found while cutting the (111) crystal plane of silicon substrate whereas the maximum chip velocity angle appeared on the (110) surface. Another key observation was that the resultant force exerted by the rake face of the tool on the chip was found to decrease by 24 % when cutting the (111) surface at 1173 K compared to that at room temperature. Besides, smaller resultant force,

friction coefficient at the tool/chip interface and chip temperature was witnessed on the (111) crystal plane, as opposed to the other planes.

The specific cutting energy required to cut the (111) surface of silicon and the von Mises stress to yield the silicon in the cutting reduces by 25% and 32%, respectively, at 1173 K compared to what is required at 300 K. The room temperature cutting anisotropy in the von Mises stress and the room temperature cutting anisotropy in the specific cutting energy (work done by the tool in removing unit volume of material) were calculated as 12% and 16% respectively. It was observed that this changes to 20% and 40%, respectively, when cutting was performed at 1500 K, signifying a very strong correlation between the anisotropy observed during cutting and the machining temperature. Furthermore, using the atomic strain criterion, the width of primary shear zone was found to vary with the orientation of workpiece surface and temperature i.e. it remains narrower while cutting the (111) surface of silicon or at higher machining temperatures. A major anecdote of the study was that irrespective of the cutting plane or the cutting temperature, the state of the cutting edge of the diamond tool did not show symptoms of any direct diamond to graphitic phase transformation under vacuum condition.

Dislocation nucleation and formation of stacking faults were identified in conjunction with amorphization of silicon as the meditators of crystal plasticity in single crystal silicon during nanometric cutting process on different crystallographic planes at various temperatures. MD simulations revealed strong anisotropic dependence behaviour of dislocation activation and stacking fault formation, resultant from the ease of activating slip systems in single crystal silicon. While a large number of defects including dislocations and three atomic layers-stacking faults

was formed during cutting the (110)$<00\bar{1}>$ at different temperatures, low dislocation activity without stacking fault formation was observed for the (010)<100> and (111)$<\bar{1}10>$ crystal setups. Also, perfect dislocation nucleation was seen to be more prone to nucleate at both low and high temperatures whereas partial dislocations were generated more at higher temperatures. Under certain circumstances, some dislocation loops composing of dissociated partial dislocations were observed to nucleate. Furthermore, amorphization of silicon atoms was found to be more likely and dominative over defect formation at the initial stage of nanometric cutting.

# Chapter 5: MD simulation results for nanometric cutting of 3C-SiC at elevated temperatures

## 5.1. Introduction

Analogous to the nanometric cutting of silicon at elevated temperatures, material flow behaviour, cutting chip characteristics, specific cutting energy, defect formation, etc. alter with the temperature and crystal plane during nanometric cutting of 3C-SiC. This chapter reports the MD simulation results concerning the plastic flow behaviour, stagnation region, chip related phenomena, cutting forces, specific cutting energies, yielding stresses, defect-mediated plasticity of 3C-SiC and the state of the diamond cutting tool post-machining in nanometric cutting on the (010), (110) and (111) crystal planes at different cutting temperatures spanning from 300 K to 3000 K. In addition, the differences in the cutting of silicon and 3C-SiC are presented. The reported results are based on the ABOP function and whenever needed, comparison is made with the results obtained by Tersoff potential. More details about the employability of the appropriate potential function can be found in Appendix I.

## 5.2. Plastic flow behaviour

In order to investigate the plastic deformation mediated flow behaviour of 3C-SiC workpiece during nanometric cutting, the atomic flow field in various zones of the workpiece (see Figure 4.1) was determined. Figure 5.1 illustrates the displacement vector of atoms after 20 nm of cutting at 300 K on the (010), (110) and (111) planes. A very clear distribution of atomic flow field is apparent in various zones of the workpiece. It can be drawn from Figure 5.1 that the atoms beneath the cutting tool in

region *III* experience a rotational flow. This particular flow behaviour of 3C-SiC is analogous to what was observed for silicon in section 4.2.1. Nevertheless, there are some discrepancies i.e. in region *IV*, the motion of atoms along the cutting direction is much more marked for the 3C-SiC than silicon workpiece. In particular, with the (111) plane at 300 K, the movement of atoms along the $[\bar{1}\bar{1}\bar{1}]$ direction alters to the $[\bar{2}0\bar{1}]$. This behaviour can be attributed to the occurrence of cleavage ahead of the cutting tool, as will be discussed in section 5.4. Another difference is that the atoms in region *I* tend to move upwards rather than downwards and backwards observed for the silicon. The upwards motion of 3C-SiC atoms is more remarkable on the (111) surface plausibly due to the higher elastic recovery, as a consequence of higher ratio of hardness to Young's modulus (H/E), and upper position of stagnation region (see section 5.3), on this crystal plane as opposed to the other planes. Similar to silicon, while cutting 3C-SiC on the (111) plane, the centre of rotational flow underneath the tool was found to be positioned lower than those of other crystal surfaces, which assists a more effective flow of the atoms within the workpiece. It can, therefore, facilitate the chip formation and material removal during nanometric cutting process.

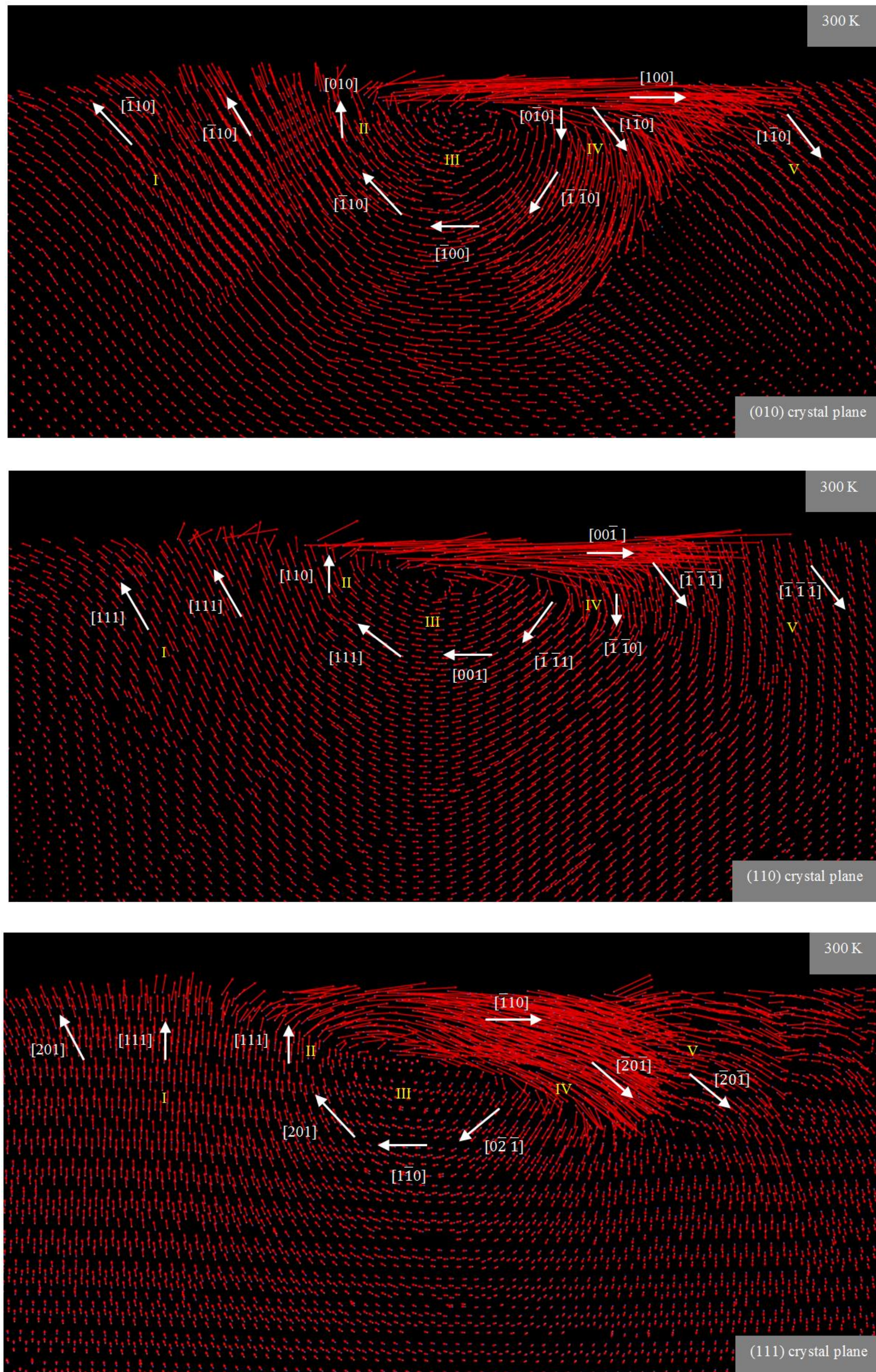


Figure 5.1: Atomic flow field in the *XY* plane during nanometric cutting of 3C-SiC on the various crystal planes at 300 K. The location of the cutting tool in connection with the different regions can be traced from Figure 4.1.

As can be seen from Figure 5.2, when nanometric cutting of 3C-SiC is carried out at 3000 K, the rotational flow of the atoms in region *III* is practically eliminated. This fact is more discernible for the (111) crystal plane and atoms show a little turbulence flow. Moreover, as a result of weak van der Waals interactions between atoms at high temperature of 3000 K, the workpiece atoms have tendency to move along the cutting direction. Another notable feature is the existence of upward motion of atoms in region *I* even at high temperature of 3000 K. Accordingly, one would expect to perceive elastic recovery at this temperature. The reason for such observation could be traced to the melting point of 3C-SiC predicted by the ABOP function. A common problem intrinsic to BOP functions for semiconductors is the overestimation of melting point. An attempt was made to calculate the melting point of 3C-SiC predicted by ABOP using one-phase method and adopting reflective boundaries to diminish the hysteresis phenomenon [122, 123]. The phase instability and entirely molten temperature of a $15 \times 15 \times 15$ lattice cell were observed at 3529 K and 3993 K, respectively, which are far above the experimental value (~2800 K). Therefore, satisfactory thermal softening and in turn decline of elastic recovery which ought to be occurred at high temperature of 3000 K cannot be achieved. The high temperature of 3000 K (which is higher than the experimental value) was selected for the simulations since the ABOP potential predicts the meltig point of 3C-SiC to be 3993 K. Hence, the simulated temperatures and results should be scaled to match the actual (experimental) temperatures. However, this is a common shortcoming of current avaialbe potential functions for SiC.

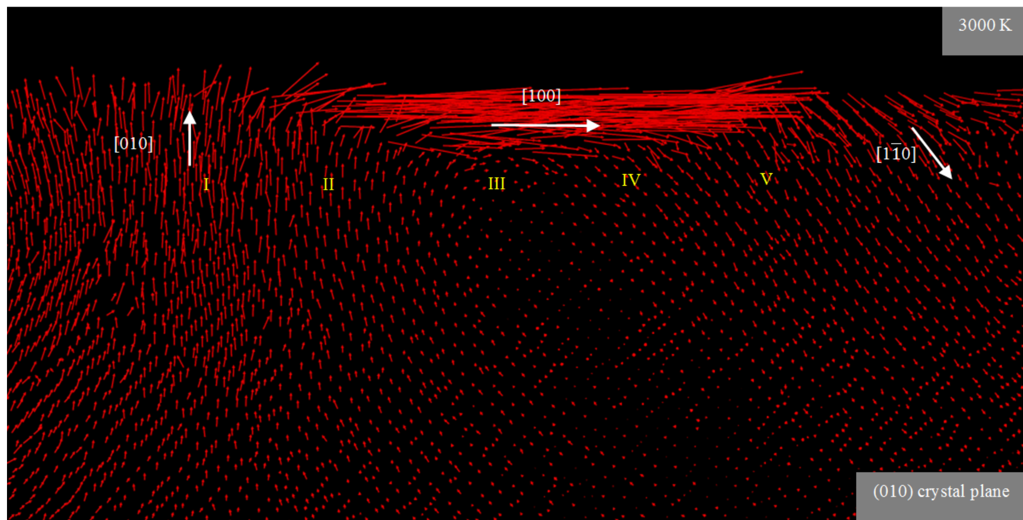


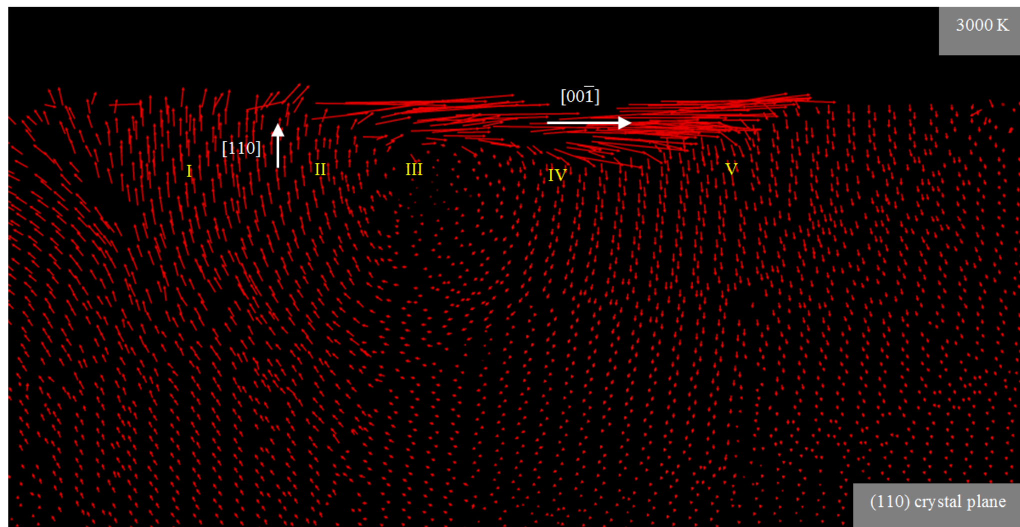


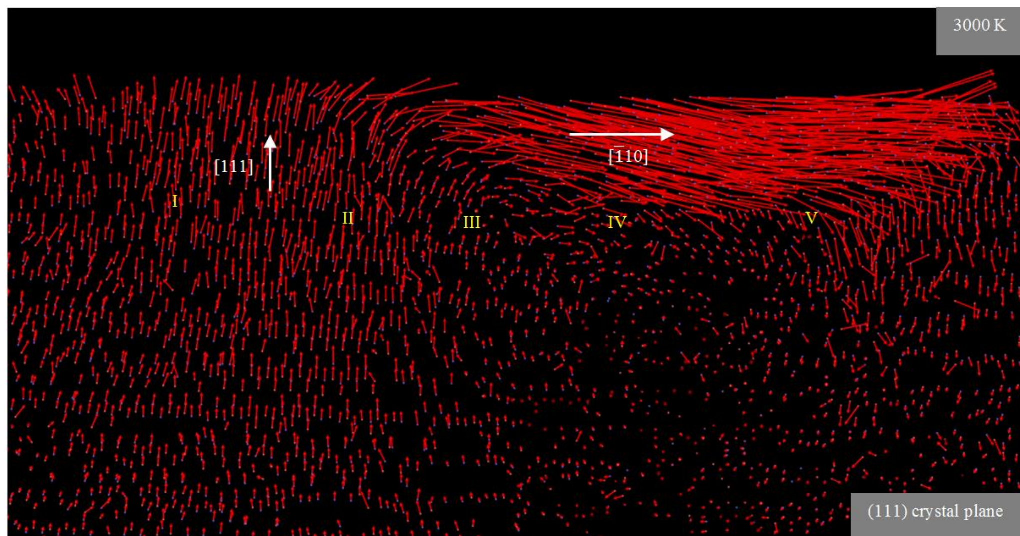


Figure 5.2: Atomic flow field during nanometric cutting of 3C-SiC on the various crystallographic surfaces at 3000 K

## 5.3. Stagnation region and friction angle

As described in section 4.2.2, the location of the stagnation region can be determined through calculation of the average displacement of workpiece atoms in *y* direction in various layers. Figure 5.3 represents displacements of different layers in the workpiece when nanometric cutting of 3C-SiC is performed on the (110) crystal surface at 1400 K. Table 5.1 summarizes the position of stagnation region and stagnation angles for the studied cases.

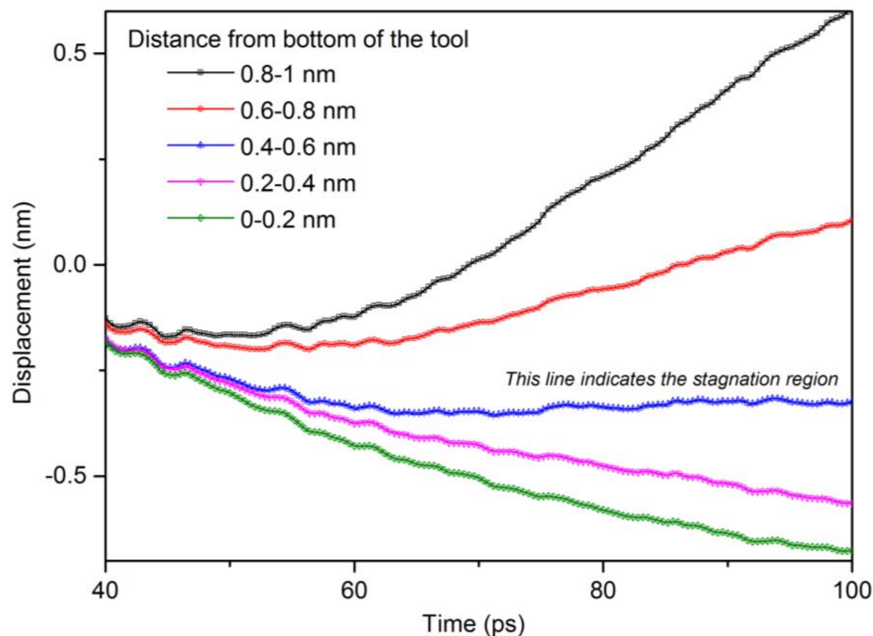


Figure 5.3: Displacement of various layers in *y* direction while cutting 3C-SiC on the (110) crystal plane at 1400 K

It can be deduced from Table 5.1 that while cutting the (111) crystal plane at different temperatures, the stagnation region is located at an upper position than for other planes, which indicates ploughing caused by compression is more pronounced on the (111) surface and therefore a thicker deformed region is expected to be generated,

which may result in higher elastic recovery. The converse scenario occurs for the (110) plane, where the stagnation region is located at a lower position than those of other crystal planes. It can be also inferred that at high temperatures the stagnation region is located lower than that at room temperature, attributable to the thermal softening and enhanced plasticity of 3C-SiC workpiece. Interestingly, it is found that the 3C-SiC exhibits the same general trend observed for the position of stagnation region during nanometric cutting of silicon at different temperatures. An attempt was also made to compare the magnitudes of stagnation angle and friction angle. It is observed from Table 5.1 that up to 1400 K, the values of stagnation and friction angle are closely correlated for the (110) crystal plane. Nonetheless, there exists a discrepancy between two angles while cutting the (010) and (111) planes or at high temperatures i.e. 2000 K and 3000 K, particularly the difference is more noticeable for the high cutting temperatures.

Table 5.1: Stagnation region, stagnation angle and friction angle while cutting 3C-SiC

| Workpiece Temperature (K) | Crystal plane | Position of Stagnation region from bottom of the tool ($h_{1,2}$) (nm) | Stagnation angles ($\theta_{s1,2}$) (degree) | Friction angle (β) (degree) |
|---|---|---|---|---|
| 300 | (010) | 0.9-1.1 | 42-46.7 | 33 |
| | (110) | 0.6-0.8 | 34-39.9 | 34.3 |
| | (111) | 1.1-1.3 | 46.7-55.5 | 44 |
| | (010) | 0.8-1 | 39.9-44.4 | 32.4 |

| | | | | |
|---|---|---|---|---|
| 900 | (110) | 0.5-0.7 | 31-36.9 | 32.2 |
| | (111) | 1-1.2 | 44.4-48.9 | 44.9 |
| 1200 | (010) | 0.7-0.9 | 36.9-42 | 32.7 |
| | (110) | 0.5-0.7 | 31-36.9 | 31.1 |
| | (111) | 0.7-0.9 | 36.9-42 | 45.7 |
| 1400 | (010) | 0.6-0.8 | 34-39.9 | 34.1 |
| | (110) | 0.4-0.6 | 27.7-34 | 32.2 |
| | (111) | 0.7-0.9 | 36.9-42 | 47.4 |
| 1700 | (010) | 0.6-0.8 | 34-39.9 | 36.5 |
| | (110) | 0.3-0.5 | 23.9-31 | 36.2 |
| | (111) | 0.7-0.9 | 36.9-42 | 46.8 |
| 2000 | (010) | 0.5-0.7 | 31-36.9 | 37.8 |
| | (110) | 0.3-0.5 | 23.9-31 | 39 |
| | (111) | 0.6-0.8 | 34-39.9 | 49 |
| 3000 | (010) | 0.2-0.4 | 19.5-27.7 | 40.1 |
| | (110) | 0.1-0.3 | 13.7-23.9 | 41.3 |
| | (111) | 0.5-0.7 | 31-36.9 | 50.3 |

### 5.4. Occurrence of cleavage

It has been reported that during nanometric cutting of 3C-SiC on the (111) crystal plane at room temperature, cleavage occurs ahead of the cutting tool [124]. Indeed, it is generalized that cleavage is a dominant mechanism on the (111) crystal plane, and the (111) crystal plane is the most commonly observed fracture plane of 3C-SiC. In order to realize whether cleavage takes place during nanometric cutting at elevated

temperatures, the chip formation process was carefully examined and the local environment of atoms up to the second neighbour shell was monitored. Figure 5.4 illustrates the chip formation at three stages together with the evolution of cutting forces while cutting the (111) crystal surface at 1400 K. Crystallites of 3C-SiC in the cutting chip can be observed, suggesting the occurrence of cleavage at high temperature of 1400 K. In fact, the cleavage was observed to occur for all the simulated temperatures, 300 K-3000 K, while cutting the (111) surface, which have not been shown here for the purpose of brevity. However, at high temperature of 3000 K, smaller amount of crystallites were observed in the chip in comparison to those at lower temperatures, plausibly due to improved plasticity at this temperature. The substantial dominance of the (111) cleavage plane can be attributed to the lower cleavage energy and fracture surface energy of this plane as opposed to the other crystal planes. This specific characteristic of 3C-SiC is comparable with that of diamond [125]. As evident from Figure 5.4b, cutting forces experience an abrupt drop at the points where cleavage occurs, resultant from flaking off the crystallite of 3C-SiC without undergoing amorphization. Thus, as the cutting tool does not carry out any work on a portion of atoms, the cutting force drops [124].

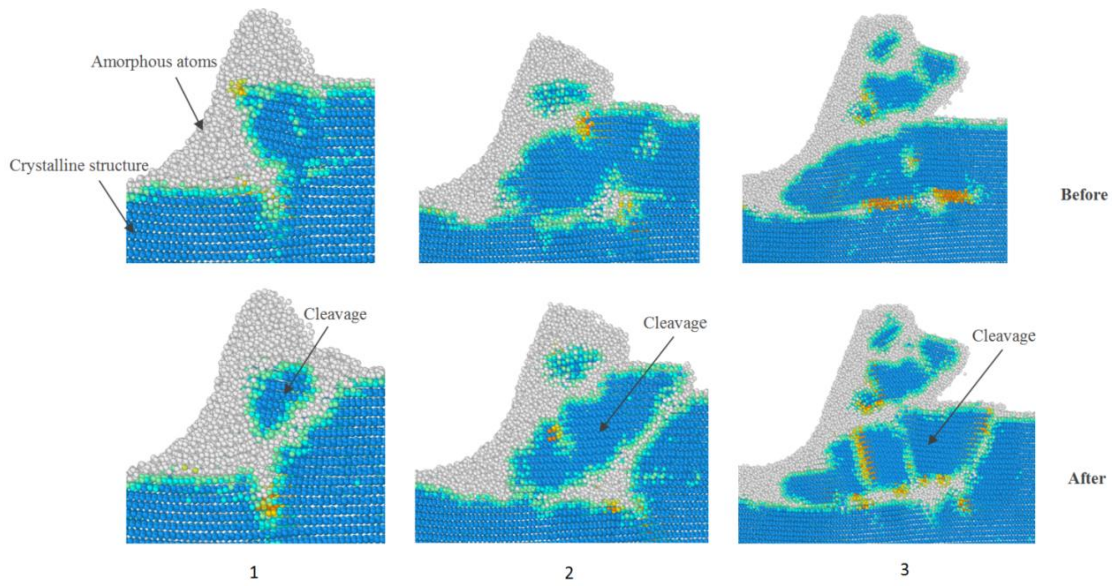


(a)

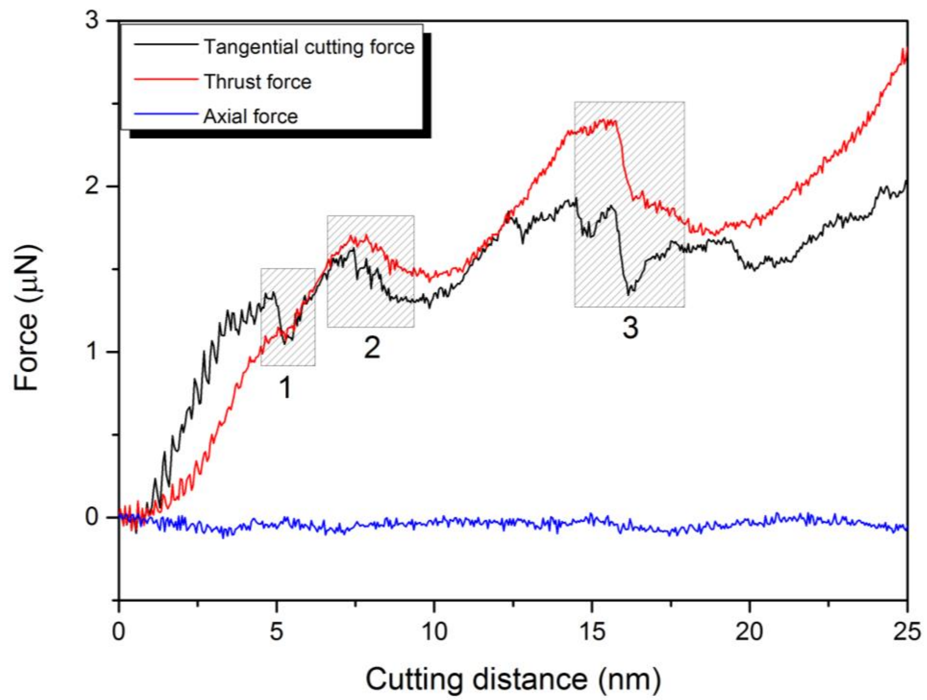


(b)

Figure 5.4: a) Snapshots from the MD simulation while cutting the (111) crystal plane at 1400 K demonstrating the occurrence of cleavage at three stages and b) the corresponding drops of cutting forces

While cleavage is anticipated to be dominant on the (111) plane, a shift to the (110) cleavage at the cutting temperatures higher than 2000 K was seen during nanometric cutting processes, as shown in Figure 5.5. It will be demonstrated in section 5.9 that the event of cleavage occurs alongside with the formation and annihilation of stacking fault-couple, locks and cross-junctions between pairs of counter stacking faults. Such (110) cleavage event is in accord with the earlier observations on the diamond under blunt indentations at high temperature [126], where shear stresses and plastic flow are thought to dictate the failure and the stress fields are inhomogeneous. It should be mentioned here that the diamond shares the same cubic lattice structure in its $sp^3$ bonded state with 3C-SiC. Hence, similarities in the material behaviour under contact loading problems could be expected. Note that very small amount of remnants of cleavage was observed for some other cases, i.e. on the (010) and (110) at 300 K.

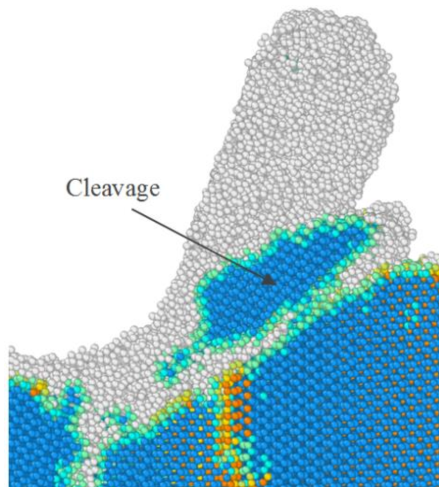


Figure 5.5: Snapshot from the MD simulation showing the event of cleavage while cutting the (110) crystal plane at 2000 K

### 5.5. Chip related phenomena

From Figure 5.6, it can be observed that the number of atoms in the cutting chip increases with the increase of workpiece temperature except for the (111) crystal plane at 3000 K. Moreover, the highest number of atoms in the chip appears on the (111) plane; however it decreases at 3000 K. As mentioned earlier, large volume of cleavage has occurred while cutting the (111) crystal plane thus it is sensible to observe higher number of atoms in the chip while cutting the (111) plane. Furthermore, as seen in Figure 5.7, the depth of subsurface deformation layer becomes deeper when the temperature of workpiece rises. As noted earlier, increase of the workpiece temperature will weaken interatomic bonding which triggers more crystal deformation within subsurface atoms. Thus, the layer depth of deformation becomes larger. This specific behaviour seemingly appears to be common in both single crystal 3C-SiC and silicon. Another light can be brought by Figure 5.7 is that the depth of subsurface deformation layer is the highest on the (111) plane whereas it is the lowest on the (110) plane. The occurrence of cleavage and pronounced ploughing due to compression as a result of the upper position of stagnation region on the (111) plane could play the key role in this observation.

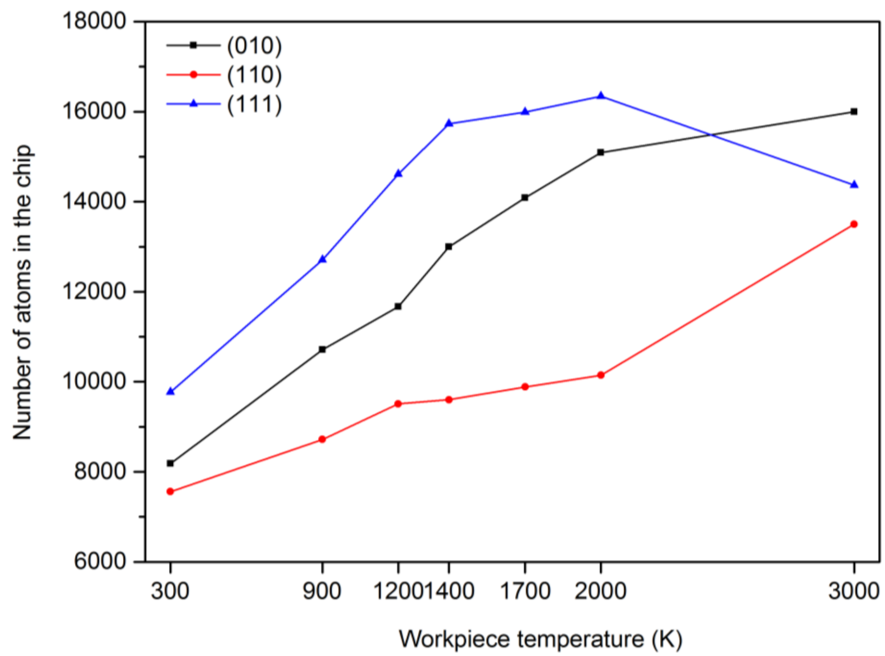


Figure 5.6: Number of atoms in the cutting chip as a function of cutting temperature and crystal plane during nanometric cutting of 3C-SiC

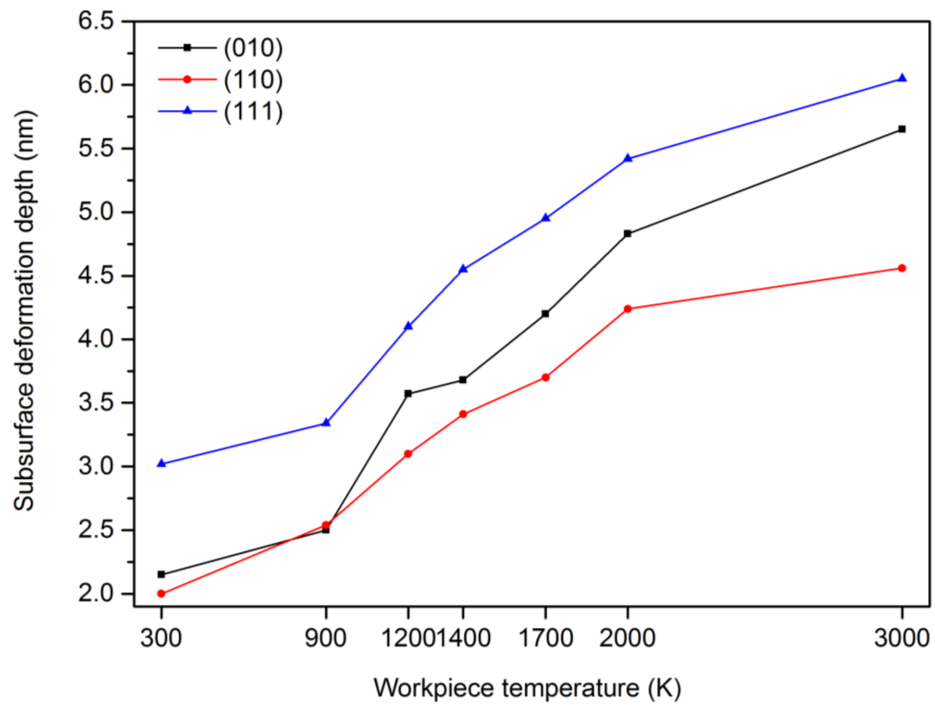


Figure 5.7: Subsurface deformation layer depth as a function of cutting temperature and crystal plane during nanometric cutting of 3C-SiC

Figure 5.8 shows the variation of resultant force exerted by the tool rake face on the chip, and friction coefficient at the tool rake face/chip interface while cutting 3C-SiC on different crystallographic planes at various temperatures. Clearly, the values of resultant force exerted by the tool rake face on the chip are found to be smallest while cutting 3C-SiC on the (111) crystal plane whereas they are largest on the (110) plane, which is consistent with the previous observations in this study. The friction coefficient at the tool rake face/chip interface varies from 0.42 to 0.9 on different crystal planes and at different temperatures. It may be noted that the friction coefficient reaches minimum for the (111) plane. A remarkable observation is that the friction coefficient at the tool rake face/chip interface on the (110) and (010) planes increases in the temperature range of 300 K to 1200 K and 300 K to 900 K, respectively, as opposed to the (111) crystal plane, where the friction coefficient constantly decreases with the increase of workpiece temperature.

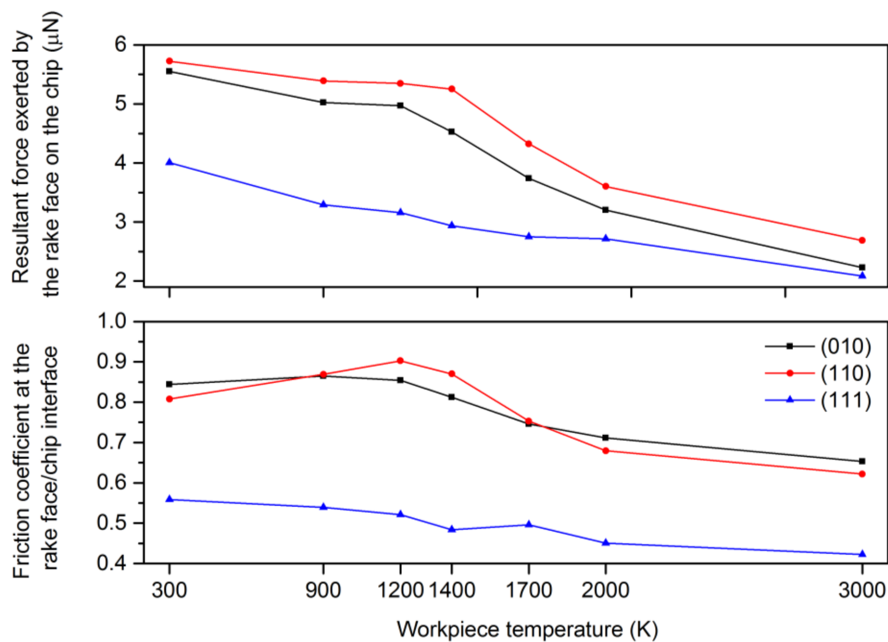


Figure 5.8: Variations of the resultant force exerted by the tool rake face on the chip, and friction coefficient at the tool rake face/chip interface while cutting 3C-SiC on different crystallographic planes at various temperatures

During nanometric cutting, heat is generated owing to the energy release as a result of the breaking and reformation of bonds in the primary deformation zone and owing to the friction at the interface of the cutting tool and the workpiece. The generated heat in the primary deformation zone is transferred into the chip thus the chip carries a great amount of heat during its separation from the workpiece. To investigate the heat generated during chip formation process and consequently the extent of temperature increase (due to the generated heat) from the initial substrate temperature, an elemental atomic volume ($1 \times 1.5 \times 3$ $nm^3$ including 442 atoms) was considered in the primary deformation zone and the variations of the temperature were monitored on this volume. It can be observed from Figure 5.9 that while cutting the (111) plane in the temperature range of 300 K to 1400 K, the extent of temperature increase caused by the generated heat in the deformation zone is much higher than those of other crystal surfaces, attributable to the release of elastic energy in the form of heat during occurrence of cleavage on this crystal plane. However, at 2000 K, the amount of release of heat is smaller than those at lower temperatures due to the weaker bonding between atoms. As stated above, the generated heat in the deformation region is dissipated into the chip thus it is not surprising to see the similar trend for the chip temperature, as depicted in Figure 5.10. It must be mentioned here that there may exist some inconsistencies in the observed trends in this study since a multifaceted interplay of various variables such as adhesive forces, interfacial energies, contact areas, number of dangling bonds, nanoscale friction etc. changes with the temperature and crystal plane during nanometric cutting at elevated temperatures.

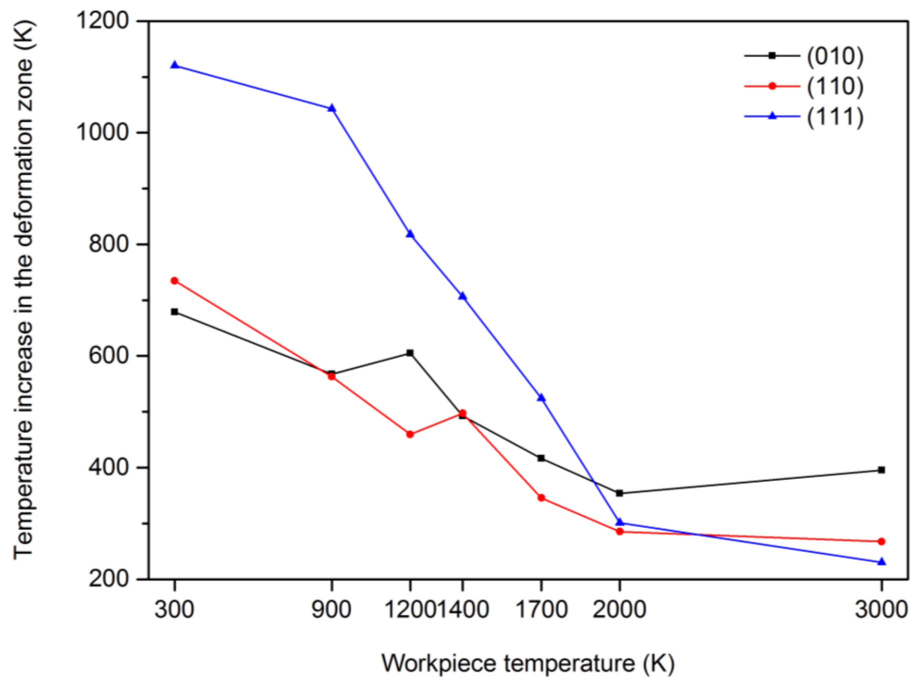


Figure 5.9: Extent of temperature increase in the primary deformation zone during chip formation

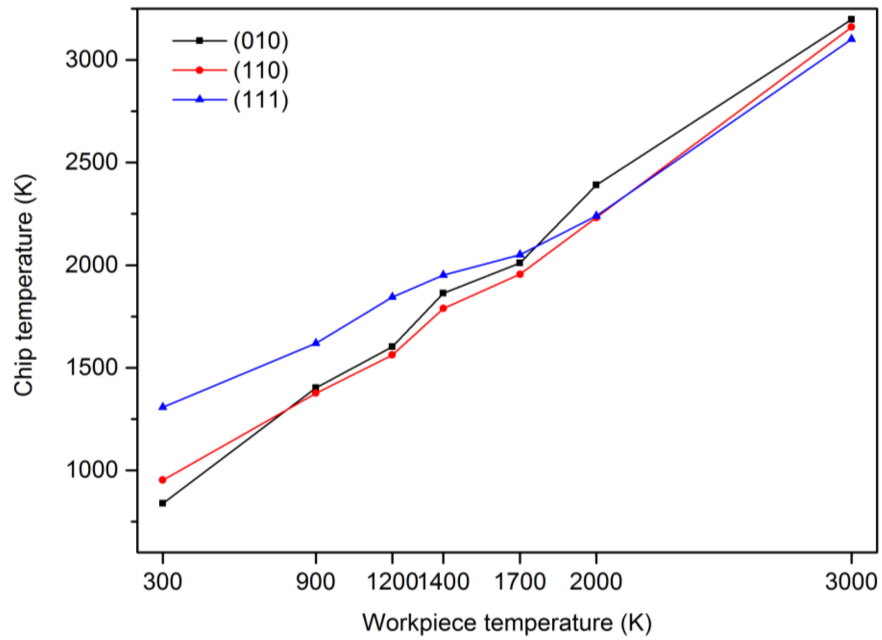


Figure 5.10: Chip temperature as a function of cutting temperature and crystal plane

## 5.6. Cutting forces and specific cutting energies

The magnitude of the average tangential cutting forces, thrust forces, resultant forces and specific cutting energies for all the studied temperatures and crystal planes has been summarized in Table J1 in Appendix J. The average values of the forces were calculated only after the tool penetrated in the workpiece by 15 to 25 nm. From Table J1 in Appendix J, it is conspicuous that the values of tangential, thrust and resultant forces decrease with the rise of workpiece temperature for various crystal surfaces. As mentioned in section 4.4, with the increase of temperature, the amplitude of atomic vibration within the workpiece increases. It is regarded as an increase in the number of phonons. This phenomenon results in generating atomic displacements. The atomic displacements within the workpiece cause a rise in the interatomic distances and a decrease in the restoring forces owing to thermal expansion, resulting in lowering the energy needed to break the atomic bonds. As a consequence, thermal softening occurs which reduces the cutting force required to deform the 3C-SiC workpiece at high temperatures.

Figure 5.11 shows that large specific cutting energy values correspond to low workpiece temperatures since the 3C-SiC workpiece at a low temperature is more difficult to be deformed. It can be also observed that the (111) crystal plane requires least specific cutting energy while the highest magnitudes emerge on the (110) plane. Hence, it can be deduced that the (111)<$\bar{1}$10> crystal setup is the easy orientation setup for cutting 3C-SiC. This particular behaviour of 3C-SiC is similar to that of silicon. Table 5.2 highlights the percentage reduction in the specific cutting energy during hot nanometric cutting with respect to cutting at 300 K on varoious crystal surfaces. It is observed that, for instance, the sepecific cutting energy reduces by 33%

while cutting the (111) crystal plane at 2000 K. Also, it can be inferred that at high temperatures, i.e. 2000 K and 3000 K, the minimum reduction in specific cutting energy appears on the (111) plane whereas at lower temperatures the maximum reduction emergies on this plane. Figure 5.12 illustrates the variation of crystallography-induced anisotropy in the specific cutting energy as a function of workpiece temperature. It can be seen that the anisotropy increases from ~30% at 300 K to ~44% at 1400 K and afterwards it decreases to ~37%, ~24% and ~22% at 1700 K, 2000 K and 3000 K, respectively. This trend is contrary to the anistropy in specific cutting energy of silicon, where it constantly increased with the increase of cutting temperature. This different trend can be attributed to the presence of carbon atoms in 3C-SiC zinc blende lattice, which have very high melting temperature.

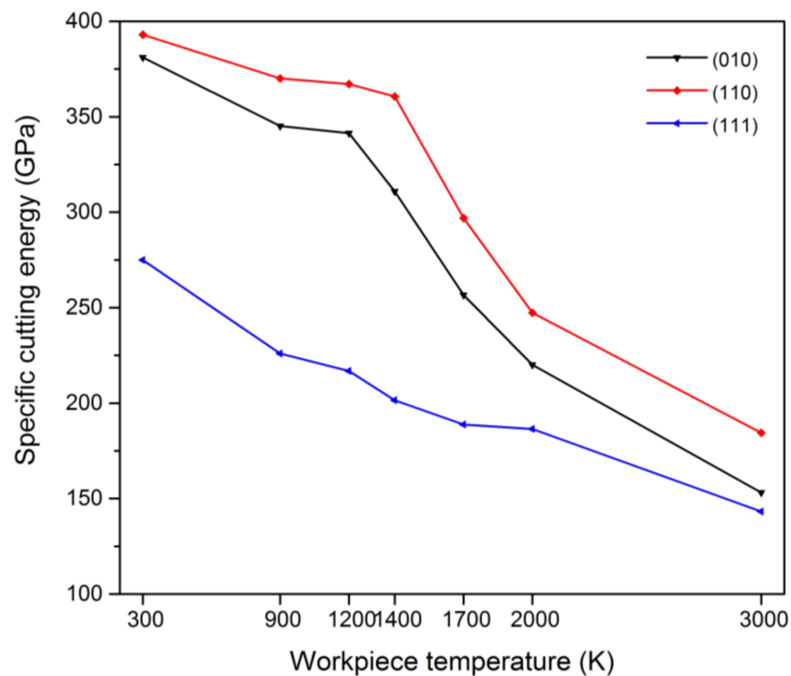


Figure 5.11: Specific cutting energy as a function of temperature and crystal plane

Table 5.2: Percentage reduction in specific cutting energy of 3C-SiC at high temperatures relative to room temperature

| Crystal plane | % reduction in cutting energy at 1400 K compared to 300 K | % reduction in cutting energy at 2000 K compared to 300 K | % reduction in cutting energy at 3000 K compared to 300 K |
|---|---|---|---|
| (010) | Up to 19% | Up to 43% | Up to 60% |
| (110) | Up to 9% | Up to 38% | Up to 54% |
| (111) | Up to 27% | Up to 33% | Up to 48% |

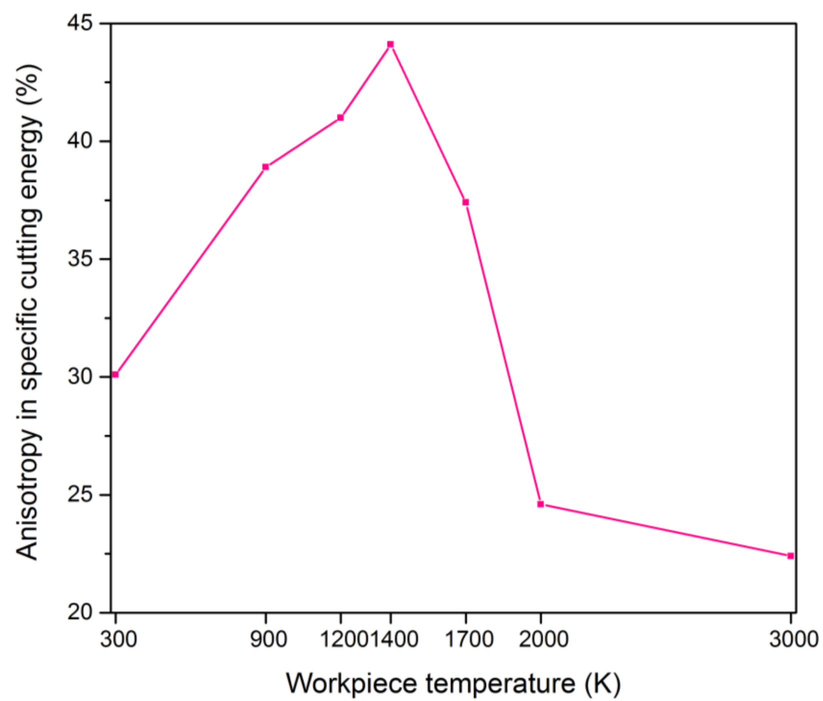


Figure 5.12: Variation of anisotropy in specific cutting energy as a function of temperature

## 5.7. Yielding stresses

Material dependent yielding criteria such as von Mises stress, Principal stress and Tresca stress measures were employed to predict yielding of 3C-SiC under various circumstances in this study. In order to compute the atomic stress tensor, an elemental atomic volume ($1\times1.5\times3$ nm$^3$ including 442 atoms) was considered in the cutting region and accordingly the physical stress tensor was obtained. Equations shown in Appendix F were adopted to calculate the aforementioned yielding measures. Table K1 in Appendix K summarizes the magnitude of all the stresses obtained from the simulation data in all the test cases at varying temperatures. Figure 5.13 compares the peak von Mises stresses obtained from the ABOP potential function at different cutting temperatures and crystal planes while cutting 3C-SiC. The von Mises stress is a very commonly used yield criterion to estimate the yielding of a material and is based on the assumption that the maximum deviatoric strain energy causes yielding in the material. It is apparent from Figure 5.13 that the peak von Mises stress triggering flow during nanometric cutting of 3C-SiC decreases with the increase of substrate temperature. It is interesting to note that the largest values of the required von Mises stress to cause yielding appears on the (110) crystal plane whereas the smallest values are observed on the (111) surface. Furthermore, at temperatures higher than 1400 K, the peak von Mises stress on the (010) and (110) shows almost the same magnitudes. It is noteworthy that the maximum reduction in yielding von Mises stress at 3000 K with respect to the room temperature cutting takes place on the (110) plane, which is up to 49%, followed by the (010) and (111) crystal planes, 40% and 37%, respectively.

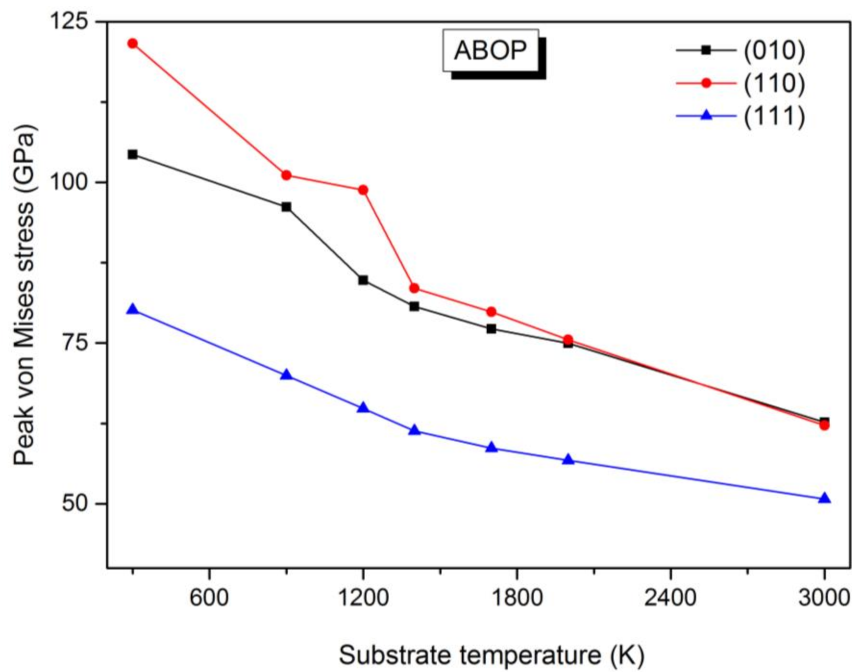


Figure 5.13: Variation of peak von Mises stress in the cutting region while cutting 3C-SiC on different crystal planes and at different temperatures obtained by ABOP potential function

Nanometric cutting is recognized as a shear dominated process which generates heat in the cutting region owing to breaking and reformation of bonds, leading to an increase of the temperature locally in the cutting region. In order to appreciate the effect of the stress and temperature on the behaviour of the substrate, evolution of average local temperature and von Mises stress in the cutting region is plotted in Figure 5.14. Almost similar trend was observed for the other crystal planes and cutting temperatures, and hence not repeated. It can be deduced from Figure 5.14 that the peak temperature and peak stress required to cause yielding in the cutting region do not take place simultaneously. This difference exists because the maximum temperature signifies complete fracture of the bonds which may not be the necessary condition for the material to flow (peak temperature at peak stress). It can be postulated that the observed trend is similar to that of silicon (see section 4.7). Table

K1 in Appendix K provides a complete list of the peak temperatures and temperatures at the onset of yielding in the cutting zone for all the simulated cases.

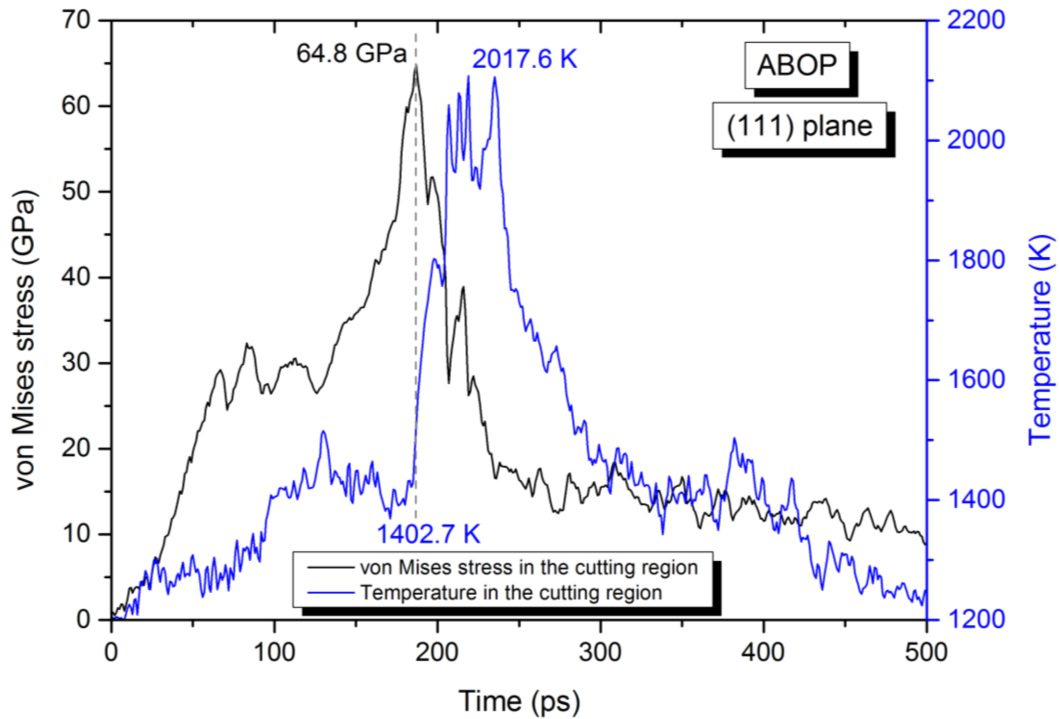


Figure 5.14: Evolution of the temperature and von Mises stress in the cutting region recorded on the same plot while cutting 3C-SiC on the (111) crystal plane at 1200 K

### 5.8. Stress, temperature and wear of the cutting edge of the tool

Figure 5.15 and Figure 5.16 demonstrate the variation of average von Mises stress and temperature measured on the cutting edge of the diamond cutting tool during nanometric cutting different orientations of single crystal 3C-SiC at various temperatures. Table L1 in Appendix L lists the average magnitude of von Mises stress measure, Tresca stress measure and temperature on the cutting edge in all the simulated test cases.

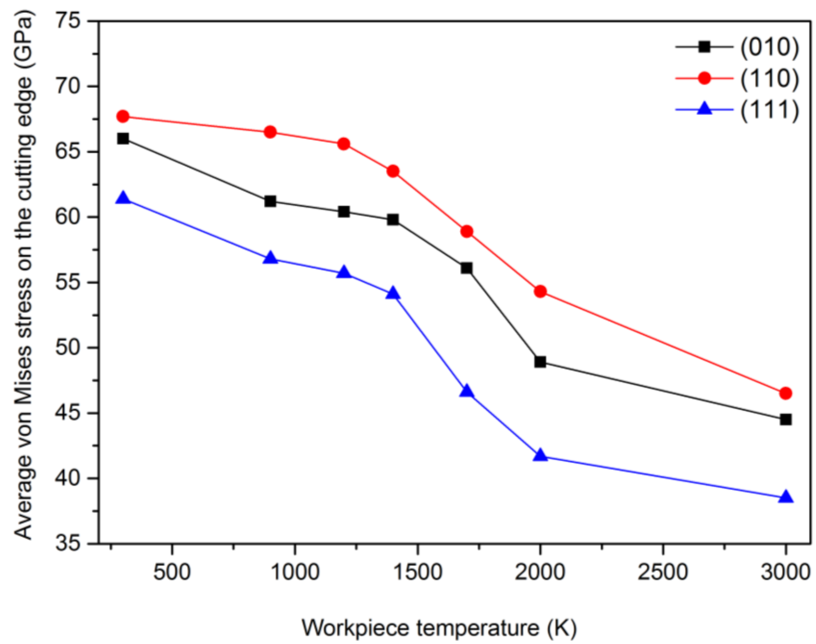


Figure 5.15: Variation of the von Mises stress measured on the cutting edge of the diamond tool while machining different orientations of 3C-SiC at different cutting temperatures

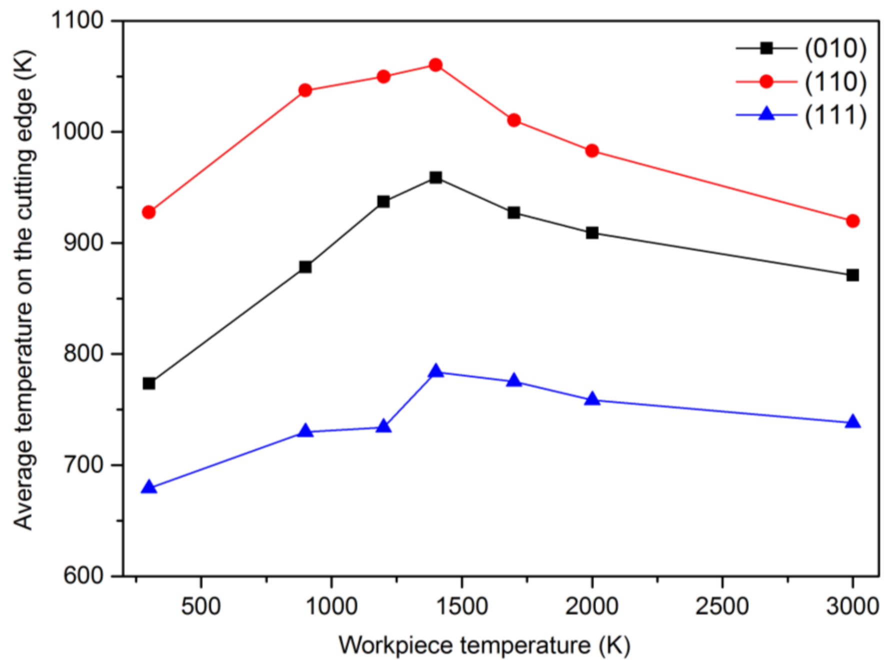


Figure 5.16: Variation of temperature measured on the cutting edge of the diamond tool while machining different orientations of 3C-SiC at different cutting temperatures

Similar to what was observed for silicon in section 4.8, the cutting tool experiences least stress and temperature on the (111) crystal plane compared to other planes, which makes it an easy cutting plane, consistent with the observed trend in peak von Mises stress to cause yielding of 3C-SiC during nanometric cutting (see section 5.7) Besides, the values of stresses on the cutting edge decrease with the increase of workpiece temperature for the different crystallographic planes. The magnitudes of Mises stress and Tresca stress acting on the cutting edge of the tool at low and high temperatures are found to be in the range of 38 to 68 GPa and 21 to 38 GPa, respectively. Clearly, the stress values are lower than 95 GPa [106], which is the minimum stress needed to cause structural instability in the diamond structure. However, as can be seen in Figure 5.16, the average temperature on the cutting edge spans from 680 K to 1060 K for the different workpiece temperatures and crystal planes. A representative illustration of the temperature distribution on atoms while cutting the (110) crystal plane at 3000 K is given in Figure 5.17. The maximum temperature on the diamond tool is observed on the atoms near the cutting edge. Note that the transient temperature at some atoms on the cutting edge might reach 3000 K but due to high heat conductivity of diamond and usage of thermostatic atoms (to ascertain plausible outward heat conduction away from the machined zone which is carried away by cutting chips and lubricants during actual machining), the average temperature on the cutting edge is in the range of 680 K to 1060 K.

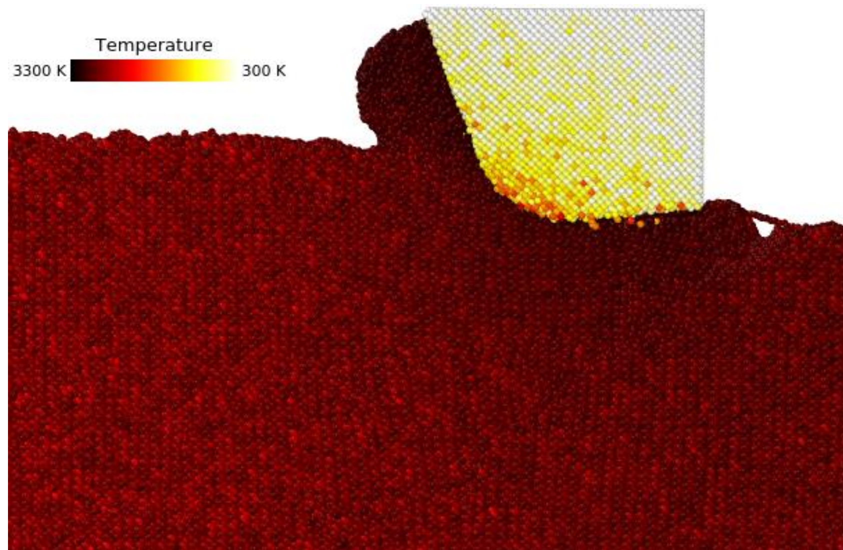


Figure 5.17: Temperature distribution on atoms while cutting the (110) crystal plane at 3000 K

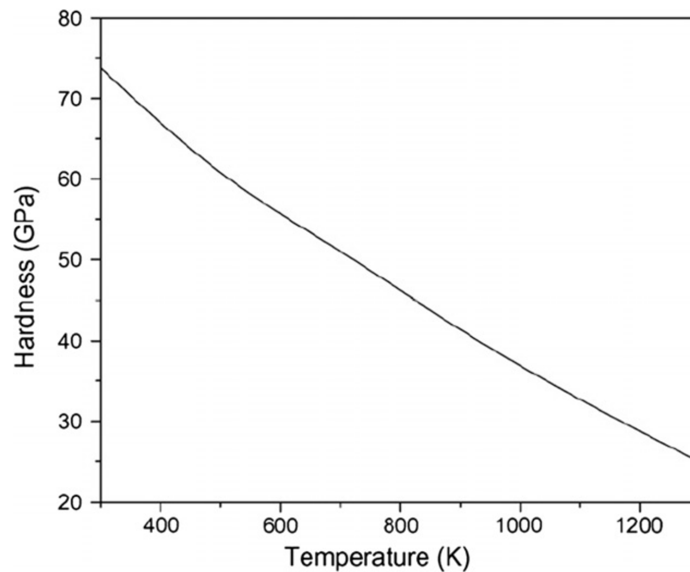


Figure 5.18: The hardness of diamond as a function of temperature [127]

As cited by Cai *et al.* [127], high temperature adversely influences the hardness of diamond i.e. the hardness of diamond drops with the rise of temperature, as illustrated in Figure 5.18. It can be observed that the hardness of diamond decreases to ~52 GPa and ~33 GPa, respectively, at temperatures of 680 K and 1060 K. On the other hand, at these temperatures i.e. 680 K and 1060 K, the von Mises stress acting

on the cutting edge is found to be 61.4 GPa while cutting the (010) surface and 63.5 GPa while cutting the (110) plane, respectively. Accordingly, it is not surprising to witness plastic deformation of cutting tool and tool wear via atom-by-atom attrition during nanometric cutting of 3C-SiC at different temperatures, as demonstrated in Figure 5.19. It is of note that abrasive action between atoms of diamond cutting tool and 3C-SiC workpiece results in increasing the temperature on the cutting edge, up to the workpiece temperature of 1400 K. However, at higher temperatures, due to enhanced thermal softening and decrease of the hardness of workpiece, abrasive action would be mitigated; hence a slight decrease in the temperature on the cutting edge is visible in Figure 5.16. Consequently, it can be seen from Figure 5.19b that at a workpiece temperature of 2000 K, the atom-by-atom attrition wear is quantitatively less severe than that of 1400 K, which correlates highly with the amount of stresses on the cutting edge at these temperatures, as depicted in Figure 5.15. Moreover, the shape of the cutting tool is found to be somewhat deformed while cutting at 1400 K in comparison with that of 2000 K. These observations confirm that while cutting at high temperatures, the atom-by-atom attrition wear and slight distortion of the diamond cutting tool could be alleviated. However, chemical wear i.e. dissolution-diffusion and adhesion wear may be accelerated at high temperatures.

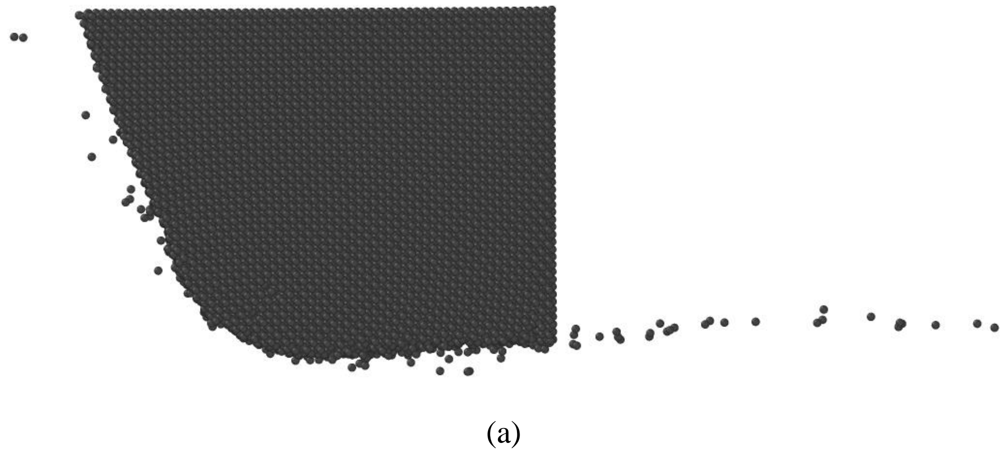

(a)

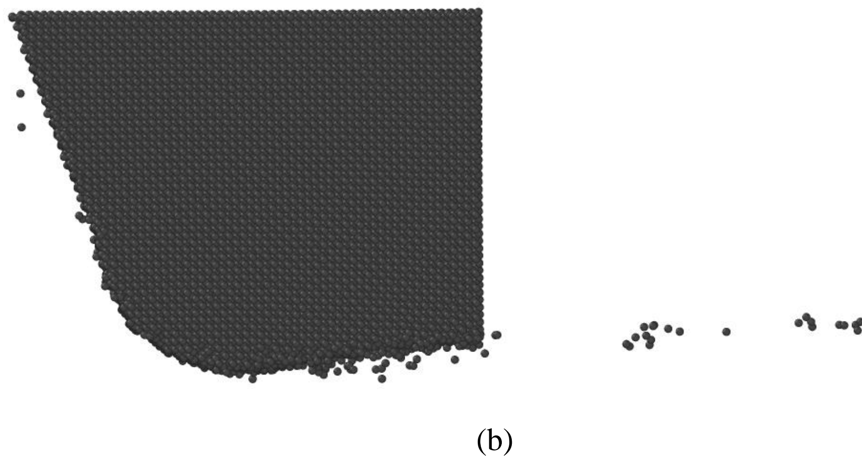

(b)

Figure 5.19: Atom-by-atom attrition wear and slight distortion of diamond cutting tool while nanometric cutting of 3C-SiC at a) 1400 K b) 2000K

## 5.9. Deformation mechanisms

### 5.9.1. Analysis of crystal defects

Single crystal 3C-SiC is regarded as a FCC crystal in the Bravais lattice group, which simply results in multiple-slips on the four equivalent {111} planes. The preferred slip systems are closely correlated to the core structure of their mobile dislocations. Hence, dislocations have to glide in these planes with a trivial lattice resistance, as estimated by P-N models [128, 129]. As a starting point, we analyse the crystal defect formation when cutting is performed on the (110) plane since this cutting

direction/plane is estimated to be more prone to defect formation according to our previous observations presented in section 4.9.2. Figure 5.20a and Figure 5.20b demonstrate the crystal defects at a cutting distance of 10 nm when nanometric cutting is implemented at 300 K. The perfect dislocation loop with $1/2 < 110 >$ Burgers vectors is seen to glide ahead of the tool tip. V-shaped perfect dislocation and partial half loop are also nucleated ahead of the tool, facilitating the plasticity of 3C-SiC. Such V-shaped dislocations were also seen by Mishra and Szlufarska [130] during sliding/cutting at a cutting depth of 3.5 nm. Additionally, it is generalized that the non-equilibrium intrinsic point defects such as vacancies can be created during plastic deformation process [131], leading to the formation of the vacancy-originated stacking fault in the Si-C monolayer. So, the stacking fault observed in Figure 5.20b could be a consequence of formation of such point defects. These observations confirm that aside from formation of one-dimensional defects, two-dimensional defects, i.e. stacking faults, can be generated within the restricted volume of 3C-SiC substrate during nanometric cutting at room temperature. Stacking fault formation in 3C-SiC was also observed in multimillion-atom MD simulation of nanoindentation [132] and in thick 3C-SiC crystals grown by CF-PVT [133]. Note that the white atoms shown in Figure 5.20 represent the highly-disordered (amorphous) atoms, which have been obtained through monitoring the local environment of atoms up to the second neighbour shell [95]. In Figure 5.20, the chip and subsurface of substrate attain amorphous state, signifying order-disorder (amorphization) transition of 3C-SiC atoms. The results are in accord with the simulations of Goel *et al.* [124] which showed that atoms in the chip and subsurface of the substrate lose their pristine diamond cubic lattice. Indeed, the initial response of substrate was observed to be the

formation of amorphous atoms followed by the defect formation. In section 5.9.2, amorphization is discussed in detail. Of interest is that Mishra and Szlufarska [134] reported that dislocation activity can lead to amorphization near the surface of 3C-SiC during nanoindentation, and connected their observations to the amorphous chips observed in nanomachining experiments on 6H-SiC [135]. However, dislocation-induced amorphization near the surface was not observed in our nanometric cutting simulations.

It can be seen from Figure 5.20c that with the progress of cutting, the stacking faults are decomposed and Shockley partials with $1/6 < 112 >$ Burgers vectors are formed, gliding on the closely packed $\{111\}$ planes, which are the glide planes of a zinc blende crystal, accompanied by the perfect dislocations. Some dislocation interactions and junctions were also observed in both cases, viz. at 10 nm and 20 nm cutting distance. Similar to what was observed in section 4.9.2, the DXA analysis reveals some dislocations, which cannot be regarded as physical dislocations and they are merely artefacts since no continuous chain of core atoms along the dislocation line was observed in Figure 5.20.

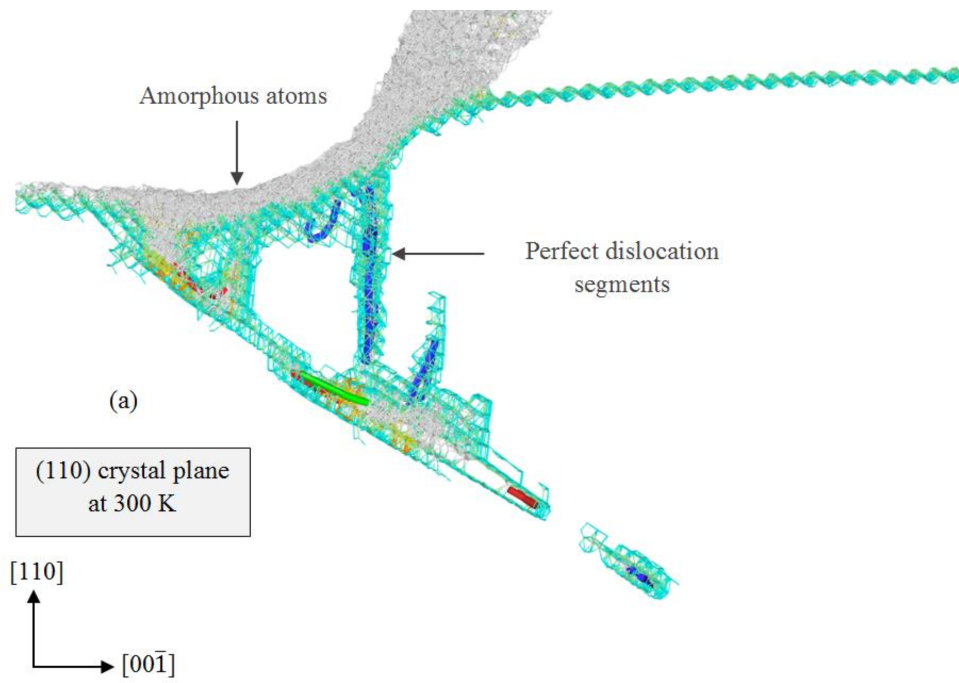
Amorphous atoms
Perfect dislocation segments
(a)
(110) crystal plane at 300 K
[110]
[00$\bar{1}$]

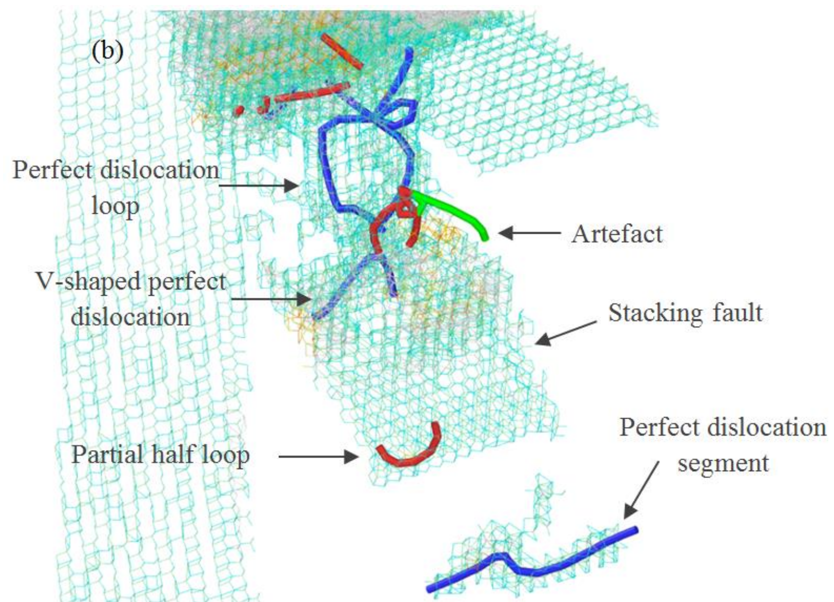
(b)
Perfect dislocation loop
Artefact
V-shaped perfect dislocation
Stacking fault
Perfect dislocation segment
Partial half loop

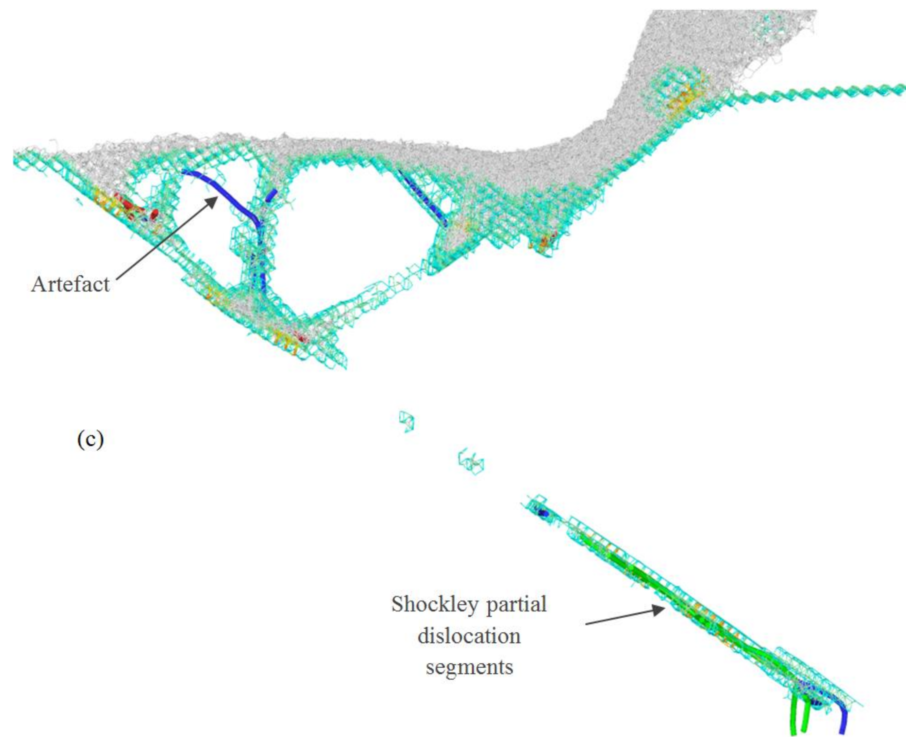


Figure 5.20: MD simulation output illustrating amorphous atoms (white atoms), dislocation nucleation and formation of stacking faults while cutting the (110) plane at 300 K at a cutting distance of a, b) 10 nm c) 20 nm. Blue, green and red rods, respectively, stand for the perfect, Shockley partial and other partial dislocations.

During deformation processes, it is anticipated that increase of the temperature leads to an increase in the energy available for thermal activation; hence the deformation rate enhances [136]. In general, the thermal fluctuations facilitate to overcome the energy barrier for dislocation nucleation. As seen in Figure 5.21a, more dislocations are nucleated when nanometric cutting is performed at 900 K. The total length of dislocations nucleated within the 3C-SiC substrate is ~2.5 times higher than that of 300 K. Shockley partial segments, loop and half loop are observed to nucleate. Furthermore, a stacking fault sandwiched between two Shockley partials is formed. Of interest is the nucleation of long perfect dislocations within the substrate. At 20 nm cutting distance, dislocations are further propagated within the substrate which

improves the crystal plasticity of 3C-SiC. Dislocation multijunction and dissociation of perfect dislocations into Shockley partials and stair-rod partials with $1/6 < 110 >$ Burgers vectors can be witnessed in Figure 5.21b. Interestingly, Frank-type sessile partials with $1/3 < 111 >$ Burgers vectors were observed to nucleate. It is informative to mention that the partial dislocations in 3C-SiC are assumed to be terminated by only one element, either Si-core or C-core. The Si-core dislocation nucleation is more energy-favourable whereas the C-core dislocation is more likely to nucleate under higher temperatures [137].

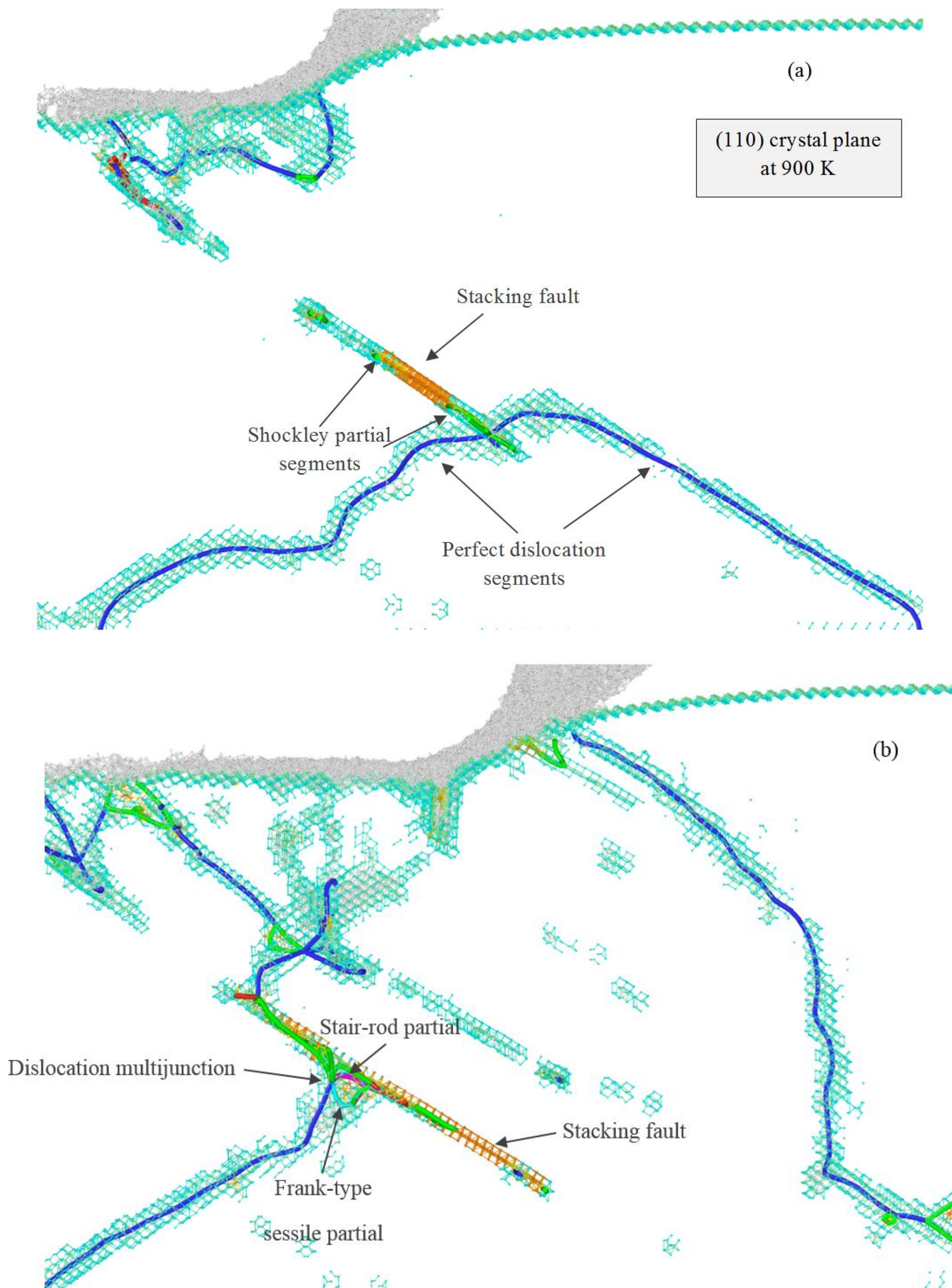


Figure 5.21: Formation of crystal defects while cutting the (110) plane at 900 K at a cutting distance of a) 10 nm b) 20 nm. Pink and aqua rods represent the stair-rod and Frank partial dislocations.

Figure 5.22a demonstrates that the defect formation mode at 1200 K is relatively similar to that of 900 K. However, longer perfect dislocation ahead of the tool and a stacking fault beneath the tool tip can be seen to form in this case. Thermal vibration of the atoms within the substrate rises due to the thermal excitation, leading to an increase in the probability of having atoms with higher energy state in the system. When the thermal energy is adequately high, there exists the possibility of having an atom jump out of the lattice, creating a point defect in the material. The generated point defect can lead to the formation of the vacancy-originated stacking fault. Hence, the stacking fault observed underneath the tool tip in Figure 5.22a could be a result of a point defect. Shockley partial loops and dislocation-originated stacking fault are also nucleated. Analogous to what was observed in Figure 5.20b and Figure 5.21b, dislocations are multiplied continuously while cutting process advances, as shown in Figure 5.22b. Frank-type sessile partials and stair-rod partial were also witnessed to nucleate in this case.

At 1400 K, perfect dislocation segments, stacking fault bounded between Shockley partial segments, Shockley partial loops between perfect dislocation segments and V-shaped partial segment are nucleated. A key observation at the cutting distance of 20 nm is the formation of a V-shape lock including Shockley, stair-rod and other partial segments, as depicted in Figure 5.23. Nevertheless, the configuration has positioned far behind the cutting tool; thus does not affect the crystal plasticity of 3C-SiC.

Figure 5.24 shows the defect formation mode at 1700 K. It can be observed that stacking faults bounded between Shockley partial segments and perfect dislocation segments are formed.

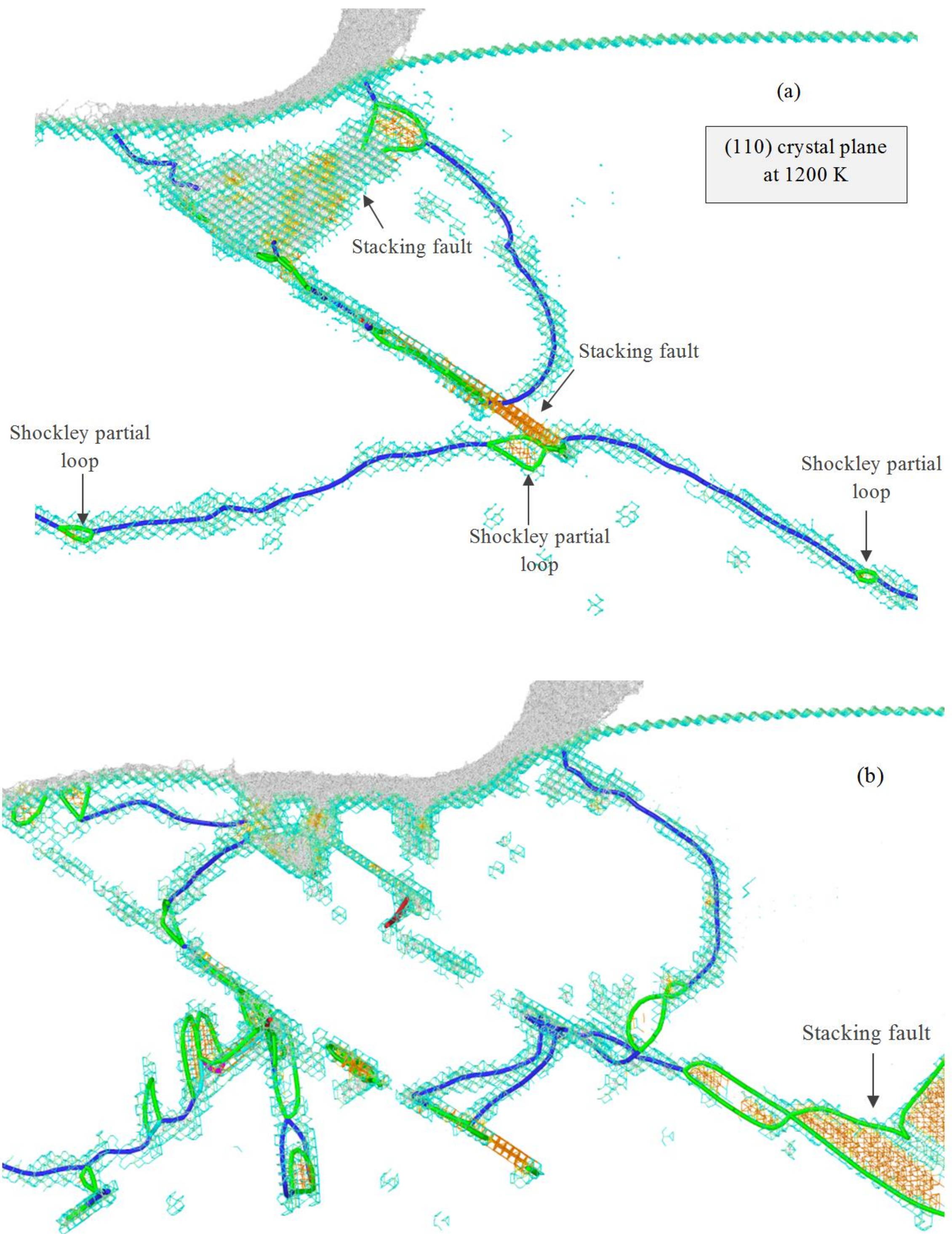


Figure 5.22: Formation of crystal defects while cutting the (110) plane at 1200 K at a cutting distance of a) 10 nm b) 20 nm. Pink and aqua rods represent the stair-rod and Frank partial dislocations.

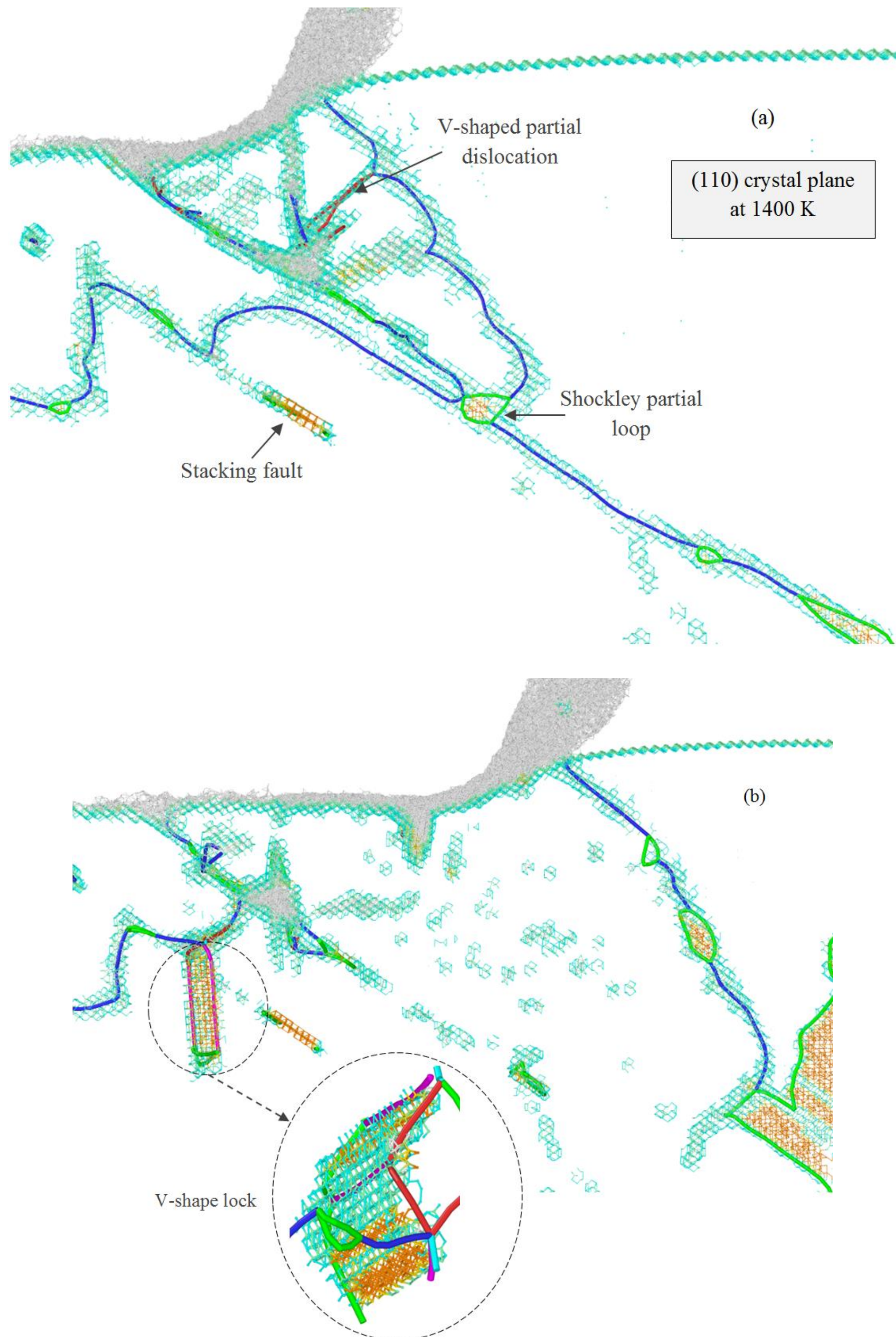


Figure 5.23: Formation of crystal defects while cutting the (110) plane at 1400 K at a cutting distance of a) 10 nm b) 20 nm. Stacking fault-couple and V-shape lock are formed. Pink and aqua rods represent the stair-rod and Frank partial dislocations.

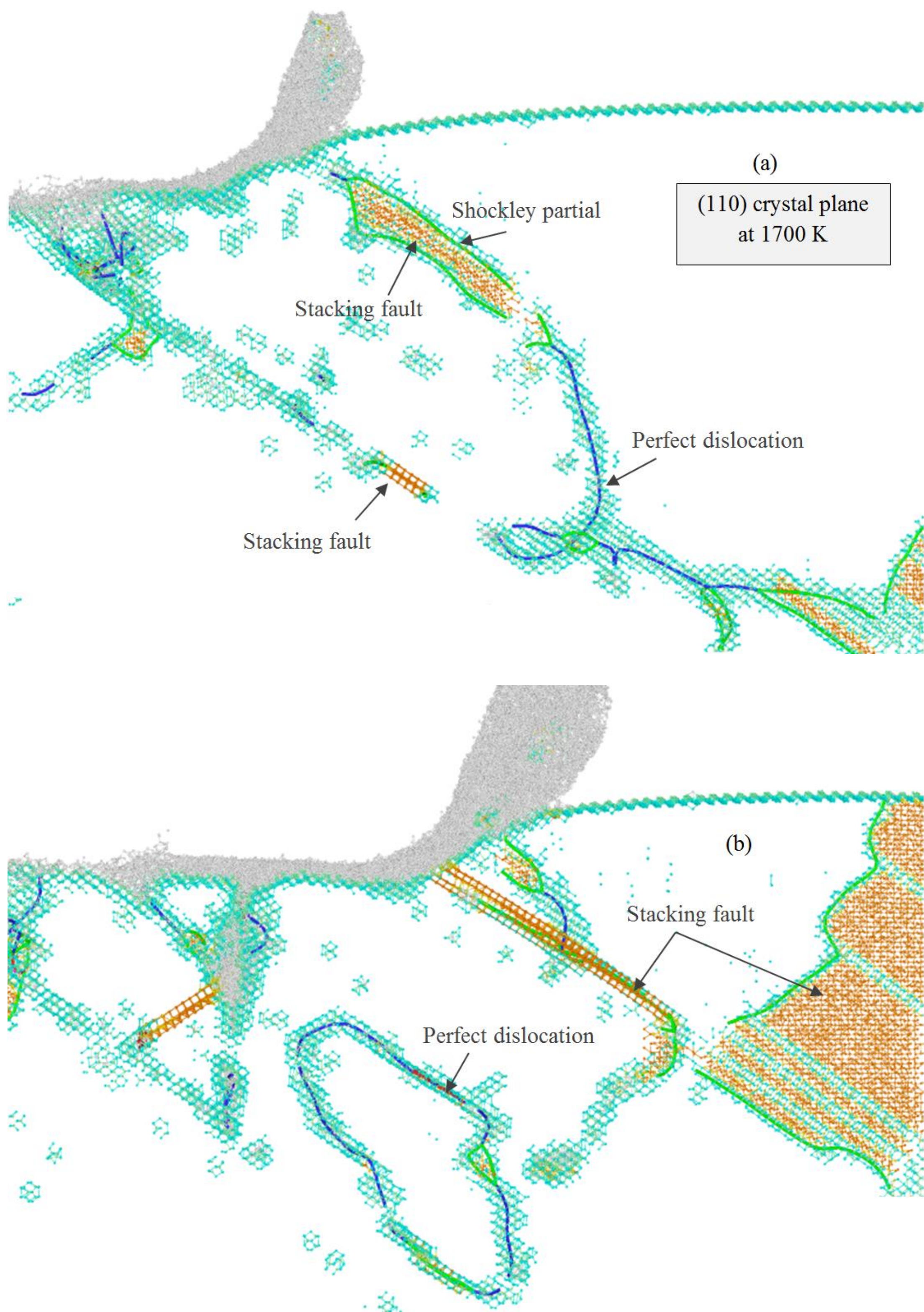


Figure 5.24: Formation of crystal defects while cutting the (110) plane at 1700 K at a cutting distance of a) 10 nm b) 20 nm.

Considering thermally activated defect formation, noticeable dislocation activities including perfect, Shockley, stair-rod, Frank-type sessile and other partials are observed when nanometric cutting of 3C-SiC is performed on the (110) plane at 2000 K, as illustrated in Figure 5.25. The total length of dislocations was found to be ~6.5 times higher than that of 300 K. It is of note that at higher temperatures, shorter segments of perfect dislocations and longer segments of partials are nucleated within the substrate, which can be regarded as a transition from perfect dislocation emission to partial nucleation. It is also observed that the size of stacking faults ahead of the tool become larger and the gradual growth of stacking faults on the glide plane is intensified at higher temperatures. The size of stacking fault is indeed influenced by the stable GSFE, i.e. lower the stable GSFE, wider the stacking fault [138]. Thus, since the stable GSFE decreases as the temperature increases [136], wider stacking faults are observed at elevated temperatures. It has been reported that the plastic deformation of 4H-SiC during compression loading at high temperatures is driven by Shockley partials that bound a ribbon of stacking fault in an experimental study [139]. Since Polytypism of SiC has been reported to have a trivial effect on the dislocation core energies and Peierls stress [6], the obtained results could be comparable with the aforementioned study.

Stacking fault-couple is also formed, which is bounded between Shockley and other partial segments. The bands of stacking faults form a configuration resembling steps on a stairway. These steps are barriers to further slip on the atomic planes involved, as well as in the adjacent planes. These arrangements, i.e. steps, could culminate in the consolidation of material [140], which is analogous to what has been observed for the low stacking fault energy metals [141]. Hence, it can be postulated that such

phenomena are likely to happen for low stacking fault energy materials including metals and semiconductors. Note that with further progress of the cutting tool, the configuration could become unlocked. Hence, it can be regarded as an unstable combination. In such condition, stacking faults could be decomposed by their counterparts owing to the disconnected slip planes and thus new stacking faults can be formed, as seen in Figure 5.25b. As a demonstration of the occurrence of locking/unlocking event, the evolution of cutting forces is plotted in Figure 5.26. This figure provides the overall mechanical response of 3C-SiC substrate during nanometric cutting at 2000 K. Abrupt drops in the cutting force can be observed at the highlighted regions, indicating the unlocking process. Upon careful examination, it was observed that the last unlocking was accompanied by the occurrence of cleavage, as discussed in section 5.4.

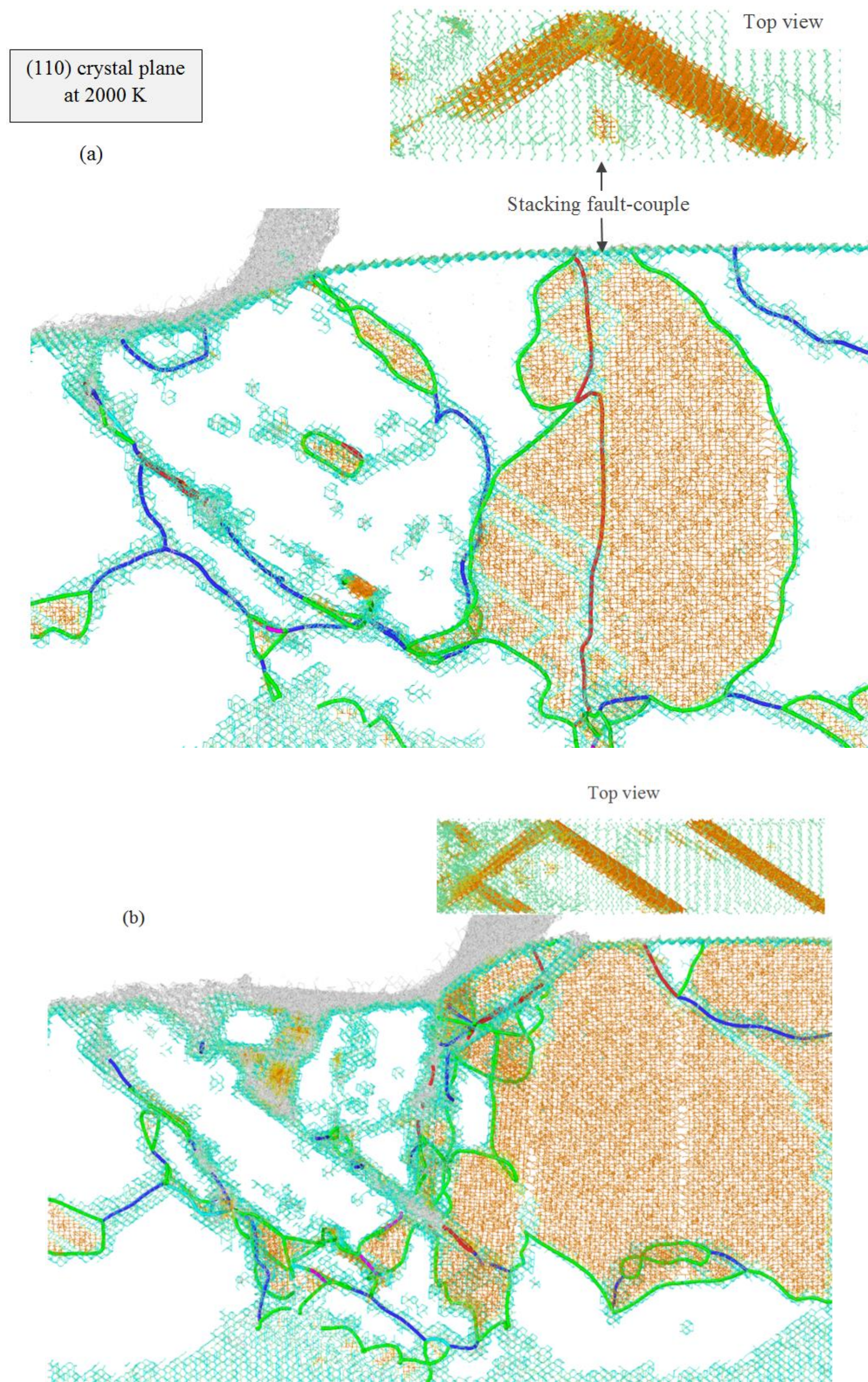


Figure 5.25: Formation of crystal defects while cutting the (110) plane at 2000 K at a cutting distance of a) 10 nm b) 20 nm. Large stacking fault-couple is visible in the figure.

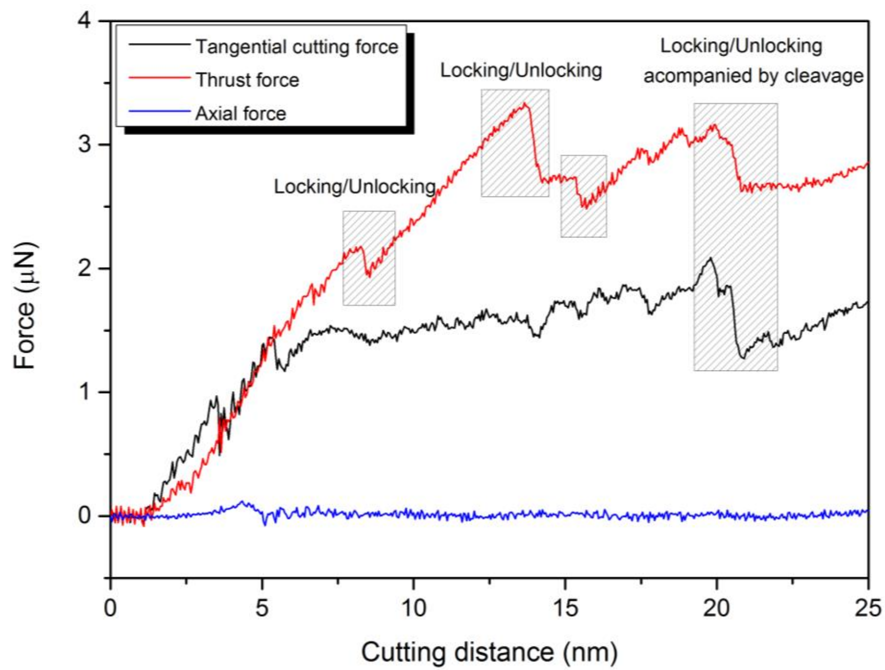


Figure 5.26: Evolution of the cutting forces illustrating the locking/unlocking while cutting the (110) plane at 2000 K

At 3000 K, numerous dislocations and large stacking faults are formed. The total length of dislocations nucleated within the 3C-SiC substrate was found to be ~10 times higher than that of 300 K. Intersections of dislocations are also seen, which could cause formation of vacancies, locks and dislocation loops. Successive lock structures, dislocation dendrites, are formed and broken (nucleation-interaction-unzipping cycles) with the progress of the cutting tool; thus, they do not block the plastic flow. Similar to the case of 2000 K, large stacking faults and steps were observed at the cutting distance of 10 nm, as shown in Figure 5.27a. It can be seen from Figure 5.27b that, at a cutting distance of 20 nm, partial dislocations, particularly Shockley partials, are nucleated ahead of the cutting tool. However, some perfect dislocations can be also observed. It can be inferred that there is no sharp transition between two regimes of dissociated and non-dissociated dislocations

over a large temperature range. This observation is consistent with the *ab initio* results [142]. It is interesting to see that cross-junctions between pairs of counter stacking faults meditated by the gliding of Shockley partials on different slip planes are formed. The intersection of counter pairs of stacking faults could possibly create forest dislocations. This fact can be attributed to the decrease of activation energy of dislocations with the temperature rise. Accordingly, the C-core dislocations turn into mobile leading to the expansion of Si-terminated stacking faults. Intersection of the counter pairs of stacking faults with each other, therefore, could result in the generation of forest dislocations. This phenomenon could impede propagation of successive mobile dislocations. Overall, It can be concluded that while cutting the (110) crystal plane at high temperatures, the plasticity of 3C-SiC is mediated by large stacking faults gliding ahead of the tool tip and continuous movement, multiplication, and entanglement of perfect and dissociated dislocations ahead, underneath and behind of the cutting tool.

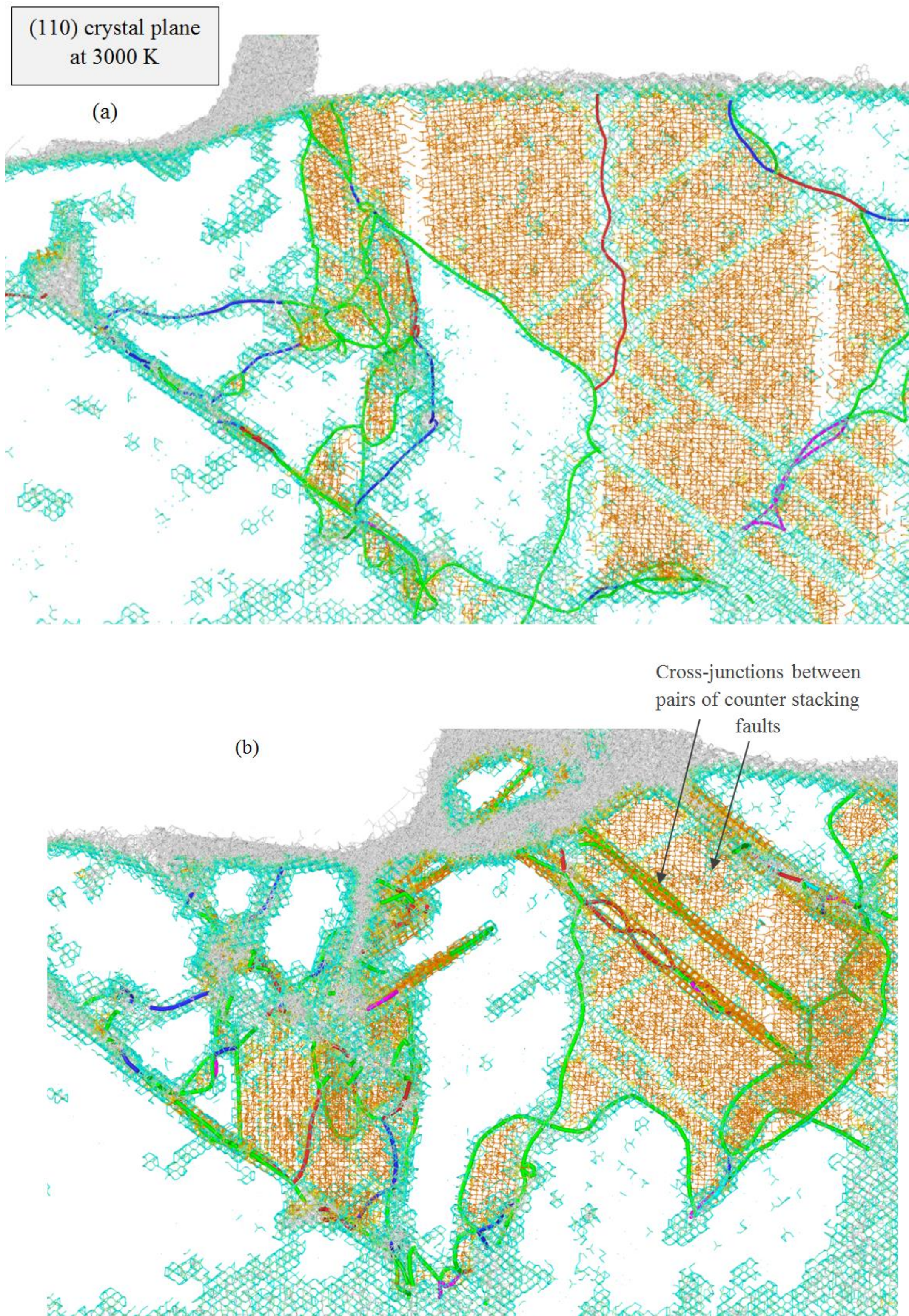


Figure 5.27: Formation of crystal defects while cutting the (110) plane at 3000 K at a cutting distance of a) 10 nm b) 20 nm

In the following session, the plasticity mechanisms of 3C-SiC while cutting the (010) and (111) crystal planes are briefly discussed. In general, lower dislocation activity and stacking fault formation than those of the (110) plane was observed for the aforementioned orientations. As seen in Figure 5.28a, while cutting the (010) surface at 300 k, two dislocation segments are nucleated beneath the cutting tool at the short cutting distance of 10 nm. Figure 5.28b shows that, at the cutting distance of 20 nm, some perfect dislocations are nucleated. However, similar to the aforementioned case, these dislocations are nucleated underneath and behind the cutting tool, which implies that they hardly assist the crystal plasticity of 3C-SiC during nanometric cutting. In general, only mobile dislocations ahead of the tool tip in the substrate are of importance in the case of one-pass nanometric cutting. In Figure 5.28b, some partial dislocations are visible, which have been attached to the surface. However, they are mere artefacts owing to the limitations of the DXA.

As shown in Figure 5.28c and Figure 5.28d, when the substrate temperature is raised to 3000 K, Shockley and stair-rod partials are nucleated accompanied by stacking faults. Furthermore, dissociation of perfect dislocations to partial ones, especially Shockley partials, at higher temperatures can be noticed. It is of note that at high temperatures, dislocations and stacking faults were mostly formed underneath the flank face and tool tip, and glided with the movement of tool. Hence, similar to the case of 300 K, they are less effective on enhancing plasticity than those located ahead of the cutting tool. Another point is that no Frank-type sessile partial dislocations were seen to nucleate for this cutting surface. It should be mentioned here that no considerable defect formation was observed for the other tested temperatures thus not reported here for the sake of brevity. Overall, it can be deduced

that the plasticity of 3C-SiC while cutting the (010) plane at room and high temperatures is marginally governed by the defect formation processes. On the other hand, amorphization and weak bonding between atoms at high temperatures play the key role in plastic flow of 3C-SiC when nanometric cutting is performed on the (010) crystal plane. It is interesting to note that the total length of dislocations nucleated within the 3C-SiC substrate at 3000 K in the (010) plane was found to be only ~3 times higher than that of 300 K.

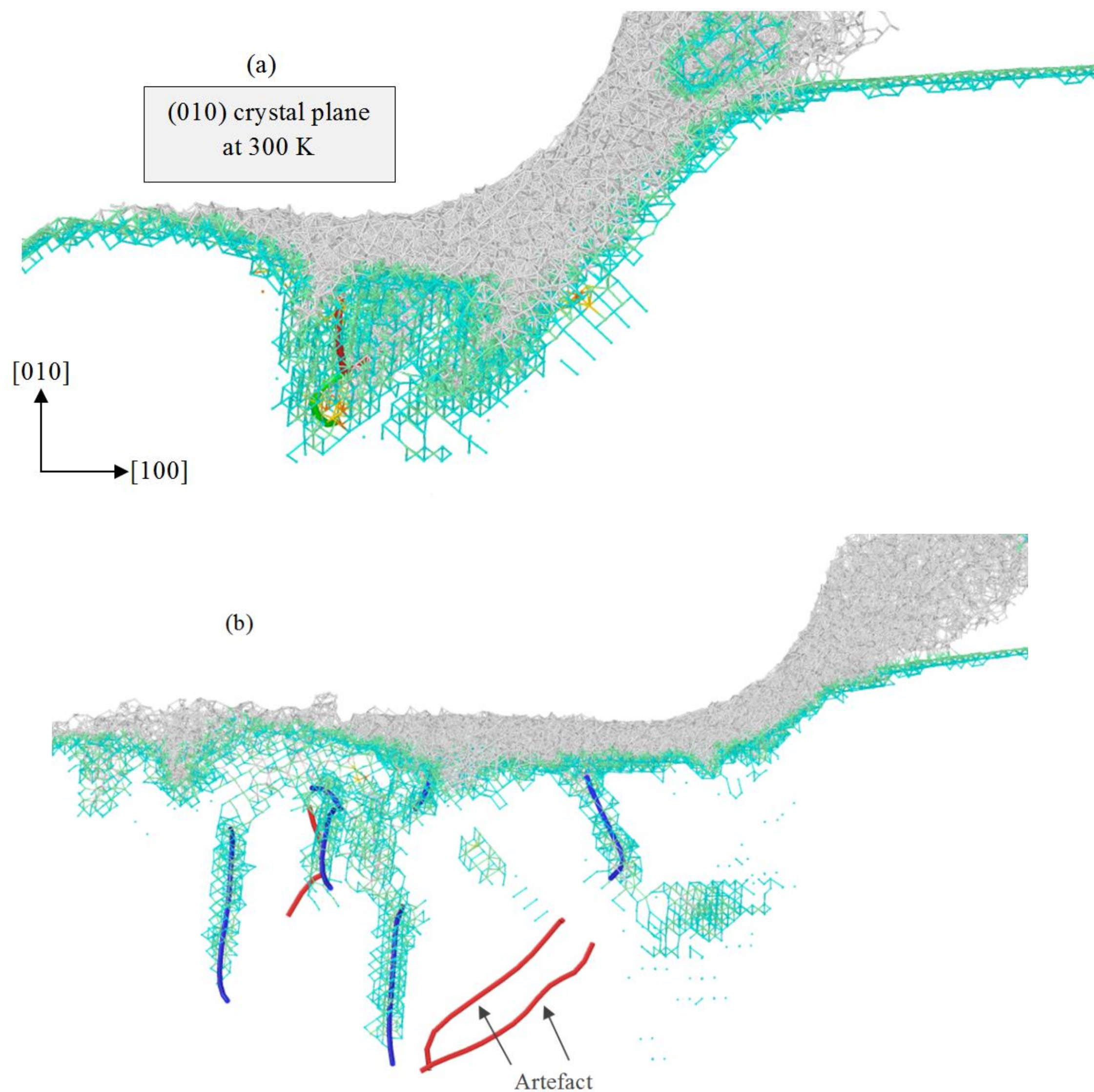

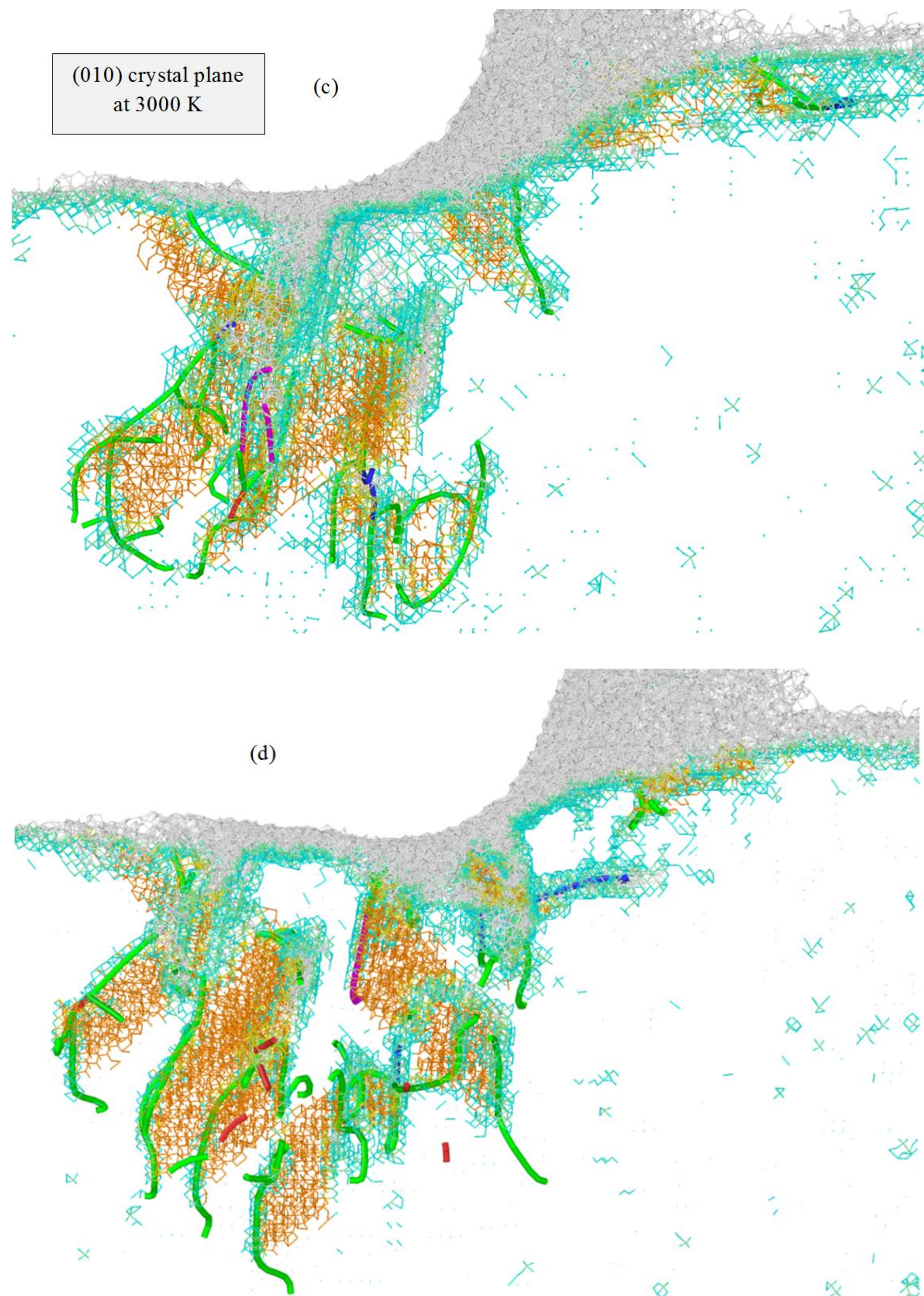


Figure 5.28: Formation of crystal defects while cutting the (010) plane at 300 K and at a cutting distance of a) 10 nm b) 20 nm, and at 3000 K at a cutting distance of c) 10 nm d) 20 nm

Defect formation processes while cutting 3C-SiC on the (111) plane are shown in Figure 5.29. In this case, defects are found to be positioned ahead of the tool tip rather than underneath the cutting tool. However, the dislocation activity while cutting the (111) surface is seen to be low at short cutting distances, i.e. 10 nm, as illustrated in Figure 5.29a, as opposed to the (110) crystal plane. With the progress of cutting, more dislocations are nucleated ahead of the tool, as demonstrated in Figure 5.29b. At higher temperatures i.e. 3000 K, dislocation nucleation and stacking fault formation were observed at short cutting distances. Formation of stacking fault-couple at high temperatures of 2000 K and 3000 K at the cutting distance of 20 nm was seen, as shown in Figure 5.29d. Also, Frank-type sessile partial dislocation was seen to nucleate as opposed to the (010) plane. The total length of dislocations nucleated within the 3C-SiC substrate at 3000 K was found to be ~4 times higher than that of 300 K.

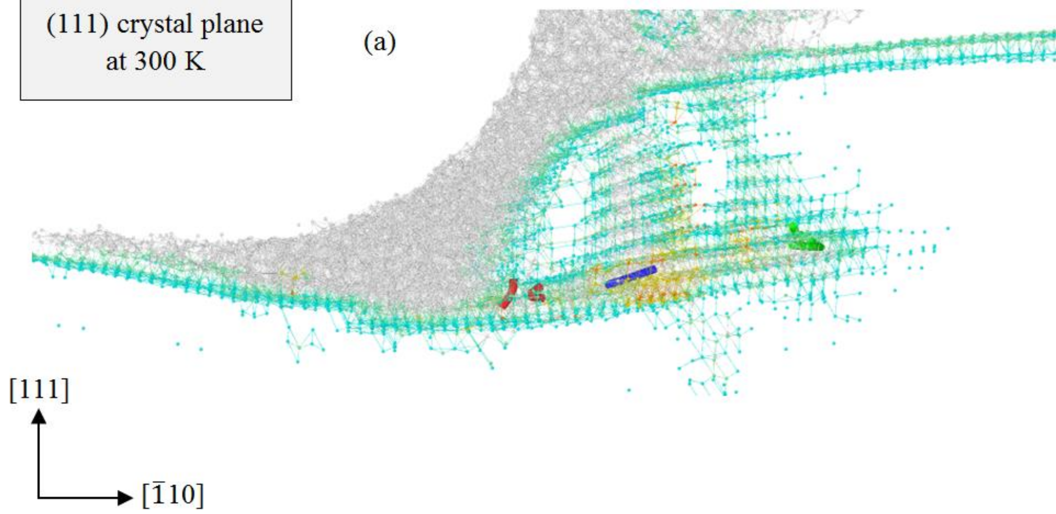
(111) crystal plane
at 300 K
(a)
[111]
[$\bar{1}$10]

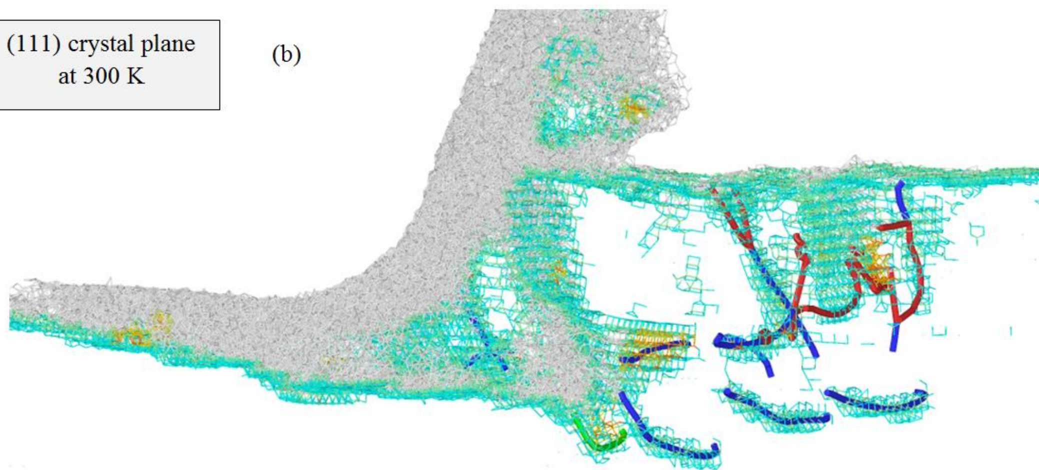
(111) crystal plane
at 300 K
(b)

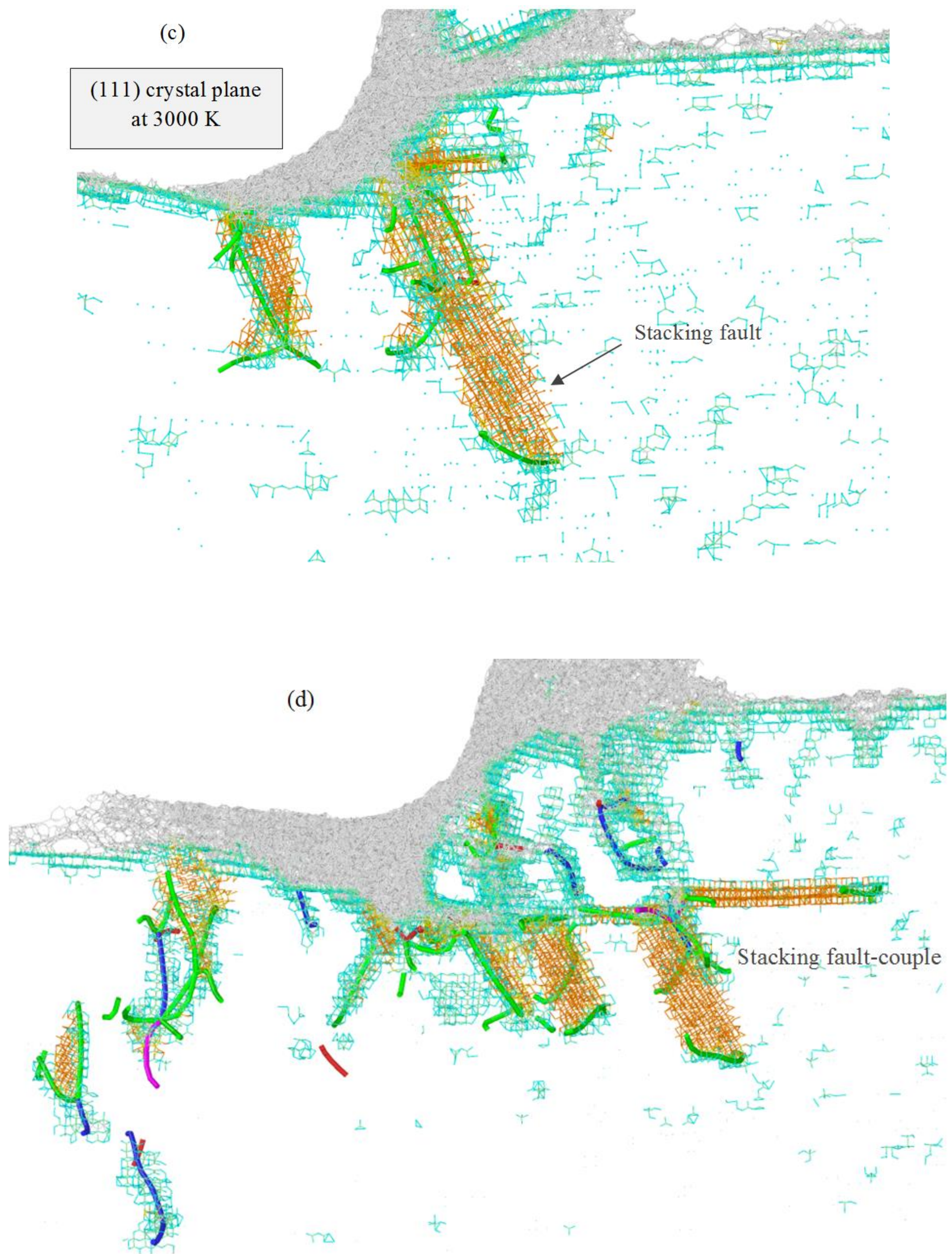


Figure 5.29: Formation of crystal defects while cutting the (111) plane at 300 K and at a cutting distance of a) 10 nm b) 20 nm, and at 3000 K at a cutting distance of c) 10 nm d) 20 nm

All in all, it can be concluded that a large number of defects is formed while cutting 3C-SiC on the (110)<00$\bar{1}$>; hence dislocation nucleation and stacking fault formation are the primary deformation response for this crystal setup. However, at room and high temperatures, amorphization also assists the plasticity of 3C-SiC. Overall, the initial response of substrate in all the studied cases was the formation of disordered (amorphous) atoms thus it can be generalized that the incipient plasticity of 3C-SiC in nanometric cutting occurs by solid-state amorphization. In addition, at high temperatures, the amplitude of atomic vibration of the substrate atoms increases, which is regarded as an increase in the number of phonons. This phenomenon results in generating atomic displacements. The atomic displacements within the substrate cause an increase in the interatomic distances and a decrease in the restoring forces due to thermal expansion, which lowers the energy required to break the atomic bonds. As a consequence, deformation of 3C-SiC at high temperatures is facilitated. When nanometric cutting is performed on the (010)<100> orientation setup at room and high temperatures, the plasticity of 3C-SiC is marginally governed by the defect formation processes. Thus, the plasticity is primarily meditated by the amorphization and weak bonding between atoms at high temperatures. With the (111)<$\bar{1}$10> setup, room temperature plasticity at short cutting distances is mainly governed by the amorphization whereas at long distances, dislocation nucleation also assists the plastic deformation of 3C-SiC. At higher temperatures, the plasticity of 3C-SiC on the (111) plane is meditated by the defect formation, as well as the amorphization and weak bonding between atoms. It should be also noted that, at higher temperatures, a small number of stair-rod and Frank-type sessile partials are observed to nucleate while cutting 3C-SiC on the different crystal planes.

It is instructive to note that in the cases where the Tersoff potential was applied, no stacking fault formation was observed, attributable to the high stacking fault energy given by this potential, as calculated in Appendix I. In addition, very low dislocation activity was observed while applying Tersoff potential. For instance, while cutting 3C-SiC on the (010) and (111) planes in the temperature range of 900 K to 3000 K, no dislocation was nucleated. In the case of (110) plane, a low density of dislocations was observed at temperatures higher than 900 K.

### 5.9.2. Structural changes

To obtain better insights about structural changes of the zinc blende structure, the RDF before and after nanometric cutting of 3C-SiC at elevated temperatures are plotted. It can be seen from Figure 5.30 that various peaks occur in the RDF for each individual cutting temperature. The bond length at the peaks has a small discrepancy. The first three peaks of RDF correspond to C-Si, C-C and C-Si bonds relative to the equilibrium bond lengths of 1.88 Å, 3.08 Å and 3.62 Å, respectively, as shown in Figure 5.30. Evidently, the peaks become weaker as temperature of the substrate increases, which is an indication of increased amplitude of atomic displacements from their original equilibrium positions. Apart from the peaks, the bond length increases with the increase of temperature, representing the enhanced structural changes and consequently superior plasticity of 3C-SiC before and during the cutting. An interesting observation from Figure 5.30 is the growth of an embryo peak at the interatomic distance of 1.45 Å, which is the equilibrium bond length of C-C, signifying the formation of C-C bond. It should be noted here that the analogous qualitative trend was observed for the three crystal planes.

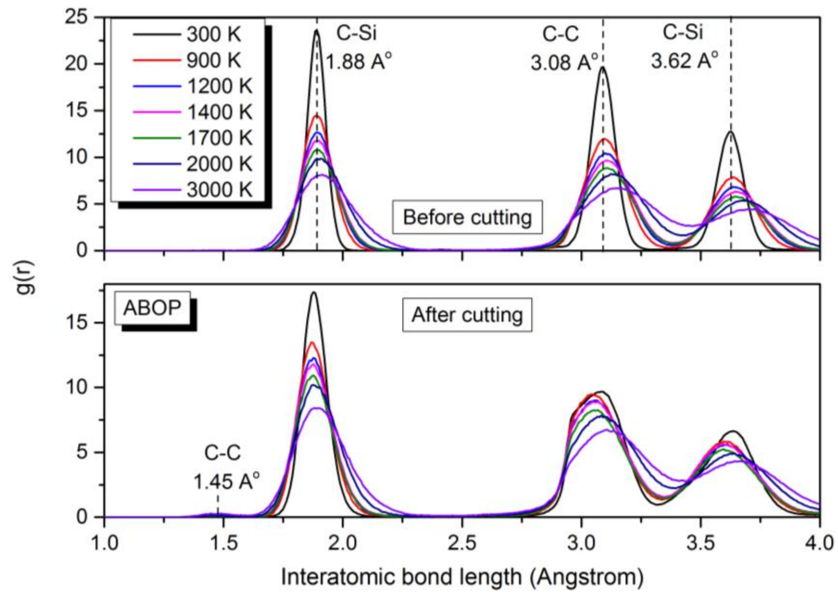


Figure 5.30: Radial distribution function showing interatomic bond lengths at different temperatures before and after nanometric cutting on the (010) crystal surface.

As mentioned before, the white atoms in the cutting chip and subsurface of substrate presented in Figure 5.20, Figure 5.21, Figure 5.22, Figure 5.23, Figure 5.24, Figure 5.25, Figure 5.27, Figure 5.28 and Figure 5.29 have experienced the transition to a disordered state, a phenomenon known as solid-state amorphization [143]. In order to further characterize the crystal qualities of 3C-SiC substrate during nanometric cutting, virtual XRD [114] with Cu Kα radiation (1.5418 Å) was carried on an elemental atomic volume ($3\times3\times3$ $nm^3$ including 2552 atoms) in the cutting region. The XRD spectrums obtained from the simulations are illustrated in Figure 5.31. Peaks at 2θ value of 35.96°, 40.38°, 55.13° and 76.19° shown in Figure 5.31a correspond to the crystalline 3C-SiC, which is consistent with the standard XRD pattern of 3C-SiC powders displayed in Figure 5.31d [144]. Note that a small amount of mismatch in peak position is commonly acceptable. The prominent peak at 2θ=35.96° is diffracted from 3C-SiC (111) according to the database of joint

committee on powder diffraction standards (JCPDS). The second, third and fourth ones are diffracted form 3C-SiC (200), (220) and (311), respectively. It can be seen from Figure 5.31c that, after cutting, both relative intensities and number of the diffraction peaks alter noticeably, and several new diffractions appear. The peaks possess lower relative intensities, particularly the strong peaks shown in Figure 5.31a almost disappear, signifying the amorphization of atoms in the cutting deformation zone owing to the large shear stresses and plastic strains. Note that an increase in the intensity of 3C-SiC (200) can be seen. However, due to the fact that Si and C atoms have ionicity so the local crystal structures are not simple like elements. Hence, it is very challenging to give a specific reason for this observation. Figure 5.31b shows the XRD profile of 3C-SiC during the cutting, a mixture of crystalline and amorphous atoms in the cutting region, where the pattern could be assumed as a combination of crystalline and amorphous XRD spectra observed in Figure 5.31a and Figure 5.31c. It can be found from Figure 5.31b that the intensity maxima of 3C-SiC (111) at $2\theta=35.96°$ is approximately 3.8 times lower than that of the crystalline 3C-SiC, indicating an inferior crystal quality in presence of both crystalline and amorphous structure in the cutting region.

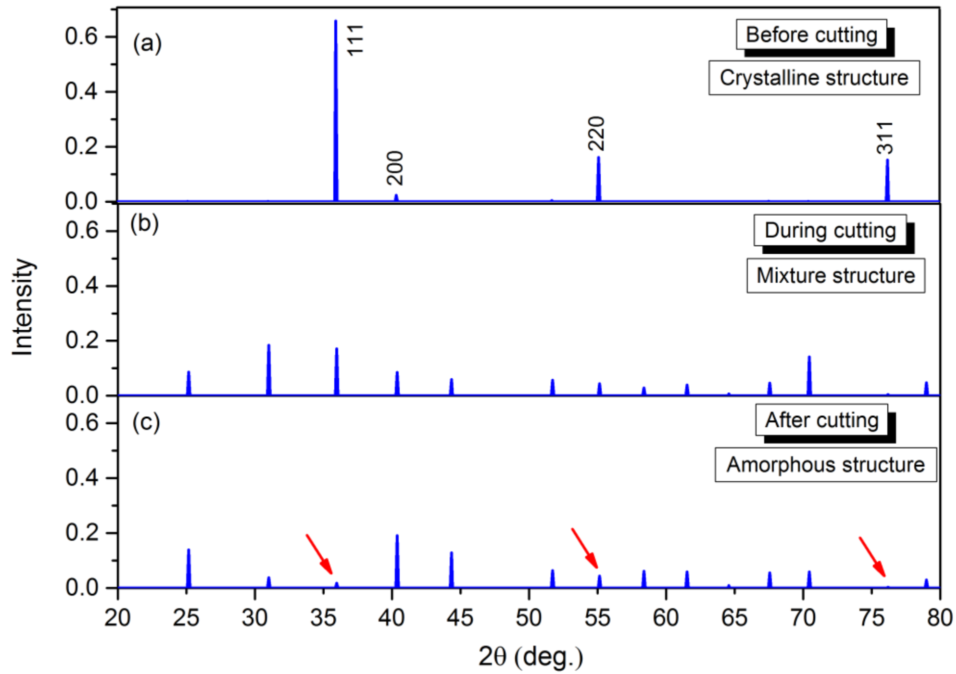


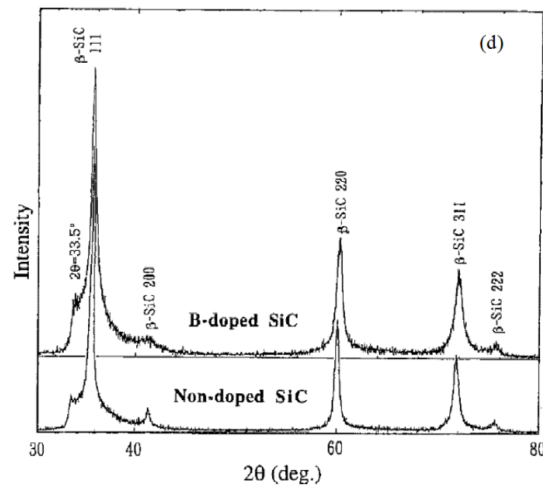


Figure 5.31: XRD spectrum of 3C-SiC in the cutting region a) before b) during and c) after nanometric cutting on the (010) crystal surface. d) Standard XRD pattern of 3C-SiC powders [144]

It should be mentioned here that the available BOP functions, including ABOP and Tersoff potentials, are not robust in describing and capturing all the structural phases as they are not able to properly resolve competing mechanisms involving subtle influences of chemical bonding, i.e. ionic bonding. Thus, phase transformation

mechanisms cannot be realized using BOP potentials. Moreover, using a defect-free specimen in MD simulation might play a role in hindering the occurrence of such transition in MD simulations of SiC. It is instructive to note that there has been a long debate on the possibility of polymorphic transition to another lattice structure during contact loading of SiC polytypes. Such mechanism has been proposed from experimental studies on 3C-SiC [145]; however, in almost all MD studies no direct evidence has been presented. Instead, indirect observation has been reported, meaning that if SiC undergoes a local pressure as high as 100 GPa then the transformation to rocksalt structure would take place [146]. Nevertheless, Mishra and Szlufarska [134] have shown that, using Vashishta *et al's*. potential function [147] which has been reported to be more accurate for describing the high pressure phase transformation of SiC, even under the local atomic pressures as high as 100 GPa, the polymorphic transition does not occur in SiC. The only direct observation of phase transformation in MD simulation was provided by Xiao *et al.* [148], where very small amount of atoms were seen to undergo phase transition from 6H-SiC to rocksalt structure. However, more evidence is needed to be able to generalize occurrence of the phase transition at a strictly nanometre level in MD trials. Hence, polymorphic transition is still a hypothesis for the deformation mechanisms of SiC in MD simulation. As mentioned in section 4.9.1, it has been revealed that [112] even silicon undergoes solid-state directional amorphization without prior Si-I to Si-II (beta tin) transformation during cutting.

## 5.10. Summary

This chapter presented the MD simulation results obtained during the nanometric cutting of single crystal 3C-SiC on the three principal crystal planes at various cutting temperatures spanning from 300 K to 3000 K. The dominance of the (111) cleavage was observed for all the tested temperatures. An observation of particular interest was the shift to the (110) cleavage at cutting temperatures higher than 2000 K. Another key finding was the increase of anisotropy in specific cutting energy from ~30% at 300 K to ~44% at 1400 K, followed by a drop to ~37% and ~24% at 1700 K and 2000 K, respectively. The obtained results also indicated that the specific cutting energies required for cutting surfaces of different orientations decrease by 33%-43% at 2000 K compared to what are required at 300 K. Moreover, the position of stagnation region was observed to vary with changes in temperature and crystal plane. Further analysis revealed that the subsurface deformation was maximal on the (111) surface whereas it was minimal on the (110) plane: this is attributable to the occurrence of cleavage and the location of the stagnation region. In addition, the amount of damage scaled linearly with the increase of cutting temperature. A vortex flow of atoms beneath the cutting tool was also observed. The simulations also predicted that the atom-by-atom attrition wear and plastic deformation of the diamond cutting tool could be alleviated while cutting at high temperatures. Nevertheless, chemical wear i.e. dissolution-diffusion and adhesion wear is plausible to be accelerated at high temperatures.

MD simulation results concerning dislocation/amorphization-based plasticity mechanisms showed that while cutting the $(110)\langle 00\bar{1}\rangle$ there was the formation and subsequent annihilation of stacking fault-couple at high temperatures, i.e. 2000 K

and 3000 K, and generation of the cross-junctions between pairs of counter stacking faults meditated by the gliding of Shockley partials at 3000 K. Another point of interest was the directional dependency of the mode of nanoscale plasticity, i.e. while dislocation nucleation and stacking fault formation were observed to be dominant during cutting the $(110)\langle 00\bar{1}\rangle$, low defect activity was witnessed for the (010)<100> and $(111)\langle \bar{1}10\rangle$ crystal setups. Nonetheless, the initial response of 3C-SiC substrate was found to be solid-state amorphization for all the studied cases. Further analysis through virtual XRD and RDF showed the crystal quality and structural changes of the substrate during nanometric cutting. A key observation was that the von Mises stress to cause yielding was reduced by 49% on the (110) crystal plane at 3000 K compared to what it took to cut at 300 K.

# Chapter 6: Experimental studies on nanometric cutting of silicon at elevated temperatures

## 6.1. Introduction

In the preceding chapters, MD simulation studies were conducted on high temperature nanometric cutting of hard-brittle materials such as silicon and silicon carbide for the sake of making important contributions to our fundamental understanding of the occurring processes at the atomic scale at elevated temperatures. It was revealed that MD simulation is a robust numerical analysis tool in addressing a range of complex nanometric cutting problems that are otherwise difficult or impossible to understand using other methods. For example the mechanics of high temperature nanometric cutting of silicon and silicon carbide is influenced by a number of variables such as machine tool performance, machining conditions, material properties, and cutting tool performance (material microstructure and physical geometry of the contact) and all these variables cannot be monitored online through experimental examination. However, these could suitably be studied using an advanced simulation based approach such as MD simulation. Although MD simulations offers a unique opportunity to explore the atomic level discrete processes of nanometric cutting of silicon and silicon carbide with desired conditions, there exists some other phenomena which are impossible to be investigated using MD simulation, attributable to either the lack of a proper interatomic potential function or the excessive intricacy of the phenomena. For instance, the available potential functions are not robust in describing and capturing all the structural phases of silicon and silicon carbide; hence phase transformation mechanisms during nanometric cutting cannot be understood through MD simulation. Therefore,

experimental determination of the formation of polymorphs is required. In this chapter, the focus will be on the experimental studies of the pressure-induced silicon polymorphs, nanoscratch topography, nanoscratch hardness and condition of the tool tip in nanoscratching at elevated temperatures. To this end, using the state-of-the-art nanoindentation equipment, high temperature nanoscratching trials on single crystal silicon wafer under inert gas were performed to shed some light on the aforementioned processes. Note that the material removal mechanism in scratching is similar to that in cutting/machining. Hence, it is possible to substitute the complicated cutting/machining with a relatively simple scratching so as to study material removal mechanism involved in cutting/machining [149].

## 6.2. Experimental setup and test procedure

### 6.2.1. Equipment

Nanoscratching trials were performed on a MicroMaterials Ltd. (MML) nanoindenter called NanoTest Vantage. This equipment permits testing at elevated temperatures with low thermal drifts under reduced oxygen/purged condition and controlled humidity levels, which offers the perfect capability of testing materials in extreme conditions. Figure 6.1 demonstrates the heating arrangement in the MML NanoTest Vantage system.

It is known that silicon is reactive with oxygen at high temperatures; hence performing nanoscratching trials under reduced oxygen condition is indispensable. NanoTest Vantage system uniquely features a chamber which can be over-pressurized with a shield gas i.e. high purity Argon to surround the hot zone during testing. Figure 6.2 shows the configuration of NanoTest Vantage system employed for conducting the nanoscratching tests.

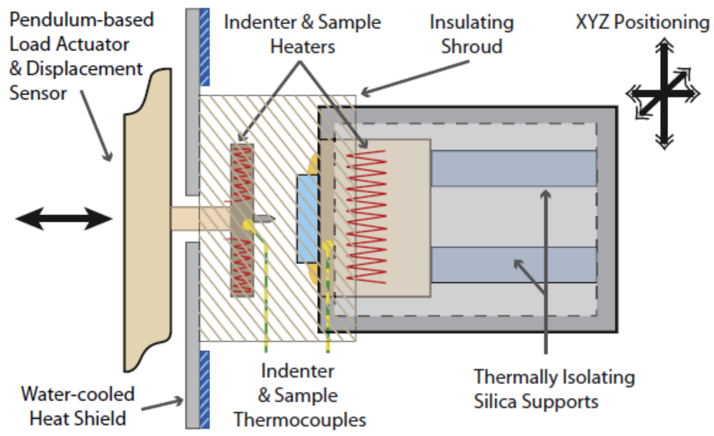


Figure 6.1: Schematics of the heating arrangement of NanoTest Vantage [52]

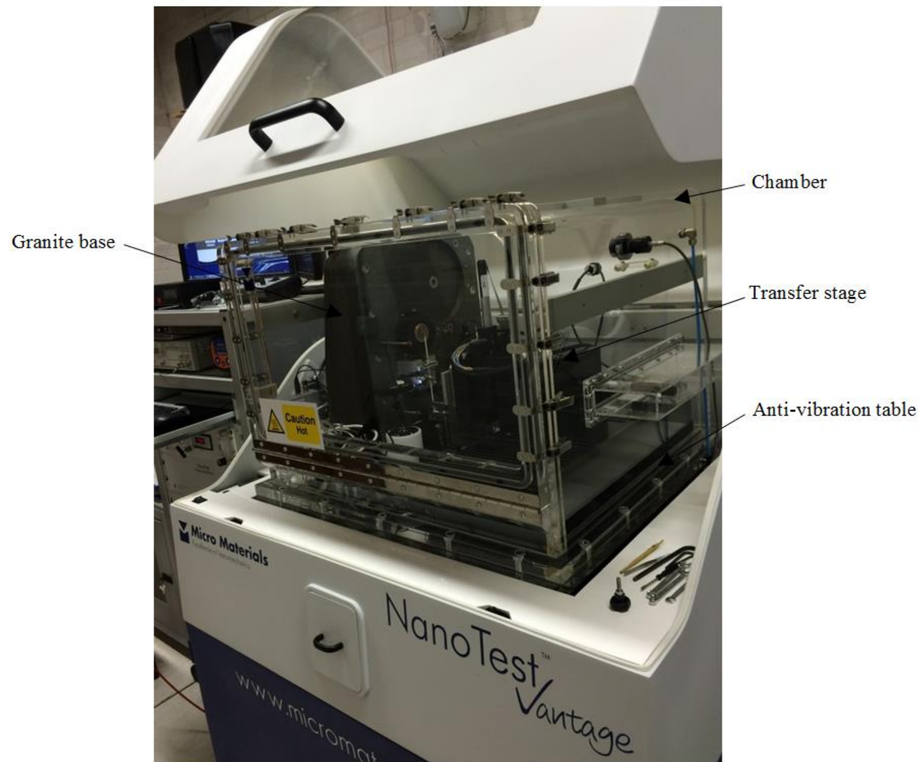


Figure 6.2: NanoTest Vantage equipment used to perform nanoscratching trials

### 6.2.2. Workpiece and cutting tool

The polished undoped n-type single crystal silicon wafers with the orientation (110) of size 10×10×0.5 mm were utilized for the experiments. As pointed out recently by Gerbig *et al.* [150], the increased shear stress for the Si(110) as compared with the Si(100) and Si(111) could ease the plastic deformation processes leading to decreased transformation pressures in silicon. Moreover, there is little work on the material removal mechanisms of the Si(110) wafer in nanoscratch testing [151].

Prior to trials, the silicon wafers were first ultrasonically cleaned for 20 min in acetone, then dipped into 2% HF (Hydrofluoric) aqueous solution for 60 min to remove the oxide layers, followed by a thorough rinse in de-ionized water. The surface roughness of the etched wafers was measured in four areas using a white light interferometer (Zygo CP300). A snapshot of the measured Peak-to-valley (PV) and Ra for an area is shown in Figure 6.3. The etched wafers had an average flatness of ~239±65 nm in terms of PV height while average Ra was measured as ~0.56±0.06 nm.

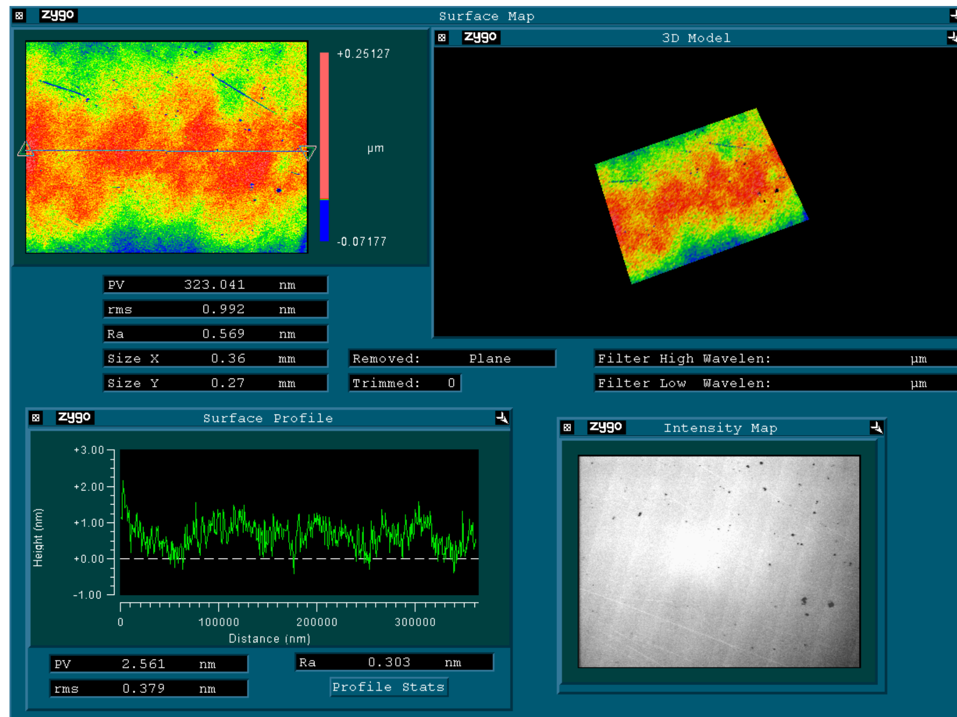


Figure 6.3: Surface roughness and PV of the etched wafer measured by white light interferometer

Berkovich nanoindenter with a nominal tip radius of ≥ 50 nm and having 3-sided pyramidal faces forming an angle of 65.03° with the vertical axis was employed in the nanoscratching experiments reported here. SEM photograph of the Berkovich nanoindenter before the experiment is shown in Figure 6.4. The Berkovich nanoindenter would provide the more pragmatic conditions which could be confronted with actual applications. In addition, the use of this type of nanoindenter would lead to the much higher local pressure with similar load thus would be beneficial in elucidating the pressure-induced phase transformation.

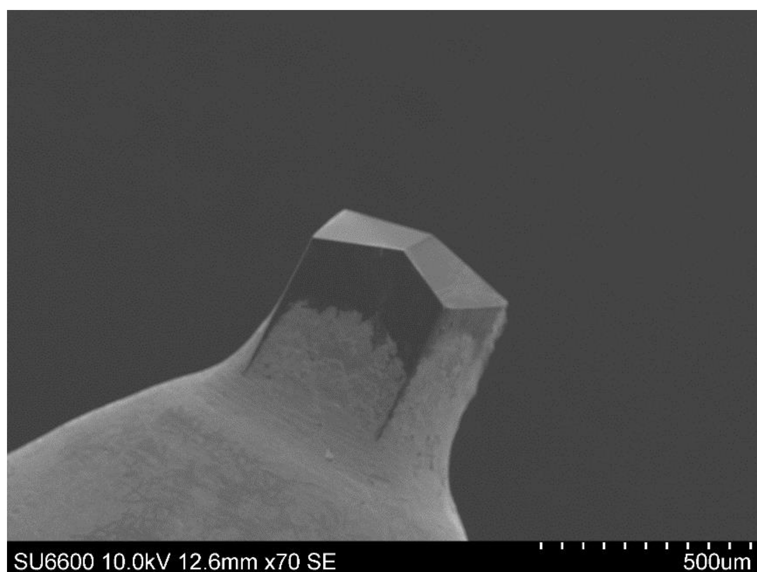


Figure 6.4: SEM image of Berkovich nanoindenter used in the trials

### 6.2.3. Experimental procedure

Nanoscratching experiments were carried out at substrate temperatures of 25°C and 500°C using a linearly increasing load spanning from 0 to 10 mN along a total scratch length of 100 μm at two constant velocities of 0.1 $\mu m/s$ (low speed) and 10 $\mu m/s$ (high speed). At each scratching speed, three scratches were produced. The nanoscratches were made along the Si<100> direction. Nanoscratching trials at room temperature (25°C) were conducted under atmospheric conditions whereas hot nanoscratching experiments were performed under reduced oxygen condition through an overpressure of pure Argon in the chamber. The amount of oxygen in the chamber was kept in the range of ~0.2-0.3% during the experiments. The experimental parameters and conditions used for the trials are summarized in Table 6.1.

Table 6.1: Nanoscratching conditions

| Silicon wafer | Scratching direction | Temperature (°C) | Scratching speed ($\mu m/s$) | Ramp load (mN) | Total scratch length (µm) | Inert gas for high temperature testing |
|---|---|---|---|---|---|---|
| Si (110) | Si <100> | 25 and 500 | 0.1 and 10 | 0-10 | 100 | Argon |

For the room temperature experiments, the wafer was glued with Cyanoacrylate onto a stainless steel disc and then fixed on the metal holder of the nanoindenter machine. For the high temperature nanoscratch testing, the wafer was glued onto the hot stage using high temperature cement, as shown in Figure 6.5.

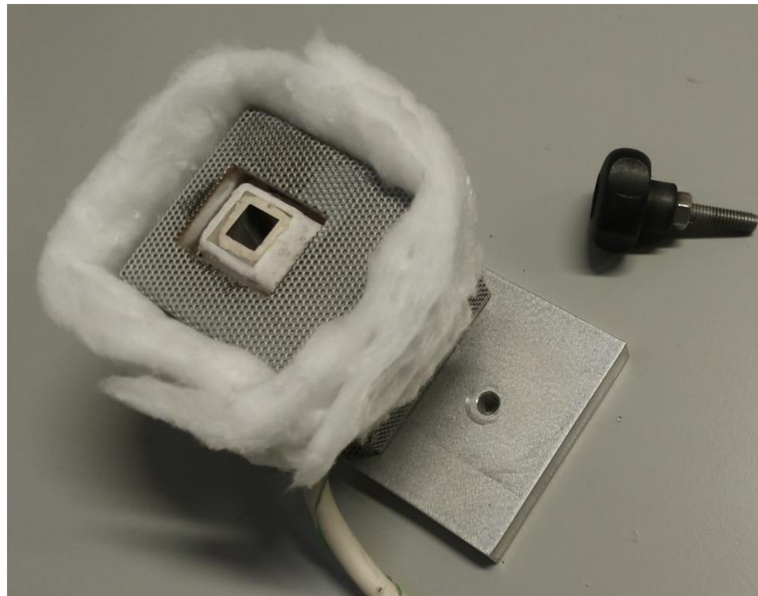

Figure 6.5: Glued silicon wafer on the hot stage

To perform high temperature nanoscratching experiments, the wafer was heated at a low rate of 1.6°C/min to reach the target temperature. It should be mentioned that the nanoindenter was not independently heated. The swift heat transfer and thermal

gradients between the heated wafer and the cold nanoindenter tip could lead to a substantial thermal drift, which influences the reliability of the results. In order to minimize the thermal drift, the wafer-tip contact was achieved and wafer-tip was kept in contact during the heating process. Note that after performing high temperature nanoscratching, the wafer was cooled in the chamber at the same rate (1.6°C/min) until the room temperature was reached. Figure 6.6 illustrates a close snapshot of experimental system during high temperature nanoscratching. The nanoindenter and glued wafer on the hot stage were surrounded by mineral wool in order to reduce heat loss by convection and to stabilize the temperature.

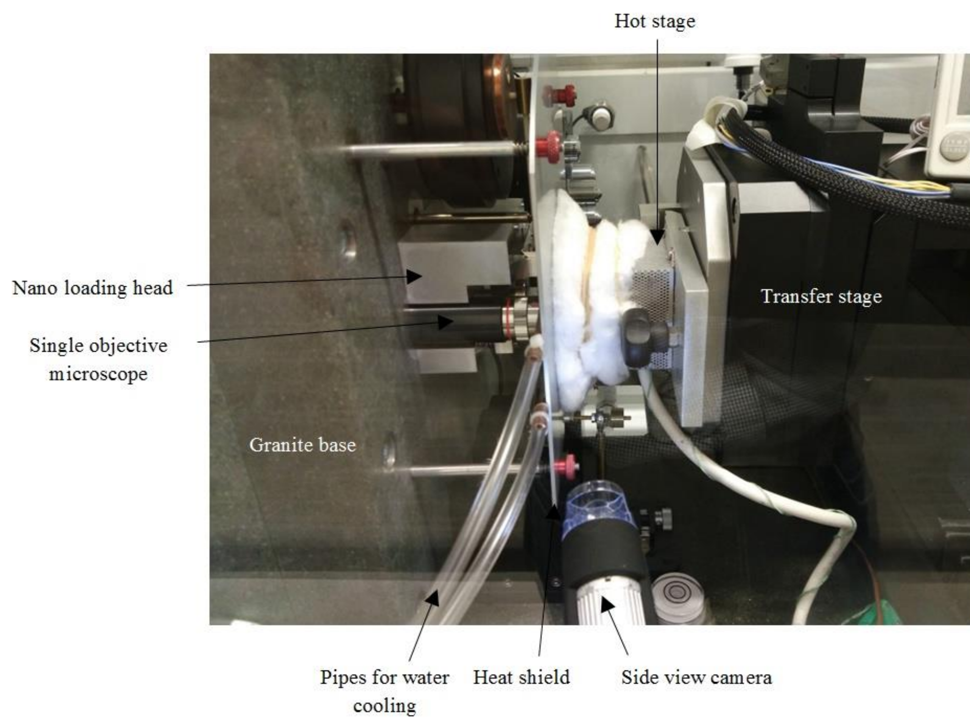


Figure 6.6: A close snapshot of experimental system during high temperature nanoscratching

After nanoscratching trials at room and high temperatures, a Thermo Scientific DXR Raman Microscope with a 532 nm diode-pumped solid state laser was used to detect the presence of crystalline and high pressure phases inside the scratches. Also, a Veeco Dimension 3100 atomic force microscope (AFM) with silicon tip was utilized to determine the topography of the nanoscratches whereas a Hitachi SU-6600 field emission scanning electron microscope (FE-SEM) was employed to take micrographs.

## 6.3. Experimental observations and discussion

### 6.3.1. Scratch topography

Figure 6.7 shows the typical topography of the residual nanoscratch measured by using the AFM at four different positions. The cross profile topography shows a permanent pile-up (vertical height from a to b and a to d illustrated in Figure 6.7) at both edges of the track, which is closely associated to the plastic extrusion of silicon during nanoscratching.

Figure 6.8 illustrates the variation of scratch depth, scratch width and total pile-up heights (sum of the left and right pile-up heights) at four various positions of the nanoscratch shown in Figure 6.7, while nanoscratchings were carried out at room and high temperatures and at two scratching speeds i.e. low speed (0.1 $\mu m/s$) and high speed (10 $\mu m/s$).

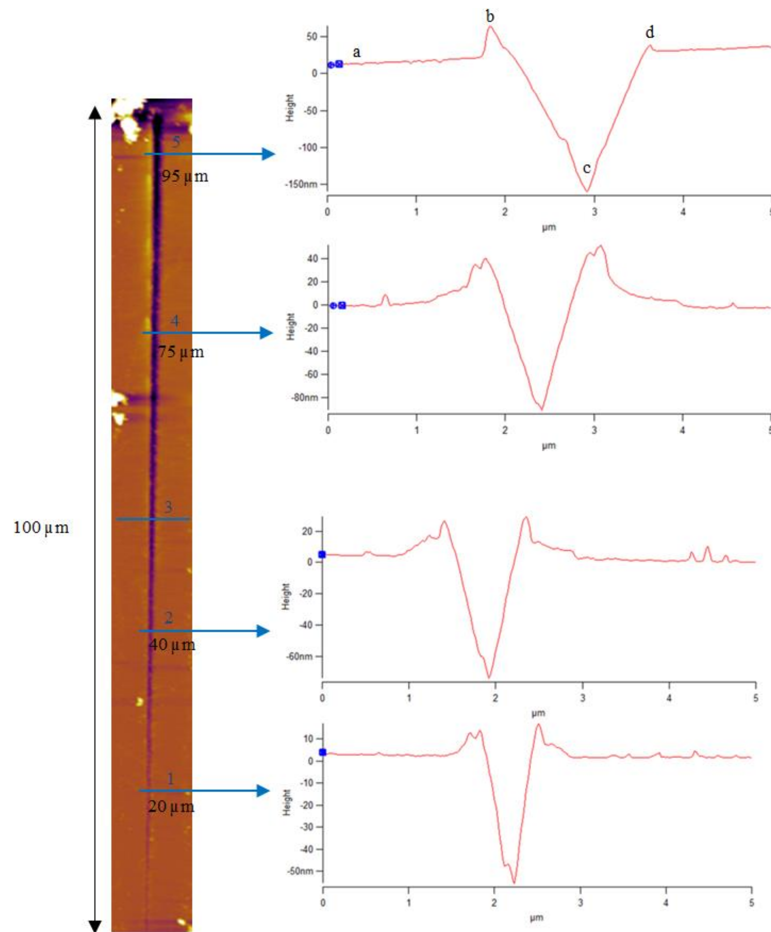


Figure 6.7: Typical AFM image of the nanoscratch and cross section profiles measured in four different positions. Scratch depth (vertical height from a to c), scratch width (horizontal width b to d) and pile-ups (vertical height a to b and a to d) are shown on the top profile.

It can be seen that with the increase of applied load and consequently pushing more material to the side of the scratches, the residual scratch depth, scratch width and total pile-up heights increase along the scratch length. Furthermore, the aforementioned parameters increase with the rise of temperature as a result of thermal softening. It is also found that the residual scratch morphologies are strongly affected by the scratching speed i.e. scratch depth, scratch width and total pile-up heights decrease with the increase of scratching speed. It can be inferred that the

degree of nanoscale elastic recovery during nanoscratching is more serious in high speeds than at low speeds. The obtained results are in accord with the trend reported by Li *et al.* [152], where the residual scratch depth of K9 glass decreased with the increase of the scratching speed at the same normal load.

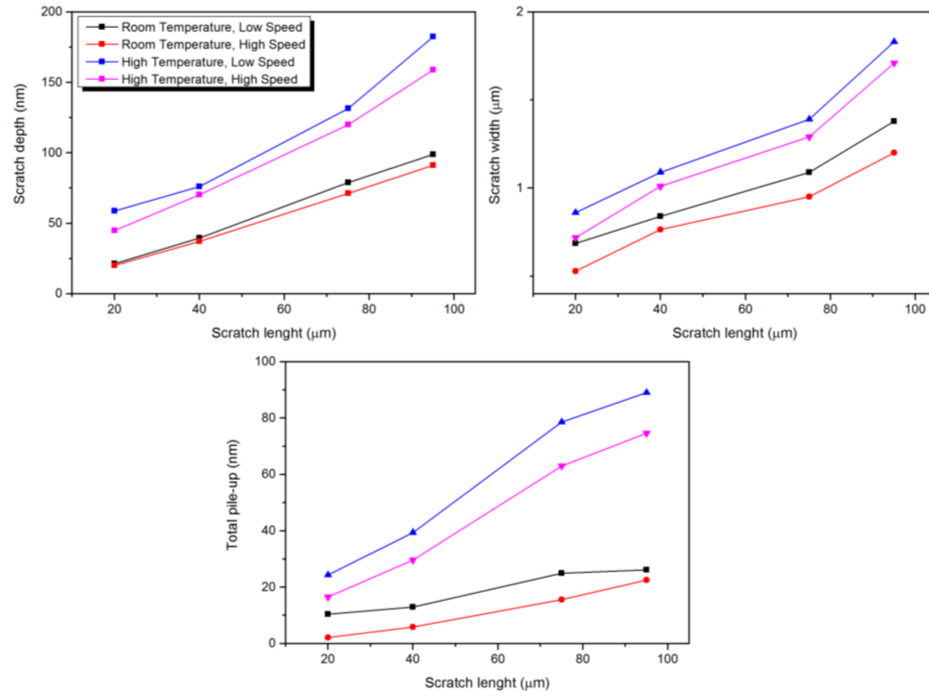


Figure 6.8: Variation of scratch depth, scratch width and total pile-up heights along the scratch length with the temperature and scratching speed

Nanoscratch hardness ($H$) can be employed so as to ascertain the resistance of material to the scratch, and it is described as the response of material under dynamic deformation of the surface. This parameter is defined as the ratio of the vertical load ($P$) to the surface area of the tip-sample contact or the contact area projection onto the horizontal plane which depend on the residual scratch width ($b$):

$$H = k\frac{P}{b^2} \tag{6.1}$$

where $k$ is the nanoindenter tip shape factor, which is dependent on the tip configuration. For a Berkovich indenter, this factor is 2.31 [153]. The average values of scratch hardness obtained from the trials are listed in Table 6.2. Due to an effective reduction in the shear stress at high temperatures, the scratch hardness has lower magnitudes at high temperatures. Moreover, the scratch hardness increases as the scratching speed increases, signifying a strain rate strengthening of the silicon material at higher scratching speed. In scratch hardness, the effective strain rate can be defined as the ratio of the scratching speed to the scratch width. The strain rate hardening effect means that the material provides a greater resistance to plastic deformation [154].

Table 6.2: Scratch hardness at different conditions

| Nanoscratching condition | Scratch hardness (GPa) |
|---|---|
| Room temperature, Low speed | 12.2 |
| Room temperature, High speed | 16.7 |
| High temperature, Low speed | 7.4 |
| High temperature, High speed | 9 |

### 6.3.2. Nanoscratching-induced phase transformation

In order to identify the existence of high pressure phases of silicon inside the nanoscratch tracks, Raman spectroscopy was employed. For each scratch, the Raman spectra were collected at five different locations i.e. at the position of blue lines shown in Figure 6.7. It should be mentioned here that the reported phases in this study are the stable or remnant phases since the residual nanoscratch impressions

were measured at room temperature after the nanoscratching experiments. Figure 6.9 and Figure 6.10 illustrate the Raman spectra of silicon obtained from the five various locations of the scratch made at room and high temperatures, respectively, at low (0.1 $\mu m/s$) and high (10 $\mu m/s$) scratching speeds. On all spectra, the single line at 519.4 $cm^{-1}$ can be observed, which is close to the reported 520 $cm^{-1}$ optical mode of bulk silicon (Si-I). Note that a small amount of stress may cause a shift. It can be inferred from Figure 6.9a that while room temperature nanoscratching at low scratching speed, the nanoscratch is composed of Si-I (bands at 520 and 300 $cm^{-1}$) and high pressure phase Si-XII (band at 352 $cm^{-1}$) when the scratching load is lower than ~4 mN, corresponding to the locations 1 and 2 in Figure 6.7. However, the intensity of the peak corresponding to Si-XII is very low, signifying that the content of Si-XII is relatively small. Above the transition load of ~5 mN, the nanoscratch is formed of Si-I, Si-XII characterized by bands at 166, 182, 352, 374, 396, 440, and 491 $cm^{-1}$, and Si-III (bc8, body-centred cubic structure) identified by bands at 166 and 385 $cm^{-1}$. Both Si-III and Si-XII (r8, the rhombohedral distortion of bc8) are known to show semi-metallic electronic behaviours. It is of note that the band at 385 $cm^{-1}$ predicted by Plitz *et al.* [155] for the bc8 structure, was attributed by Ge *et al.* [156] to Si-III together with other bands at 415 and 465 $cm^{-1}$. Nevertheless, the absence of these last bands would indicate that Si-III is in minor quantity in the nanoscratch track. This observation is in good agreement with the decompression path proposed by Gassilloud *et al.* [157]. It is informative to note that there are strong indications that the presence of metastable crystalline phases (Si-XII and Si-III) in the residual imprints can be a consequence of formation of β-tin silicon (Si-II) during contact loading of silicon [158]. In other words, metallic Si-II is formed during

nanoscratching owing to the highly localized stresses underneath the indenter and subsequently transformed to Si-III and Si-XII, accompanied by >10% volume increase [149], which contributes to the elastic recovery of the scratched surface.

Interestingly, above the transition load of ~5 mN, the probability of forming Si-III and Si-XII phases was found to increase. However, the intensities remain almost constant for these phases, suggesting that the volume of Si-III and Si-XII phases does not change at scratching loads higher than ~5 mN.

The literature suggests that the mode of unloading/release of the pressure plays a crucial role in reverse transformation from metallic phase (Si-II phase) to other polymorphs, i.e. upon slow unloading, Si-XII and Si-III phases may persist whereas Si-IX, amorphous silicon and Si-I could be obtained upon fast unloading [2]. The Raman spectra shown in Figure 6.9b demonstrate that the nanoscratch fabricated at high scratching speed is composed of Si-I when the scratching load is below ~7.5 mN. At higher loads i. e. ~9.5 mN, some small remnants of Si-XII and Si-III can be observed inside the scratch. As mentioned above, the high scratching speed corresponds to a high unloading rate, which likely leads to the formation of the Si-I.

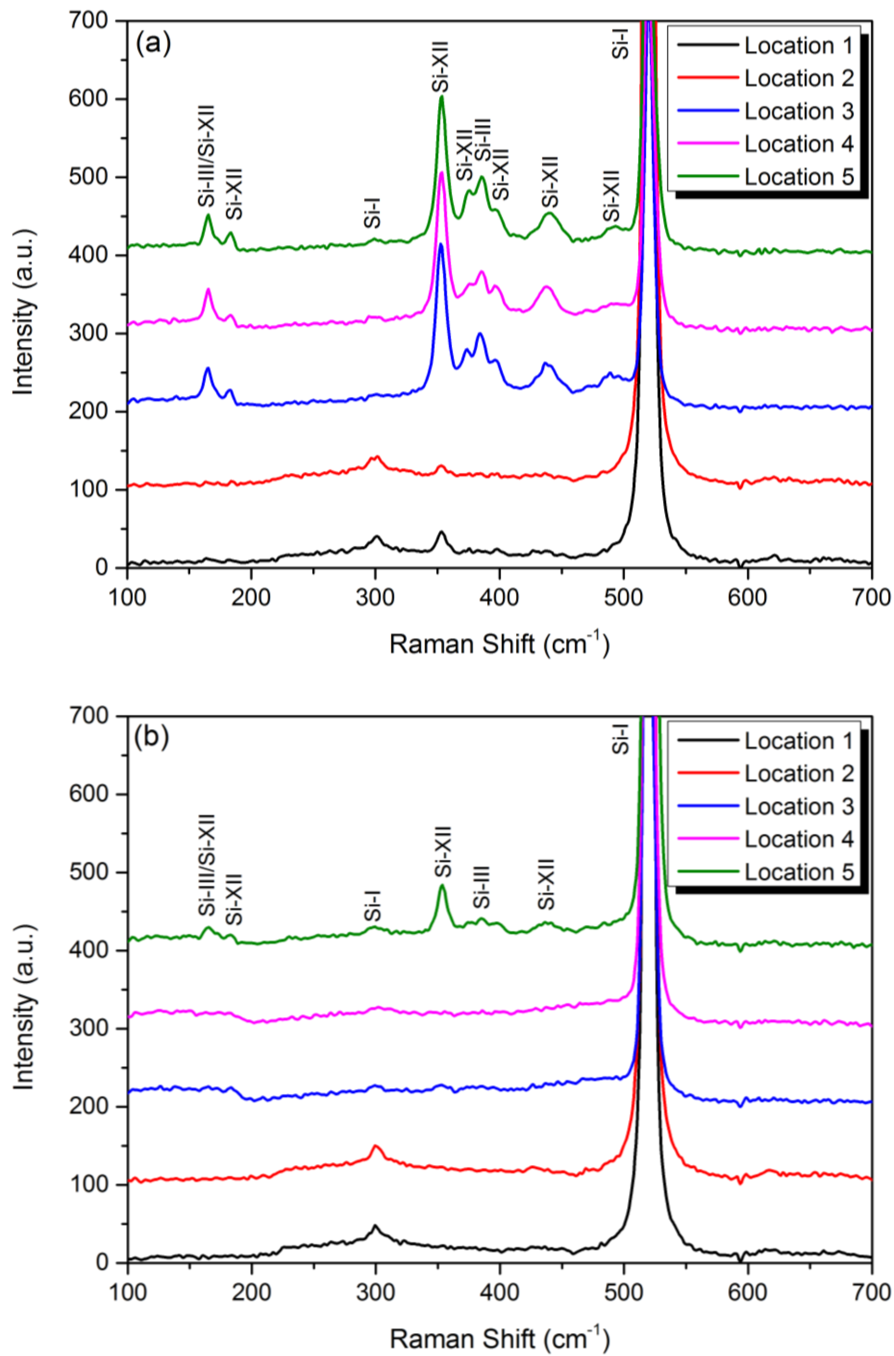


Figure 6.9: Raman spectra collected from five different locations of the nanoscratch shown in Figure 6.7, and machined under room temperature condition at constant scratching speed of a) 0.1 µm/s (low speed) and b) 10 µm/s (high speed)

As evident in Figure 6.10a and Figure 6.10b, the Raman peaks for the Si-III and Si-XII phases disappear and no remnants of polymorph phases are detected all along the

nanoscratch residual track when high temperature nanoscratching is performed at low and high speeds. This means the Si-III/XII → Si-I phase transition occurs during the nanoscratching at high temperature of 500°C. This observation agrees with the idea that high temperature promotes the transition of metastable silicon phases (Si-III and Si-XII) into thermodynamic stable Si-I [77]. In nanoindentation process of silicon, Domnich *et al.* [77] observed that when the temperature was above 300-350°C, only cubic diamond silicon was detected, which is in excellent agreement with the obtained results of high temperature nanoscratching in our study. Moreover, there is some evidence that Si-III and Si-XII transform back to Si-I with annealing. Ruffle *et al.* [159] reported that the intensity of the peaks related to the Si-III and Si-XII phases drops with increasing annealing time at 175°C, and after 120 min, none of these phases are detected and the Raman spectrum is similar to that of pristine silicon. Moreover, they claimed that the lifetime of the Si-III/XII is temperature dependent, and it is over 1 min at 320°C and at ambient pressure. Taking into account the high temperature nanoscratching at 500°C performed in this study, it can be assumed that annealing at 500°C with the cooling rate of 1.6°C/min can commence a fast Si-III/XII → Si-I phase transition during the trials. Hence, the only stable phase which is detectable from the Raman spectra shown in Figure 6.10 is the pristine silicon (Si-I). The obtained results in this study are also consistent with the high power laser irradiation of the indentations carried out by Zeng *et al.* [160], where rapid Si-III/XII → Si-I phase transition within 1s was realized.

It should be noted here that other metastable phases like hexagonal diamond (Si-IV), which is characterized by a broad band at 510 $cm^{-1}$, or amorphous silicon (a-Si), which is characterized by broad bands at near 170 and 490 $cm^{-1}$, were not observed

within the residual scratches while nanoscratching of silicon at room temperature and high temperature of 500°C using the adopted ramp load ranging from 0 to 10 mN at two constant speeds of 0.1 μm/s (low speed) and 10 μm/s (high speed). A possible hypothesis is that the adequate pressure for amorphization of silicon is not attained inside the scratch tracks. It can also be postulated that a-Si crystallizes during high temperature nanoscratching trials since very small volumes of a-Si typically do not require annealing temperatures exceeding 550°C in order to exhibit significant crystallization [161]. Meanwhile, there is some evidence that nanoclusters of a-Si can crystallize at temperatures as low as 70°C [162, 163]. Therefore, it is not surprising to observe the absence of a-Si within the scratch tracks. However, there might exist a small amount of residual a-Si within the phase transformed zone, yet its amount (if present) should be very limited which cannot be detected since Raman spectroscopy itself is not very sensitive and trace amounts may not be detectable with this technique. This may be resolved by using more advanced Raman techniques such as surface-enhanced Raman scattering (SERS) and tip-enhanced Raman scattering (TERS) etc. It can be argued that cross-sectional transmission electron microscopy (XTEM) analysis can be employed to further investigate the presence of a-Si in the scratch. However, the focused ion beam (FIB) can damage the cross-sectional sample which in turn could generate a-Si within the scratch.

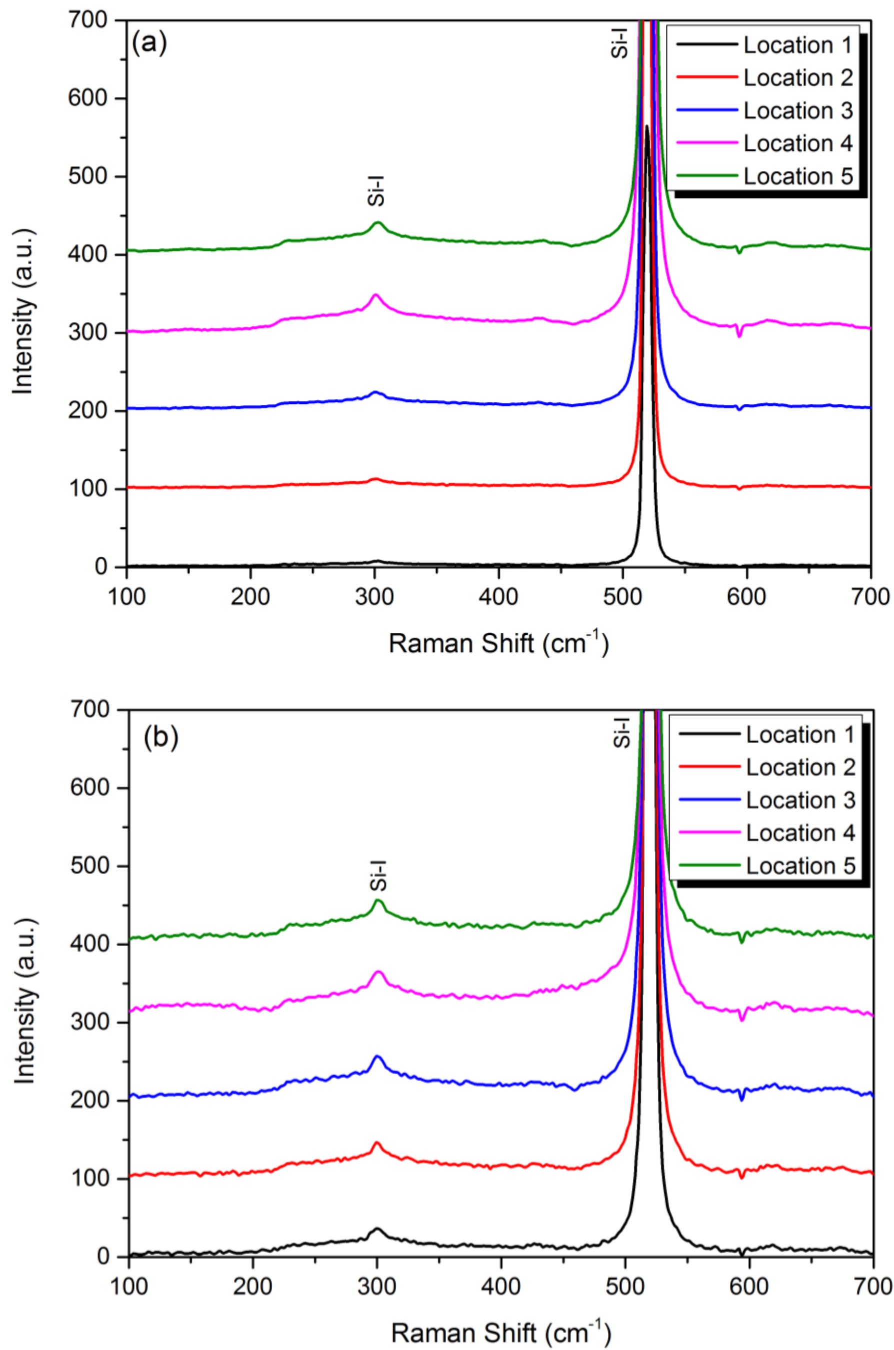


Figure 6.10: Raman spectra collected from five different locations of the nanoscratch shown in Figure 6.7, and machined under high temperature condition (500°C) at constant scratching speed of a) 0.1 µm/s (low speed) and b) 10 µm/s (high speed)

### 6.3.3. Condition of the nanoindenter tip after nanoscratching

The wear mechanism of a diamond nanoindenter is very complex, involving chemical, physical, electrical, and mechanical interactions between diamond and

substrate [164]. Figure 6.11 shows the SEM micrograph of the nanoindenter tip after nanoscratching of silicon at room and high temperature. As can be seen from the figure, under the present scratching conditions, the nanoindenter tip is visually sharp and is not blunted i.e. no drastic mechanical wear occur for both cases owing to high surface hardness and wear resistance of diamond.

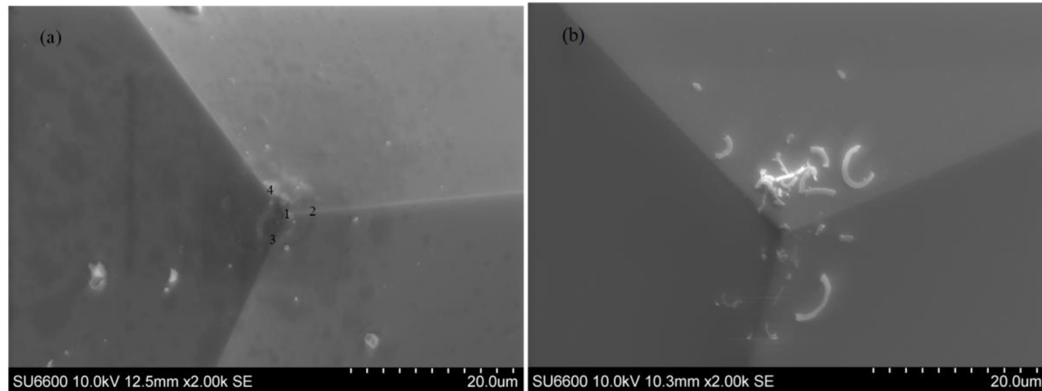


Figure 6.11: SEM image of Berkovich nanoindenter tip used for nanoscratching at a) room temperature and b) high temperature (500°C). The nanoindenter tips are not blunted under the present scratching conditions.

In order to study the probable microstructural changes of the diamond nanoindenter tip, Raman spectroscopy was performed at four different points on the nanoindenter edges shown in Figure 6.11a. Figure 6.12 illustrates the Raman spectra of the diamond obtained from the four locations of the nanoindenter tips used for nanoscratching at room and high temperatures. The strong sharp peak at 1332 $cm^{-1}$ corresponds to the first-order Raman peak of crystalline diamond [165]. Disordered graphite displays two distinct modes in the Raman spectrum: the G band centred at ~1580 $cm^{-1}$ and the D band centred at ~1350 $cm^{-1}$ [166]. However, such peaks were not observed in Figure 6.12, suggesting that under the present nanoscratching

conditions, no direct diamond to graphite transformation occurred. Hence, the diamond nanoindenter is not supposed to be worn by graphitization.

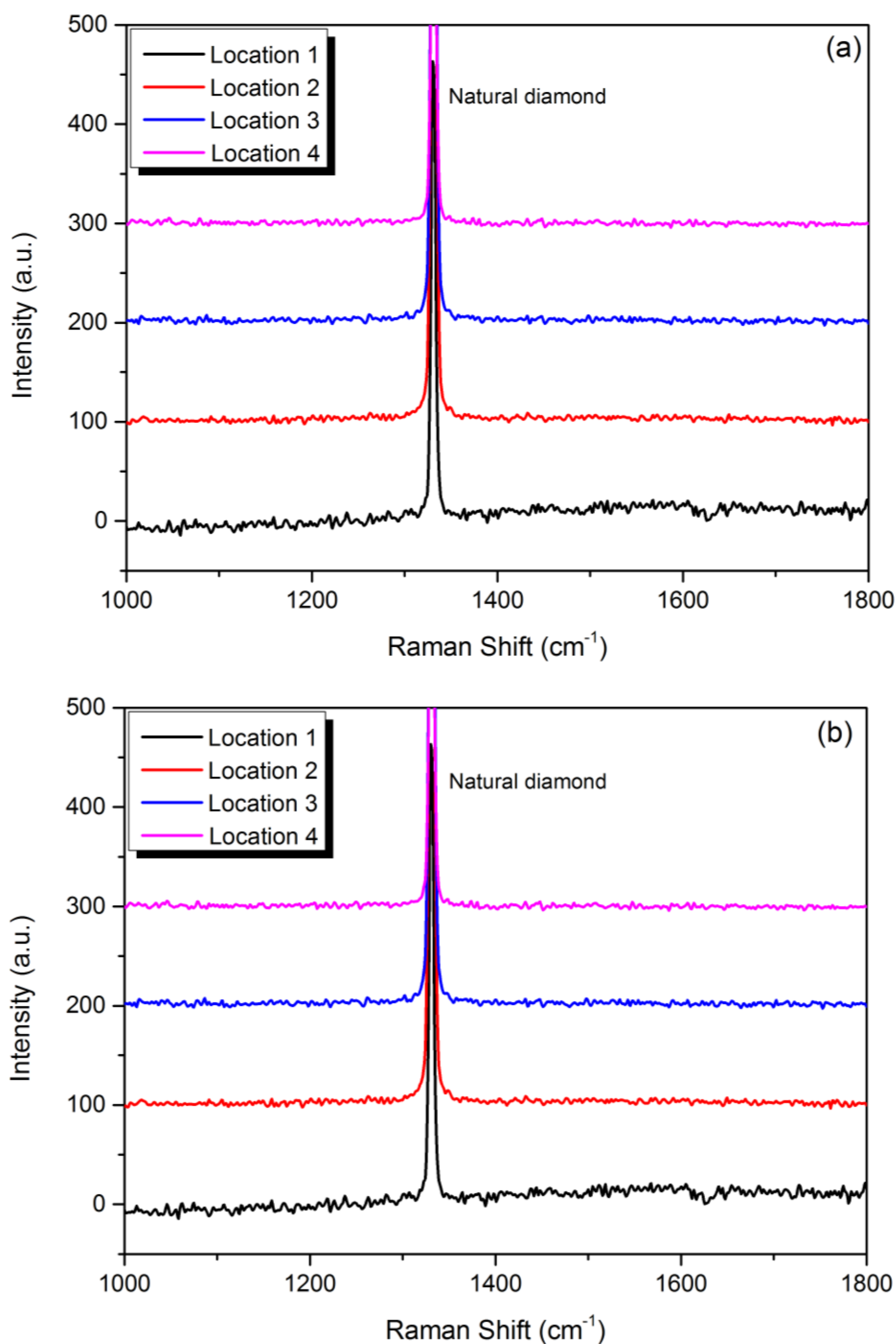


Figure 6.12: Raman spectra collected from four different locations of the nanoindenter shown in Figure 6.11a, used for nanoscratching at a) room temperature and b) high temperature (500°C).

### 6.4. Summary

Single crystal silicon nanoscratching experiments were performed at room and high temperature to comprehend the influence of substrate temperature on the nanoscratch topography, nanoscratch hardness, high pressure phase transformation and condition of the tool tip in nanoscratching. AFM measurements revealed that the residual scratch morphologies are profoundly influenced by the scratching speed viz. scratch depth, scratch width and total pile-up heights decrease with the increase of scratching speed. Moreover, the aforementioned parameters were observed to increase with the rise of temperature as a result of thermal softening. Further analysis through calculating the nanoscratch hardness showed a reduction at high temperatures. Additionally, the nanoscratch hardness was found to increase as the scratching speed increases, signifying a strain rate strengthening of silicon material at higher scratch speeds.

The Raman spectroscopy results revealed that while room temperature nanoscratching at low scratching speed, above the transition load of ~5 mN, the nanoscratch is formed of Si-I, Si-XII and Si-III, and the probability of forming high pressure phases of Si-III and Si-XII increases above this load. Nevertheles, Si-III phase was found to be in minor quantity in the nanoscratch track. At high scratching speed, small remnants of Si-XII and Si-III phases were detected when the scratching load was greater than a threshold value i. e. ~9.5 mN. When high temperature nanoscratching was carried out at low and high speeds, no remnants of polymorph phases were observed all along the nanoscratch residual track, suggesting the transition of metastable silicon phases (Si-III and Si-XII) into thermodynamic stable Si-I.

Under the present nanoscratching conditions, SEM and Raman spectroscopy studies showed the nanoindenter tip is not worn i.e. mechanical wear and direct diamond to graphite transformation do not occur during nanoscratching at room and high temperature.

# Chapter 7: Conclusions and recommendations

## 7.1. Assessment of the research

The general objective of this dissertation was to employ MD simulation together with experimental trials to elucidate atomic scale mechanisms involved in nanometric cutting of hard-brittle materials such as silicon and silicon carbide at elevated temperatures. To this end, atomistic models were developed using various interatomic potential functions and high temperature experimental testing was carried to comprehend the microscopic behaviours of silicon and silicon carbide during nanometric cutting at elevated temperatures. These MD simulations and experimental trials have provided novel insights into the temperature dependence of the occurring mechanisms during nanometric cutting of hard-brittle materials. Accordingly, being a preliminary work in this direction, this study can be seen as a test bed with the follow-on work aiming to develop high temperature ultra-precision mechanical machining of hard-brittle materials. The following contributions from this dissertation can be itemized:

- Development of the MD models to simulate high temperature nanometric cutting of hard-brittle materials such as silicon and silicon carbide using different interatomic potential functions i.e. Tersoff, modified Tersoff, ABOP and SW.
- Enhancement of our understanding concerning the plastic deformation mediated flow behaviour, cutting chip characteristics and anisotropic behaviour of silicon and 3C-SiC during nanometric cutting
- Quantification and analysis of the cutting indicators like specific cutting

energy, friction coefficient and cutting temperature as well as the critical yield stresses e.g. von Mises stress during hot machining of silicon and 3C-SiC

- A comprehensive illumination of the dislocation/amorphization-based plasticity mechanisms in silicon and 3C-SiC during nanometric cutting on different crystal planes across a range of cutting temperatures
- Elucidation of the phase transformation mechanisms, scratch topography and nanoscratch hardness in high temperature experimental trials

It is also found that empirical potential energy functions developed for silicon carbide such as ABOP possess only restricted transferability, i.e. they fail in accurately predicting the melting point. Hence, the simulated temperatures and results for the silicon carbide in this stydy should be scaled to match the actual (experimental) temperatures.

## 7.2. Conclusions

This research work employed MD simulation to explore the nanometric cutting mechanics for silicon and 3C-SiC on the different crystallographic planes at elevated temperatures. Complimentary experimental trials lend further credence to the reported findings. The key conclusions based on the research objectives could be as follows:

I. The flow behaviour of solid silicon and 3C-SiC in the machining zone was elucidated during nanometric cutting akin to fluids using a parameter called as atomic displacement vector. MD simulations revealed that a vortex flow brings higher machinability on the (111) plane than the other two major

orientations. Furthermore, it was observed that the degree of turbulence in the machining zone increases with the increase in the machining temperature. Also, it was found that at higher temperatures, elastic recovery is negated by the turbulence.

II. It was recognized that the stagnation region during cutting of silicon and 3C-SiC is highly dependent on the crystal plane and the machining temperature. In general, when cutting was performed on the (111) plane, the stagnation region (irrespective of the cutting temperature) was observed to locate at an upper position than for the (010) and (110) planes. This signifies that ploughing due to compression is relatively higher on the (111) plane and thus the extent of deformed surface and sub-surface as well, leading to higher spring-back on this orientation. Also, at high temperatures, the stagnation region was observed to shift downwards than what was observed at room temperature. Additionally, the analysis showed that the values of the stagnation and friction angle were identical when the cutting of silicon was performed on the (111) and (010) crystal planes at low temperatures. With the 3C-SiC, the stagnation and friction angles were closely correlated while cutting the (110) crystal plane in the temperature range of 300 K-1400 K.

III. While cutting silicon, the anisotropy in the cutting forces and specific cutting energies was observed to increase with the increase of machining temperature. However, while cutting 3C-SiC, the anisotropy in the specific cutting energy initially increased with the increase of cutting temperature up to 1400 K and then decreased at higher temperatures i.e. 1700 K and 2000 K. Besides, narrower shear zones were observed while machining the (111)

crystal plane or at higher machining temperatures. Consequently, irrespective of the machining temperature, (111) plane is suggested to be superior for machining silicon and 3C-SiC over other orientations which is in accord with the experiments.

IV. The increase of cutting temperature led to the formation of deeper subsurface deformation layer. Maximum subsurface deformation layer depth for the (111) crystal plane was found to be consistently larger than those of other planes.

V. A shift to the (110) cleavage at the cutting temperatures higher than 2000 K was witnessed while cutting 3C-SiC. Moreover, crystallites of 3C-SiC in the cutting chip were observed in the all simulated temperatures i.e. 300 K-3000 K while cutting the (111) plane. Nevertheless, at 3000 K, the amount of cleavage was smaller than those of lower temperatures.

VI. More atoms in the cutting chip were observed while cutting silicon on the (110) crystal plane, attributable to the lower position of stagnation region which causes less ploughing action of the cutting tool. However, occurrence of large volume of cleavage while cutting 3C-SiC on the (111) crystal plane led to the observation of higher number of atoms in the chip while cutting the (111) plane.

VII. The magnitudes of the forces exerted by the tool rake face on the cutting chip decreased with the increase of the temperature of substrate for the studied crystallographic planes. Moreover, the minimum resultant force and friction coefficient at the tool rake face/chip interface were found when cutting the (111) crystal plane, whereas they reached their maximum value when cutting

the (110) plane, which confirmed that the mentioned surfaces are the easy and difficult-to-cut surfaces, respectively.

VIII. Lower thermal energy and in turn smaller extent of temperature increase (due to the generated heat) in the deformation zone were noticed while cutting silicon on the (111) plane or at high temperatures. Nevertheless, while cutting 3C-SiC, much higher extent of temperature increase caused by the generated heat in the deformation region was witnessed while cutting the (111) plane in the cutting temperature range of 300 K to 1400, plausibly due to occurrence of cleavage on this crystal plane.

IX. According to the stress state on the cutting edge of the diamond cutting tool, the atom-by-atom attrition wear was seen to be alleviated while cutting 3C-SiC at high temperatures i.e. 2000 K. On the other hand, the stress state and the temperature on the cutting edge of the diamond cutting tool during cutting of silicon suggested that a direct diamond to graphitic transformation or the plastic deformation of the diamond cutting tool is less likely under vacuum condition.

X. Substantial difference was observed in both the relative intensities and number of the diffraction peaks of the virtual XRD spectrums before and after cutting, signifying the amorphization of atoms in the cutting deformation region. In addition, the peaks in RDF became weaker and bond length was seen to increase as substrate temperature increased or after cutting.

XI. Dislocation nucleation and formation of stacking faults were identified in conjunction with amorphization of silicon as the meditators of crystal

plasticity in single crystal silicon during nanometric cutting process on different crystallographic planes at various temperatures. MD simulations revealed strong anisotropic dependence behaviour of dislocation activation and stacking fault formation, resultant from the ease of activating slip systems in single crystal silicon. While a large number of defects including dislocations and three atomic layers-stacking faults were formed during cutting the $(110)<00\bar{1}>$ orientation setup at different temperatures, low dislocation activity without stacking fault formation was observed for the $(010)<100>$ and $(111)<\bar{1}10>$ crystal plane setups. Furthermore, amorphization of silicon atoms was found to be more likely and dominative over defect formation at the initial stage of nanometric cutting.

XII. Successive formation and destruction of stacking fault-couple bounded between partial dislocation segments were observed while cutting 3C-SiC on the $(110)<00\bar{1}>$ plane setup at high temperatures. Furthermore, cross-junctions between pairs of counter stacking faults meditated by the gliding of Shockley partials on different slip planes were formed at 3000 K for the aforementioned crystal setup. Dislocation nucleation and stacking fault formation were observed to be dominant during cutting the $(110)<00\bar{1}>$ crystal setup. More importantly, the incipient plasticity of 3C-SiC in nanometric cutting was observed to occur by solid-state amorphization.

XIII. Through Raman spectroscopy, it was found that while room temperature nanoscratching of single crystal silicon at low scratching speed, above the transition load of ~5 mN, the nanoscratch is formed of Si-I, Si-XII and Si-III. The probability of forming high pressure phases of Si-III and Si-XII

increased above this load threshold. Moreover, Si-III phase was seen to be in minor quantity in the nanoscratch track. At high scratching speed, small remnants of Si-XII and Si-III phases were detected when the scratching load was greater than a threshold value i.e. ~9.5 mN. When high temperature nanoscratching was carried out at low and high speeds, no remnants of polymorph phases were observed all along the nanoscratch residual tracks, suggesting the transition of metastable silicon phases (Si-III and Si-XII) into thermodynamic stable Si-I.

XIV. AFM measurements revealed that the residual scratch morphologies were profoundly influenced by the scratching speed i.e. scratch depth, scratch width and pile-up heights decreased with the increase of scratching speed. Moreover, the aforementioned parameters were witnessed to increase with the rise of temperature as a result of thermal softening. Further analysis through calculating the nanoscratch hardness showed a reduction at high temperatures. Additionally, the nanoscratch hardness was found to increases as the scratching speed increased, signifying a strain rate strengthening of silicon material at higher scratching speeds.

## 7.3. Recommendations for future work

The present dissertation provided an in-depth understanding of nanometric cutting of hard-brittle materials i.e. silicon and silicon carbide at elevated temperatures through simulation and the experiment, including material removal phenomenon, anisotropic behaviour, chip related phenomena, tool wear, deformation mechanisms and phase transformation. Such information provides opportunities for the state-of-the-art

technological and scientific developments in the field of high temperature cutting of silicon and silicon carbide. However, there exist numerous facets which deserve further work, in particular:

### 7.3.1. Study on mechanisms involved in tool wear

Even though a preliminary assessment of the tool wear was carried out in this study, more research is required to fully understand the mechanisms involved in the tool wear i.e. mechanical and chemical wear during high temperature nanometric cutting of silicon and silicon carbide. Since there is still no robust potential function that can accurately describe all binary and tertiary phases of carbon, MD simulation cannot be applied in this case. Hence, experimental trials have to be performed at different temperatures under the atmospheric, reduced oxygen and vacuum conditions to determine the wear mechanisms and amount of tool wear during nanometric cutting at elevated temperatures in different conditions. This opens up the possibility for development of high temperature nanometric cutting more efficiently. Additionally, this evaluation helps us develop a cutting tool material which can withstand high temperatures without quickly blunting.

### 7.3.2. Research on polycrystalline silicon and silicon carbide

Much work has been performed on the nanometric cutting of single crystal silicon and silicon carbide at room and high temperatures. Nevertheless, polycrystalline silicon and silicon carbide are also employed in numerous real world applications such as solar panel, thin transistors, and VLSI manufacturing. The nanomechanical response of a polycrystalline material is expected to be different from that of a single crystal material primarily due to three-dimensional grain cell (GC), two-dimensional

grain boundary (GB), one-dimensional triple junction (TJ), and zero-dimensional vertex point (VP). Hence, an in-depth understanding of simultaneously occurring mechanisms during high temperature nanometric cutting of polycrystalline silicon and silicon carbide is vital.

#### 7.3.3. Investigation on influence of coolant

Surface integrity, chip generation process and tribo-chemistry of the diamond cutting tool can be affected by the application of coolant during nanometric cutting at elevated temperatures. Accordingly, it is crucial to investigate the influence of various types of coolants i.e. liquid nitrogen, odourless mineral spirits (OMS), water etc. on the aforementioned parameters. Such study would aid to optimize high temperature nanometric cutting of silicon and silicon carbide.

#### 7.3.4. Development of interatomic potential functions

Although several formalisms and refinements have been developed to describe interatomic interactions between silicon atoms as well as silicon and carbon atoms, there still exists a need to propose new potential functions having higher levels of transferability i.e. capable of correctly predicting both the mechanical and thermal properties such as elastic constants and melting temperature of these materials. Existence of separate parameter sets for an element under different conditions (e.g., liquid or solid phases) in the potential functions results in the lack of transferability. In such cases, the desired accuracy may be obtained by adopting new correction schemes i.e. recent Gaussian approximation potentials [33]. Furthermore, there is lack of a robust potential function to properly model phase transformation of silicon, carbon and silicon carbide at low and elevated temperatures during contact problems.

Such potential function will be very useful to improve our understanding of deformation mechanisms of silicon and silicon carbide, and help us have an enhanced understanding of the tool wear.

### 7.3.5. In situ observation of the scratching-induced phase transformation

While using an ex situ Raman microscope, the structure and phases of the material are detected only after the completion of the nanoscratch trials thus only remnant phases can be determined in this case. In order to probe the exact path of transformation and presence of intermediate phases for nanoscratched material, the nanoindentation/scratching machine should be coupled with a microscope so as to enable in situ Raman measurements.

### 7.3.6. Study on multi-pass nanometric cutting

All the MD simulation and experimental studies performed in this study have considered only one-pass cutting. Considering that the use of multi-pass cutting would be more economic to obtain the machined surface with minimum defects, multi-pass nanometric cutting simulatiuons and experiments at high temperatures could be performed to understand deformation mechanisms and material removal traits of silicon and silicon carbide in such process.

### 7.3.7. Investigation on effect of cutting speed

Due to computational limitations, the MD simulations in this work were performed at high cutting speed. It is suggested that in order to understand the effect of cutting speed on the dynamics of system and occurring phenomena in high temperature

nanometric cutting of silicon and silicon carbide, MD simulations using realistic cutting speeds (about 1 to 2 m/s) could be carried out and consequently the results could be compared with the obtained results in this study.

# Appendices

## A. Phase instability and melting temperature of silicon predicted by the ABOP and modified Tersoff

In order to calculate the phase instability temperature ($T_{inst}$) and entirely molten temperature ($T_{em}$) of silicon predicted by the ABOP and modified Tersoff interatomic potentials, the one-phase method was employed. Accordingly, a $15 \times 15 \times 15$ lattice cell of silicon containing 27,000 atoms was heated up under the NVT ensemble. Reflective boundaries and low heating rate of $9 \times 10^9 K/s$ were adopted in order to avoid the hysteresis phenomenon and superheating [122, 123]. $T_{inst}$ was observed at 2481 K and 1397 K, respectively, for the ABOP and the modified Tersoff potentials, where the Lindemann index [167] experienced an upward jump, as indicated in Figure A1. Due to the alteration of the atomic bonding of silicon from the covalent bond to metallic bond upon melting, atomic volume shrinkage (calculated using Voronoi tessellation [168]) equal to ~10.1% and ~9.2% was noticed when using the ABOP and the modified Tersoff potential functions, respectively, which are consistent with the reported experimental values [169, 170]. $T_{em}$ was calculated to be 2549 K and 1616 K when using the ABOP and modified Tersoff potential functions, respectively.

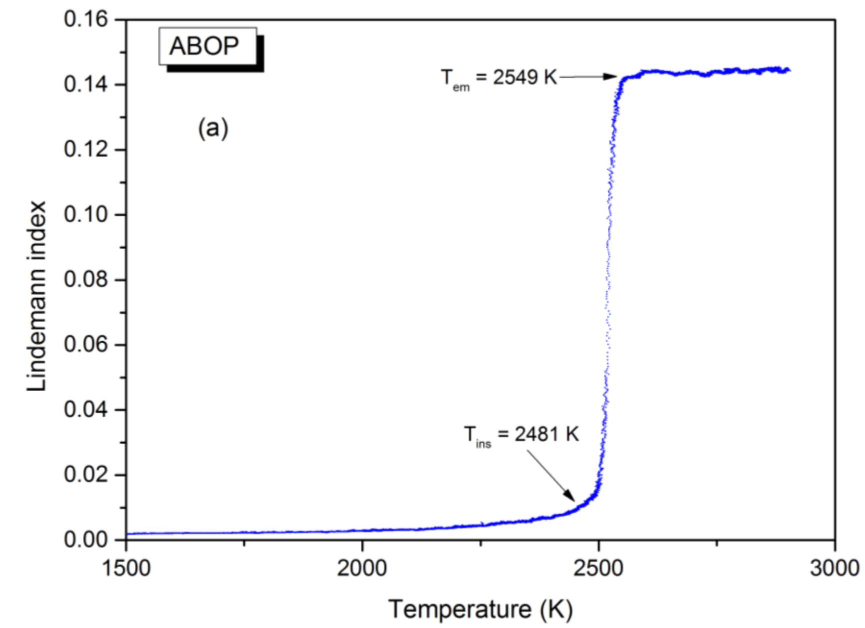


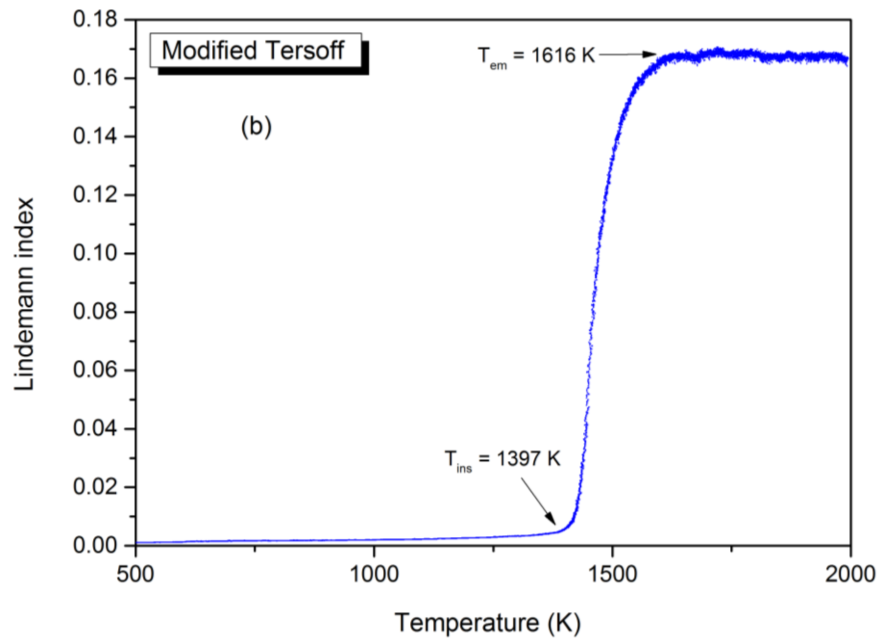


Figure A1. Variation of the Lindemann index upon incremental heating. $T_{inst}$ corresponds to the phase instability temperature while $T_{em}$ stands for the entirely molten temperature.

**B. Forces and associated parameters related to the chip while cutting silicon**

Table B1. Forces, friction, shear plane angle, chip velocity and chip temperature while cutting silicon on different crystal planes at various temperatures obtained by the ABOP potential function

| Temperature of the substrate (K) | Crystal plane | Tangential force exerted by the rake face on chip (nN) | Normal force exerted by the rake face on chip (nN) | Resultant force exerted by the rake face on chip (nN) | Friction coefficient at the rake face/chip interface | Shear plane angle (°) | Chip velocity (m/s) | Chip temperature (K) |
|---|---|---|---|---|---|---|---|---|
| 300 | (010) | 523.01 | 896.37 | 1037.8 | 0.5835 | 23.48 | 30.05 | 638.7 |
| | (110) | 560.52 | 898.98 | 1059.41 | 0.6235 | 22.8 | 28.85 | 657.7 |
| | (111) | 380.86 | 808.71 | 893.9 | 0.4709 | 23.65 | 30.35 | 659.7 |
| 500 | (010) | 492.29 | 825.59 | 961.22 | 0.5963 | 23.82 | 30.65 | 738.9 |
| | (110) | 519.07 | 867.4 | 1010.8 | 0.5984 | 23.0 | 29.35 | 760.6 |

| | | | 3 | 7 | | 9 | | |
|---|---|---|---|---|---|---|---|---|
| | (111) | 342.59 | 724.18 | 801.13 | 0.4731 | 24.21 | 31.35 | 736.9 |
| 750 | (010) | 455.81 | 785.25 | 907.95 | 0.5804 | 24.14 | 31.25 | 865.3 |
| | (110) | 511.66 | 784.12 | 936.29 | 0.6525 | 23.38 | 29.85 | 918.8 |
| | (111) | 314.38 | 679.18 | 748.41 | 0.4629 | 24.9 | 32.65 | 833.1 |
| 850 | (010) | 438.79 | 764.58 | 881.54 | 0.5739 | 24.14 | 31.25 | 940 |
| | (110) | 504.76 | 764.46 | 916.07 | 0.6603 | 23.38 | 29.85 | 999.3 |
| | (111) | 310.75 | 653.55 | 723.66 | 0.4754 | 25.31 | 33.45 | 900.7 |
| 1173 | (010) | 378.85 | 694.38 | 791.01 | 0.5456 | 24.46 | 31.85 | 1228.6 |
| | (110) | 468.13 | 727.47 | 865.08 | 0.6435 | 23.25 | 29.65 | 1286.2 |
| | (111) | 290.6 | 609.92 | 675.61 | 0.4764 | 26.44 | 35.7 | 1218.3 |
| 1500 | (010) | 366.47 | 620.32 | 720.48 | 0.5908 | 20.69 | 25.3 | 1596.4 |
| | (110) | 468.64 | 678.7 | 824.79 | 0.6905 | 19.2 | 22.95 | 1608.9 |

| | | | 2 | | | | | |
|---|---|---|---|---|---|---|---|---|
| | (111) | 161.53 | 465.97 | 493.17 | 0.3466 | 20.41 | 24.8 | 1589.7 |

**C. Accuracy of the modified Tersoff and ABOP potentials in reproducing the mechanical properties of silicon**

The accuracy of the modified Tersoff and ABOP in reproducing the mechanical properties of silicon such as elastic constants, Bulk modulus, Shear modulus, Young's modulus (on three different planes), anisotropy ratio and Voigt Poisson's ratio are examined in order to make a judgement for the employability of the appropriate potential function. Table C1 presents a comparison of the aforementioned parameters obtained by ABOP and modified Tersoff potentials against experimental values. It may be seen from Table C1 that the predictions made by the ABOP potential are consistent with the experiments whereas there exists a remarkable discrepancy between the experimental values and the predictions made by the modified Tersoff potential.

Table C1. Experimental properties of single crystal silicon compared with the MD simulation

| **Mechanical properties of silicon** | **ABOP** | **Modified Tersoff** | **Experiment** [171] |
|---|---|---|---|
| $C_{11}=C_{22}=C_{33}$ (GPa) | 167 | 121 | 168 |
| $C_{12}=C_{13}=C_{23}$ (GPa) | 65 | 86 | 65 |
| $C_{44}=C_{55}=C_{66}$ (GPa) | 60 | 49 | 80 |
| Anisotropy ratio (A) $\frac{2C_{44}}{C_{11}-C_{12}}$ | 1.176 | 2.8 | 1.553 |
| Bulk modulus (B) (GPa) | 99 | 98 | 99 |

| $\frac{C_{11}+2C_{12}}{3}$ | | | |
|---|---|---|---|
| Shear modulus (G) (GPa) $\frac{C_{11}-C_{12}+C_{44}}{3}$ | 54 | 28 | 61 |
| Young's modulus ($E_{100}$) (GPa) $C_{11}-2\frac{C_{12}}{C_{11}+C_{12}}C_{12}$ | 130.5 | 49.5 | 132 |
| Young's modulus ($E_{110}$) (GPa) $4\frac{(C_{11}^{2}+C_{12}C_{11}-2C_{12}^{2})C_{44}}{2C_{44}C_{11}+C_{11}^{2}+C_{12}C_{11}-2C_{12}^{2}}$ | 144 | 91 | 171 |
| Young's modulus ($E_{111}$) (GPa) $3\frac{C_{44}(C_{11}+2C_{12})}{C_{11}+2C_{12}+C_{44}}$ | 150 | 126 | 189 |
| Voigt Poisson's ratio ($\nu$) $\frac{C_{12}-\frac{2C_{44}+C_{12}-C_{11}}{5}}{2(C_{12}+C_{44}-2\frac{2C_{44}+C_{12}-C_{11}}{5})}$ | 0.26 | 0.33 | 0.22 |

In order to further cross-examine the employability of the potentials, we carried out nanoscale tensile and shear tests on silicon. The strain controlled simulation tests were prescribed a strain rate of $(5 \times 10^{7})s^{-1}$ along the <100> axis of silicon nanowire. The size of the silicon nanowire employed during the tensile test was $32.5 \times 8.1 \times 8.1 nm^{3}$, while the one used for the shear test was $16.3 \times 16.3 \times 8.1 nm^{3}$. PBC was applied along the direction of applied strain (*x*-axis) whereas shrink-wrapped boundaries were applied in the lateral dimensions. The typical tensile

and shear stress-strain response of the [100]-oriented silicon nanowire at room temperature is shown in Figure C1. The values of Young's modulus (*E*) and shear modulus (*G*) were also obtained by fitting the stress-strain curves to straight lines in the strain range of 0 to 5%. The Young's modulus calculated by the ABOP at room temperature is around 131 GPa, which is close to the Young's modulus of Si <001> nanowires obtained from first-principle density functional theory (~122 GPa) [172]. The stress curve follows the non-linear elastic behaviour and the specimen deforms until abrupt fracture occurs. As shown in Figure C1, while using the ABOP, the stress suddenly drops to zero immediately after the fracture and can be regarded as a typical cleavage fracture on a transverse (010) plane. The fracture surface in the tensile test specimen was found to be perpendicular to the pulling direction, which is the *x*-axis. Thus, the ABOP potential shows brittle fracture behaviour as the mode of failure of silicon nanowire. Conversely, the modified Tersoff variant showed ductile deformation and predicts a much lower value of the elastic modulus of silicon. Also, the modified Tersoff showed that the shear failure takes place on a (111) sliding plane, as evident in Figure C1b.

From what has been discussed above, one may deduce that ABOP is robust in describing the mechanical properties of silicon over the modified variant of Tersoff. Therefore, we adopt the ABOP potential for reporting mechanical properties of silicon and whenever needed a comparison is made between the results obtained by both the potentials.

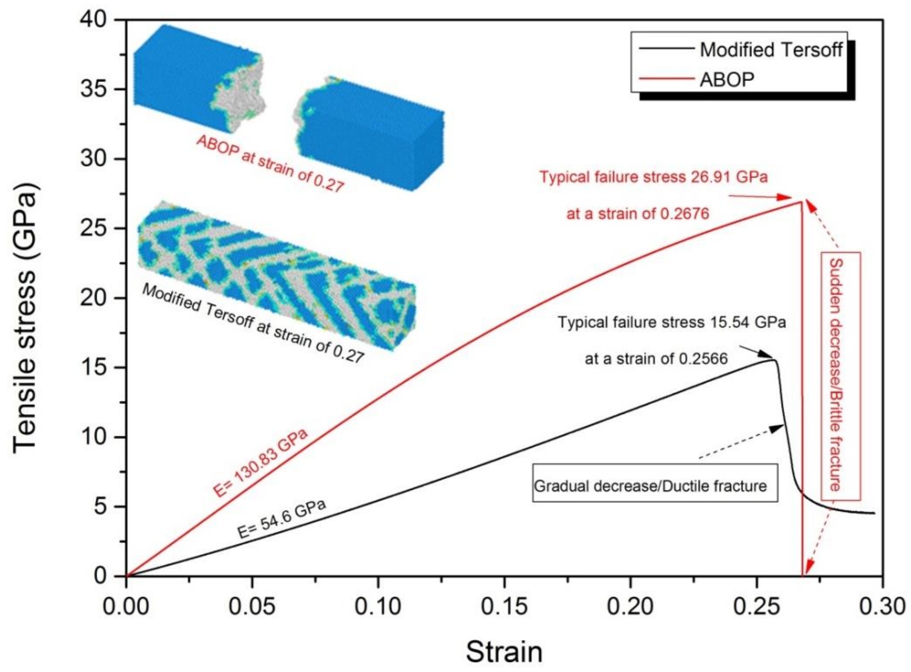


(a)

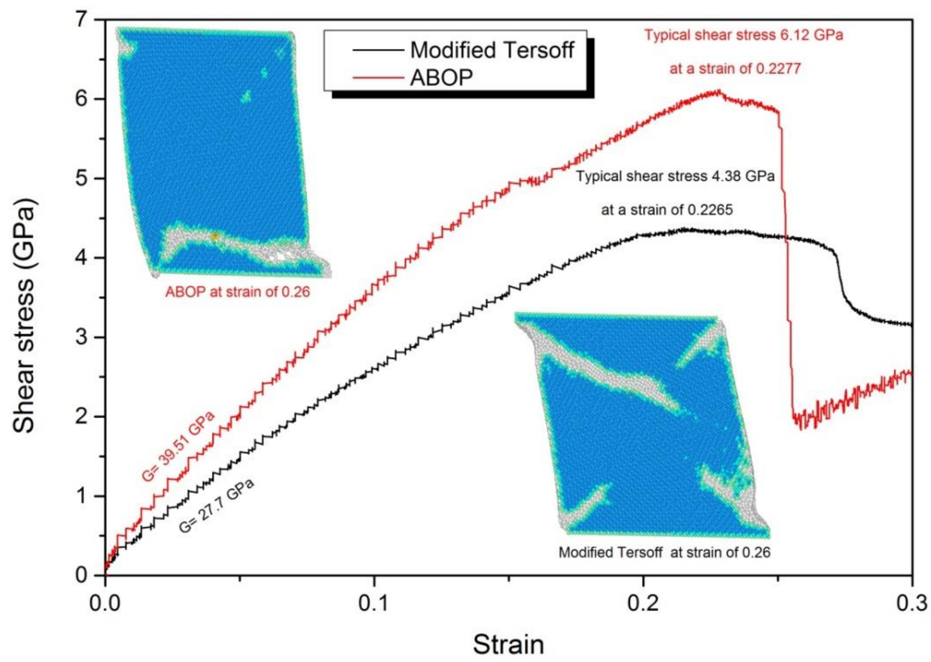


(b)

Figure C1. (a) Tensile stress-strain curve and (b) shear stress-strain curve of the [100]-oriented single crystal silicon at 300 K obtained by modified Tersoff and ABOP potential energy functions

## D. Cutting forces and associated parameters while cutting silicon

Table D1. Average forces and associated parameters while cutting silicon on different crystal planes at various temperatures obtained by ABOP potential function

| Workpiece temperature (K) | Crystal plane | Average tangential cutting force (nN) | Average thrust force (nN) | Average resultant force (nN) | Average specific cutting energy (GPa) | Average force ratio |
|---|---|---|---|---|---|---|
| 300 | (010) | 535.9 | 772.9 | 940.5 | 58 | 0.69 |
| | (110) | 523.7 | 804.7 | 960.2 | 59.3 | 0.65 |
| | (111) | 518.4 | 622.6 | 810.1 | 50 | 0.83 |
| 500 | (010) | 489.6 | 720.6 | 871.2 | 53.8 | 0.68 |
| | (110) | 513.7 | 758.6 | 916.2 | 56.5 | 0.67 |
| | (111) | 463.6 | 558.8 | 726.1 | 44.8 | 0.83 |
| 750 | (010) | 470.4 | 675.2 | 822.9 | 50.8 | 0.69 |
| | (110) | 448.1 | 720.6 | 848.6 | 52.4 | 0.62 |
| | (111) | 437.5 | 518.4 | 678.3 | 41.9 | 0.84 |
| 850 | (010) | 459.9 | 653.3 | 798.9 | 49.3 | 0.7 |
| | (110) | 434.6 | 707.4 | 830.2 | 51.2 | 0.61 |
| | (111) | 417.8 | 505.6 | 655.9 | 40.5 | 0.82 |
| 1173 | (010) | 425.2 | 577.1 | 716.9 | 44.2 | 0.73 |
| | (110) | 418.2 | 663.2 | 784 | 48.4 | 0.63 |
| | (111) | 389.7 | 472.3 | 612.3 | 37.8 | 0.82 |

| | | | | | | |
|---|---|---|---|---|---|---|
| 1500 | (010) | 369.2 | 538.6 | 652.9 | 40.3 | 0.68 |
| | (110) | 378 | 644.9 | 747.5 | 46.1 | 0.58 |
| | (111) | 320.9 | 311.2 | 446.9 | 27.6 | 1.03 |

## E. Yielding stresses while cutting silicon

Table E1. Stresses and temperatures in the cutting zone while machining silicon on different crystal planes obtained by ABOP potential function

| Workpiece temperature (K) | Crystal plane | Von Mises stress (GPa) | Octahedral stress (GPa) | Tresca stress (GPa) | Minor principal stress (GPa) | Major principal stress (GPa) | Peak temperature in the cutting zone (K) | Temperature at the onset of plastic yielding (K) |
|---|---|---|---|---|---|---|---|---|
| 300 | (010) | 13.6 | 6.41 | 7.74 | -0.87 | -16.36 | 670.8 | 594.6 |
| | (110) | 12.89 | 6.08 | 7.12 | -1.95 | -16.2 | 677.7 | 607.5 |
| | (111) | 14.58 | 6.87 | 8.38 | 3.14 | -13.63 | 663.1 | 562.8 |
| 500 | (010) | 12.58 | 5.93 | 7.16 | -0.53 | -14.85 | 780.1 | 708.5 |
| | (110) | 12.59 | 5.93 | 7.05 | -3.76 | -17.87 | 795.8 | 744.2 |
| | (111) | 14.25 | 6.72 | 7.62 | 1.1 | -14.15 | 751.1 | 676 |
| 750 | (010) | 11.85 | 5.57 | 6.74 | -0.02 | -13.51 | 925.8 | 858.3 |

| | (110) | 12.45 | 5.87 | 6.95 | -0.38 | -14.29 | 971.4 | 908.1 |
|---|---|---|---|---|---|---|---|---|
| | (111) | 13.82 | 6.51 | 7.24 | -0.55 | -15.03 | 865.4 | 824.1 |
| 850 | (010) | 11.69 | 5.51 | 6.67 | -0.38 | -13.72 | 973.5 | 908.1 |
| | (110) | 12.56 | 5.92 | 7.06 | -0.88 | -15 | 1076.7 | 967.4 |
| | (111) | 11.88 | 5.6 | 6.5 | 1.48 | -11.52 | 952.7 | 876.5 |
| 1173 | (010) | 11.96 | 5.64 | 6.74 | -2.44 | -15.93 | 1320.7 | 1152 |
| | (110) | 12.52 | 5.9 | 7.13 | -0.65 | -14.91 | 1415.7 | 1223.2 |
| | (111) | 9.97 | 4.7 | 5.57 | 1.9 | -9.25 | 1245.5 | 1094.9 |
| 1500 | (010) | 10.85 | 5.11 | 6.16 | 0.84 | -11.48 | 1618.3 | 1304.9 |
| | (110) | 11.46 | 5.4 | 6.38 | -0.48 | -13.24 | 1781.7 | 1364.2 |
| | (111) | 9.16 | 4.32 | 4.96 | 0.86 | -9.06 | 1593.6 | 1234.7 |

## F. Equations used for calculating yielding measures

$$\text{Stress tensor} = \begin{bmatrix} \sigma_{xx} & \tau_{xy} & \tau_{xz} \\ \tau_{xy} & \sigma_{yy} & \tau_{yz} \\ \tau_{xz} & \tau_{xz} & \sigma_{zz} \end{bmatrix} \quad (1)$$

$$I_1 = \sigma_{xx} + \sigma_{yy} + \sigma_{zz} \quad (2)$$

$$I_2 = \sigma_{xx}\sigma_{yy} + \sigma_{yy}\sigma_{zz} + \sigma_{zz}\sigma_{xx} - \tau_{xy}^2 - \tau_{xz}^2 - \tau_{yz}^2 \quad (3)$$

$$I_3 = \sigma_{xx}\sigma_{yy}\sigma_{zz} + 2(\tau_{xy}\tau_{yz}\tau_{xz}) - \tau_{xz}^2\sigma_{yy} - \tau_{yz}^2\sigma_{xx} - \tau_{xy}^2\sigma_{zz} \quad (4)$$

$$A_1 = -I_1;\ A_2 = I_2;\ A_3 = -I_3 \quad (5)$$

$$Q = \frac{3A_2 - A_1^2}{9} \quad (6)$$

$$R = \frac{9A_1A_2 - 27A_3 - 2A_1^3}{54} \quad (7)$$

$$D = Q^3 + R^2 \quad (8)$$

If D<0 then as follows: else the condition is 2D stress

$$\theta = cos^{-1}\left(\frac{R}{\sqrt{-Q^3}}\right) \quad (9)$$

$$R_1 = 2\sqrt{-Q} \times cos\left(\frac{\theta}{3}\right) - \frac{A_1}{3} \quad (10)$$

$$R_2 = 2\sqrt{-Q} \times cos\left(\frac{\theta + 4\pi}{3}\right) - \frac{A_1}{3} \quad (11)$$

$$R_3 = 2\sqrt{-Q} \times cos\left(\frac{\theta + 2\pi}{3}\right) - \frac{A_1}{3} \quad (12)$$

$$\sigma_1 = \max(R_1, R_2, R_3);\ \sigma_3 = \min(R_1, R_2, R_3) \quad (14)$$

$$\sigma_{tresca} = \frac{\sigma_1 - \sigma_3}{2} \quad (15)$$

$$\sigma_{\text{von Mises}} = \sqrt{\frac{(\sigma_{xx} - \sigma_{yy})^2 + (\sigma_{yy} - \sigma_{zz})^2 + (\sigma_{zz} - \sigma_{xx})^2 + 6(\tau_{xy}^2 + \tau_{yz}^2 + \tau_{zx}^2)}{2}} \quad (16)$$

$$\sigma_{oct} = \frac{\sqrt{(\sigma_{xx} - \sigma_{yy})^2 + (\sigma_{yy} - \sigma_{zz})^2 + (\sigma_{zz} - \sigma_{xx})^2 + 6(\tau_{xy}^2 + \tau_{yz}^2 + \tau_{zx}^2)}}{3} = \frac{\sqrt{2}}{3}\sigma_{\text{von Mises}} \quad (17)$$

## G. Stresses and temperatures on the cutting edge of the diamond tool while cutting silicon

Table F1. Average stresses and temperatures on the cutting edge of the diamond tool while machining silicon on different crystal planes obtained by ABOP potential function

| Workpiece temperature (K) | Crystal plane | von Mises stress on the cutting edge (GPa) | Tresca stress on the cutting edge (GPa) | Temperature on the cutting edge (K) |
|---|---|---|---|---|
| 300 | (010) | 25.2 | 14.1 | 347.5 |
| | (110) | 25.8 | 14.6 | 347.7 |
| | (111) | 24.4 | 13.9 | 337.4 |
| 500 | (010) | 24.8 | 14 | 351 |
| | (110) | 25.4 | 14.1 | 349.6 |
| | (111) | 23.9 | 13.4 | 346.1 |
| 750 | (010) | 24.8 | 13.7 | 370.6 |
| | (110) | 23.1 | 13.4 | 366.6 |
| | (111) | 22.7 | 12.1 | 356.8 |
| 850 | (010) | 24.1 | 13.7 | 382.3 |
| | (110) | 22.9 | 12.6 | 379.1 |
| | (111) | 22.2 | 12 | 365.3 |
| 1173 | (010) | 18.8 | 10.8 | 406.7 |
| | (110) | 19 | 10.7 | 399.4 |

| | | | | |
|---|---|---|---|---|
| | (111) | 18.4 | 10.3 | 366.9 |
| 1500 | (010) | 18.6 | 10.5 | 410 |
| | (110) | 18.6 | 10.6 | 413.1 |
| | (111) | 18.1 | 10 | 375 |

### H. Testing of the SW potential energy function

The robustness of SW potential in reproducing the stacking fault energy (SFE), melting temperature, the elastic constants and other relevant mechanical properties of silicon were assessed so as to ensure that the appropriate potential function has been selected for the study of defect-mediated plasticity at a wide range of temperatures. The SW potential provides a better approximation of the maximum restoring force, the theoretical shear strength, and the strain associated with the critical stress for both shuffle and glide sets planes than the Tersoff [39] and Environment-Dependent Interatomic Potential (EDIP) [173] potentials. Moreover, the SW potential leads to smooth SFE variations, in agreement with the *ab-initio* simulations [111, 174, 175]. Some caveats of the SW potential include an underestimation of the unstable/stable SFE for the shuffle set-plane and an overestimation of them for the glide set-plane. The space between two successive double-layers is known as the shuffle set, while the space between the two planes of the double-layer is called glide set. As a result, it is expected that for the glide set-plane, using the SW potential, (1) both the leading and trailing partials are more difficult to nucleate and (2) the stacking fault width is smaller, compared with the *ab-initio* simulations. The opposite is true for the shuffle set-plane. Nevertheless, in the motion of dislocations, the unstable SFE is less important than the rebound force of the lattice subject to large deformations, which is accurately given by the SW potential [111].

In order to obtain the melting point of silicon estimated by SW potential, the solid-liquid coexistence method was employed. A $15 \times 15 \times 60$ lattice cell comprising of 108000 atoms was equilibrated at an initial guess in a way that the longer direction (<001>) was normal to the solid-liquid interface, and the entire simulation was

repeated so as to bracket the melting point. The detailed procedure can be found elsewhere [176, 177]. It can be seen from Figure H1 that the simulation cell solidifies completely at 1670 K after 8.4 ns. Similarly, the simulation cell melts entirely at 1690 K after 5.7 ns. The melting point is determined to be $T_m = 1678\ K$, where the line of average potential energy has almost zero slope, as demonstrated in Figure H1. Clearly, there is a good consistency between the experimental value of melting point (1687 K) [178] and that predicted by the SW potential.

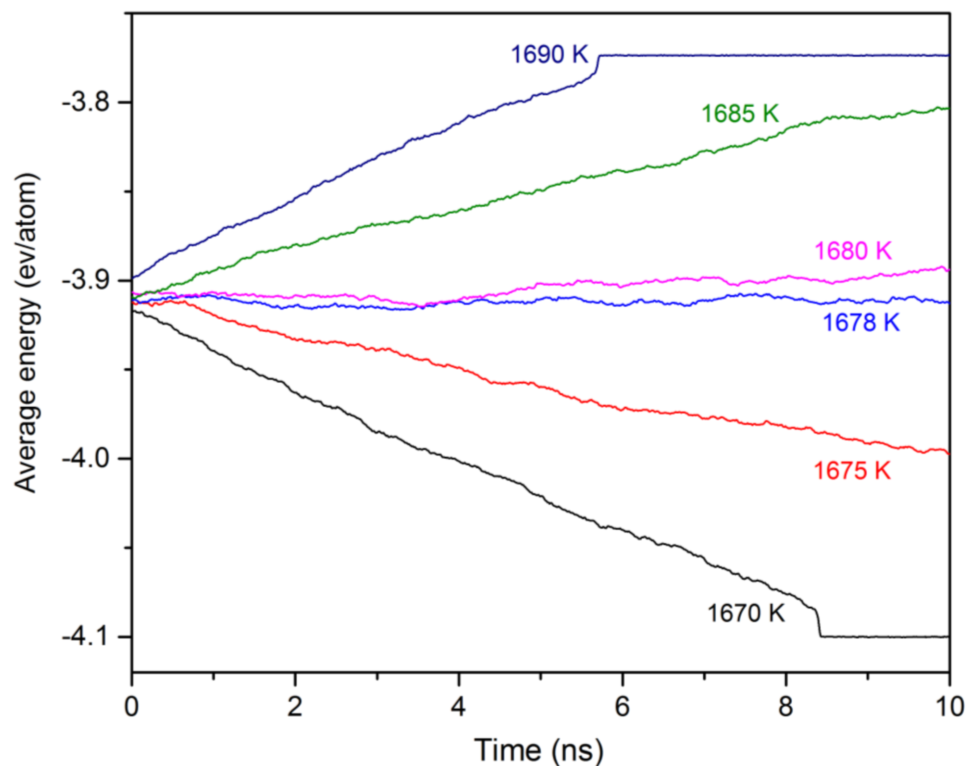


Figure H1. Evolution of average potential energy versus simulation time for an initially coexisting solid-liquid structure equilibrated at various temperatures using an NPT ensemble

The accuracy of the SW potential function in reproducing the mechanical properties of silicon such as elastic constants, bulk modulus, shear modulus, Young's modulus

on the three crystallographic planes and Voigt averages were also evaluated and compared with the corresponding experimental magnitudes, listed in Table H1. It was found that the SW potential accurately reproduces the melting temperature of silicon which, however, comes as a price that the cohesive energy is rescaled; by consequence, the elastic constants are also rescaled, leading to some inconsistencies in reproducing relevant mechanical properties of silicon with those of experiments, as indicated in Table H1. Taking into account the restricted transferability of empirical potentials, the SW potential is a good choice for exploring dislocation-mediated plasticity of silicon at room and elevated temperatures during nanometric cutting.

Table H1. Material properties of single crystal silicon obtained by experiment and MD simulations.

| **Properties of silicon** | **SW** | **Experiment** [171] |
|---|---|---|
| $C_{11}=C_{22}=C_{33}$ (GPa) | 151.4 | 168 |
| $C_{12}=C_{13}=C_{23}$ (GPa) | 76.4 | 65 |
| $C_{44}=C_{55}=C_{66}$ (GPa) | 56.4 | 80 |
| Young's modulus ($E_{100}$) (GPa) $C_{11}-2\frac{C_{12}}{C_{11}+C_{12}}C_{12}$ | 100.1 | 131.7 |
| Young's modulus ($E_{110}$) (GPa) $4\frac{(C_{11}^2+C_{12}C_{11}-2C_{12}^2)C_{44}}{2C_{44}C_{11}+C_{11}^2+C_{12}C_{11}-2C_{12}^2}$ | 129 | 170.6 |
| Young's modulus ($E_{111}$) (GPa) | 142.7 | 189.2 |

| | | |
|---|---|---|
| $3\frac{C_{44}(C_{11}+2C_{12})}{C_{11}+2C_{12}+C_{44}}$ | | |
| Bulk modulus (B) (GPa) $\frac{C_{11}+2C_{12}}{3}$ | 101.4 | 99.3 |
| Shear modulus (G) (GPa) $\frac{C_{11}-C_{12}+C_{44}}{3}$ | 43.8 | 61 |
| Anisotropy factor (H) (GPa) $2C_{44}+C_{12}-C_{11}$ | 37.8 | 57 |
| Voigt shear modulus (μ) (GPa) $C_{44}-\frac{1}{5}H$ | 48.8 | 68.6 |
| Voigt Poisson's ratio ( $\nu$ ) $\frac{C_{12}-\frac{H}{5}}{2(C_{12}+C_{44}-2\frac{H}{5})}$ | 0.29 | 0.22 |

## I. Testing of the ABOP and Tersoff potential energy functions for 3C-SiC

The accuracy of the employed potential functions i.e. ABOP and Tersoff in reproducing of elastic constants and other mechanical characteristics of 3C-SiC was assessed and summarized in Table I1. In general, ABOP potential is more precise particularly in producing the Voigt averages, which are known to be better to deal with local strains around dislocations [179].

Table I1. Material properties of single crystal 3C-SiC obtained by experiment and MD simulations.

| **Properties of 3C-SiC** | **ABOP** | **Tersoff** | **Experiment** [180] |
|---|---|---|---|
| $C_{11}=C_{22}=C_{33}$ (GPa) | 382 | 447 | 390 |
| $C_{12}=C_{13}=C_{23}$ (GPa) | 145 | 134 | 142 |
| $C_{44}=C_{55}=C_{66}$ (GPa) | 240 | 293 | 256 |
| Anisotropy ratio (A) $\frac{2C_{44}}{C_{11}-C_{12}}$ | 2.02 | 1.87 | 2.06 |
| Anisotropy factor (H) (GPa) $2C_{44}+C_{12}-C_{11}$ | 243 | 273 | 264 |
| Bulk modulus (B) (GPa) $\frac{C_{11}+2C_{12}}{3}$ | 224 | 238 | 225 |
| Young's modulus ($E_{100}$) (GPa) $C_{11}-2\frac{C_{12}}{C_{11}+C_{12}}C_{12}$ | 302 | 385 | 314 |
| Young's modulus ($E_{110}$) (GPa) | 446 | 540 | 467 |

| $4\frac{(C_{11}^{2}+C_{12}C_{11}-2C_{12}^{2})C_{44}}{2C_{44}C_{11}+C_{11}^{2}+C_{12}C_{11}-2C_{12}^{2}}$ | | | |
|---|---|---|---|
| Young's modulus ($E_{111}$) (GPa) $3\frac{C_{44}(C_{11}+2C_{12})}{C_{11}+2C_{12}+C_{44}}$ | 531 | 623 | 557 |
| Voigt shear modulus (μ) (GPa) $C_{44}-\frac{1}{5}H$ | 191.4 | 238.4 | 203.2 |
| Voigt Poisson's ratio ( $\nu$ ) $\frac{C_{12}-\frac{H}{5}}{2(C_{12}+C_{44}-2\frac{H}{5})}$ | 0.167 | 0.125 | 0.152 |
| Voigt Young's modulus (E) (GPa) $2\mu(1+\nu)$ | 446.9 | 536.4 | 468.4 |

In order to obtain a better understanding of defect formation, the GSFE surfaces and ideal shear stresses required to nucleate dislocations for the two main slip systems of the zinc blende structure of 3C-SiC, shuffle <110>{111} and glide <112>{111}, were assessed via block shearing process [181, 182]. 3C-SiC structure is defined as the stacking of double-layers {111} planes. The lowest energy barrier required to be crossed for the slip from the ideal configuration to the intrinsic stacking fault configuration is called unstable GSFE surfaces, which is improbable to be measured experimentally [183]. The unstable GSFE surfaces can be combined with Peierls-Nabarro (P-N) models [128, 129] to estimate dislocation core properties; hence an accurate prediction of GSFE surfaces determines the ability of the interatomic

potential in producing the nucleation, dissociation and mobility of dislocations [116, 121, 184-187]. It has been reported that the energy release rate during the dislocation nucleation corresponds to the unstable GSFE or the lowest energy barrier to be crossed during a slip along a specific crystallographic direction [188]. Figure I1a and Figure I1b depict the GSFE curves obtained via block shearing process. Two interatomic potentials exhibit almost similar qualitative behaviour for the shuffle and glide sets. The unstable and intrinsic stacking fault configurations correspond to a slip of $0.342a_0$ and $0.409a_0$ ($a_0$ is the lattice constant), respectively, in the <112> directions. The projection of GSFE curves on the <110> direction is symmetric corresponding to a slip of $0.353a_0$. As seen in Figure I1a, the value of unstable stacking fault energy ($\gamma_{us}$) in the glide <112>{111} predicted by the ABOP is lower than that of the Tersoff potential, indicative of smaller energy barrier, suggesting that dislocations can be nucleated more easily while using the ABOP potential. It is worth pointing out here that the DFT calculates the unstable GSFE surfaces in the glide set to be 0.1747 $^{eV}/_{Å^2}$ [147, 189], suggesting the overestimation of the unstable GSFE by the two empirical potentials employed in this study. Nevertheless, the given value by the ABOP is closer to the DFT calculation. Furthermore, the intrinsic stacking fault energy ($\gamma_{isf}$) for Tersoff function is found much higher than that of ABOP, indicating that the stacking faults are less likely to form while applying Tersoff potential. It is generalized that stacking faults are common in SiC owing to the low stacking fault energy [190]. The *ab initio* calculations revealed a value of $\gamma_{isf} = 0.2323$ $^{eV}/_{Å^2}$ [191], which is close to the magnitude given by the ABOP (0.2717 $^{eV}/_{Å^2}$).

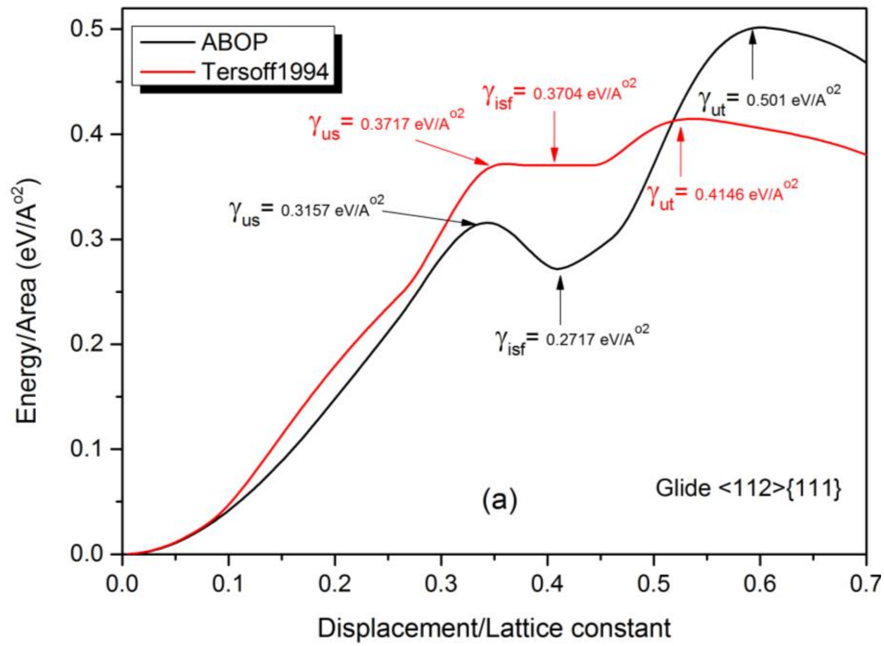


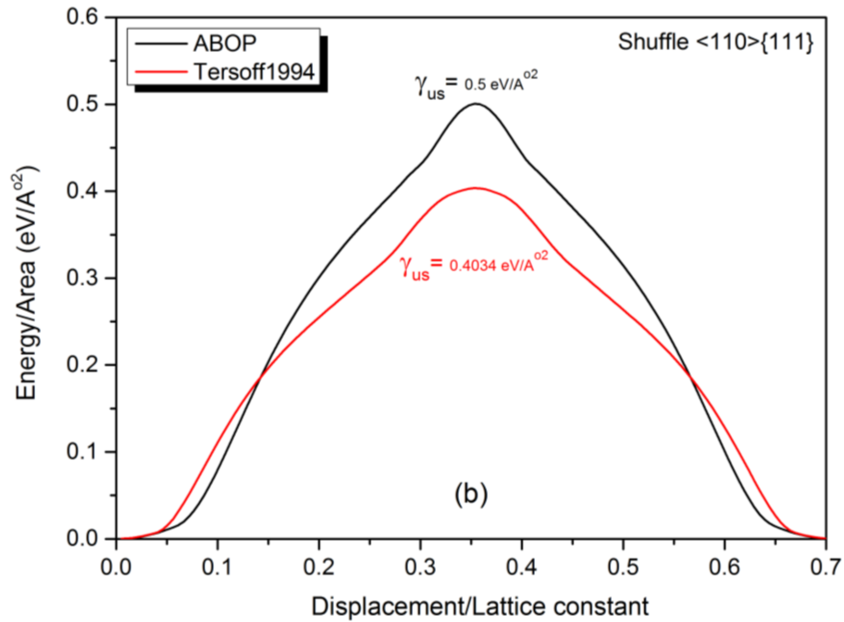


Figure I1. GSFE curves for the glide <112>{111} and shuffle <110>{111} slip systems obtained by the ABOP and Tersoff interatomic potentials

It is also instructive to mention that the unstable twinning fault energy ($\gamma_{ut}$) estimated by the ABOP is higher than that of the Tersoff. The high ratio of $\gamma_{ut}/\gamma_{us}$

(~1.58) for the ABOP shows that the energy barriers for twinning formation are higher than those for dislocation nucleation thus twinning is difficult to form (low twinability) while utilizing this potential. However, this value for the Tersoff potential is close to unity, signifying the ease of twinning formation under specific circumstances.

As for the shuffle <110>{111} slip, the predicted unstable GSFE by the Tersoff potential is lower than that of the ABOP. The calculated unstable GSFE surface in the shuffle set by the DFT is 0.169 $^{eV}/_{Å^2}$ [147, 189], which is much lower than those estimated by the two potential functions. It is of note that the dislocation activity is strongly subject to the crystal planes of cutting plane and cutting direction [130].

More importantly, the Schmid factor of glide slip system is 0.471 which is larger than that of shuffle slip system, i.e. 0.408, indicating a higher likelihood for slip in the glide slip system. In addition, glide dislocations are more sensitive to thermal activation [192].

Overall, it can conclude that ABOP is more robust in predicting the mechanical properties especially Voigt averages which are associated to the dislocations. Besides, dislocation nucleation in the glide set and stacking fault formation given by ABOP are in better agreement with the DFT and *ab initio* calculations. Hence, we report the results based on the ABOP function and whenever needed, comparison is made with the results obtained by Tersoff potential.

## J. Forces and specific cutting energy while cutting 3C-SiC

Table J1. Average forces and specific cutting energy while cutting single crystal 3C-SiC on different crystal planes at various temperatures

| Workpiece temperature (K) | Crystal plane | Average tangential cutting force (nN) | Average thrust force (nN) | Average resultant force (nN) | Average specific cutting energy (GPa) |
|---|---|---|---|---|---|
| 300 | (010) | 2112 | 4564.8 | 5029.7 | 381 |
| | (110) | 2280.5 | 4660.6 | 5188.6 | 393.1 |
| | (111) | 2122.3 | 2943.1 | 3628.5 | 274.9 |
| 900 | (010) | 1863.7 | 4156.8 | 4555.5 | 345.1 |
| | (110) | 1988 | 4462.9 | 4885.7 | 370.1 |
| | (111) | 1781 | 2393.4 | 2983.4 | 226 |
| 1200 | (010) | 1869.7 | 4100.4 | 4506.6 | 341.4 |
| | (110) | 1888.5 | 4463.5 | 4846.6 | 367.2 |
| | (111) | 1741.6 | 2270.7 | 2861.7 | 216.8 |
| 1400 | (010) | 1792.9 | 3691.4 | 4103.8 | 310.9 |
| | (110) | 1934.8 | 4349.3 | 4760.2 | 360.6 |
| | (111) | 1680.3 | 2062.3 | 2660.1 | 201.5 |
| 1700 | (010) | 1604.7 | 2983.1 | 3387.3 | 256.6 |
| | (110) | 1841.1 | 3459.6 | 3919 | 296.9 |
| | (111) | 1554.9 | 1947.8 | 2492.3 | 188.8 |

| | | | | | |
|---|---|---|---|---|---|
| 2000 | (010) | 1433.6 | 2526.2 | 2904.7 | 220 |
| | (110) | 1672.7 | 2804.8 | 3265.7 | 247.4 |
| | (111) | 1606.3 | 1864.1 | 2460.7 | 186.4 |
| 3000 | (010) | 1067.1 | 1717 | 2021.6 | 153.1 |
| | (110) | 1330.6 | 2039.5 | 2435.2 | 184.5 |
| | (111) | 1267.6 | 1402.9 | 1890.8 | 143.2 |

**K. Yielding stresses while cutting 3C-SiC**

Table K1. Stresses and temperatures in the cutting region while cutting 3C-SiC on different crystal planes obtained by ABOP potential function

| Substrate temperature (K) | Crystal plane | Von Mises stress (GPa) | Octahedral stress (GPa) | Tresca stress (GPa) | Minor principal stress (GPa) | Major principal stress (GPa) | Peak temperature in the cutting zone (K) | Temperature at the onset of plastic yielding (K) |
|---|---|---|---|---|---|---|---|---|
| 300 | (010) | 104.33 | 49.18 | 60.02 | -147.02 | -26.98 | 979.2 | 832 |
| | (110) | 121.62 | 57.33 | 61.63 | -157.84 | -34.58 | 1034.9 | 806.7 |
| | (111) | 80.14 | 37.78 | 43.93 | -82.85 | 5.01 | 1420.4 | 948.3 |
| 900 | (010) | 96.16 | 45.33 | 55.38 | -110.46 | 0.31 | 1467.3 | 1303.6 |
| | (110) | 101.13 | 47.67 | 56.69 | -119.44 | -6.05 | 1463 | 1327.8 |
| | (111) | 69.95 | 32.97 | 37.59 | -72.4 | 2.78 | 1942.7 | 1312.3 |
| 1200 | (010) | 84.81 | 39.98 | 48.47 | -114.74 | -17.79 | 1804.7 | 1407.5 |
| | (110) | 98.82 | 46.58 | 54.32 | -128.62 | -19.98 | 1659.5 | 1490.3 |
| | (111) | 64.8 | 30.55 | 35.11 | -62.64 | 7.59 | 2017.6 | 1402.7 |
| 1400 | (010) | 80.73 | 38.05 | 42.58 | -84.63 | 0.54 | 1892.7 | 1748.1 |
| | (110) | 83.56 | 39.39 | 48.22 | -95.63 | 0.81 | 1897.2 | 1544.2 |
| | (111) | 61.34 | 28.91 | 31.97 | -82.34 | -18.54 | 2106.2 | 1613.9 |
| | (010) | 77.21 | 36.39 | 41.32 | -80.8 | 2.41 | 2195.7 | 2035.6 |

| | | | | | | | | |
|---|---|---|---|---|---|---|---|---|
| 1700 | (110) | 79.86 | 37.9 | 42.21 | -93.9 | 1.93 | 2098.6 | 1862.8 |
| | (111) | 58.64 | 27.8 | 29.73 | -78.2 | -15.56 | 2243.5 | 1729.1 |
| 2000 | (010) | 74.94 | 35.35 | 40.3 | -77.81 | 2.79 | 2353.9 | 2164.4 |
| | (110) | 75.51 | 35.59 | 42.48 | -99.16 | -14.19 | 2285.5 | 1835.1 |
| | (111) | 56.76 | 26.75 | 28.78 | -52.53 | 5.04 | 2301.8 | 1930.5 |
| 3000 | (010) | 62.68 | 29.55 | 36.02 | -66.76 | 5.28 | 3395.6 | 2590.1 |
| | (110) | 62.17 | 29.31 | 34.87 | -80.34 | -10.59 | 3267.5 | 2527.6 |
| | (111) | 50.71 | 23.9 | 26.36 | -49.88 | 2.85 | 3230 | 2565.3 |

## L. Stresses and temperature on the cutting edge of the diamond tool while cutting 3C-SiC

Table L1. Average stresses and temperature on the cutting edge of the diamond tool while cutting single crystal 3C-SiC on different crystal planes obtained by ABOP potential function

| Workpiece temperature (K) | Crystal plane | von Mises stress on the cutting edge (GPa) | Tresca stress on the cutting edge (GPa) | Temperature on the cutting edge (K) |
|---|---|---|---|---|
| 300 | (010) | 66 | 38 | 773.6 |
| | (110) | 67.7 | 38.3 | 927.8 |
| | (111) | 61.4 | 34.3 | 679.1 |
| 900 | (010) | 61.2 | 34.3 | 878.5 |
| | (110) | 66.5 | 38 | 1037.3 |
| | (111) | 56.8 | 32.6 | 729.9 |
| 1200 | (010) | 60.4 | 34.1 | 937.2 |
| | (110) | 65.6 | 37 | 1049.8 |
| | (111) | 55.7 | 32.9 | 733.9 |
| 1400 | (010) | 59.8 | 33.7 | 958.9 |
| | (110) | 63.5 | 36.3 | 1060.3 |
| | (111) | 54.1 | 31.3 | 783.8 |
| 1700 | (010) | 56.1 | 32.2 | 927.3 |
| | (110) | 58.9 | 35.3 | 1010.4 |
| | (111) | 46.6 | 28.9 | 775.3 |

| | | | | |
|---|---|---|---|---|
| 2000 | (010) | 48.9 | 27.1 | 909.5 |
| | (110) | 54.3 | 30.1 | 983 |
| | (111) | 41.7 | 22.6 | 758.6 |
| 3000 | (010) | 44.5 | 24.7 | 871.4 |
| | (110) | 46.5 | 25.2 | 919.8 |
| | (111) | 38.5 | 21.1 | 738.2 |

# References


1. Brinksmeier, E. and O. Riemer, *Measurement of optical surfaces generated by diamond turning*. International Journal of Machine Tools and Manufacture, 1998. **38**(5): p. 699-705.

2. Goel, S., X. Luo, A. Agrawal, and R.L. Reuben, *Diamond machining of silicon: a review of advances in molecular dynamics simulation.* International Journal of Machine Tools and Manufacture, 2015. **88**: p. 131-164.

3. Goel, S., S.Z. Chavoshi, and A. Murphy, *Molecular dynamics simulation (MDS) to study nanoscale machining processes*, in *Nanofinishing Science and Technology*, V.K. Jain, Editor. 2016, Taylor and Francis: USA.

4. Ding, Y., *Quantum well state of cubic inclusions in hexagonal silicon carbide studied with ballistic electron emission microscopy*. 2004, The Ohio State University.

5. Goel, S., *The current understanding on the diamond machining of silicon carbide.* Journal of Physics D: Applied Physics, 2014. **47**(24): p. 243001-243037.

6. Pizzagalli, L., *Stability and mobility of screw dislocations in 4H, 2H and 3C silicon carbide.* Acta Materialia, 2014. **78**: p. 236-244.

7. Luo, X., S. Goel, and R.L. Reuben, *A quantitative assessment of nanometric machinability of major polytypes of single crystal silicon carbide.* Journal of the European Ceramic Society, 2012. **32**(12): p. 3423-3434.

8. Alder, B.J. and T.E. Wainwright, *Phase Transition for a Hard Sphere System.* J. Chem. Phys., 1957. **1208**(27).

9. Goel, S., N.H. Faisal, X. Luo, J. Yan, and A. Agrawal, *Nanoindentation of polysilicon and single crystal silicon: Molecular dynamics simulation and experimental validation.* Journal of Physics D: Applied Physics, 2014. **47**(27): p. 275304.

10. Dang, N.M., *Simultaneous micro-EDM and micro-ECM in low-resistivity deionized water*. 2013, National University of Singapore.

11. Chang, W., *Development of hybrid micro machining approaches and test-bed*. 2012, Heriot-Watt University.

12. Madou, M.J., *Fundamentals of microfabrication: the science of miniaturization*. 2002: CRC press.

13. Rai-Choudhury, P., *Handbook of microlithography, micromachining, and microfabrication: microlithography*. Vol. 1. 1997.

14. Luo, X., K. Cheng, D. Webb, and F. Wardle, *Design of ultraprecision machine tools with applications to manufacture of miniature and micro components.* Journal of Materials Processing Technology, 2005. **167**(2): p. 515-528.

15. El-Hofy, H., *Advanced machining processes: nontraditional and hybrid machining processes*. 2005: McGraw Hill Professional.

16. Zhu, Z., V. Dhokia, A. Nassehi, and S.T. Newman, *A review of hybrid manufacturing processes–state of the art and future perspectives.* International Journal of Computer Integrated Manufacturing, 2013. **26**(7): p. 596-615.

17. Aspinwall, D., R. Dewes, J.M. Burrows, M. Paul, and B. Davies, *Hybrid high speed machining (HSM): system design and experimental results for grinding/HSM and EDM/HSM.* CIRP Annals-Manufacturing Technology, 2001. **50**(1): p. 145-148.

18. She, C.-H. and C.-W. Hung, *Development of multi-axis numerical control program for mill—turn machine.* Proceedings of the Institution of Mechanical Engineers, Part B: Journal of Engineering Manufacture, 2008. **222**(6): p. 741-745.

19. Curtis, D., S. Soo, D. Aspinwall, and C. Sage, *Electrochemical superabrasive machining of a nickel-based aeroengine alloy using mounted grinding points.* CIRP Annals-Manufacturing Technology, 2009. **58**(1): p. 173-176.

20. Chavoshi, S.Z. and X. Luo, *Hybrid micro-machining processes: a review.* Precision Engineering, 2015. **41**: p. 1-23.

21. Lauwers, B., F. Klocke, A. Klink, A.E. Tekkaya, R. Neugebauer, and D. Mcintosh, *Hybrid processes in manufacturing.* CIRP Annals-Manufacturing Technology, 2014. **63**(2): p. 561-583.

22. Lauwers, B., *Surface integrity in hybrid machining processes.* Procedia Engineering, 2011. **19**: p. 241-251.

23. Sun, S., M. Brandt, and M. Dargusch, *Thermally enhanced machining of hard-to-machine materials—a review.* International Journal of Machine Tools and Manufacture, 2010. **50**(8): p. 663-680.

24. Belak, J.F. and I.F. Stowers, *A Molecular Dynamics model of Orthogonal Cutting process.* Proceedings of American Society Precision Engineering Annual conference, 1990: p. 76-79.

25. Landman, U., W.D. Luedtke, N.A. Burnham, and R.J. Colton, *Atomistic Mechanisms and Dynamics of Adhesion, Nanoindentation, and Fracture.* Science, 1990. **248**(4954): p. 454-461.

26. Belak, J., *Nanotribology: modeling atoms when surfaces collide*. 1994, Lawrence Livermore National Lab., CA (United States).

27. Ikawa, Naoya, Shimada, Shoichi, Tanaka, and Hiroaki, *Minimum thickness of cut in micromachining*. Nanotechnology, 1992. **1**(3): p. 6-9.

28. Voter, A.F. and J.D. Kress. *Atomistic Simulation of Diamond-Tip Machining of Nanoscale Features*. in *Principles of Cutting Mechanics: Applications of Ultra-Precision Machining and Grinding, 1993 Spring Topical Meeting* 1993. Tucson, AZ, USA: ASPE Proceedings.

29. Inamura, T., S. Shimada, N. Takezawa, and N. Nakahara, *Brittle/Ductile Transition Phenomena Observed in Computer Simulations of Machining Defect-Free Monocrystalline Silicon.* CIRP Annals - Manufacturing Technology, 1997. **46**(1): p. 31-34.

30. Rentsch, R. *Influence of Crystal Plane on the Nanomeric Cutting Process*. in *Proceedings of the First International Euspen Conference*. 1999. Bremen, Germany,.

31. Komanduri, R., N. Chandrasekaran, and L.M. Raff, *Effect of tool geometry in nanometric cutting: a molecular dynamics simulation approach.* Wear, 1998. **219**(1): p. 84-97.

32. Verlet, L., *Computer" experiments" on classical fluids. I. Thermodynamical properties of Lennard-Jones molecules.* Physical review, 1967. **159**(1): p. 98-103.

33. Pastewka, L., M. Mrovec, M. Moseler, and P. Gumbsch, *Bond order potentials for fracture, wear, and plasticity.* MRS Bulletin-Three decades of many-body potentials in materials research, 2012. **37**(5): p. 493-503.

34. Atkins, A. and D. Tabor. *Hardness and deformation properties of solids at very high temperatures*. in *Proceedings of the Royal Society of London A: Mathematical, Physical and Engineering Sciences*. 1966. The Royal Society.

35. Daw, M.S. and M.I. Baskes, *Embedded-atom method: Derivation and application to impurities, surfaces, and other defects in metals.* Physical Review B, 1984. **29**(12): p. 6443-6453.

36. Stillinger, F.H. and T.A. Weber, *Computer simulation of local order in condensed phases of silicon.* Physical Review B, 1985. **31**(8): p. 5262-5271.

37. Tersoff, J., *Empirical interatomic potential for silicon with improved elastic properties.* Physical Review B, 1988. **38**(14): p. 9902-9905.

38. Tersoff, J., *New empirical approach for the structure and energy of covalent systems.* Physical Review B, 1988. **37**(12): p. 6991-7000.

39. Tersoff, J., *Modeling solid-state chemistry: Interatomic potentials for multicomponent systems.* Physical Review B, 1989. **39**(8): p. 5566-5568.

40. Tersoff, J., *Erratum: Modeling solid-state chemistry: Interatomic potentials for multicomponent systems.* Physical Review B, 1990. **41**(5): p. 3248-3248.

41. Abell, G., *Empirical chemical pseudopotential theory of molecular and metallic bonding.* Physical Review B, 1985. **31**(10): p. 6184-6196.

42. Tersoff, J., *Chemical order in amorphous silicon carbide.* Physical Review B, 1994. **49**(23): p. 16349-16352.

43. Agrawal, P.M., L.M. Raff, and R. Komanduri, *Monte Carlo simulations of void-nucleated melting of silicon via modification in the Tersoff potential parameters.* Physical Review B, 2005. **72**(12): p. 125206-125217.

44. Erhart, P. and K. Albe, *Analytical potential for atomistic simulations of silicon, carbon, and silicon carbide.* Physical Review B, 2005. **71**(3): p. 035211-035225.

45. van Duin, A.C.T., S. Dasgupta, F. Lorant, and W.A. Goddard, *ReaxFF: A Reactive Force Field for Hydrocarbons.* The Journal of Physical Chemistry A, 2001. **105**(41): p. 9396-9409.

46. Pastewka, L., A. Klemenz, P. Gumbsch, and M. Moseler, *Screened empirical bond-order potentials for Si-C.* Physical Review B, 2013. **87**(20): p. 205410-205422.

47. Pastewka, L., P. Pou, R. Pérez, P. Gumbsch, and M. Moseler, *Describing bond-breaking processes by reactive potentials: Importance of an environment-dependent interaction range.* Physical Review B, 2008. **78**(16): p. 161402-161406.

48. Goel, S., W.B. Rashid, X. Luo, A. Agrawal, and V. Jain, *A theoretical assessment of surface defect machining and hot machining of nanocrystalline silicon carbide.* Journal of Manufacturing Science and Engineering, 2014. **136**(2): p. 021015-021027.

49. Fang, T.-H., C.-I. Weng, and J.-G. Chang, *Molecular dynamics analysis of temperature effects on nanoindentation measurement.* Materials Science and Engineering: A, 2003. **357**(1): p. 7-12.

50. Liu, C.-L., T.-H. Fang, and J.-F. Lin, *Atomistic simulations of hard and soft films under nanoindentation.* Materials Science and Engineering: A, 2007. **452**: p. 135-141.

51. Hsieh, J.-Y., S.-P. Ju, S.-H. Li, and C.-C. Hwang, *Temperature dependence in nanoindentation of a metal substrate by a diamondlike tip.* Physical Review B, 2004. **70**(19): p. 195424-195433.

52. Wheeler, J., D. Armstrong, W. Heinz, and R. Schwaiger, *High temperature nanoindentation: The state of the art and future challenges.* Current Opinion in Solid State and Materials Science, 2015. **19**(6): p. 354-366.

53. Wheeler, J., P. Brodard, and J. Michler, *Elevated temperature, in situ indentation with calibrated contact temperatures.* Philosophical Magazine, 2012. **92**(25-27): p. 3128-3141.

54. Wheeler, J. and J. Michler, *Elevated temperature, nano-mechanical testing in situ in the scanning electron microscope.* Review of Scientific Instruments, 2013. **84**(4): p. 045103-045118.

55. Schuh, C.A., C.E. Packard, and A.C. Lund, *Nanoindentation and contact-mode imaging at high temperatures.* Journal of materials research, 2006. **21**(03): p. 725-736.

56. Trenkle, J.C., C.E. Packard, and C.A. Schuh, *Hot nanoindentation in inert environments.* Review of Scientific Instruments, 2010. **81**(7): p. 073901-073914.

57. Suzuki, T. and T. Ohmura, *Ultra-microindentation of silicon at elevated temperatures.* Philosophical Magazine A, 1996. **74**(5): p. 1073-1084.

58. Smith, J. and S. Zheng, *High temperature nanoscale mechanical property measurements.* Surface Engineering, 2000. **16**(2): p. 143-146.

59. Beake, B.D. and J.F. Smith, *High-temperature nanoindentation testing of fused silica and other materials.* Philosophical Magazine A, 2002. **82**(10): p. 2179-2186.

60. Xia, J., C. Li, and H. Dong, *Hot-stage nano-characterisations of an iron aluminide.* Materials Science and Engineering: A, 2003. **354**(1): p. 112-120.

61. Lund, A.C., A.M. Hodge, and C.A. Schuh, *Incipient plasticity during nanoindentation at elevated temperatures.* Applied physics letters, 2004. **85**(8): p. 1362-1364.

62. Schuh, C.A., A.C. Lund, and T. Nieh, *New regime of homogeneous flow in the deformation map of metallic glasses: elevated temperature nanoindentation experiments and mechanistic modeling.* Acta Materialia, 2004. **52**(20): p. 5879-5891.

63. Sawant, A. and S. Tin, *High temperature nanoindentation of a Re-bearing single crystal Ni-base superalloy.* Scripta materialia, 2008. **58**(4): p. 275-278.

64. Trelewicz, J.R. and C.A. Schuh, *Hot nanoindentation of nanocrystalline Ni–W alloys.* Scripta Materialia, 2009. **61**(11): p. 1056-1059.

65. Beake, B., J. Smith, A. Gray, G. Fox-Rabinovich, S. Veldhuis, and J. Endrino, *Investigating the correlation between nano-impact fracture resistance and hardness/modulus ratio from nanoindentation at 25–500° C and the fracture resistance and lifetime of cutting tools with Ti 1− x Al x N (x= 0.5 and 0.67) PVD coatings in milling operations.* Surface and Coatings Technology, 2007. **201**(8): p. 4585-4593.

66. Beake, B.D., G. Fox-Rabinovich, S. Veldhuis, and S. Goodes, *Coating optimisation for high speed machining with advanced nanomechanical test methods.* Surface and Coatings Technology, 2009. **203**(13): p. 1919-1925.

67. Bhakhri, V. and R. Klassen, *Investigation of high-temperature plastic deformation using instrumented microindentation tests. Part IThe deformation of three aluminum alloys at 473 K to 833 K.* Journal of materials science, 2006. **41**(8): p. 2259-2270.

68. Fox-Rabinovich, G., S. Veldhuis, G. Dosbaeva, K. Yamamoto, A. Kovalev, D. Wainstein, I. Gershman, L. Shuster, and B. Beake, *Nanocrystalline coating design for extreme applications based on the concept of complex adaptive behavior.* Journal of Applied Physics, 2008. **103**(8): p. 083510-083520.

69. Giuliani, F., A. Goruppa, S. Lloyd, D. Teer, and W. Clegg. *Indentation of AlN/CrN Multilayers from Room Temperature to 400° C.* in *Materials Science Forum*. 2005. Trans Tech Publ.

70. Gray, A. and B.D. Beake, *Elevated temperature nanoindentation and viscoelastic behaviour of thin poly (ethylene terephthalate) films.* Journal of nanoscience and nanotechnology, 2007. **7**(7): p. 2530-2533.

71. Liu, Y., J. Teo, S. Tung, and K. Lam, *High-temperature creep and hardness of eutectic 80Au/20Sn solder.* Journal of Alloys and Compounds, 2008. **448**(1): p. 340-343.

72. Packard, C.E., J. Schroers, and C.A. Schuh, *In situ measurements of surface tension-driven shape recovery in a metallic glass.* Scripta Materialia, 2009. **60**(12): p. 1145-1148.

73. Schuh, C., J. Mason, and A. Lund, *Quantitative insight into dislocation nucleation from high-temperature nanoindentation experiments.* Nature Materials, 2005. **4**(8): p. 617-621.

74. Wood, A.M. and T. Clyne, *Measurement and modelling of the nanoindentation response of shape memory alloys.* Acta materialia, 2006. **54**(20): p. 5607-5615.

75. Bhuyan, S., J. Bradby, S. Ruffell, B. Haberl, C. Saint, J. Williams, and P. Munroe, *Phase stability of silicon during indentation at elevated temperature: evidence for a direct transformation from metallic Si-II to diamond cubic Si-I.* MRS Communications, 2012. **2**(01): p. 9-12.

76. Ruffell, S., J. Bradby, J. Williams, D. Munoz-Paniagua, S. Tadayyon, L. Coatsworth, and P. Norton, *Nanoindentation-induced phase transformations in silicon at elevated temperatures.* Nanotechnology, 2009. **20**(13): p. 135603-135608.

77. Domnich, V., Y. Aratyn, W.M. Kriven, and Y. Gogotsi, *Temperature dependence of silicon hardness: experimental evidence of phase transformations.* Rev. Adv. Mater. Sci, 2008. **17**: p. 33-41.

78. Brinksmeier, E. and W. Preuss, *Micro-machining.* Philosophical Transactions of the Royal Society A: Mathematical, Physical and Engineering Sciences, 2012. **370**(1973): p. 3973-3992.

79. Zhang, Z., F. Fang, X. Hu, and C. Sun, *Molecular dynamics study on various nanometric cutting boundary conditions.* Journal of Vacuum Science & Technology B, 2009. **27**(3): p. 1355-1360.

80. Yoo, S., X.C. Zeng, and J.R. Morris, *The melting lines of model silicon calculated from coexisting solid–liquid phases.* The Journal of chemical physics, 2004. **120**(3): p. 1654-1656.

81. Cook, S.J. and P. Clancy, *Comparison of semi-empirical potential functions for silicon and germanium.* Physical Review B, 1993. **47**(13): p. 7686-7699.

82. Goel, S., X. Luo, and R.L. Reuben, *Wear mechanism of diamond tools against single crystal silicon in single point diamond turning process.* Tribology International, 2013. **57**(0): p. 272-281.

83. Plimpton, S., *Fast parallel algorithms for short-range molecular dynamics.* Journal of computational physics, 1995. **117**(1): p. 1-19.

84. Okada, Y. and Y. Tokumaru, *Precise determination of lattice parameter and thermal expansion coefficient of silicon between 300 and 1500 K.* Journal of applied physics, 1984. **56**(2): p. 314-320.

85. Li, Z. and R. Bradt, *Thermal expansion of the cubic (3C) polytype of SiC.* Journal of materials science, 1986. **21**(12): p. 4366-4368.

86. Stukowski, A., *Visualization and analysis of atomistic simulation data with OVITO–the Open Visualization Tool.* Modelling and Simulation in Materials Science and Engineering, 2009. **18**(1): p. 015012-015019.

87. Stukowski, A. and K. Albe, *Extracting dislocations and non-dislocation crystal defects from atomistic simulation data.* Modelling and Simulation in Materials Science and Engineering, 2010. **18**(8): p. 085001-085014.

88. Komanduri, R., Ch, N. rasekaran, and L.M. Raff, *Molecular dynamics simulation of the nanometric cutting of silicon.* Philosophical Magazine Part B, 2001. **81**(12): p. 1989 - 2019.

89. Korte, S., J. Barnard, R. Stearn, and W. Clegg, *Deformation of silicon–insights from microcompression testing at 25–500 C.* International Journal of Plasticity, 2011. **27**(11): p. 1853-1866.

90. Shibata Y., F.S., Makino E. and Ikeda M., *Ductile-regime turning mechanism of single-crystal silicon.* Precision Engineering, 1996. **18**: p. 129-137.

91. Malekian, M., M. Mostofa, S. Park, and M. Jun, *Modeling of minimum uncut chip thickness in micro machining of aluminum.* Journal of Materials Processing Technology, 2012. **212**(3): p. 553-559.

92. Toenshoff, H.K. and B. Denkena, *Basics of cutting and abrasive processes*. 2013: Springer Publication.

93. Jasinevicius, R., J. Duduch, and P. Pizani, *Structure evaluation of submicrometre silicon chips removed by diamond turning.* Semiconductor science and technology, 2007. **22**(5): p. 561-573.

94. Koné, F., C. Czarnota, B. Haddag, and M. Nouari, *Modeling of velocity-dependent chip flow angle and experimental analysis when machining 304L austenitic stainless steel with groove coated-carbide tools.* Journal of Materials Processing Technology, 2013. **213**(7): p. 1166-1178.

95. Maras E., Trushin O., Stukowski A., Ala-Nissila T., and Jonsson H., *Global transition path search for dislocation formation in Ge on Si(001).* Computer Physics Communications, 2016. **205**: p. 13-21.

96. Wang, M., W. Wang, and Z. Lu, *Anisotropy of machined surfaces involved in the ultra-precision turning of single-crystal silicon—a simulation and experimental study.* The International Journal of Advanced Manufacturing Technology, 2012. **60**(5-8): p. 473-485.

97. Al-Sayegh, R. and C. Makatsoris, *Vision-Augmented Molecular Dynamics Simulation of Nanoindentation.* Journal of Nanomaterials, 2015. **2015**: p. 1-11.

98. Robinson, G. and M. Jackson, *A review of micro and nanomachining from a materials perspective.* Journal of Materials Processing Technology, 2005. **167**(2): p. 316-337.

99. Usui, E., T. Shirakashi, and T. Kitagawa, *Analytical prediction of three dimensional cutting process—Part 3: Cutting temperature and crater wear of carbide tool.* Journal of Engineering for industry, 1978. **100**(2): p. 236-243.

100. Childs, T., *Metal machining: theory and applications*. 2000: Butterworth-Heinemann Publication.

101. Shimizu, F., S. Ogata, and J. Li, *Theory of shear banding in metallic glasses and molecular dynamics calculations.* Materials transactions, 2007. **48**(11): p. 2923-2927.

102. Domnich, V. and Y. Gogotsi, *Phase transformations in silicon under contact loading.* Reviews on Advanced Materials Science(Russia), 2002. **3**(1): p. 1-36.

103. Goel, S., X. Luo, and R.L. Reuben, *Wear mechanism of diamond tools against single crystal silicon in single point diamond turning process.* Tribology International, 2013. **57**: p. 272-281.

104. Mussi, A., D. Eyidi, A. Shiryaev, and J. Rabier, *TEM observations of dislocations in plastically deformed diamond.* physica status solidi (a), 2013. **210**(1): p. 191-194.

105. Yu, X., P. Raterron, J. Zhang, Z. Lin, L. Wang, and Y. Zhao, *Constitutive law and flow mechanism in diamond deformation.* Scientific reports, 2012. **2**(876): p. 1-7.

106. Chacham, H. and L. Kleinman, *Instabilities in diamond under high shear stress.* Physical review letters, 2000. **85**(23): p. 4904-4907.

107. Zhao, S., E. Hahn, B. Kad, B. Remington, C. Wehrenberg, E. Bringa, and M. Meyers, *Amorphization and nanocrystallization of silicon under shock compression.* Acta Materialia, 2016. **103**: p. 519-533.

108. Zhao, S., B. Kad, E. Hahn, B. Remington, C. Wehrenberg, C. Huntington, H.-S. Park, E. Bringa, K. More, and M. Meyers, *Pressure and shear-induced amorphization of silicon.* Extreme Mechanics Letters, 2015. **5**: p. 74-80.

109. El Nabi, F.A., J. Godet, S. Brochard, and L. Pizzagalli, *Onset of ductility and brittleness in silicon nanowires mediated by dislocation nucleation.* Modelling and Simulation in Materials Science and Engineering, 2015. **23**(2): p. 025010-025023.

110. Godet, J., E. Nabi, F. Abed, S. Brochard, and L. Pizzagalli, *Surface effects on the mechanical behavior of silicon nanowires: Consequence on the brittle to ductile transition at low scale and low temperature.* physica status solidi (a), 2015. **212**(8): p. 1643-1648.

111. Li, Z. and R. Picu, *Shuffle-glide dislocation transformation in Si.* Journal of Applied Physics, 2013. **113**(8): p. 083519-083526.

112. Goel, S., A. Kovalchenko, A. Stukowski, and G. Cross, *Influence of microstructure on the cutting behaviour of silicon.* Acta Materialia, 2016. **105**: p. 464-478.

113. Li, J., Q. Fang, L. Zhang, and Y. Liu, *Subsurface damage mechanism of high speed grinding process in single crystal silicon revealed by atomistic simulations.* Applied Surface Science, 2015. **324**: p. 464-474.

114. Coleman, S., D. Spearot, and L. Capolungo, *Virtual diffraction analysis of Ni [0 1 0] symmetric tilt grain boundaries.* Modelling and Simulation in Materials Science and Engineering, 2013. **21**(5): p. 055020-055036.

115. Odo, E., D. Britton, G. Gonfa, and M. Harting, *Structure and characterization of silicon nanoparticles produced using a vibratory disc mill.* The African Review of Physics, 2012. **7**: p. 45-56.

116. Joos, B., Q. Ren, and M. Duesbery, *Peierls-Nabarro model of dislocations in silicon with generalized stacking-fault restoring forces.* Physical Review B, 1994. **50**(9): p. 5890-5898.

117. Izumi, S. and S. Yip, *Dislocation nucleation from a sharp corner in silicon.* Journal of Applied Physics, 2008. **104**(3): p. 033513-033517.

118. Luzzi, D. and M. Meshii, *The crystalline to amorphous transition of intermetallic compounds under electron irradiation-a review.* Res Mechanica, 1987. **21**(3): p. 207-247.

119. Meng, W., P. Okamoto, L. Thompson, B. Kestel, and L. Rehn, *Hydrogen-induced crystal to glass transformation in Zr3Al.* Applied physics letters, 1988. **53**(19): p. 1820-1822.

120. Godet, J., P. Hirel, S. Brochard, and L. Pizzagalli, *Evidence of two plastic regimes controlled by dislocation nucleation in silicon nanostructures.* Journal of Applied Physics, 2009. **105**(2): p. 026104-026107.

121. Godet, J., L. Pizzagalli, S. Brochard, and P. Beauchamp, *Theoretical study of dislocation nucleation from simple surface defects in semiconductors.* Physical Review B, 2004. **70**(5): p. 054109-054117.

122. Nguyen, H.T. and V. Van Hoang, *Melting of crystalline silicon thin films.* Computational Materials Science, 2014. **89**: p. 97-101.

123. Zhang, Q., Q. Li, and M. Li, *Melting and superheating in solids with volume shrinkage at melting: A molecular dynamics study of silicon.* The Journal of chemical physics, 2013. **138**(4): p. 044504-044511.

124. Goel, S., A. Stukowski, X. Luo, A. Agrawal, and R.L. Reuben, *Anisotropy of single-crystal 3C–SiC during nanometric cutting.* Modelling and Simulation in Materials Science and Engineering, 2013. **21**(6): p. 065004-065024.

125. Field, J., *The mechanical and strength properties of diamond.* Reports on Progress in Physics, 2012. **75**(12): p. 126505-126540.

126. Waddington, C.P., *A comparison of the plastic deformation and creep of type I, type II and synthetic diamonds at 1100 C under conditions of point loading.* Journal of Hard Materials, 1990. **1**(1): p. 3-10.

127. Cai, M., X. Li, and M. Rahman, *Study of the temperature and stress in nanoscale ductile mode cutting of silicon using molecular dynamics simulation.* Journal of Materials Processing Technology, 2007. **192**: p. 607-612.

128. Nabarro, F., *Dislocations in a simple cubic lattice.* Proceedings of the Physical Society, 1947. **59**(2): p. 256-274.

129. Peierls, R., *The size of a dislocation.* Proceedings of the Physical Society, 1940. **52**(1): p. 34-38.

130. Mishra, M. and I. Szlufarska, *Dislocation controlled wear in single crystal silicon carbide.* Journal of Materials Science, 2013. **48**(4): p. 1593-1603.

131. George, A., *Plastic deformation of semiconductors: some recent advances and persistent challenges.* Materials Science and Engineering: A, 1997. **233**(1): p. 88-102.

132. Chen, H.-P., R.K. Kalia, A. Nakano, P. Vashishta, and I. Szlufarska, *Multimillion-atom nanoindentation simulation of crystalline silicon carbide: Plane dependence and anisotropic pileup.* Journal of Applied Physics, 2007. **102**(6): p. 063514-063523.

133. Boulle, A., D. Chaussende, F. Pecqueux, F. Conchon, L. Latu-Romain, and O. Masson, *Determination of stacking fault densities in 3C-SiC crystals by diffuse X-ray scattering.* physica status solidi (a), 2007. **204**(8): p. 2528-2534.

134. Mishra, M. and I. Szlufarska, *Possibility of high-pressure transformation during nanoindentation of SiC.* Acta Materialia, 2009. **57**(20): p. 6156-6165.

135. Patten, J., W. Gao, and K. Yasuto, *Ductile regime nanomachining of single-crystal silicon carbide.* Journal of manufacturing science and engineering, 2005. **127**(3): p. 522-532.

136. Yamakov, V., D. Warner, R. Zamora, E. Saether, W. Curtin, and E. Glaessgen, *Investigation of crack tip dislocation emission in aluminum using multiscale molecular dynamics simulation and continuum modeling.* Journal of the Mechanics and Physics of Solids, 2014. **65**: p. 35-53.

137. Sun, Y., S. Izumi, S. Sakai, K. Yagi, and H. Nagasawa, *Core element effects on dislocation nucleation in 3C–SiC: Reaction pathway analysis.* Computational Materials Science, 2013. **79**: p. 216-222.

138. Hirth, J.P. and J. Lothe, *Theory of dislocations*. 1982: Wiley Publication.

139. Demenet, J.-L., M. Hong, and P. Pirouz, *Plastic behavior of 4H-SiC single crystals deformed at low strain rates.* Scripta materialia, 2000. **43**(9): p. 865-870.

140. Lee, J.H., T.B. Holland, A.K. Mukherjee, X. Zhang, and H. Wang, *Direct observation of Lomer-Cottrell Locks during strain hardening in nanocrystalline nickel by in situ TEM.* Scientific reports, 2013. **3**(1061): p. 1-6.

141. Yamakov, V., D. Wolf, S. Phillpot, A. Mukherjee, and H. Gleiter, *Deformation-mechanism map for nanocrystalline metals by molecular-dynamics simulation.* nature materials, 2004. **3**(1): p. 43-47.

142. Sitch, P., R. Jones, S. Öberg, and M. Heggie, *Ab initio investigation of the dislocation structure and activation energy for dislocation motion in silicon carbide.* Physical Review B, 1995. **52**(7): p. 4951-4955.

143. Li, J., W. Cai, J. Chang, and S. Yip, *Commentary on Atomistic Simulations of Materials Strength and Deformation: Prospects for Mechanistic Insights.* ISMS-2, A, 2001: p. 220-233.

144. Huang, D., Y. Ikuhara, M. Narisawa, and K. Okamura, *Characterization of β-Silicon Carbide Powders Synthesized by the Carbothermal Reduction of Silicon Carbide Precursors.* Journal of the American Ceramic Society, 1998. **81**(12): p. 3173-3176.

145. Yoshida, M., A. Onodera, M. Ueno, K. Takemura, and O. Shimomura, *Pressure-induced phase transition in SiC.* Physical Review B, 1993. **48**(14): p. 10587-10590.

146. Noreyan, A., J. Amar, and I. Marinescu, *Molecular dynamics simulations of nanoindentation of-SiC with diamond indenter.* Materials Science and Engineering: B, 2005. **117**(3): p. 235-240.

147. Vashishta, P., R.K. Kalia, A. Nakano, and J.P. Rino, *Interaction potential for silicon carbide: a molecular dynamics study of elastic constants and vibrational density of states for crystalline and amorphous silicon carbide.* Journal of applied physics, 2007. **101**(10): p. 103515-103528.

148. Xiao, G., S. To, and G. Zhang, *The mechanism of ductile deformation in ductile regime machining of 6H SiC.* Computational Materials Science, 2015. **98**: p. 178-188.

149. Gogotsi, Y., G. Zhou, S.-S. Ku, and S. Cetinkunt, *Raman microspectroscopy analysis of pressure-induced metallization in scratching of silicon.* Semiconductor science and technology, 2001. **16**(5): p. 345-352.

150. Gerbig, Y., S. Stranick, D. Morris, M. Vaudin, and R. Cook, *Effect of crystal plane on phase transformations during indentation of silicon.* Journal of Materials Research, 2009. **24**(03): p. 1172-1183.

151. Wu, H., *Fundamental investigations of cutting of silicon for photovoltaic applications*. 2012, Georgia Institute of Technology.

152. Li, Z.P., H. Zhao, and F.H. Zhang. *Study on the Ductile Removal Behavior of K9 Glass with Nano-Scratch*. in *Advanced Materials Research*. 2016. Trans Tech Publ.

153. Williams, J., *Analytical models of scratch hardness.* Tribology international, 1996. **29**(8): p. 675-694.

154. Briscoe, B.J., E. Pelillo, and S.K. Sinha, *Scratch hardness and deformation maps for polycarbonate and polyethylene.* Polymer Engineering & Science, 1996. **36**(24): p. 2996-3005.

155. Piltz, R., J. Maclean, S. Clark, G. Ackland, P. Hatton, and J. Crain, *Structure and properties of silicon XII: a complex tetrahedrally bonded phase.* Physical Review B, 1995. **52**(6): p. 4072-4085.

156. Ge, D., V. Domnich, and Y. Gogotsi, *High-resolution transmission electron microscopy study of metastable silicon phases produced by nanoindentation.* Journal of applied physics, 2003. **93**(5): p. 2418-2423.

157. Gassilloud, R., C. Ballif, P. Gasser, G. Buerki, and J. Michler, *Deformation mechanisms of silicon during nanoscratching.* physica status solidi (a), 2005. **202**(15): p. 2858-2869.

158. Domnich, V. and Y. Gogotsi, *Handbook of surface and interface of materials*. 2001, New York: Academic Press.

159. Ruffell, S., J. Bradby, and J.S. Williams, *Annealing kinetics of nanoindentation-induced polycrystalline high pressure phases in crystalline silicon.* Appl. Phys. Lett., 2007. **90**: p. 131901-131904.

160. Zeng, Z., Q. Zeng, W.L. Mao, and S. Qu, *Phase transitions in metastable phases of silicon.* Journal of Applied Physics, 2014. **115**(10): p. 103514-103520.

161. Olson, G. and J. Roth, *Kinetics of solid phase crystallization in amorphous silicon.* Materials Science Reports, 1988. **3**(1): p. 1-77.

162. Donnelly, S., R. Birtcher, V. Vishnyakov, and G. Carter, *Annealing of isolated amorphous zones in silicon.* Applied physics letters, 2003. **82**(12): p. 1860-1862.

163. Donnelly, S.E., R. Birtcher, V. Vishnyakov, P. Edmondson, and G. Carter, *Anomalous annealing behavior of isolated amorphous zones in silicon.* Nuclear Instruments and Methods in Physics Research Section B: Beam Interactions with Materials and Atoms, 2006. **242**(1): p. 595-597.

164. Zhang, Z., J. Yan, and T. Kuriyagawa, *Study on tool wear characteristics in diamond turning of reaction-bonded silicon carbide.* The International Journal of Advanced Manufacturing Technology, 2011. **57**(1-4): p. 117-125.

165. Vogelgesang, R., A. Alvarenga, H. Kim, A. Ramdas, S. Rodriguez, M. Grimsditch, and T. Anthony, *Multiphonon Raman and infrared spectra of isotopically controlled diamond.* Physical Review B, 1998. **58**(9): p. 5408-5416.

166. Bachmann, P.K. and D.U. Wiechert, *Optical characterization of diamond.* Diamond and Related Materials, 1992. **1**(5): p. 422-433.

167. Stillinger, F. and T. Weber, *Lindemann melting criterion and the Gaussian core model.* Physical Review B, 1980. **22**(8): p. 3790-3794.

168. Rycroft, C., *Voro++: A three-dimensional Voronoi cell library in C++*. Lawrence Berkeley National Laboratory, 2009.

169. Glazov, V. and O.D. Shchelikov, *Volume changes during melting and heating of silicon and germanium melts.* High Temperature, 2000. **38**(3): p. 405-412.

170. Logan, R. and W. Bond, *Density change in silicon upon melting.* Journal of Applied Physics, 1959. **30**(3): p. 322-322.

171. Soma, T. and H. Kagaya, *Properties of silicon, EMIS data reviews series No. 4.* Institution of Electrical Engineers, London, New York, 1988. **33**.

172. Lee, B. and R.E. Rudd, *First-principles study of the Young's modulus of Si〈001〉 nanowires.* Physical review B, 2007. **75**(4): p. 041305-041309.

173. Justo, J.F., M.Z. Bazant, E. Kaxiras, V. Bulatov, and S. Yip, *Interatomic potential for silicon defects and disordered phases.* Physical Review B, 1998. **58**(5): p. 2539-2550.

174. Godet, J., L. Pizzagalli, S. Brochard, and P. Beauchamp, *Comparison between classical potentials and ab initio methods for silicon under large shear.* Journal of Physics: Condensed Matter, 2003. **15**(41): p. 6943-6953.

175. Godet, J., L. Pizzagalli, S. Brochard, and P. Beauchamp, *Computer study of microtwins forming from surface steps of silicon.* Computational materials science, 2004. **30**(1): p. 16-20.

176. Morris, J.R. and X. Song, *The melting lines of model systems calculated from coexistence simulations.* Journal of Chemical Physics, 2002. **116**(21): p. 9352-9358.

177. Wang, J., P.A. Apte, J.R. Morris, and X.C. Zeng, *Freezing point and solid-liquid interfacial free energy of stockmayer dipolar fluids: A molecular dynamics simulation study.* The Journal of Chemical Physics, 2013. **139**(11): p. 114705-114717.

178. Lide, D., *CRC Handbook of Chemistry and Physics 2004-2005: A Ready-Reference Book of Chemical and Physical Data*. 2004, CRC press Boca Raton.

179. Hull, R., *Properties of crystalline silicon*. 1999: IET.

180. Lambrecht, W., B. Segall, M. Methfessel, and M. Van Schilfgaarde, *Calculated elastic constants and deformation potentials of cubic SiC.* Physical Review B, 1991. **44**(8): p. 3685-3694.

181. Juan, Y.-M., *Ledge effects on dislocation emission from a crack tip: a first-principles study for silicon.* Philosophical magazine letters, 1996. **73**(5): p. 233-240.

182. Zimmerman, J.A., H. Gao, and F.F. Abraham, *Generalized stacking fault energies for embedded atom FCC metals.* Modelling and Simulation in Materials Science and Engineering, 2000. **8**(2): p. 103-115.

183. Van Swygenhoven, H., P. Derlet, and A. Frøseth, *Stacking fault energies and slip in nanocrystalline metals.* Nature materials, 2004. **3**(6): p. 399-403.

184. Amodeo, J., P. Carrez, B. Devincre, and P. Cordier, *Multiscale modelling of MgO plasticity.* Acta Materialia, 2011. **59**(6): p. 2291-2301.

185. Brandl, C., P. Derlet, and H. Van Swygenhoven, *General-stacking-fault energies in highly strained metallic environments: Ab initio calculations.* Physical Review B, 2007. **76**(5): p. 054124-054132.

186. Pizzagalli, L., J. Godet, J. Guénolé, S. Brochard, E. Holmstrom, K. Nordlund, and T. Albaret, *A new parametrization of the Stillinger–Weber potential for an improved description of defects and plasticity of silicon.* Journal of Physics: Condensed Matter, 2013. **25**(5): p. 055801-055813.

187. Wang, C., H. Wang, T. Huang, X. Xue, F. Qiu, and Q. Jiang, *Generalized-stacking-fault energy and twin-boundary energy of hexagonal close-packed Au: A first-principles calculation.* Scientific reports, 2015. **5**(10213): p. 1-11.

188. Rice, J.R., *Dislocation nucleation from a crack tip: an analysis based on the Peierls concept.* Journal of the Mechanics and Physics of Solids, 1992. **40**(2): p. 239-271.

189. Thomas, T., D. Pandey, and U.V. Waghmare, *Soft modes at the stacking faults in SiC crystals: First-principles calculations.* Physical Review B, 2008. **77**(12): p. 121203-121207.

190. Cheng, G., T.-H. Chang, Q. Qin, H. Huang, and Y. Zhu, *Mechanical properties of silicon carbide nanowires: effect of size-dependent defect density.* Nano letters, 2014. **14**(2): p. 754-758.

191. Umeno, Y., K. Yagi, and H. Nagasawa, *Ab initio density functional theory calculation of stacking fault energy and stress in 3C-SiC.* physica status solidi (b), 2012. **249**(6): p. 1229-1234.

192. Kubin, L., *Dislocations, mesoscale simulations and plastic flow*. Vol. 5. 2013: Oxford University Press.